Materials Horizons: From Nature to Nanomaterials

Runa Kumari
Balamati Choudhury *Editors*

Multiscale Modelling of Advanced Materials

Springer

Materials Horizons: From Nature to Nanomaterials

Series Editor

Vijay Kumar Thakur, School of Aerospace, Transport and Manufacturing, Cranfield University, Cranfield, UK

Materials are an indispensable part of human civilization since the inception of life on earth. With the passage of time, innumerable new materials have been explored as well as developed and the search for new innovative materials continues briskly. Keeping in mind the immense perspectives of various classes of materials, this series aims at providing a comprehensive collection of works across the breadth of materials research at cutting-edge interface of materials science with physics, chemistry, biology and engineering.

This series covers a galaxy of materials ranging from natural materials to nanomaterials. Some of the topics include but not limited to: biological materials, biomimetic materials, ceramics, composites, coatings, functional materials, glasses, inorganic materials, inorganic-organic hybrids, metals, membranes, magnetic materials, manufacturing of materials, nanomaterials, organic materials and pigments to name a few. The series provides most timely and comprehensive information on advanced synthesis, processing, characterization, manufacturing and applications in a broad range of interdisciplinary fields in science, engineering and technology.

This series accepts both authored and edited works, including textbooks, monographs, reference works, and professional books. The books in this series will provide a deep insight into the state-of-art of *Materials Horizons* and serve students, academic, government and industrial scientists involved in all aspects of materials research.

More information about this series at http://www.springer.com/series/16122

Runa Kumari · Balamati Choudhury
Editors

Multiscale Modelling of Advanced Materials

Springer

Editors
Runa Kumari
Birla Institute of Technology and Science
Hyderabad, Telangana, India

Balamati Choudhury
Centre for Electromagnetics
National Aerospace Laboratories
Bangalore, Karnataka, India

ISSN 2524-5384 ISSN 2524-5392 (electronic)
Materials Horizons: From Nature to Nanomaterials
ISBN 978-981-15-2266-6 ISBN 978-981-15-2267-3 (eBook)
https://doi.org/10.1007/978-981-15-2267-3

This Springer imprint is published by the registered company Springer Nature Singapore Pte Ltd.
The registered company address is: 152 Beach Road, #21-01/04 Gateway East, Singapore 189721, Singapore

Preface

Multiscale-modeling of materials has been considered as a challenging field because of the computational requirement to scale-up the atomic-level modeling to realizable component-level modeling. The modeling can be done from the atomic level through semi-empirical approaches with the advancements of improved algorithms and computational methods. For example, Green's function method solves complicated, inhomogeneous differential equations. However, the development of methods that efficiently couple multiple scales in material science is still a challenge. There exist several applications in the electromagnetic field which uses the advanced materials in order to investigate their electronic, optical, and thermodynamic properties. In this book, we focus on the feasibilities and applications of different advanced materials such as metamaterials, graphene, and CNT. These advanced materials bring good performance in a wide range of electromagnetic applications. Apart from the theoretical background of these advanced materials, this volume includes model-based electromagnetic engineering applications.

The first chapter gives an insight into the various material selection techniques for selecting materials in electronic devices. Material selection approaches provide an easy way to recognize the trade-offs between conflicting materials' properties and also to select the optimal material for better device performance. These approaches also help us to provide ranking to the alternatives from best to worst. This chapter describes three different material selection methodologies, Asbhy's approach, TOPSIS, and VIKOR in detail and explains the steps to be taken for each methodology to find out the most promising material for a given device.

Metamaterial (MTM) has received considerable attention in recent years due to eccentric and alluring properties compared to ordinary material which is not found in nature. Chapter 2 aims at investigating the electromagnetic and left-handed (LH) behavior of some new type of low loss planar. Three different metamaterial designs have been described. In the first model, the reflection spectra and left-hand properties of the planar broadside-coupled metamaterial structure have been discussed. The second model is a skewed omega LHM unit cell structure that has been

designed using EM simulation and measured, and its electrical characteristics have been retrieved. The third design is based on the studies of the transmission spectra and LH transmission band of the conformal Sectored Split Sierpinski Resonator LHM unit cell configuration suitable for both planar and curved surfaces' applications.

The advancements in stealth materials have come a long way since the primitive technologies of the past century. Chapter 3 provides the challenge of achieving dual stealth with respect to radars and IR with the help of RAMs such as CNT composites with their high thermal conductivity, metamaterials with flexible properties and IR coatings that can be applied on top of existing RAMs. The limit of narrow bandwidths is overcome by using metamaterials that are tunable to frequencies or by adding thin graphene layers on top of them. The advancements in radars such as the bistatic radar can be countered by upcoming technologies like invisibility cloak.

Chapter 4 includes design and RCS estimation of different radar absorbing structures based on nanomaterials. Detailed literature in the field of nano metamaterials has been carried out. Analysis of RCS Radar has been included for novel design with a reference of PEC. The absorber revealed a significant reduction in RCS when it is compared with PEC. Similarly, a graphene-based radar absorber has been designed in the X band. The design has given absorption of more than 85%. Unlike the conventional radar absorber designs, the nanomaterial-based designs have been presented which show better performance in broadband frequencies.

In Chap. 5, an extended study has been conducted on 3D metamaterial multilayer structures with circuit and EM simulation to validate the geometry as metamaterial structure. The S-parameters are analyzed for these 3D-structures to calculate the effective material parameters such as permittivity ($\mathcal{E}_r$), permeability (μ_r) and refractive index (n). The analysis for 3D metamaterial structures exhibits negative material characteristics that are suitable for various high-frequency wireless applications. In addition, the 3D metamaterial structures can be used as metamaterial antennas, passive substrate elements for MMICs such as filters and phase shifter, and radar signature of antenna arrays.

Chapter 6 provides an insight into the different approaches for designing and miniaturization of metamaterial-inspired planar filters. This chapter outlines and develops compact metamaterial-inspired microstrip filters, in particular, printed band-pass filters (BPFs) and band-stop filters (BSFs) by utilizing a planar resonant transmission line by loading with an array of electrically small metamaterial resonators. Comparative investigations of different SRR-based CPW band-pass filter configurations are presented here. These BPFs are obtained by loading the CPW lines with TSRRs in a series of gaps. In the second model, a microstrip transmission line based on hex-omega metamaterial resonator cell has been investigated to design a novel narrow-band band-pass and band-stop filter configurations. In brief, a potential application of metamaterial to design compact planar filters is explained.

In recent years, the Global Positioning System has become one of the most commonly used Global Navigation and Satellite System (GNSS). In Chap. 7, a GPS fractal antenna made from a PEDOT polymer and a PPy conductor with patches on FR4 substrate have been modeled. A reference structure with a copper patch has also been designed for the comparative analysis. The performance of CP-based microstrip patch antennas at 1.5754GHz has been compared with an equivalent Cu patch antenna. It shows that the proposed structures of PEDOT patch on FR4 substrate have analogous applications to copper patch in microwave applications. From the comparison between three designs, it can be easily concluded that PEDOT and PPy materials give a good competition to copper with the comparative values for gain and return loss, respectively. The array design of PEDOT and PPy MPAs results in high directivity and radiation intensity. Conducting polymers have now become an area of interest for researchers to obtain much better results for the electronic communication system.

Metamaterials (MTMs) are the synthetic materials engineered to have electromagnetic properties that are not usually found in nature. Chapter 8 presents a comprehensive review of MTM resonator antennas. The theories and designs of various MTM resonator antennas have been described in detail. In theory part, the MTM unit cell structures, their mathematical analysis, and basic operating principles are discussed, whereas the design part covers the specific examples of MTM antennas. In these examples, all design aspects have been revealed along with the analysis of simulated reflection coefficients to find the bandwidth responses.

Nowadays, the two-dimensional version of metamaterial called metasurface finds its application in the entire electromagnetic spectrum. In Chap 9, the possibility of metasurface has been explored for the application of antenna performance enhancement. Toward this, an extensive literature survey on the possible applications of the metasurface in the microwave regime has been carried out. It shows that currently there is tremendous growth in the metasurface field in the entire electromagnetic spectrum compared to metamaterials. Several techniques for antenna performance enhancement have been proposed. Two different antennas are designed by placing two different superstrates such as metafilm and metascreen. The designed metasurfaces showed enhancement in antenna characteristics such as bandwidth and gain, at desired frequencies. The designed metafilm superstrate has improved both bandwidth and gain of the source antenna.

Electromagnetic Bandgap structures (EBGs) can be used for designing a compact antenna with enhanced performance and efficiency. Chapter 10 gives an overview of EBG theory. The need for designing EBGs and how EBGs address the drawbacks of the patch antenna are discussed. Various EBG antenna designs based on different applications such as gain and bandwidth enhancement and mutual coupling reduction are discussed. In PCB manufacturing, a wide signal-to-noise suppression is achieved with different EBG designs. Using EBGs, reduction in SAR values of antennas for the wearable application can also be achieved.

The tremendous growth in the field of mobile communication and wireless communication enforces antenna engineers to meet the current technological advancement. As mobile and communication users are increasing very fast to avail the facility of a communication network, the requirement of high spectral efficiency and ultra-high data rate must be the motivated area of research. Chapter 11 explores systematical studies of SIW antenna, Dielectric resonator antenna, and 5G MIMO antenna with all the isolation improvement techniques to meet the current requirement.

Hyderabad, India — Runa Kumari
Bangalore, India — Balamati Choudhury

Contents

About the Editors

Dr. Runa Kumari is an Assistant Professor in the Department of Electrical and Electronics Engineering, BITS Pilani Hyderabad Campus. She has done her M.Tech. and PhD from National Institute of Science and Technology (NIST), Odisha and National Institute of Technology (NIT), Rourkela in 2008 and 2014 respectively. Her areas of interest are primarily focused on antenna research, design and applications, and she has authored 28 research publications in reputed journals and conference proceedings.

Dr. Balamati Choudhury is a scientist at the Centre for Electromagnetics of the CSIR-National Aerospace Laboratories, Bangalore, India. She received her M.Tech. (ECE) degree from the National Institute of Science and Technology (NIST), India and PhD (Eng.) degree in Microwave Engineering from Biju Patnaik University of Technology (BPUT), India in 2013. From 2006–2008, she was a senior lecturer at the Department of Electronics and Communication at the NIST, Orissa, India. Her research and teaching interests are in the domain of soft-computing techniques in electromagnetic design and optimization, computational electromagnetics for aerospace applications, metamaterial design applications, radio frequency (RF), and microwaves. She has contributed to a number of projects, including the development of ray tracing techniques for RF analysis of propagation in an indoor environment, low radar cross section (RCS) design, phased arrays and adaptive arrays, and conformal antennas. She was also the recipient of the CSIR-NAL Young Scientist Award for the year 2013–2014 for her contribution in the area of computational electromagnetics for aerospace applications. Dr. Balamati has authored or co-authored over 140 scientific research papers and technical reports, five SpringerBriefs and three book chapters as well as a book entitled: Soft Computing in Electromagnetics: Methods and Applications. Dr. Balamati is also an assistant professor of the Academy of Scientific and Innovative Research (AcSIR), New Delhi.

Chapter 1
Material Selection Techniques in Materials for Electronics

Navneet Gupta and Kavindra Kandpal

1 Introduction

Material selection is an important step prior to the actual fabrication of any electronic device. Owing to the availability of large set of materials, it is important to select the best possible material in order to enhance the performance of a device. Material selection approaches provide an easy way to recognize the trade-offs between conflicting materials properties and also to select the optimal material for better device performance. In addition to this, these approaches also help us to provide ranking to the alternatives from best to worst. Therefore, these approaches provide a platform to select and prioritize the possible materials and also provide support to perform rigorous evaluation of the possible alternatives. This chapter describes material selection methodologies in detail and explains the steps to be taken for each methodology to find out the most promising material for a given device.

2 Material Selection Methodologies

As each material to be selected for any device to enhance the performance will have its own advantages and limitations, so to find out the best possible alternative, one can use multi-criteria decision-making (MCDM) approach when there is more than one attribute. The MCDM approach is further subdivided into multi-objective decision making (MODM) and multi-attribute decision-making (MADM) approaches. These approaches are well studied by many researchers in engineering regime [1–4]. The most popular material selection methodologies are Ashby's approach, Technique for

N. Gupta (✉) · K. Kandpal
BITS-Pilani, Rajasthan, India
e-mail: ngupta@pilani.bits-pilani.ac.in

R. Kumari and B. Choudhury (eds.), *Multiscale Modelling of Advanced Materials*,
Materials Horizons: From Nature to Nanomaterials,
https://doi.org/10.1007/978-981-15-2267-3_1

Order Preference by Similarity to Ideal Solution (TOPSIS) and VlseKriterijumska Optimizacija I Kompromisno Resenjein in Serbian (VIKOR).

Ashby's approach is one of the most commonly used MODM approach as it optimizes alternatives based on the prioritized objectives. VIKOR and TOPSIS are MADM techniques and the alternatives are ranked on the basis of weighted attributes. Ashby's approach is very easy when performance indices are less in number; however, it does not generate ranking score. VIKOR and TOPSIS are widely used for a wide range of material selection problem which gives ranking solution. VIKOR and TOPSIS approaches differ in the fact that VIKOR uses linear normalization method, whereas TOPSIS uses vector normalization to convert different scales of various criteria into standard units. TOPSIS method gives the solution by finding the shortest distance from the ideal solution and longest distance from worst-case solution, whereas the VIKOR gives the compromise solution by determining least individual regret of the opponent and highest group utility of majority. Let us now discuss these techniques and approaches in detail.

3 Ashby's Approach

M. F. Ashby provides effective material selection approach to select the best material based on their material and performance indices for better device performance. Material indices are group of material properties which enhance the device performance for a given requirement. These material indices are derived based on the device requirement through the investigation of objectives and constraint. Performance index is a combination of material indices which governs some characteristics of device performance.

The Ashby's approach tells how to characterize the appropriate material for desired performance depending upon their attributes (mechanical, electrical and thermal properties of the material). A design demands a certain profile of these attributes. The identification and shortlisting of these attribute profiles are done by screening and ranking.

Ashby's material selection approach involves five steps, as illustrated in Fig. 1. In the first step, the design requirements for the structural component are derived based on function, objectives and constraints. The next step of Ashby methodology shows that the immense wide choice is narrowed, first by applying property limits that screen out the material which cannot meet the design requirements. Further narrowing is achieved by applying the material indices and ranking the candidate based on their ability to provide best performance. Then the detailed supporting information of each shortlisted candidate, called as prime candidates, provide the final choice of material. A material index is a combination of material properties which maximize the performance of a component for a given requirement. These material indices are derived from the design requirement for a component through an analysis of function, objectives and constraints. A performance index is a group of material properties which governs some aspect of the performance of a component. A material selection

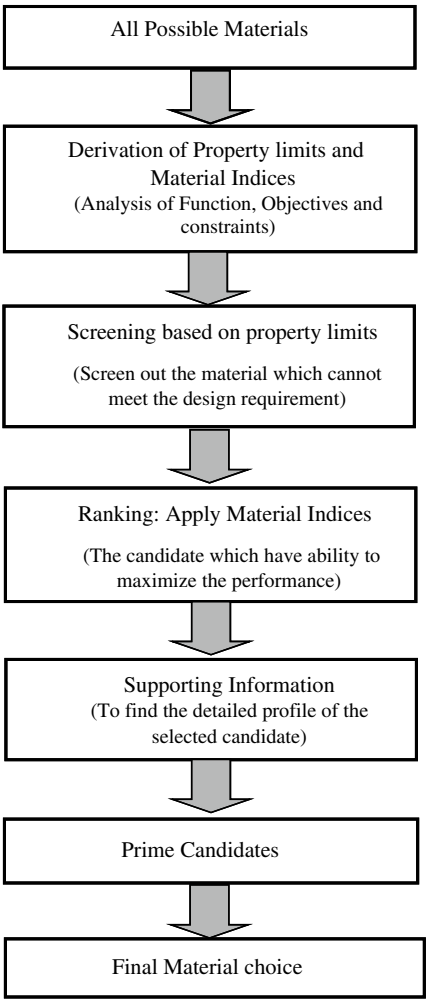

Fig. 1 Material selection chart for Ashby's approach

using performance indices is best achieved by plotting one material property on each axis of material selection chart. The design of a component is specified by three parameters: functional requirements, geometrical properties and material properties. The performance of element is described by

$$P = f[(FGM)] \tag{1}$$

Here P describes the performance of element and f describes the function of the functional requirement (F), geometrical properties (G) and material properties (M), respectively.

4 Topsis Approach

This approach is used to find out the best alternative by finding out the shortest Euclidean distance (S*) from ideal solution (A*) and largest distance (S^-) from worst-case solution (A^-) (or negative ideal solution). The steps followed in TOPSIS approach are:

Step 1: Preparation of normalized decision matrix *N*

Normalized decision matrix N consists of n_{ij}, elements with *i*th number of alternatives under *j*th number of criterion. This matrix is normalized with RMS value given by:

$$n_{ij} = \frac{x_{ij}}{\sqrt{\sum_{i=1}^{u} \left(x_{ij}\right)^2}} \tag{2}$$

where *i* represents the set of alternative = 1, 2, 3, …, *u*, and *j* represents set of criteria = 1, 2, …, *v*.

Step 2: Preparation of weighted normalized matrix

In this step we assign weight of all criteria where the value of weights is chosen such that $\sum_{J=1}^{v} w_j = 1$. Now weighted normalized matrix

$$M_{ij} = n_{ij} \times w_j \tag{3}$$

Step 3: Computation of ideal and negative ideal solution

If J_1 is associated with the benefit criteria and J_2 is associated with cost criteria, then the ideal solution A* is defined as: $A^* = \{\max M_{ij} \mid j \in J_1\}$ or $(\min M_{ij} \mid j \in J_2) = \{M_1^*, M_2^*, M_3^* \ldots, M_v^*\}$, and the worst-case solution A^- is defined as: $A^- = \{\min M_{ij} \mid j \in J_1\}$ or $(\max M_{ij} \mid j \in J_2) = \{M_1^-, M_2^-, M_3^-, \ldots, M_v^-\}$.

Step 4: Calculation of separation measure from ideal and non-ideal solution

Euclidean distance from ideal solution S_i^* can be measured as:

$$S_i^* = \sqrt{\sum_{j=1}^{v} \left(M_{ij} - M_j^*\right)^2} \tag{4}$$

Euclidean distance from non-ideal solution S_i^- can be measured as:

$$S_i^- = \sqrt{\sum_{j=1}^{v} \left(M_{ij} - M_j^-\right)^2} \tag{5}$$

Step 5: Measurement of relative closeness (C_i) from ideal solution

The relative closeness from ideal solution C_i can be obtained using Eq. (6) as:

$$C_i = \frac{S_i^-}{S_i^- + S_i^*} \text{ for } 0 < C_i < 1 \tag{6}$$

The ranking of alternatives now depends upon the value of C_i; larger the value of C_i, better will be the performance of the alternative.

5 VIKOR Approach

This approach is also widely accepted for selecting the material for engineering design. This method focuses on ranking and selecting from various alternatives. It is a fuzzy logic-based methodology which provides a compromising solution based on the following steps:

Step 1: Determination of x_j^* and x_j^- values

If x_{ij} element belongs to the ith row (alternatives) and jth column (criterion) of fundamental decision matrix, then we first determine x_j^* either as $\max\{x_{ij}\}$ if it represents benefit criteria or as $\min\{x_{ij}\}$ if it represents cost criteria, where $i = 1, 2,\ldots, u$, and $j = 1, 2, \ldots, v$. Similarly, x_j^- is defined as $\min\{x_{ij}\}$ or $\max\{x_{ij}\}$ if it represents benefit criteria or cost criteria, respectively.

Step 2: To construct the maximum group utility G_i and minimum regret of the opponent R_i

If w_j is the weight of jth criteria and $\sum_{j=1}^{v} w_j = 1$, then the values for G_i and R_i are given by the following equations:

$$G_i = \sum_{j=1}^{v} w_j \frac{\left(x_j^* - x_{ij}\right)}{\left(x_j^* - x_j^-\right)} \tag{7}$$

$$R_i = \max_j \left[w_j \frac{\left(x_j^* - x_{ij}\right)}{\left(x_j^* - x_j^-\right)} \right] \tag{8}$$

Step 3: Calculation of Q_i for ith alternative

If $G^- = \max\{G_i\}$, $G^* = \min\{G_i\}$, $R^- = \max\{R_i\}$, $R^* = \min\{R_i\}$ and σ is defined as weight of strategy G_i and (1-σ) as weight of strategy R_i, then the value of ith alternative of VIKOR (Q_i) is given as:

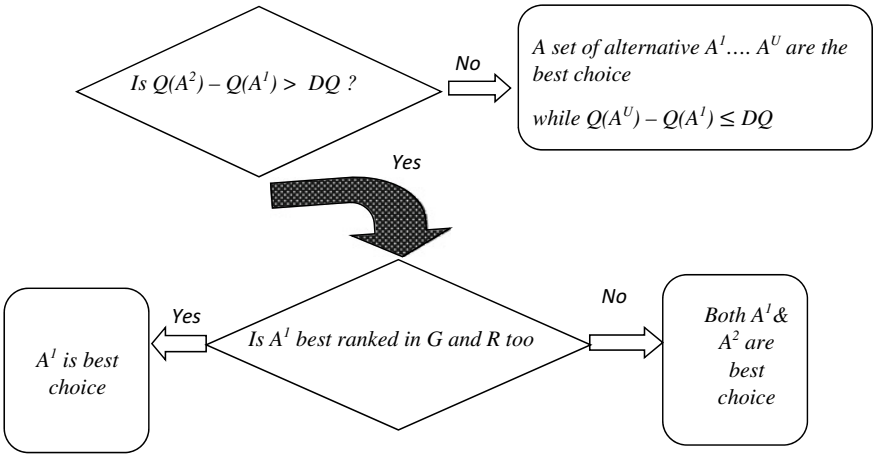

Fig. 2 Flowchart illustrating the decision making in VIKOR approach

$$Q_i = \sigma \frac{(G_i - G^*)}{(G^- - G^*)} + (1 - \sigma) \frac{(R_i - R^*)}{(R^- - R^*)} \tag{9}$$

Usually the value of weight of maximum group utility (σ) is chosen to be 0.5.

Step 4: Sorting the value of R, G and Q

This step includes finding out the value of R, G and Q in increasing order to compute the ranking order of alternatives (A^1, A^2, A^3… A^u).

Step 5: Now one can find out the best alternative based upon the flowchart illustrated in Fig. 2, where $DQ = 1/(U - 1)$; and U is the number of alternatives.

6 Applications for Various Devices

These material selection techniques have been extensively used and implemented to select the best possible materials for various devices. Our research group has presented and proposed the best materials to be used for: Radio frequency (RF) microelectromechanical (MEMS) capacitive shunt switch [5], gate dielectric material in CMOS devices [6], zinc oxide thin-film transistor (TFT) [7], MEMS disk resonator [8], hybrid microwave-integrated circuits (HMICs) [9], nanocrystalline silicon (nc-Si) thin-film transistors (TFTs) [10], nanowire transistors [11], dielectric resonator antennas [12], microstrip patch antenna for wireless communication applications [13], RF-MEMS switch used for reconfigurable antenna [14], MOS devices [15], thin-film solar cells (TFSC) [16], electrostatic microactuators [17] and microelectronic heat sinks [18].

Readers are suggested to go through these papers to get the details of steps included to get best possible material for each one of the device mentioned here. However, let us see one example how material selection techniques are used to select the best gate dielectric for ZnO-based thin-film transistor [7].

The objective is to minimize leakage and minimize equivalent oxide thickness (EOT) so that ZnO TFT can be operated at low voltage. EOT is a measure of the scaling capability of high-κ dielectric compared to SiO_2 dielectric. The EOT of a high-κ dielectric is defined as the thickness required by SiO_2 to achieve same voltage modulation effect or same equivalent capacitance density as of high-κ dielectric [19] and is given by:

$$EOT = \frac{\kappa_{SiO_2}}{\kappa_{ox}} t_{ox}$$

The constraints for Ashby analysis for this device are band-gap should be high (>5 eV) [20], dielectric constant (κ_{ox}) > 15 [20] and conduction band offset (ΔE_c) > 1 eV [21].

Here the variables are the choice of materials (from set of material reported for ZnO TFT in literature) and material indices (M) are band-gap (E_g), dielectric constant (κ_{ox}) and CBO (ΔE_c). The functional parameter (F) is leakage current and the geometrical parameter is scaling limit (t_{ox} or EOT). Now, one can define Ashby function A, which will determine the performance of TFT as: $A = f\ \{F, G, M\}$.

In any field effect transistor, the leakage current density for the case when tunneling is dominated by ECB (conduction band electron) tunneling mechanism can be modeled by a semi-empirical equation [22] and given by

$$J_{GL} \propto \exp\left\{-\frac{4\pi(2q)^{\frac{1}{2}}}{h} * \left(m_{eff}\varphi_b\right)^{\frac{1}{2}} k * EOT\right\} \tag{10}$$

where h is Planck's constant, q is electron charge, m_{eff} is electron tunneling mass and ϕ_b is barrier height. In this case barrier height ϕ_b is ΔE_c. Equation (10) can be rewritten as:

$$J_{GL} = b * \exp\{-a * f * EOT\} \tag{11}$$

where $f = (m_{eff}\varphi_b)^{1/2}\kappa_{ox}$ and a, b are the constants. From Eq. (10) it can be seen that higher the value of f, lower will be the gate leakage current density (J_{GL}). For a given value of supply voltage and maximum leakage current density $J_{GL,max}$, the scaling limit is reciprocally related to the gate dielectric figure of merit (f) as:

$$t_{ox} = \frac{\ln\left(\frac{b}{J_{GL,max}}\right)}{a} f^{-1} \tag{12}$$

Table 1 Material indices matrix

Dielectric materials	E_g (eV)	κ_{ox}	ΔE_c (eV)	|ΔTEC| PPM/K
HfO_2	6	25	2.2	0.1
ZrO_2	5.8	25	2.1	2.8
$HfSiO_4$	6.5	11	2.7	6.3
La_2O_3	6	30	3.1	4.1
$LaAlO_3$	5.6	30	1.9	7.1
Ta_2O_5	4.4	22	1.1	0.5
Ga_2O_3	4.8	23	1.5	2.8
Gd_2O_3	5.8	16	2.9	1.26
Al_2O_3	8.8	9	3.3	3.9
SiO_2	9	3.9	3.7	4
Si_3N_4	5.3	7	2.5	1.7
Y_2O_3	6	15	3.1	2.9
Sc_2O_3	6.3	14	3.1	2.2
$BaTiO_3$	3.1	2000	−0.45	–
$SrTiO_3$	3.3	2000	0.8	–

The first step is to find out the material indices like band-gap (E_g), dielectric constant (κ), conduction band offset to ZnO (CBO or ΔE_c) and difference in temperature coefficient of ZnO and high-κ dielectric which has been reported by various researchers. This will lead to construction of fundamental decision matrix. This is followed by particular material selection methodology, to find out the best suitable material candidate out of all the possible alternatives. Table 1 provides the values for band-gap (E_g), dielectric constant (κ_{ox}) and conduction band offset (ΔE_c). Along with the material indices listed in Table 1, thermal expansion coefficient mismatch (|ΔTEC|) also plays an important role in deciding the performance of TFT because deposition of thin film on a substrate or channel may include high temperature process like post annealing treatment. Also a significant amount of temperature coefficient mismatch may lead to considerable amount of stress which will eventually leads to defects in interface, or excessive stress which can cause the device failure. ZnO has a thermal expansion coefficient close to 4.6×10^{-6}/°C [23]. |ΔTEC| in PPM/°C is computed by taking the difference between TEC of ZnO and dielectric irrespective of the nature of stress, that is, compressive or tensile. So |ΔTEC| is a cost criterion for TOPSIS and VIKOR approach.

6.1 Ashby's Analysis

In this approach to find out the best gate dielectric, the first step is to plot the graphs between various material indices. Then it is required to apply the constraints to find

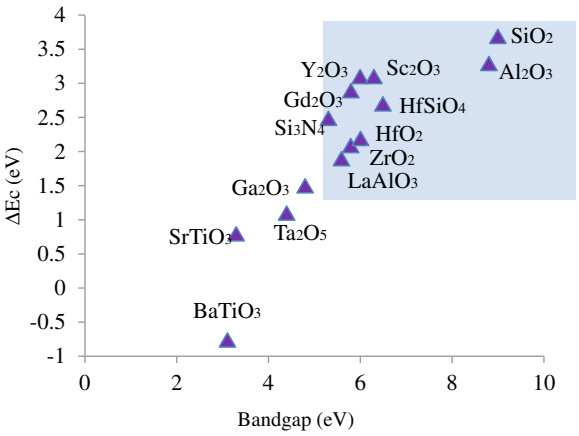

Fig. 3 Plot of conduction band offset versus band-gap of various dielectrics

out possible sets of dielectrics. Figure 3 shows the plot between conduction band offset and band-gap for all the possible high-κ dielectric. As one requires E_g more than 5 eV and ΔE_c more than 1 eV, it is clear that Ga_2O_3, $SrTiO_3$, Ta_2O_5, $BaTiO_3$ do not fulfill the required conditions. The materials that satisfy the requirements are shown under the shaded rectangle.

Figure 4 shows the plot between band-gap and dielectric constant of all possible materials. As one needs E_g more than 5 eV and κ_{ox} more than 15, SiO_2, Al_2O_3, $HfSiO_4$, Si_3N_4, Ta_2O_5, Ga_2O_3, Sc_2O_3, Gd_2O_3 violate the constraints and are removed from the selection of gate dielectric. Shaded rectangle shown in Fig. 4 covers all those materials that satisfy the conditions.

Figure 5 shows the plot between conduction band offset and dielectric constant. As stated, one needs ΔE_c greater than 1 eV and κ_{ox} greater than 15, SiO_2, Al_2O_3, Sc_2O_3, $HfSiO_4$, Si_3N_4 do not fit in constraint. Hence the material left that satisfies all the constraints are HfO_2, ZrO_2, La_2O_3, $LaAlO_3$, while Ga_2O_3 and Ta_2O_5 narrowly violate these constraints. Finally, for the dielectrics satisfying Ashby constraints,

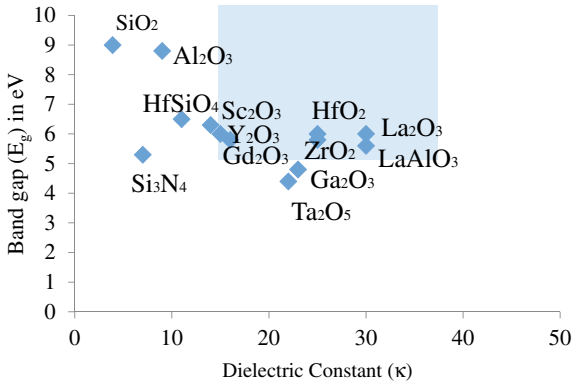

Fig. 4 Plot of band-gap versus dielectric constant of various dielectrics

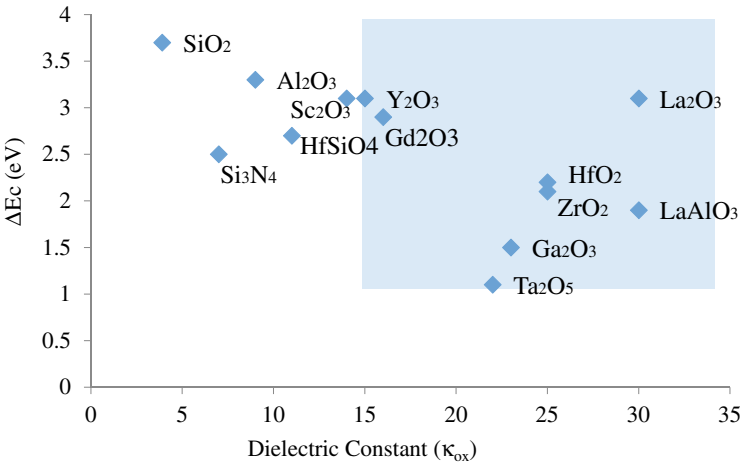

Fig. 5 Plot of conduction band offset versus dielectric constant

gate dielectric figure of merit (f) as given in Eq. (11) is plotted. The typical values of tunneling effective mass for the dielectrics ranges from 0.1 to 0.5 m_o. It is clear from Fig. 6 that the best alternative as a gate dielectric of ZnO TFT for low leakage operation is La_2O_3. This is followed by $LaAlO_3$, ZrO_2 and HfO_2.

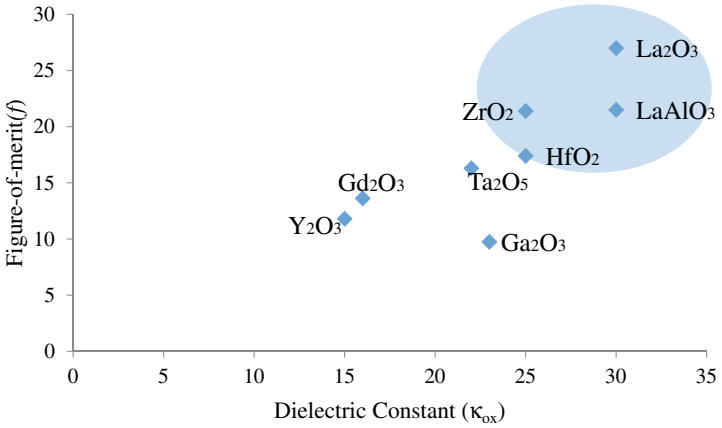

Fig. 6 Plot of figure of merit (f) versus dielectric constant

Table 2 Weighted normalized matrix

Dielectric	0.4*[κ_{ox}]	0.3*[ΔE_c]	0.2*[E_g]	0.1*[|ΔTEC|]
HfO_2	0.141334	0.06893	0.05275	0.000763
ZrO_2	0.141334	0.065796	0.050992	0.021363
$HfSiO_4$	0.062187	0.084595	0.057146	0.048067
La_2O_3	0.1696	0.097128	0.05275	0.031282
$LaAlO_3$	0.1696	0.05953	0.049233	0.054171
Ta_2O_5	0.124374	0.034465	0.038683	0.003815
Ga_2O_3	0.130027	0.046997	0.0422	0.021363
Gd_2O_3	0.090453	0.090862	0.050992	0.009613
Al_2O_3	0.05088	0.103394	0.077367	0.029756
SiO_2	0.022048	0.115927	0.079125	0.030519
Si_3N_4	0.039573	0.078329	0.046596	0.01297
Y_2O_3	0.0848	0.097128	0.05275	0.022126
Sc_2O_3	0.079147	0.097128	0.055388	0.016785

6.2 TOPSIS Analysis

For the TOPSIS and VIKOR one needs a weight matrix with proper justification. The dielectric constant can be given highest weight for low threshold voltage TFT. It is followed by conduction band offset (ΔE_c) and then by band-gap (E_g) and the least weight is given to temperature coefficient mismatch (|ΔTEC| PPM/°K) because various process techniques are available which can either deposit oxides in low thermal budget or can use additional deposition of stress relieving material which can overcome the induced intrinsic stress. In addition, TFT fabrication is preferred with low thermal budget to allow wide range of compatible substrate material. So keeping $\sum_{J=1}^{v} w_j = 1$ in view, the weight matrix is $W = [0.4, 0.3, 0.2, 0.1]$. Using this weight matrix, a weighted normalized matrix is constructed, as shown in Table 2.

From Table 2 one can find out the ideal (A*) and negative ideal (A^-) solution as:

$A^* = \{0.1696, 0.115927, 0.079125, 0.000763\}$

$A^- = \{0.022048, 0.034465, 0.038683, 0.054171\}$

Table 3 gives the values of Euclidean distance from ideal and non-ideal solution, relative closeness from ideal solution (C) and the TOPSIS rank. From Table 3, top three ranked materials are La_2O_3, HfO_2 and ZrO_2.

6.3 VIKOR Analysis

VIKOR also uses the same weight matrix, as used for TOPSIS analysis. From the calculation of maximum group utility G_i and minimum regret of the opponent R_i, one can find out the following:

Table 3 TOPSIS results with ranks

Dielectric	S^-	S^+	C	Rank
HfO_2	**0.135894**	**0.060856**	**0.690695**	**2**
ZrO_2	**0.128213**	**0.06729**	**0.655811**	**3**
$HfSiO_4$	0.067099	0.123451	0.352135	12
La_2O_3	**0.162543**	**0.044502**	**0.785061**	**1**
$LaAlO_3$	0.150037	0.083226	0.643211	4
Ta_2O_5	0.114045	0.101619	0.528809	7
Ga_2O_3	0.113601	0.090029	0.557881	5
Gd_2O_3	0.099984	0.088104	0.531581	6
Al_2O_3	0.087607	0.122863	0.416246	10
SiO_2	0.093974	0.150523	0.384356	11
Si_3N_4	0.063177	0.139742	0.31134	13
Y_2O_3	0.095337	0.093255	0.505521	8
Sc_2O_3	0.094147	0.096723	0.493251	9

Minimum $R_i = R^* = 0.130435$, Maximum $R_i = R^- = 0.4$

G^* = Minimum $G_i = 0.256808$, G^- = Maximum $G_i = 0.674679$

Table 4 gives the value of R, G and Q for all the dielectrics and their ranking based on the values of corresponding R, G and Q.

Table 4 VIKOR R_i, G_i and Q_i values with respective ranks

Dielectric	R_i	Ranking based on (R)	G_i	Ranking based on (G)	Q	Ranking based on Q
HfO_2	0.173076923	2	0.380140058	2	0.2267	2
ZrO_2	0.184615385	3	0.4389456	4	0.3184	3
$HfSiO_4$	0.291187739	9	0.603839436	11	0.7134	10
La_2O_3	0.130434783	1	0.256808409	1	0	1
$LaAlO_3$	0.207692308	4	0.455518395	5	0.3811	4
Ta_2O_5	0.3	10	0.62831965	12	0.759	12
Ga_2O_3	0.253846154	8	0.582305972	10	0.6184	9
Gd_2O_3	0.214559387	5	0.462568943	8	0.4022	5
Al_2O_3	0.32183908	11	0.430974293	3	0.5634	8
SiO_2	0.4	13	0.455714286	6	0.738	11
Si_3N_4	0.352490421	12	0.674678668	13	0.9119	13
Y_2O_3	0.229885057	6	0.469550609	9	0.439	6
Sc_2O_3	0.245210728	7	0.461832802	7	0.4582	7

Table 5 Experimental data for the validation of proposed analysis [7]

Performance parameter	La_2O_3 [24]	HfO_2 [25]	ZrO_2 [26]
μ_{eff} ($cm^2V^{-1}s^{-1}$)	12.1	7.95	28
V (V)	1.85	2	3.2
I_{on}/I_{off}	1.5×10^7	4.1×10^8	4.8×10^7
I_{off} (A)	3.29×10^{-11}	2.2×10^{-9}	$\sim 10^{-10}$
SS (V/Dec)	0.234	0.215	0.560
Deposition technique	RF sputtering	RF sputtering	RF sputtering

Now using the flowchart given in Fig. 2, VIKOR rank can be decided. Since $Q(A^2) - Q(A^1) > 0.08334$ and A^1 is the same for R and G, hence La_2O_3 is the best choice material followed by HfO_2. While comparing the result of all the three approaches all gives La_2O_3 a lead over other dielectrics. Other suitable dielectric materials that can be used are HfO_2, ZrO_2 and $LaAlO_3$.

To validate the findings of this work, the results of the proposed analysis are compared with the experimental data. Table 5 shows the comparative analysis of ZnO-based TFT using different dielectrics, namely La_2O_3, HfO_2 and ZrO_2, which are deposited using RF sputtering. It clearly indicates that all the ZnO-based TFT with high-κ gate dielectric (La_2O_3, HfO_2 and ZrO_2) shows a very low value of threshold voltage than SiO_2 and Si_3N_4 gate dielectrics [10–20 V]. It also shows that using La_2O_3 as a gate dielectric shows superior performance than HfO_2 and ZrO_2 in terms of threshold voltage (V_T) and leakage current (I_{off}). The close match between outcome of this work and experimental results shows the validity of the proposed analysis for the low voltage and low leakage TFT. However, other performance parameters like I_{on}/I_{off}, SS and mobility depends on quality of ZnO deposition and quality of gate dielectric and ZnO interface. These need experimental parameters (like grain size and grain boundaries in ZnO channel, D_{it} at ZnO interface and many more) and cannot be simply decided from material intrinsic properties. But, material selection methodologies have clearly helped to rank the dielectric material based upon intrinsic properties of materials. Top-ranked dielectric material can be chosen for experimental analysis purpose, and interface can be further studied and optimized.

All the three methodologies show that the top-three ranked materials are La_2O_3, HfO_2 and ZrO_2. The result shows good agreement among Ashby, TOPSIS and VIKOR approaches.

7 Conclusion

This chapter highlighted the various material selection techniques for selecting materials in electronic devices. Three different material selection methodologies, Asbhy's approach, TOPSIS and VIKOR were explained in detail. In order to better understand the steps, one example for selecting best gate electric for ZnO TFT is considered.

Three different material selection methodologies, like Ashby, TOPSIS and VIKOR, were used to find out the best gate dielectric material. All the three methodologies converge to the same result which is also supported by experimental findings.

References

1. Ashby MF (2000) Multi-objective optimization in material design and selection. Acta Mater 48(1):359–369
2. Ashby MF, Cebon D (1993) Materials selection in mechanical design. Le J Phys IV 3(C7):C7–1
3. Opricovic S, Tzeng G-H (2004) Compromise solution by MCDM methods: a comparative analysis of VIKOR and TOPSIS. Eur J Oper Res 156(2):445–455
4. Sharma P, Gupta N (2015) Investigation on material selection for gate dielectric in nanocrystalline silicon (nc-Si) top-gated thin film transistor (TFT) using Ashby's, VIKOR and TOPSIS. J Mater Sci Mater Electron 26(12):9607–9613
5. Gupta N, Ashwin R (2018) Material selection methodology for radio frequency (RF) microelectromechanical (MEMS) capacitive shunt switch. Microsystem Technologies. Springer-Nature, 2018. https://doi.org/10.1007/s00542-018-3761-1
6. Gupta Navneet, Haldiya Varun (2018) High-k gate dielectric selection for Germanium based CMOS Devices. Int J Nanoelectron Mater 11(2):119–126
7. Kandpal Kavindra, Gupta Navneet (2016) Investigations on high-κ dielectrics for low threshold voltage and low leakage zinc oxide thin-film transistor, using material selection methodologies. J Mater Sci Mater Electron Springer 27(6):5972–5981
8. Sundarama GM, Angiraa M, Guptaa N, Rangra K (2016) Material selection for CMOS compatible high Q and high frequency MEMS disk resonator using Ashby's approach. Int J Nanoelectron Mater Malaysia 9:157–164
9. Gupta Navneet, Mishra Abhinav (2016) Selection of substrate material for hybrid microwave integrated circuits (HMICs). Energetika 62:78–86
10. Sharma Prachi, Gupta Navneet (2015) Investigation on material selection for gate dielectric in nanocrystalline silicon (nc-Si) thin-film transistors (TFTs) using Ashby's, VIKOR and TOPSIS. J Mater Sci Mater Electron Springer, Berlin 26:9607–9613
11. Gupta N, Mishra A (2015) Material selection methodology for minimizing direct tunneling in nanowire transistors. J Electr Dev Perpignan University, France, 21:1811–1815
12. Kumar Jitendra, Gupta Navneet (2015) Investigation on microwave dielectric materials for dielectric resonator antennas. Int J Appl Electromag Mech IOS Press, Japan 47:263–272. https://doi.org/10.3233/JAE-140051
13. Choudhary P, Kumar R, Gupta N (2014) Dielectric material selection of microstrip patch antenna for wireless communication applications using Ashby's Approach. Int J Microw Wireless Technol Cambridge University Press and European Microwave Association. https://doi.org/10.1017/s1759078714000877. Published July 14, 2014
14. Sharma AK, Gupta N (2012) Material selection of RF-MEMS switch used for reconfigurable antenna using Ashby's methodology. Prog Electromagnet Res Lett (PIER-L), 31:147–157
15. Aditya BN, Gupta N (2012) Material selection methodology for gate dielectric material in metal-oxide-semiconductor devices. Mater Design 35:696–700
16. Gupta N (2011) Material selection for thin-film solar cells using multiple attribute decision making approach. Mater Design 32:1667–1671
17. Parate O, Gupta N (2011) Material selection for electrostatic microactuators using Ashby approach. Mater Design 32:1577–1581
18. Reddy GP, Gupta N (2010) Material selection for microelectronic heat sinks: an application of the Ashby approach. Mater Design 31:113–117
19. Wilk GD, Wallace RM, Anthony J (2001) High-κ gate dielectrics: current status and materials properties considerations. J Appl Phys 89(10):5243–5275

20. Association SI (2006) International technology roadmap for semiconductors. http//www.itrs.net
21. Huang AP, Yang ZC, Chu PK (2010) Hafnium-based high-k gate dielectrics. Advanc Solid State Circuit Technol. InTech
22. Yeo YC, King TJ, Hu C (2003) MOSFET gate leakage modeling and selection guide for alternative gate dielectrics based on leakage considerations. IEEE Trans Electron Devices 50(4):1027–1035
23. Yamamoto N, Makino H, Yamamoto T (2011) Young's modulus and coefficient of linear thermal expansion of ZnO conductive and transparent ultra-thin films. Adv Mater Sci Eng
24. Qian LX, Lai PT, Tang WM (2014) Effects of Ta incorporation in La_2O_3 gate dielectric of InGaZnO thin-film transistor. Appl Phys Lett 104(12):1–6
25. Ji L-W et al (2013) Characteristics of flexible thin-film transistors with ZnO channels. IEEE Sens J 13(12):4940–4943
26. Lee JS, Chang S, Koo SM, Lee SY (2010) High-performance a-IGZO TFT with ZrO_2 gate dielectric fabricated at room temperature. IEEE Electron Device Lett 31(3):225–227

Chapter 2
Some Aspects of Artificial Engineered Materials: Planar and Conformal Geometries

Asit K. Panda

1 Introduction

Artificial engineered materials or metamaterial (MTM) have received considerable attention in recent years due to eccentric and alluring properties compared to ordinary material which are not found in nature. MTM consists of unit cells of different shapes with periodic intervals which are much smaller than operation wavelength. Because of these fascinating EM characteristics, LHM has been widely used in numerous applications at microwave band, such as filters, antennas, and flat lens.

These advances flourish to enhance the performance of the circuits and devices by incorporating novel structures and materials. Artificial engineered materials have been known to scientists and researchers since 1998 when J. C. Bose used chiral materials for the demonstration of polarization [1]. These artificial materials are embedded in host medium when electromagnetic waves are impinged on them. Thus, artificial materials that exhibit unusual properties have been the subject of research interest for most of the microwave and millimeter-wave applications.

Based on the effective parameters of materials, they are alienated into four categories [2]. Double positive material possesses positive permittivity and positive permeability ($\varepsilon > 0$ and $\mu > 0$). The largest part of the materials found in nature is double positive material. They support propagation waves. In the second category, the permittivity of the material is negative, but permeability is positive ($\varepsilon > 0$ and $\mu < 0$). These are called epsilon negative materials (ENM). Plasma at certain frequency exhibits these properties and attenuates the electromagnetic waves. These materials attenuate the waves. Double negative material (DNG) has both permittivity and permeability as negative ($\varepsilon > 0$ and $\mu < 0$). These materials support propagation waves, but the phase and group velocity are anti-parallel. In 1968, Veselago first

A. K. Panda (✉)
National Institute of Science & Technology (NIST), Brahmapur, Odisha, India

R. Kumari and B. Choudhury (eds.), *Multiscale Modelling of Advanced Materials*,
Materials Horizons: From Nature to Nanomaterials,
https://doi.org/10.1007/978-981-15-2267-3_2

introduced the theoretical study of a medium with simultaneous negative permeability and permittivity, which leads to the negative value of index of refraction in a specific frequency band [3]. Later, Pendry et al. examined the periodic cascaded of split-ring resonators (SRRs) and periodic thin metal wires for the assembly of metamaterial with negative permeability and permittivity simultaneously [4]. Afterward, the first practical realization of left-handed material (LHM) based on Pendry's idea attains negative permittivity and permeability at microwave regime, which was made by Smith et al. [5]. Based on these efforts numerous new approaches of accomplishing LHMs have been investigated. To achieve NRI medium, an immense number of periodic split-ring resonators and thin metallic strips have to arrange in stack. Also, the above methods for realization of LHM create a major alignment problem with produced MTM layers, where the incident EM waves propagate parallel to the LHM medium, which make it relatively hard to construct and employ such left-handed material (LHM) at the microwave frequency range. To overcome these problems, a great variety of MTM structures have reported and successfully demonstrated the existence of negative refractive index (NRI) characterization in microwave and visible frequency band [6–11].

This chapter aims at investigating the electromagnetic and left-handed (LH) behavior of some new type of low loss with wideband planar and conformal artificially engineered structure based on edge-coupled and broadside-coupled techniques. The electromagnetic and LHM behavior at microwave frequency band is designed and demonstrated numerically and experimentally. It comprises three different metamaterial designs. In the first model, the reflection spectra and left-hand properties of the planar broadside-coupled metamaterial structure are based on design and systematical analysis of a pair of E-shaped resonators. The symmetrical ESR structure exhibits low loss with wideband LHM behavior when aligned normally to incident E-polarized plane wave. The numerical results have verified with experiments using the waveguide setup. In the second design, a skewed omega LHM unit cell structure has been designed and investigated using EM simulation and measurements. Its electrical characteristics are retrieved. The experimental results reveal that the proposed modified skewed omega LHM structure provides better transmission passband a DNG compared to existing omega-type MTM inclusions. In the third design, an effort is made to study the transmission spectra and LH transmission band of the conformal sectored split Sierpinski resonator LHM unit cell configuration suitable for both planar and curved surfaces applications. Owing to conformal and space filling property of the proposed SRR structure, it is highly beneficial in the application of microwave passive circuit design.

2 Low Loss Planar Wideband LHM Structure Based on E-Shaped Resonator

Recently, a great variety of MTM structures have reported and successfully demonstrated the existence of left-handed (LH) characterization in microwave and visible frequency band. At early stage, various kinds of planar metamaterial structures [7, 12–17] based on single resonators were proposed and investigated left-handed behavior using EM coupling within the periodic cell. However, such planar MTMs designs have demonstrated that single-negative (SNG) behavior with only permittivity or permeability is negative in desired frequency band.

Later, planar metamaterials [10, 18–21] composed of metallic inclusions on both sides of host medium have been proposed. Such planar MTM medium could exhibit LHM behavior when the electromagnetic wave vector propagates transversal to the plane of MTM layer, therefore easier to fabricate and measure. Recent studies have demonstrated that the relative orientation between coupled SRRs determines the characteristics of strong electromagnetic coupling. However, to date the existing planar MTMs exhibit high loss and narrow NRI pass-band, which limit wide applications (in antenna filters, sensors, super-lens) of these planar MTMs.

To resolve these tribulations, in this paper, a broadside-coupled planar MTM structure consisting of a pair of E-shaped resonator (ESR) on both sides of host medium has been proposed. The proposed MTM structure exhibits a low loss with wideband double negative (DNG) characteristics. In addition, the dimension of MTM unit cell aligned with EM wave is very small.

2.1 Unit Cell Analysis

The schematic of broadside-coupled E-shaped resonator metamaterial (MTM) unit cell is shown in Fig. 1. This metamaterial is denoted as ESR. The ESR MTM unit cell structure is constituted by a pair of symmetric E-shaped metallic inclusions on both sides of the microwave laminator by using 0.02 mm thick copper clad. Here, we have used a low loss FR4 microwave laminator with dielectric constant (ε_r= 4.4), loss tangent (tanδ = 0.002), and substrate thickness (h = 0.5 mm), respectively. The geometrical dimensions of ESR MTM unit cell are as follows (in mm): l = 6 mm, a = 7 mm, d = 0.5 mm, a_x = 7 mm, a_y = 8 mm.

The numerical analysis of the proposed MTM unit cell has been carried out by using time-domain solver of the CST Microwave Studio (CST MWS) EM solver based on full-wave finite-element method (FIT) code.

To verify the LHM characteristics of the proposed MTM structure, a plane wave incident normal to the metamaterial surface (along z-direction) with the electric field along y-direction ($E||y$) and magnetic field along x-direction ($H||x$), respectively (Fig. 1a). Since the studied MTM unit cell is a periodic structure, the transmission and reflection coefficient (S_{11} and S_{21}) are calculated by modeling a single unit cell

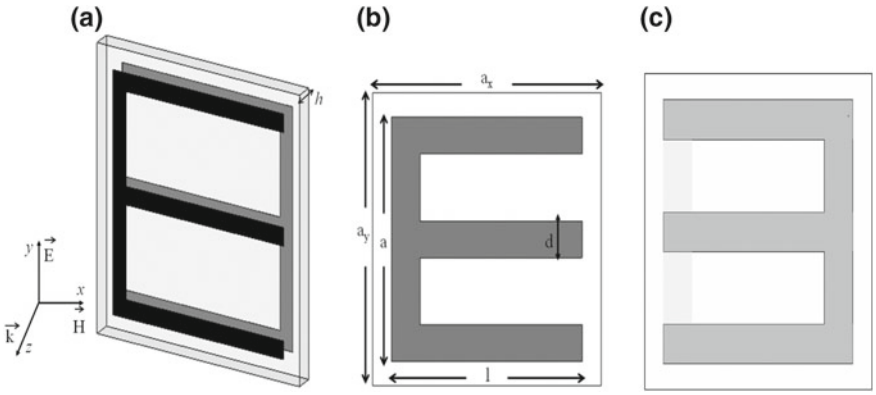

Fig. 1 Configuration of ESR MTM unit cell **a** 3D view, **b** Front side, and **c** Back side

with a PEC-PMC boundary condition in the simulation setup. Hence the designed structure in numerical solver behaves as a periodic structure that is unbounded in the XY plane. Two waveguide ports with open boundary condition are assigned along the z-axis to excite the LHM band in the desired frequency regime.

2.2 Results and Discussion

Based on the simulation setup explained in the previous section, complex values of S-parameters (S_{22} and S_{12}) were calculated for ESR MTM unit cell over the frequency range 3–7 GHz using CST MWS EM solver. Figure 2 depicts the amplitude and phase of the computed S-parameters. Owing to structural symmetric in nature, the amplitude and the phase of S_{22} and S_{12} are equal to that of S_{22} and S_{12}.

As observed in Fig. 2a, there is a transmission peak and pass-band that appeared at around 4.16 GHz, which indicates the existence of LHM band (the location of electric and magnetic resonance frequency). Figure 2b shows the phases of S_{11} and S_{21} where a clear phase reversal for S_{11} near the resonant frequency (4.16 GHz) verifies the existence of LHM characteristic.

The effective parameters can be retrieved from the calculated scattering parameters using the modified revival method reported in [22], and the numerical code is implemented using MATLAB. The extracted effective permittivity (ε) permeability (μ), negative refraction index (NRI) (n) and characteristic impedance (z) are shown in Figs. 3, 4 and 5, where the strong and specked lines mean the real and imaginary values of the homogenous parameters, correspondingly.

As shown in Fig. 3a, the magnetic resonate frequency occurred at 3.8 GHz and the negative frequency band due to permeability extends from 4.29 to 5.24 GHz. The strong magnetic resonance is introduced by the discontinuous branches of ESR.

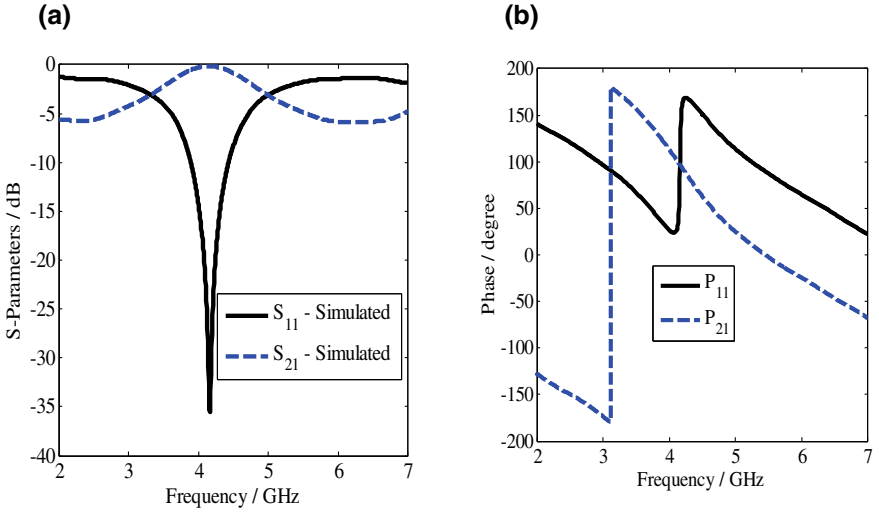

Fig. 2 Simulated S–parameters **a** Magnitude, **b** Phase

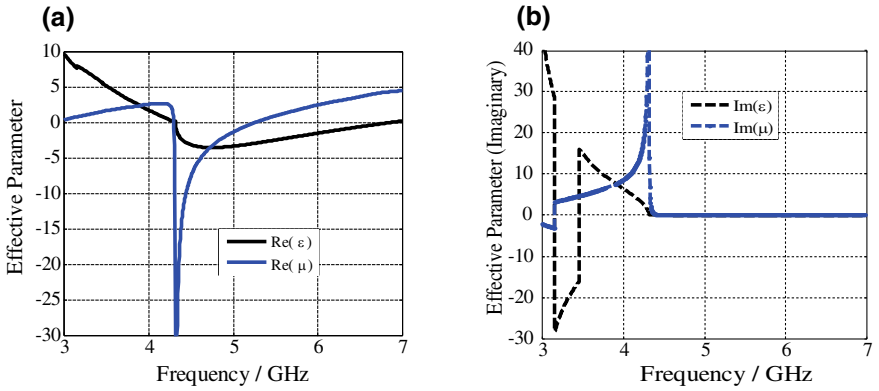

Fig. 3 Retrieval effective parameter **a** Real part and **b** Imaginary part

Similarly, the electrical resonance frequency occurred at 4.31 GHz and the electrical negative band extends from 4.31 to 6.82 GHz. It is observed from Fig. 4a that broadside-coupled ESR MTM structure shows NRI in a large frequency band from 4.31 to 5.24 GHz with concurrent negative permittivity and negative permeability (DNG band).

In 4.31–5.24 GHz frequency range, the imaginary parts of the permittivity, permeability and refractive index are nearly zero (Fig. 3b); hence both electric and magnetic losses in this region are very low. The electric resonant frequency is introduced by the gap between the metallic inclusion branches on both sides of the substrate.

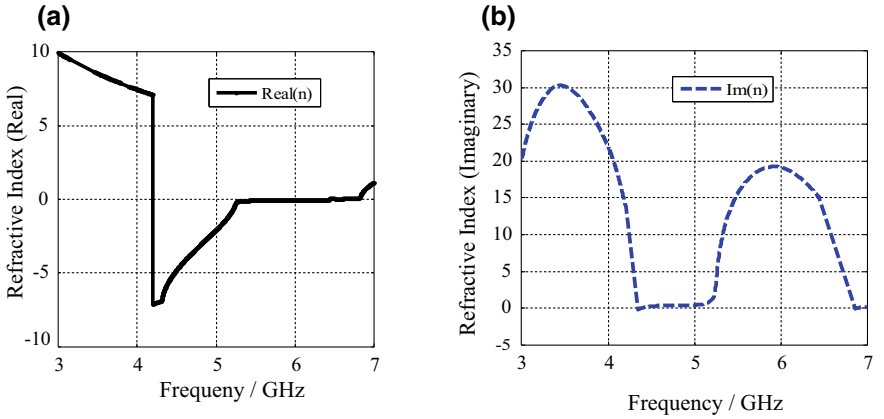

Fig. 4 Refractive index **a** Real part and **b** Imaginary part

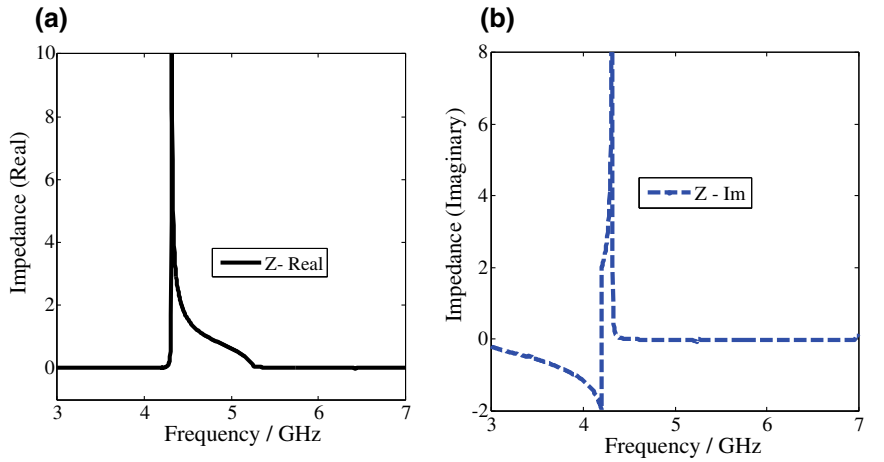

Fig. 5 Relative impedance **a** Real part and **b** Imaginary part

As depicted in Fig. 4a, the real part of refractive index (Re(n)) is nearly zero below the electric plasma frequency up to the LHM region (4.31–6.82 GHz), so by changing the length and width of the ESR unit cell, the desired near-zero refractive index bands can be achieved. In 3.6–4.2 GHz region, the imaginary parts of the permittivity, permeability and refractive index are nearly zero, hence both electric and magnetic losses in this region are very low. It can be seen that the index of refraction imaginary part has large positive values between 5.24 and 6.82 GHz, which exactly matches with the stop-band for the ESR LHM medium. In the region from 4.31 to 5.24 GHz, the refractive index becomes negative and the proposed ESR MTM structure behaves as LHM medium where both the real parts of permittivity and permeability become negative. The relative complex impedance of ESR MTM structure is depicted in

Fig. 5. It can be observed from Fig. 5a that the real part of the relative impedance (Z_{real}) is positive in LHM band. This band actually corresponds to the transmission pass-band of MTM structure. As observed from Fig. 5a, the impedance value in LHM band is very low and does not match well with free space impedance. Note that the imaginary part of impedance (Z_{im}) at 4.16 GHz (transmission peak) of ESR is negative. This anti-resonance physical phenomenon is caused by finite dimension of unit cell and periodicity nature of LHM [16].

Figure-of-merit (FOM) is an important parameter which measures the losses of MTM medium. A high value of FOM leads to low loss in the LHM medium. It can be defined using [23], which is shown in Eq. 1

$$\mathrm{FOM} = -\left[\frac{\mathrm{Re(n)}}{\mathrm{Im(n)}}\right] \tag{1}$$

The FOM is depicted in Fig. 6 for the DNG bands, and it varies from 4.31 to 5.24 GHz for the DNG band. The high value of FOM indicates high transmission with low loss within the NRI medium. The corresponding 1-D dispersion diagram for periodic metamaterial ESR structure is shown in Fig. 7. It is calculated by substituting simulated S-parameters data, which are derived from EM simulation, shown in Eq. 2 as follows [23]:

$$\beta \mathrm{p} = \cos^{-1}\left(\frac{1 - \mathrm{S}_{11}\mathrm{S}_{22} + \mathrm{S}_{12}\mathrm{S}_{21}}{\mathrm{S}_{21}}\right) \tag{2}$$

where p the periodicity of the unit cell = length of the unit cell (l).

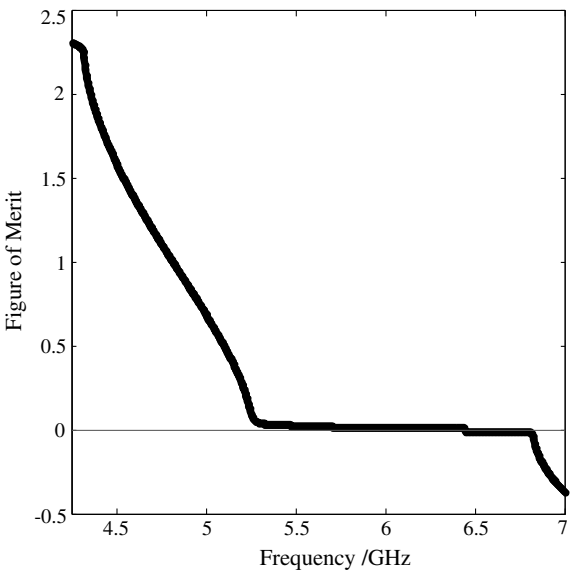

Fig. 6 Figure-of-merit (FOM)

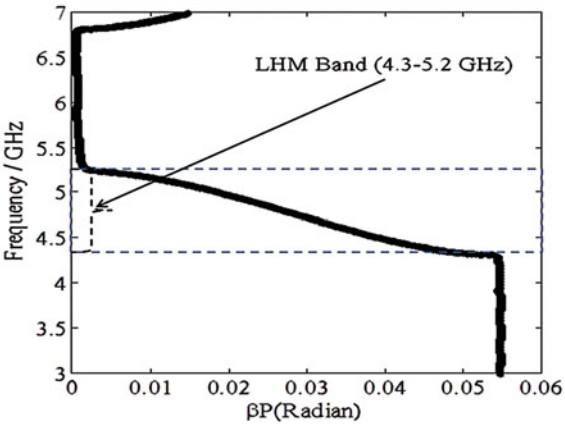

Fig. 7 Dispersion characteristics

From the phase–frequency variation (dispersion) characters curve, as depicted in Fig. 7, it is evident that the proposed planar MTM structure exhibits backward wave propagation from 4.3 to 5.2 GHz and forward wave from 5.2 GHz to higher. So the slow wave region appears in 4.3–5.2 GHz band region, where the ESR MTM structure behaves as LHM medium. From 5.2 to 6.8 GHz, the phase variation with respect to frequency is almost zero, which corresponds to an almost stop-band in the dispersion characteristics plot.

Since we have considered a low-loss FR4 substrate with a loss tangent (tan δ) = 0.02 for our design, the absorbance is expected to be low. The maximum absorbance is about 15% at 4.16 GHz (Fig. 8). It is noted that the dielectric material, substrate

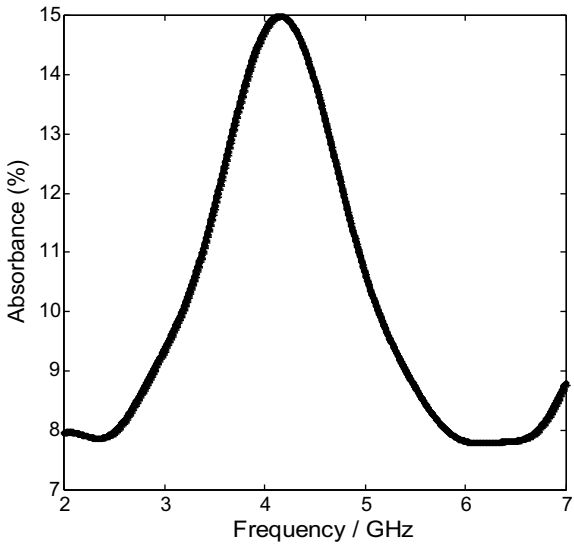

Fig. 8 Absorbance curve

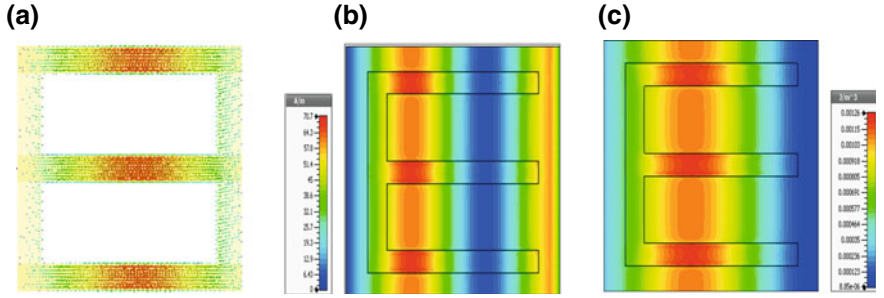

Fig. 9 Absolute value of **a** surface current distribution, **b** E-field intensity and **c** H-field intensity at the resonance frequency of ESR MTM unit cell

thickness and pattern of MTM structure significantly influence on the absorbance property of the LHM.

To enable a clear understanding of the basic mechanism of resonance for our proposed ESR MTM structure, we performed the surface current distribution of ESR pairs on both sides of resonators and as well as electric and magnetic field intensity at the resonance frequency of the ESR by using field monitor in CST MWS. The simulation was performed at 4.16 GHz, which corresponds to the transmission peak in the simulated ESR, as depicted in Fig. 9a–c.

As clearly seen in Fig. 9a, the maximum current is concentrated throughout on most of the ESR branches. This excites the magnetic resonance, and therefore transmission peak occurred at 4.16 GHz in numerical analysis. The direction of current on top and bottom side of ESR is opposite to each other. The opposite directional current on the slab region and on both sides of ESR branches support maximum charges amassing around the capacitive gaps and after that creates E-fields among the ESR metallic inclusions of two surfaces, as depicted in Fig. 9a. From the E-field distribution as shown in Fig. 9c, the energy mainly exists in the gap between the upper and lower metallic inclusions pair of ESR, which effectively demonstrates the behavior. The magnitude of magnetic field intensity is shown in Fig. 9b. It is observed that a circular current distribution on the ESR structure excites magnetic resonating frequency at transmission pass-band.

2.3 Experimental Result

To verify the numerical results as studied before, experiments have been performed using the waveguide setup. In the experiment, the S_{11} and S_{21} parameters of the proposed ESR MTM structure were measured to verify the existence of the pass-band due to the LHM behavior. The geometrical dimensions of the fabricated MTM sample are the same as the numerical EM simulation. The sample under test is two unit cells in the x direction and three unit cells in the y direction, with spacing between

two cells is 0.8 mm in both x and y directions. The developed prototype is shown in Fig. 10.

The measurement setup consists of two coaxial-to-waveguide probes connected to a WR90 waveguide loaded with sample under measurement and an Agilent E8364B vector network analyzer (VNA). The pair of adapters inside the waveguide acts as transmitter and receiver along with the absorbing foam kept on both sides of the adapter probe to fix the sample under measurement (SUT). The SUT is placed inside the waveguide and both magnitudes and phase of the S-parameters are measured using VNA. In the transmission and reflection measurements, the plane waves are incident normal to the MTM sample layer as mentioned in the simulation.

Figure 11 shows the magnitude and phase of the measured scattering parameters. The retrieved effective parameters of the prototype using measured data compared with the simulation results are in good agreement with the simulation results. The discrepancy between the simulated and measurement results in some frequency band is due to fabrication tolerance.

From the measured S-parameter results, it is quite evident that a transmission peak appeared at 4.17 GHz. The measured transmission pass-band occurs during the frequency region from 3.3 to 5.35 GHz for ESR MTM structure. The transmission bands confirm the existence of retrieved DNG band between 4.3 and 5.26 GHz (Fig. 12), which validates that the measured transmission pass-band indeed exhibits a LHM pass-band.

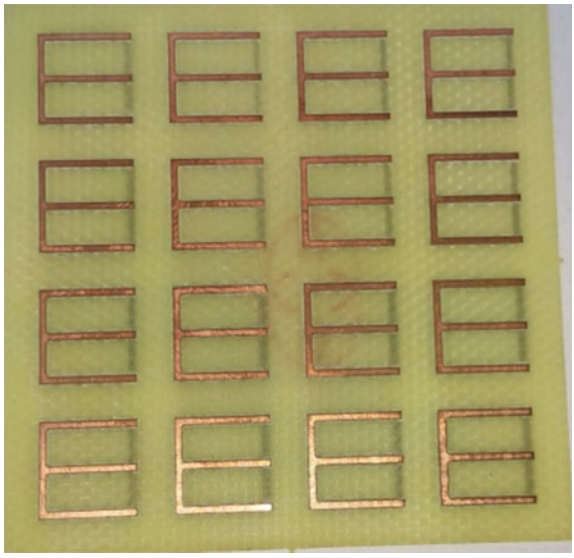

Fig. 10 Prototype of the proposed ESR MTM unit cell

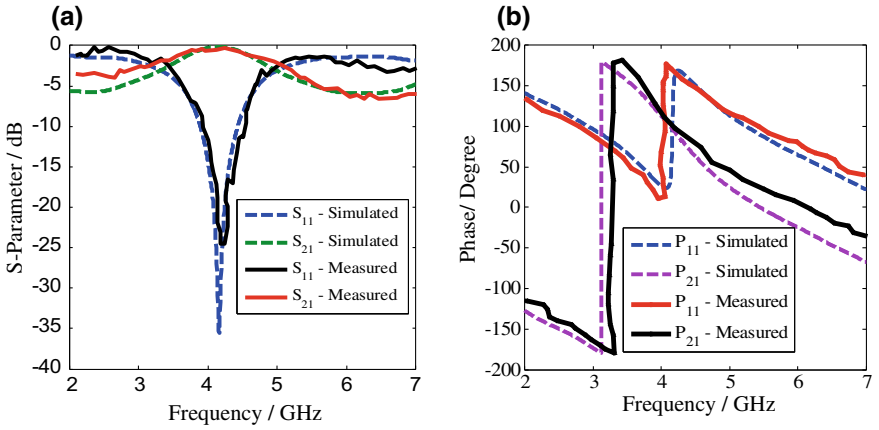

Fig. 11 Measurement transmission and reflection spectra **a** Magnitude and **b** Phase

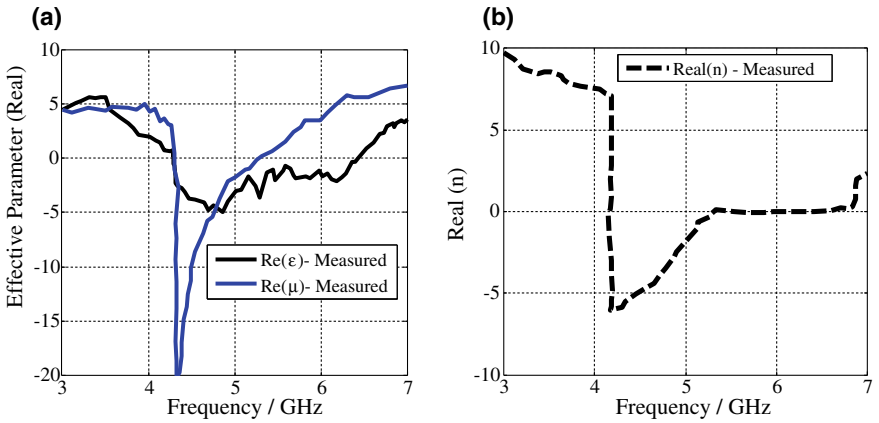

Fig. 12 Measured retrieved effective constitutive parameters **a** effective parameters, and **b** refractive index

3 A Skewed Omega for LHM Characteristics

Owing to resonant structures, metamaterials [2, 3, 5] are inherently limited left-handed (LH) transmission BW. This work presents a study systematically, using transmission and reflection spectra of a new skewed omega engineered subwavelength resonator, which is a adaption of the omega-type DNG structure [11, 19], as DNG MTM with low loss and wide LH-band attributes. Performance regarding left-handed transmission band, refractive index, dispersion characteristics and loss is investigated using measurement as well as numerical analysis on designed prototype. The unit cell comprises twisted omega-type resonator on the front side of substrate and a capacitive loaded strip on the rear. Simulation results demonstrate

that the aforementioned structure has better performance as far as size, LHM behavior and bandwidth are concerned. The effects of different designed parameters, such as side length, strip width, split gap, metal width and arc length are examined for characteristics and performance.

3.1 Numerical and Experiment Analysis of Skewed Omega MTM Unit Cell

Figure 13 illustrates the configuration of a unit cell of designed skewed omega resonator structure, where for simulation the outer radius (L) is 7 mm, strip width (W) is 0.56 mm, split gap (g) is 0.5 mm and the distance among two rings is 0.5 mm. The size of the unit cell is $a_x = a_y = 8$ mm. The skewed omega structure is made of copper deposit (0.05 mm thickness) on a FR4 substrate ($\varepsilon_r = 4.3$ and thickness is 0.716 mm).

The proposed metamaterial unit cell was simulated in two different commercial EM solvers, Ansoft HFSS and CST Microwave Studio. In the numerical using EM simulator, the DNG structure was enclosed with air layer and excited with EM wave. Two waveguide ports were set on unit cell faces transverse to x-axis; perfect magnetic (PMC) and perfect electric conductor (PEC) and boundary condition were assigned transversely aligned to y-axis and z-axis correspondingly. The time-varying EM field was excited along -x direction, with electric and magnetic field vector along -y and -z direction separately. The frequency-domain solvers with periodic boundary in CST MWS and in HFSS were used to simulate and analyze the periodic unit cell MTM construction. A hexahedral global mesh refinement was chosen and the mesh-line ratio limit was set for 30 steps per wavelength by means of advance-level technique to attain good accurateness in the simulation. The model is simulated in the frequency range between 3 and 6 GHz, to get the amplitude and phase in terms of scattering

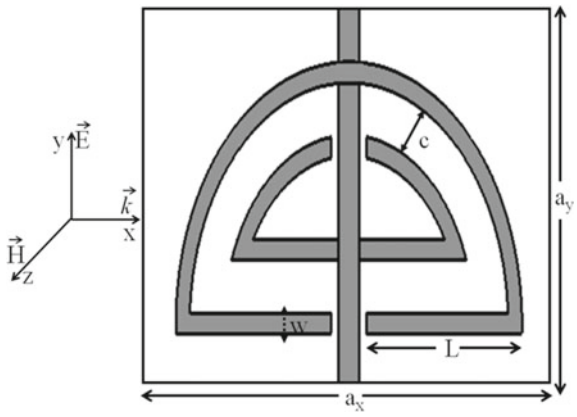

Fig. 13 Configuration of skewed omega LHM unit cell

parameters. The effective parameters and other important characteristics of the LHM medium, such as refractive index, loss, absorption and dispersion characteristics, can be retrieved from the calculated scattering parameters using modified NRW procedure and statistical code [12] contrivances by MATLAB.

3.2 Design and Characterization of MTM Unit Cell

The magnitudes for the transmission and reflection parameters (S_{21} and S_{11}) of the unit cell from CST MWS and HFSS and CST MWS and measurement on prototype, using Agilent 8719ES VNA, are compared in Fig. 14a, b, respectively, indicating good agreements. The discrepancy between the simulated and measured result can be primarily due to the use of the lossy FR4 substrates and the fabrication errors. Figure 14c shows the phases from CST, where a clear phase reversal for S_{11} near the resonant frequency (4.2 GHz) indicating LHM characteristic is visible. Figure 17 depicts the real part of effective permittivity and permeability in 3.5–6.0 GHz band, obtained from the S-parameters using modified NRW method [22, 23]. The permeability, which is due to the skewed omega, remains negative over a wideband (3.7–5.35 GHz) compared to the permittivity (3.7–4.5 GHz) and they match at 4.2 GHz, the resonant frequency. This indicates that it behaves as a DNG in 3.7–4.5 GHz band and as a single negative medium (SNG) beyond it till 5.35 GHz. The imaginary part of effective permittivity and permeability in 3.5–6.0 GHz band is nearly equal to zero as depicted in Fig. 17, which implies that the proposed structure exhibits very loss in the frequency range of interest (Figs. 15 and 16).

A slow wave characteristic is evident in 3.7–4.5 GHz band in the dispersion diagram. Over the same band, negative refractive index is also evident in Fig. 18. It is also seen that in this band the refractive index is almost linearly increasing. Beyond 4.5 GHz it is nearly zero till 5.7 GHz, corresponding to an almost stop-band in the dispersion curve.

The confinement of the E-field and the normalized surface current 2D vector plot on the surface of unit cell structure (ring and the strip) at the resonant frequency is shown in Fig. 19. It is observed that the skewed omega is circulating the current around it as required by a split-ring resonator for producing magnetic resonance, whereas the strip is supporting current for electrical resonance, thereby confining the E-field. Therefore, it can be conclusively believed that the proposed structure behaves as a left-hand medium with backward wave propagation in the 3.6–4.4 GHz frequency regime, and from 4.4 to 5.6 GHz frequency region, it act as a single negative medium band with evanescent mode characteristics.

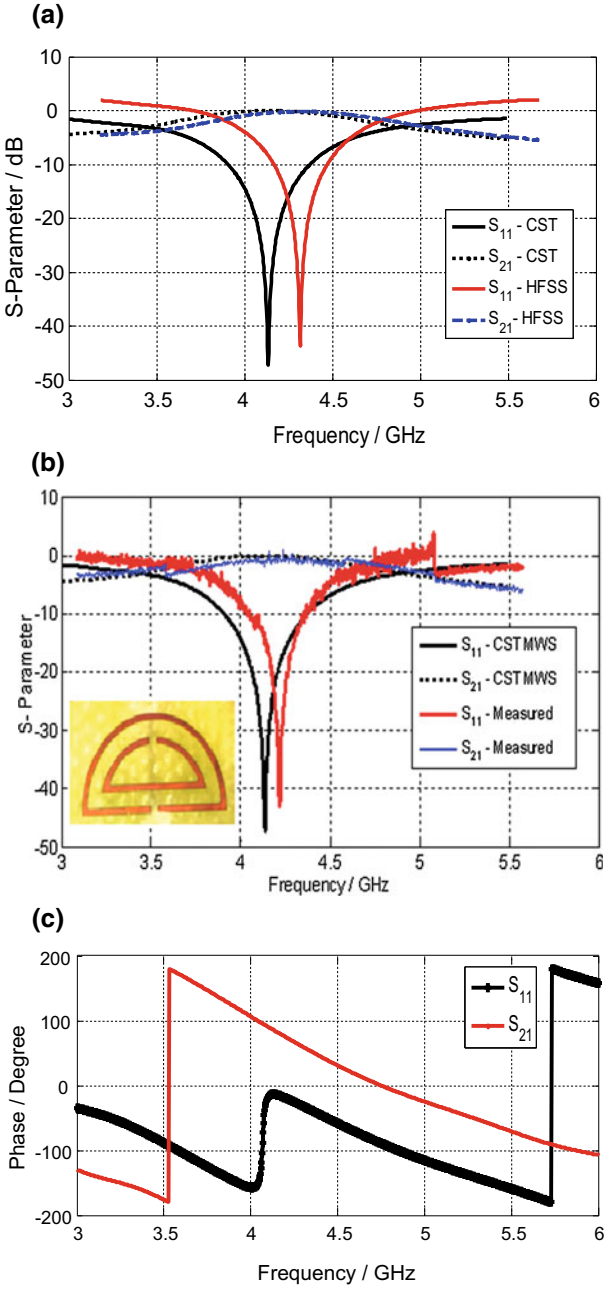

Fig. 14 Magnitude and phase of S-parameter of MTM unit cell

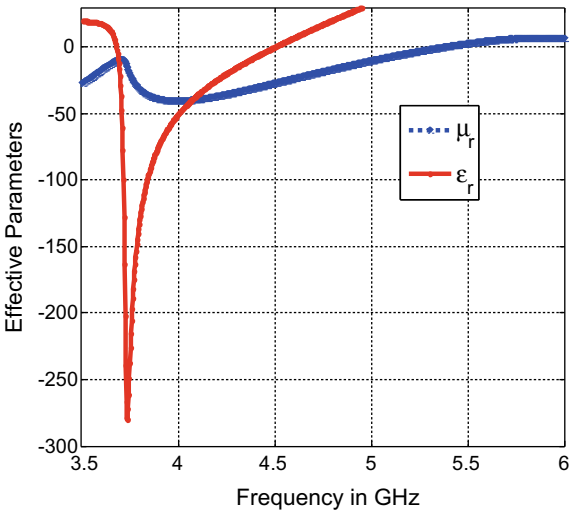

Fig. 15 Real parts of ε and μ curves

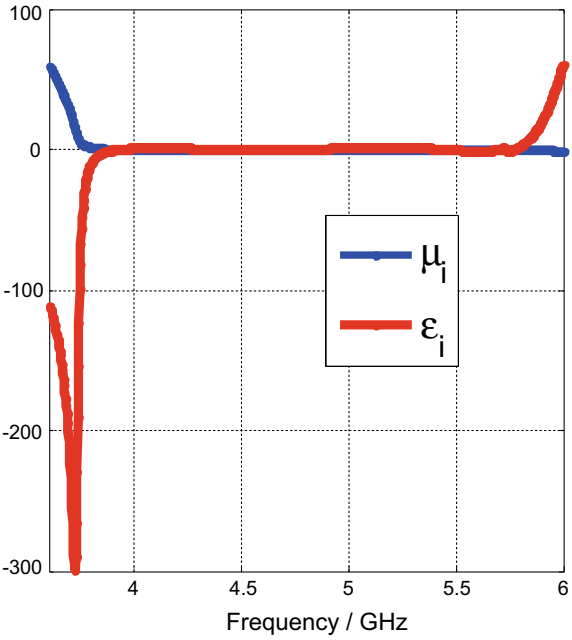

Fig. 16 Imaginary parts of ε and μ curves

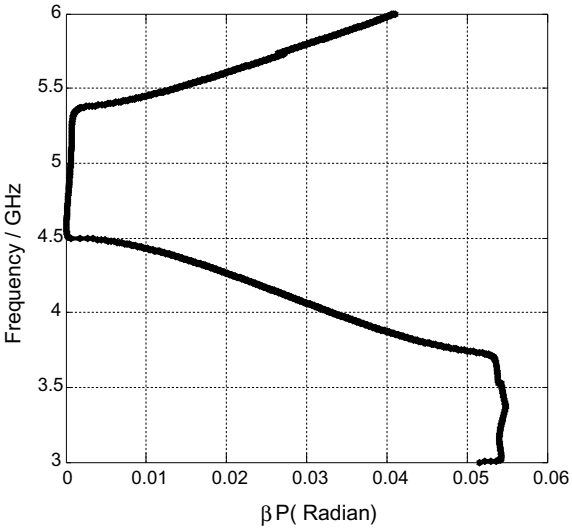

Fig. 17 Dispersion characteristic

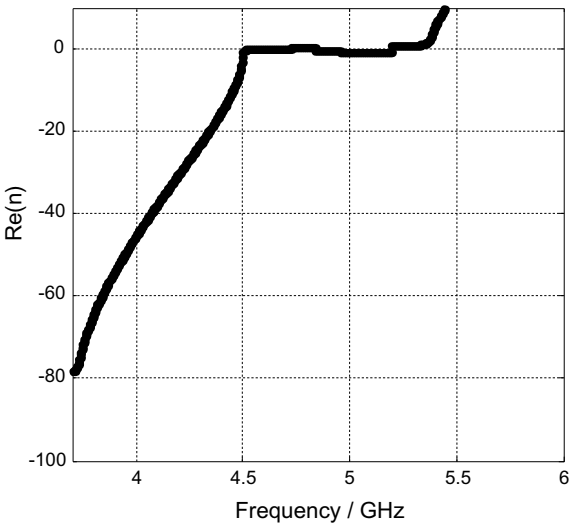

Fig. 18 Refractive index

4 Characterization and EM Response of a Conformal Concentric Sectored Split Sierpinski Resonator

In recent years, after Smith et al. [4] constructed and experimentally demonstrated the first LHM, various kinds of MTMs have been proposed for wide range of applications in antenna, filters, invisibility cloak, sensor, absorber in RF and microwave regime. For the practical applications demand, the MTM structure needs to design on planar

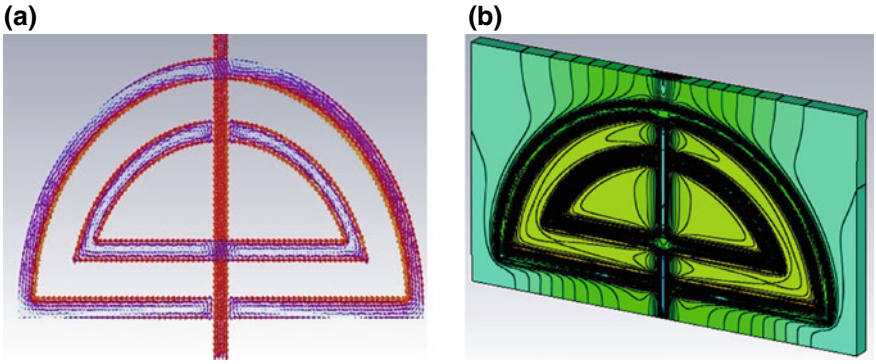

Fig. 19 **a** Surface current **b** E-field distribution

as well as curved surfaces. Several conformal and flexible metamaterial structures have been designed for curved surface application working in RF and microwave frequency band [24, 25]. In this section, we have investigated the reflection characteristics and left-handed (LH) behavior of a conformal concentric sectored split Sierpinski resonator (S-SSR) MTM structure for C-band curved surface applications. The proposed MTM unit cell consists of concentric inner and outer Sierpinski sectoral ring and wire strip. It is proposed media is based on the space filling Sierpinski geometry. Unlike conventional planar metamaterial structure, the S-SSR design on a flexible substrate can be mounted on planar as well as curved surfaces and therefore becomes extremely useful for practical wireless applications. The space-filling geometry is a potential candidate to build miniature microwave devices. Moreover, compared with the conventional planar metamaterial structure, the LHM pass-band and DNG bandwidth of the proposed MTM structure can be widened and enhanced when it was bent and conformed to the surface of objects. The left-handed medium characteristics are observed in the frequency region of interest and thus backward wave propagation.

4.1 Design of LHM Unit Cell

The configuration of conformal S-SSR MTM unit cell structure is shown in Fig. 20. It consists of two concentric sectoral rings. The outer (R_1) and inner radius (R_2) of the SSSRR are 6.9 and 3.3 mm, receptively. The separation between two concentric SRR is 0.4 mm maintained. The strip width is 0.4 mm and slit gap is 0.3 mm gap. The dimension of a unit cell SRR structure is $a_x = 8$ mm and $a_y = 8$ mm. The proposed conformal metamaterial structure has been designed on 0.3 mm FR4 substrate (dielectric constant, $\varepsilon_r = 4.4$, and loss tangent $= 0.00215$), with a copper layer of thickness 0.035 mm.

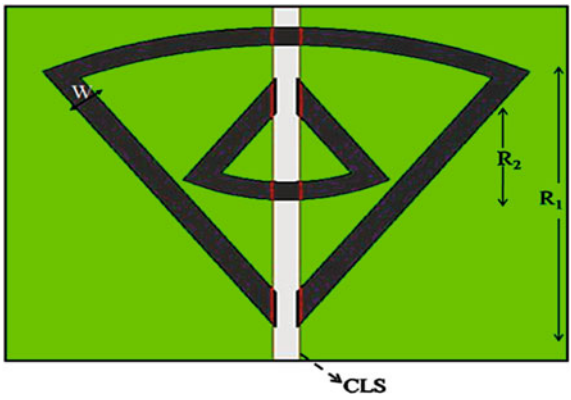

Fig. 20 Configuration of concentric sectored split Sierpinski resonator unit cell

To confirm the electromagnetic behaviors such as permittivity, permeability, refractive index and wave impedance of the planned conformal sectoral arrangement, a plane wave propagating along z-direction, the magnetic field vector along z-axis and electric field along y-direction correspondingly. The projected structure is designed and analyzed using fit-based code (CST MWS). A frequency-province solver was preferred for simulation and retrieving corresponding EM outcomes. The effective parameters can be retrieved from the calculated scattering parameters using repossession procedure and statistical code [22] contrivances by MATLAB to attain the effective medium parameters, refraction index and wave impedance characteristics.

4.2 Results and Discussion

The periodic S-SRR unit cell medium is simulated in a wide frequency ranging from 1 to 6 GHz to get the transmission and refection spectra in terms of S-parameter. Figure 21 illustrates the magnitude and phase of transmission and reflection spectra together. Because of structural symmetric in scenery, the magnitude and phase values of S_{11} and S_{21} are equivalent to that of S_{22} and S_{12}. The effective parameters can be retrieved from the calculated scattering parameters using repossession procedure and statistical code [12] contrivances by MATLAB. As shown in Fig. 21b, there is a dip in the phase and phase reversal of reflection power at 2 and 3.95 GHz. It reveals the existence of LHM band near the resonance frequencies. Transmission and reflection characteristic curve, absorption and index of refraction and dispersion behavior are outline in the range of 2–5 GHz to observe DNG behavior of proposed LHM structure.

The effective medium parameter and refractive index of the unit cell is shown in Figs. 22 and 23. The real part of effective permittivity and permeability is in

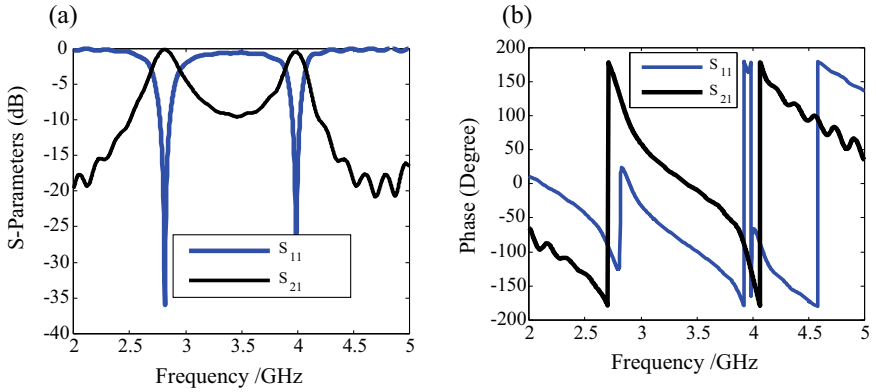

Fig. 21 Magnitude and phase of S-parameters of MTM unit cell

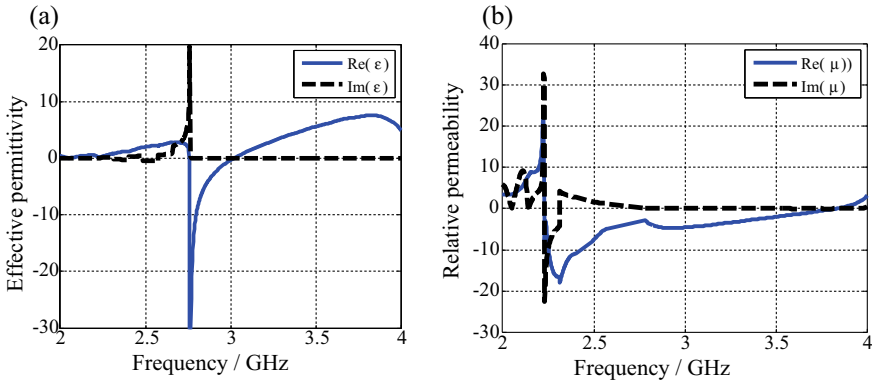

Fig. 22 Retrieval parameter: **a** permittivity (ε), and **b** permeability (μ)

negative ranges from 2.7 to 3 GHz and 2.7–3.05 GHz, respectively. So, in 2.75–3.05 GHz transmission band, the MTM behaves as DNG medium and in 3–3.05 GHz, it behaves as SNG medium. Further, we observe negative refraction retrieved from the S-parameter of the proposed sectoral-shaped split-ring resonator structure which is well-known metamaterial particles with magnetic response to incident waves. The negative refractive index is found from 2.75 to 3.05 GHz (Fig. 23). Therefore DNG occurrence results in negative index of refraction (Re(n)) and accordingly the backward wave transmission occurs within this transmission band in the purposed magnetic medium.

From the dispersion diagram as shown in Fig. 24 illustrates that the unit cell supports backward wave propagation from 2.75 to 3 GHz and forward wave from 3.05 GHz to higher. So the slow wave region occurs in 2.75–3 GHz band region, where the proposed structure behaves as MTM. Also, the simulation results shown in Fig. 24 demonstrate that the proposed structure is low pass and it could achieve a quite

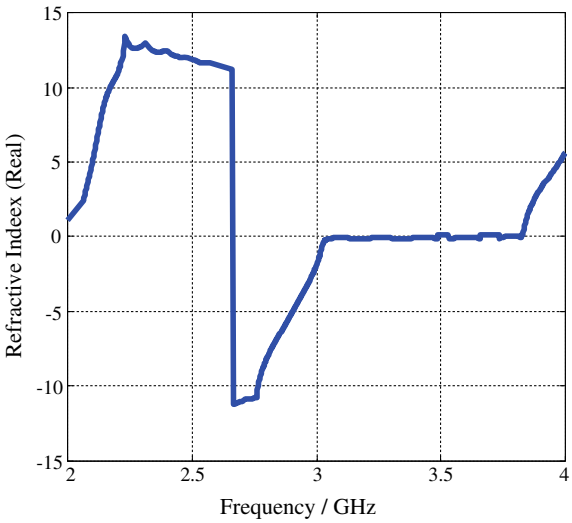

Fig. 23 Real part of refractive index (n)

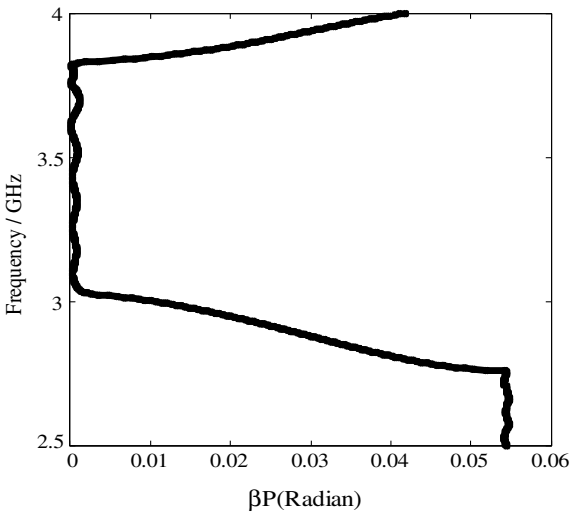

Fig. 24 Dispersion characteristic of S-SSR periodic unit cell

flat pass-band up to 2.75 GHz. Other simulation results for various gap widths and so on which are not shown in this paper also indicate that the pass-band could be well controlled by adjusting the resonance frequencies of the sectoral-shaped split-ring resonator structure. It can be observed that a band-gap is present in the transmission spectrum of sectoral-shaped split-ring resonator medium corresponding to $\mu < 0$.

5 Summary

In this chapter, different planar and curvature artificial inhomogeneous structures have been designed through the introduction of sub-wavelength metallic inclusions into a hosting medium and experimentally realized the LHM behavior at microwave frequency band.

In the first design, the reflection spectra and LHM properties of the planar metamaterial based on a pair of E-shaped resonators have been investigated numerically. The symmetrical ESR structure exhibits low loss with wideband LHM behavior when aligned normal with incident *E*-polarized plane wave. A series of parametric study of the geometrical parameters of the designed left handed medium has been performed to reveal the ramifications of resonant frequency and the retrieval homogenous parameters such as permittivity permeability and NRI. CST MWS EM tool was employed to design and obtain the transmission and reflection parameters of the MTM structure and to monitor the resonance frequency. Finally, a 3×3 array ESR MTM structure is fabricated and tested in a waveguide environment. The effective parameters are retrieved from the S-parameters at the desired frequency obtained by EM simulation and experiment.

In the second model, the electromagnetic characteristic of a novel compact skewed omega double negative metamaterial resonator is investigated numerically and experimentally using EM simulation. It is found that the uniqueness of this miniaturized configuration coordinates those of a DNG MTM with backward transmission behavior. Henceforth, it is estimated that this configuration can be used for realization of LHM for cloaking, antenna superstrate for directivity enhancement, compact resonant planar antenna and so forth cutting edge like applications.

In the last section of the chapter, an attempt has been made to study the conformal sectored split Sierpinski resonator LHM unit cell configuration which is appropriate for both planar and curved surfaces applications. The characteristics of the designed structure MTM have been studied employing CST microwave studio and the calculated reflection and transmission spectra are used to extricate the complex material properties utilizing the retrieval procedure in MATLAB. The simulated results show that the metamaterial sample has double negative property at the microwave frequency range from 2.76 to 3 GHz. Some unique characteristics have been demonstrated by full-wave analysis. Owing to conformal and space filling property of proposed SRR structure, it will be highly beneficial in the design of microwave devices, for example, filters and in antenna to suppress surface waves. Further, it is also easy to integrate with microstrip components and its electrical dimension is quite small.

References

1. Bose JC (1927) Collected physical papers. Longmans, Green and Co., New York
2. Veselago VG (1968) The electrodynamics of substances with simultaneously negative values of ε and μ. Sov Phys Usp 10:509–514

3. Pendry JB, Holden AJ, Robbins DJ, Stewart WJ (1999) Magnetism from conductors and enhanced nonlinear phenomena. IEEE Trans Microw Theory Tech 47(11):2075–2084
4. Smith DR, Padilla WJ, Vier DC, Nemat-Nasser SC, Schultz S (2000) Composite medium with simultaneously negative permeability and permittivity. Phys Rev Lett 84(18):4184
5. Aydin K, Guven K, Soukoulis Costas M, Ozbay Ekmel (2005) Observation of negative refraction and negative phase velocity in left-handed metamaterials. Appl Phys Lett 86:124102
6. Aydin K, Ozbay E (2006) Negative refraction through an impedance-matched left-handed metamaterial slab. J Opt Soc Am B 23(3):415–418
7. Ziolkowski RW (2003) Design, fabrication, and testing of double negative metamaterials. IEEE Trans Antennas Propag 51(7):1516–1529
8. Chen H, Ran L, Huangfu J, Zhang X, Chen K, Grzegorcyzk TM, Kong JA (2004) A left-handed materials composed of only S-shaped resonators. Phys Rev E 70:057605
9. Bulu I, Caglayan H, Ozbay E (2005) Experimental demonstration of labyrinth-based left-handed metamaterials. Opt Express 13(25):10238–10247
10. Bilotti F, Toscano A, Vegni L (2007) Design of spiral and multiple split-ring resonators for the realization of miniaturized metamaterial samples. IEEE Trans Antennas Propag 55(8):2258–2267
11. Saadoun MMI, Engheta N (1992) A reciprocal phase shifter using novel pseudochiral or Ω medium. Microw Opt Technol Lett 5:184–188
12. Chen H, Ran L, Huangfu J, Zhang X, Chen K, Grzegorcyzk TM, Kong JA (2004) A left-handed materials composed of only S-shaped resonators. Phys Rev E 70(5):057605
13. Khan MF, Mughal M, Bilal M (2012) Effective permeability of an S-shaped resonator. Microw Opt Technol Lett 54:282–286
14. Tang MC, Xiao S, Deng T et al (2012) Design of a broadband μ-negative planar material with low frequency dispersion. Appl Phys A 106:821
15. Lv JH, Hu XW, Liu MH, Yan BR, Kong LH (2009) Negative refraction of a double L-shaped metamaterial. J Opt A: Pure Appl Opt 11:085101
16. Dong ZG, Lei SY, Li Q, Xu MX, Liu H, Li T, Wang FM, Zhu SN (2007) Non-left-handed transmission and bianisotropic effect in a π-shaped metallic metamaterial. Phys Rev B 75:075117
17. Marathe Dushyant, Kulat Kishore (2018) A compact dual, triple band resonators for negative permittivity metamaterial. AEU—Int J Electron Commun 88:157–165
18. Aydin K, Li Z, Hudlička M, Tretyakov SA, Ozbay E (2007) Transmission characteristics of bianisotropic metamaterials based on omega shaped metallic inclusions. New J Phys 9:326
19. Panda AK, Sahu Sudhakar, Mishra Rabindra K (2015) Optimization of skewed omega for left-handed material characteristics. J Nanophotonics 9:093039
20. Cheng Z, Yang HL, Nie Y et al (2011) Investigation of negative index properties of planar metamaterials based on split-ring pairs. Appl Phys A 103:989–994
21. Amiri N, Forooraghi K, Atlasbaf Z (2011) Miniaturized resonant inclusions as non-bianisotropic double negative metamaterials for normal incidence. AEU—Int J Electron Commun 65:993–996
22. Smith DR, Vier DC, Koschny Th, Soukoulis CM (2005) Electromagnetic parameter retrieval from inhomogeneous metamaterials. Phys Rev E 71(3):36617
23. Panda Asit K, Mishra Rabindra K, Sahu Sudhakar (2016) A skewed omega for LHM characteristics. Microw Opt Technol Lett 58(4):847–850
24. Melais SE, Weller TM (2009) A multilayer jerusalem cross frequency selective surface. In: 2009 IEEE 10th annual wireless and microwave technology conference. Clearwater, FL, pp 1–5
25. Tao H, Strikwerda AC, Zhang X, Adilla W, Bingham CM, Fan K (2008) Terahertz metamaterials on free-standing highly-flexible polyimide substrates. J Phys 41:1–4

Chapter 3
Advanced Materials for Aerospace Applications

E. V. Bhavya, Shreyash Singh Thakur and Balamati Choudhury

1 Introduction

The word stealth relates to all the techniques that make it difficult to observe or detect an object. There are multiple ways of identifying objects, such as direct observation using our eyes or by using devices such as radars, sonars, and infrared sensors. In military areas, detection and counter detection methods are vital and particularly applicable as it can make a difference of detecting and planning for an adversary airship 200 km away or watching it destroy one's base. Since the improvement of the radar frameworks, the importance of stealth has reached out from microwave stealth to different parts of the electromagnetic spectrum. There has been a constant battle between the two systems of detection and stealth, where the development in one field immediately elicits a response from the other. The significant developments in detection techniques are related to active devices such as radars, sonars, IR imaging systems, and other such methods. These advancements have had such a high impact that a large number of the cutting-edge fighter aircraft are produced with a radar signature decided beforehand.

The stealth techniques came into the picture only after the detection systems were in full-fledged use. The beginning of advanced detection technologies can be attributed to the invention of the radar. The development can be traced back to 1904 when a German inventor by the name Christian Hulsmeyer patented a device which could detect and measure the distance of metallic objects far away using

E. V. Bhavya (✉) · B. Choudhury
CSIR-National Aerospace Laboratories (CSIR-NAL), Centre for Electromagnetics (CEM), Bengaluru 560017, India

E. V. Bhavya
Academy of Scientific and Innovative Research (AcSIR), Ghaziabad, India

S. S. Thakur
BITS-Pilani, Pilani, Rajasthan, India

R. Kumari and B. Choudhury (eds.), *Multiscale Modelling of Advanced Materials*,
Materials Horizons: From Nature to Nanomaterials,
https://doi.org/10.1007/978-981-15-2267-3_3

radio waves. After that, many advancements were made to the radar, but the military use was non-existent until the Second World War. The rapid development phase took place before and after the war with most of the participating countries having some or the other form of radar. The working principle of radar is echolocation. It consists of an emitter and a receiver, both usually located next to each other. The emitter sends radio waves in a particular direction, and on encountering an object, these waves are reflected, scattered, or absorbed based on the target material. The waves that are reflected or scattered back in the direction of the emitter are the ones detected by the receiver and enable the calculation of distance and velocity of the object with respect to the radar. The observability of the object depends on its size, shape, material, and the frequency of the radar which can range from 3 MHz to 100 GHz. There is an equivalent version of the radar called sonar which uses sound waves instead of electromagnetic waves to locate objects. The effectiveness of the two varies drastically depending on the medium being air or water; sonars are preferred in water because of the poor transmissivity of radio waves in water. The two techniques suffer limitations due to clutter and interference such as reflections from ground, sea, and rain. There is another method of detection which is termed infrared sensing and can account for most of the aerial combat losses for the USA in the past quarter-century. This technique uses the heat signature of an object to locate it in space and is widely used as a guidance tool for accurately hitting targets with missiles. It is a relatively modern technology as it requires sophisticated electronics for it to be small and light enough to be fitted onto missiles.

There were parallel advancements in stealth to maintain an edge over the previously mentioned detection systems. The primary device that stealth innovations aimed to counter was the radar, the reason being its widespread use and the lack of alternatives. Today, all military equipment takes into account low observability principles, trying to be discreet in all aspects such as reducing acoustic, radar, and infrared emissions, and trying to blend into the surrounding environment. When using the term low observability, one does not mean complete disappearance from the radar screens; rather it means to make objects tough to distinguish from background noise or insignificant sources such as birds and clouds. The two most often employed low observability techniques are modifying the shape and coating of outer surfaces; both are limited by aerodynamic considerations. The last three decades have seen more developments happening in shaping and are extensively used in the design of fighter aircrafts. Current design techniques commonly go for a balance between shaping and other L.O. techniques. After exhausting the possible advances in stealth with the help of shapes, radar absorbing materials (RAM) have come into the spotlight of stealth research. RAM absorbs a part of the received radar energy and converts it to heat, reducing the reflected power. RAM has been at the forefront of radar cross-section (RCS) reduction efforts since the beginning of stealth attempts, the first one being the construction of a German aircraft *Horten Ho-229*, built a little before the end of Second World War. The design included wings of plywood sandwiched around a mixture of glue, sawdust, and granulated charcoal.

A significant breakthrough in stealth came when the aircraft used a thinly curved extension for the nacelles, leading edges, and fuselage. This created a continuously

curving airframe with sharp edges and a mostly flat underside that reduced RCS up to 90%. The first stealth aircraft *F-117* employed a fully faceted shape, and RAM was used to deal with cavities and surface waves. Initially, the material came in linoleum-like sheets of a ferrite-loaded polymer. They were bonded to the airframe's skin with change in thicknesses at different locations. The subsequent stealth aircraft, *Northrop Grumman's B-2*, was said to depend more on shape and less on RAM than the *F-117*. As the stealth fighter's fully faceted shape only dealt well with specular reflections, surface-wave suppression needs to be addressed. The "*fibermat*" technology used in the *B-2* aircraft is considered a technological breakthrough. The fibermat would replace many RAM structures by being cured into the composite skin, making it durable [1]. In the twenty-first century, a large amount of research has been done for materials relating to stealth using multi-disciplinary techniques, and the recent challenges and progress are detailed ahead.

2 Challenges in Developing Stealth Materials

It is a common practice in engineering to have multiple disciplines collaborating and leading up to the development of novel technologies. This is mostly applicable in the case of stealth as it requires in-depth knowledge of electromagnetism, aerodynamics, material science, electronics, manufacturing, and numerical simulation. It is a tough task to achieve mastery in all these fields within a lifetime to realize true stealth; there is an added layer of difficulty on considering that the area is continuously evolving. This makes it clear that any significant development in the direction of practically achieving stealth requires collaboration between researchers and engineers in vastly different fields. A good example to understand this would be the development of RAM. The first task is to know what types of radars are used for aircraft detection and how they work. Then one requires a model for understanding the interaction of radio waves with aircraft and how this interaction will affect its observability using radar. This task itself requires knowing electromagnetism and numerical simulation techniques. Next, there is the task of modeling material behavior such as coatings on aircraft, along with experimental verification at each step. The materials also need to be tested for their compatibility with aircraft standards such as thermal stability, mechanical durability, and low mass density. This is a challenging task for implementing principles such as design for manufacturing as the disciplines involved are not simply related.

The multiple ways of detection also pose a challenge for developing an all-encompassing stealth material. Even if one considers a narrow outlook of focusing only on radars, one discovers the numerous frequencies of its operation, demanding the RAM to have a broadband capability. Especially at lower frequency bands, the RCS of a low observable aircraft is expected to increase significantly. This is because the wavelength becomes comparable in size with parts of the plane, and light follows the Mie scattering model. The permittivity and permeability of a material dictate its electromagnetic behavior, and these properties usually vary with frequency and

polarization of the electromagnetic wave. This leads to inevitable trade-offs between broadband capability and the radar cross-section reduction (RCSR). There is another incompatibility that arises because of the nature of microwave and infrared stealth. Microwave stealth requires the incident microwaves to be absorbed to fool simple radars, whereas infrared waves need to be dealt with by caging the internal thermal radiation sources and selectively absorbing or reflecting the atmospheric infrared (IR) waves. It is possible for powerful radars to heat the RAM and create hotspots of thermal radiation increasing its IR signature.

Advancements in stealth technologies have always instigated the development of similar anti-stealth technologies, leading to constantly evolving challenges. There have been many reports relating to developments in counter the stealth technologies. Among these, the potential counter-stealth approaches include passive radars, multi-static radars, very low-frequency radars, over-the-horizon radars, and sensitive IR systems. Since stealth aircraft work primarily by deflecting radar signals in directions away from the source, the immediate answer for detecting them is to capture those deflected signals. A multi-static radar system works by using numerous radars all networked together. If a signal sent out by one radar is diverted, then the second radar is in a position to capture it and uses that information to deduce the aircraft's location. The main idea of the multi-static radar is to have one or more receiver antennae in a position to receive the scattered echo. Such multi-static systems have higher reliability, due to the redundancy of the receivers and their passive operation [2].

Another upcoming technology in anti-stealth is the quantum radar. The working principle involves one of the most exciting aspects of quantum physics called entanglement. Entangled pairs of particles are distinguishable from other similar particles, just like a lock and key. A particular key can be identified from a group of related keys by checking it with the corresponding lock. Once the entangled pairs of particles are created, one of them is kept idle with the detectors, and the other one is modulated and sent out by the radar. The brilliance of the system is that when the received signals are being analyzed, one can use the first idle particle to filter out the noise and figure out which wave corresponds to the one originally emitted. This makes it physically impossible to use any kind of signal jamming to spoof or confuse the radar. It also allows for even the weakest signal reflected by the stealth aircraft to be distinguishable from the noise and reveal its location.

3 Sub-domains of Stealth

When one thinks about light, one probably only considers what our eyes can see. In reality, the light to which our eyes are sensitive is just a part of the whole spectrum, similar to the frequencies of sound we cannot hear; there is an entire spectrum of light that human eyes cannot see. This whole range of electromagnetic wave that exists is named as the electromagnetic spectrum. There exist various detection techniques to detect these waves, such as radio receivers used for microwaves, cathode ray

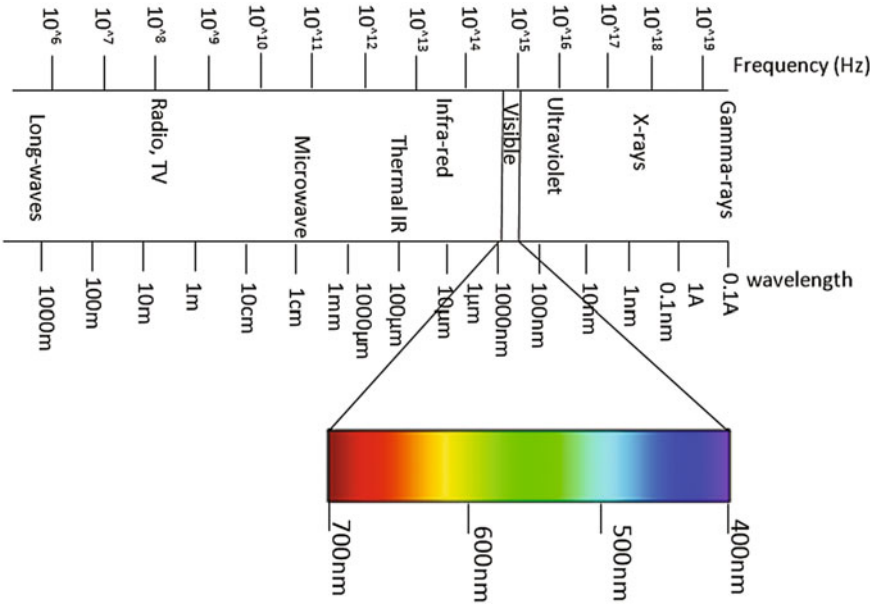

Fig. 1 Electromagnetic spectrum

oscilloscope (CRO), IR sensors, and thermal imaging cameras for infrared waves, and visible light can be detected by light meters and human eyes. The entire range of the electromagnetic spectrum and its detection techniques are described below (Fig. 1 and Table 1).

3.1 Microwave Stealth

Microwave stealth materials

Microwaves are a part of the electromagnetic spectrum most commonly used in radars. The detectability of a target in the microwave region is quantified using the RCS defined as the ratio of backscattered power per steradian to the incident power on the target. RCS depends on the objects shape, size, and material. It also varies with the frequency and direction of the incident waves and the direction in which it is being measured. For example, objects which are electrically large result in scattering including diffraction and specular reflection which enhances its detection by increasing its RCS. In this sub-domain, stealth equates to the reduction of RCS. Radar absorbing material (RAM) is the term used to describe all classes of materials that aim at reducing RCS by absorbing incident microwaves. RAMs generally exhibit selective absorption in the microwave region and often have a peak absorbance at a frequency. There may be a misconception that RAM make objects invisible to radars,

Table 1 Regions of the electromagnetic spectrum with its detection techniques

Type of wave	Example of a detector (sensor)	Approximate wavelength	Typical users
Microwaves	Antenna (aerial), RADAR, crystal detectors, solid-state diodes	1 cm	Communications satellites, telephony, Cooking in microwave cookers In speed cameras
Infrared (IR)	Thermopile, bolometer, black-bulb thermometer, photographic film	0.1 mm	Photography, Burglar alarms, night vision missiles, cooking, heating, in remote controls for TVs and VCD/DVDs
Visible light	Eye, photographic film, electronic components (e.g., LDR) photocell	0.001 mm	Photography, vision (sight), optical fiber, laser beams, weapon aiming systems, CD players, laser surgery

but in reality, they only reduce the RCS at specific frequencies such that they become indistinguishable from the background clutter.

Radar cross-section reduction techniques include shaping, active loading, passive loading, and distributed loading. Shaping aims to counter monostatic radars by avoiding surfaces perpendicular to the incoming waves such that reflected waves do not go in the same direction as the source. Passive and active loadings reduce the scattering from hotspots through the use of resistive sheets or jamming techniques, respectively. In active loading, the object detects the incoming electromagnetic wave and sends an electromagnetic wave with equal magnitude and opposite phase to cancel the incoming EM wave, while in passive loading, the material with a surface resistance is considered to modify the surface impedance of the structure to cancel the scattered signal. Radar absorbing material comes under distributed loading, in which the surface is covered by using RAM material. In this section, an attempt is made to review the RAM with consideration of the materials property required, current developments, and upcoming absorbing materials.

RAM—properties of the material needed

Microwave absorbing materials are a type of functional materials which can dissipate electromagnetic energy by converting it into thermal energy and is found applications in radar absorbers. The concepts behind the design of radar absorber are matched characteristic impedance and matched wave impedance. That is, the characteristic impedance of front face of an absorber should be equal to that of free space and is the criteria for zero reflection. While the matched wave impedance means the input impedance of the front face should be equal to the impedance of free space, it ensures that entire energy is transmitted into the absorber structure. So it is necessary

to select the permittivity and permeability of the material to minimize both reflection and transmission through a material simultaneously.

Electromagnetic energy absorption can be increased by adequately choosing the intrinsic characteristics of the material such as permittivity, permeability, and loss tangents. When permittivity, permeability, and loss components increase, EM energy absorption in RAM improves. However, when waves reach a boundary between two mediums, energy can be reflected rather than absorbed. And the amount of reflected energy depends on their impedance and is given regarding materials permeability and permittivity. For perfect matching, the ratio of relative permeability to relative permittivity should be equal to unity. The imaginary parts of permeability and permittivity indicate the losses in the dielectric material. So for minimum transmission value, the imaginary parts of the material properties might be as large as possible. RAM design must have a balance between absorptivity and surface reflectivity to achieve maximum absorption because if an impedance change occurs more energy is reflected rather than absorbed.

RAM constitutes a matrix material and a filler. The matrix material is considered to be a low loss dielectric material with significant permittivity and negligible permeability and is transparent to EM waves. Insulating polymers like plastic, glass, resin, polyurethane, and rubber are most commonly used as the matrix material. The RAM filler is usually particles composed or coated with a lossy material.

Researchers are always in search of new materials to substitute the existing high-density RAM for stealth applications. Conventional absorbers are generally either magnetic or dielectric types. The working principle of magnetic absorbers is based on the magnetic hysteresis effect using magnetic substances such as ferrites. The disadvantages of a magnetic RAM material are its high density and narrow bandwidth. Instead, dielectric materials are lightweight but do not have the absorption capability as good as magnetic RAM. So both these have benefits and downsides when used as absorbers. Both of these can be used as a composite with magnetic material as the bottom one and dielectric material as top one, though the high density of the material remains a significant challenge in RAM designs.

3.1.1 Carbon-based Material

Many materials have been proposed to meet microwave stealth requirements, with carbon-based materials being one of the most promising candidates. Carbon is a suitable material for dielectric absorption because its electric loss is proportional to conductivity and carbon's conductivity lies below metals but above insulators. Carbon-based materials are abundant in nature and are synthesized or retrieved from organic and inorganic compounds. By controlling the parameters such as temperature and pressure during the processing, the physical, mechanical, electrical, and thermal properties of carbon material can be altered. Usually, researchers are in search of highly efficient, thermally conducting, mechanically stable, and lightweight material with high values of dielectric and magnetic losses for RAM application.

Carbon Foam

Carbon foam is a high-performance, sponge-like rigid material in which carbon ligaments are interconnected to each other. The electric conductivity of the material directly depends on its carbonization temperature, enhancement in carbonization temperature increases the conductivity of a material, and conductivity directly influences its absorbing character. As the electric conductivity changes from 0.02 to 1.03 S/m, the foam changes its characteristics from transmitting to reflecting [3]. The best microwave absorption obtained was for the carbon foam with an electric conductivity of 0.46 S/m, with absorption exceeding 7 dB across the measured frequency range of 4–15 GHz [4]. To enhance microwave absorption, the material is heat treated at a lower temperature to make it a dielectric or a material with low electrical conductivity. However, to utilize carbon foam as a RAM in stealth applications, it is also required for it to be thermally stable and conductive for quick dissipation of heat. As it turns out, the carbon foam treated at low temperature does not have sufficient thermal stability or conductivity, and one needs to infuse the foam with other materials such as magnetic or dielectric nanoparticles to match the standards.

Carbon foam was first prepared using heat treatment of thermosetting polymeric materials in a controlled environment. Later, coal tar and petroleum pitches were used for production. Carbon foam obtained from the above technique gives low thermal conductivity and is primarily considered as a thermally insulating material. High electrical and thermal conductivity can be achieved in crystalline carbon foam by using meso-phase pitch with high-temperature and high-pressure foaming techniques.

Carbon Fiber

Carbon fibers are fibers of carbon atoms about 5–10 μm in diameter. Carbon fibers are widely used in civil and military applications because of its high tensile strength, high stiffness, low weight, high chemical resistance, high heat tolerance, and small thermal expansion. While comparing similar fibers, such as glass fibers or plastic fibers, with carbon fiber it has superior tensile strength but comes with a high price.

Carbon fibers as such are not used in any of the applications. Usually, it is used as a composite by combining the fiber with other materials. The most commonly used carbon fiber composite is a carbon-fiber-reinforced polymer (CFRP), which is obtained by infusing the fiber with a plastic resin. This is often called as the carbon fiber, exceptionally rigid material with a very high strength-to-weight ratio. CFRP consists of two parts: a matrix and a reinforcement. The matrix is used to keep the reinforcement together, whereas the reinforcement should be a high strength material. In CFRP, carbon fiber acts as the reinforcement and a polymer resin, such as epoxy, is used as the matrix which is mixed with a hardening agent to form a solid. Carbon fibers are also used as composites of graphite to former in forced carbon–carbon composites with superior heat tolerance. Untreated carbon fiber is a strong

radar reflector, and it is a specially treated carbon fiber that absorbs microwaves. Thus carbon fiber processing methods improve its electromagnetic parameters.

Carbon fiber (CF)/FeCoNi composites, another type of carbon fiber composite, are composed of carbon fibers and magnetic material, like Fe_3O_4, $NiFe_2O_4$, $CoFe_2O_4$, and Ni_3Fe. The magnetic particles in these composites are spread equivalently along the axial direction of the material and electromagnetic waves undertake numerous reflections in the fiber. CF/FeCoNi composites exhibit also excellent performances by uniting the properties of carbon fiber and magnetic loss materials [5]. These composite materials can also be used as lightweight and high-performance radar absorbing materials, by adjusting their treatment parameters such as temperature and time.

The most recently introduced carbon fiber-based composite is the frequency-selective fabric composite (FSFC), which is fabricated by weaving carbon fibers and dielectric fibers in periodic patterns. This is similar to the frequency selective surface (FSS), where carbon fibers correspond to metal parts due to its high electrical conductivity, and reflects the incident waves, and glass fibers with low permittivity, corresponding to aperture parts, transmit most of the incident waves. Therefore, FSFC is used as an inductive frequency selective surface (FSS) and is a promising candidate for radar absorbing structure (RAS). Carbon fiber production is done mainly using two components: (i) poly acrylonitrile (PAN) and (ii) pitch.

Carbon Nanotubes (CNT)

Nanostructured materials have been broadly researched for radar absorbing properties. The carbon nanotube is used as a conductive element in RAM design due to its material characteristics. CNTs have a pipe-like structures with walls made of carbon atoms linked neatly together. The carbon nanotube is 1 nm in diameter. When compared with carbon fiber it is 2000 times smaller than a carbon fiber filament. There is a significant difference between carbon nanotubes and carbon fiber based on its crystal structure and physical properties. The carbon nanotube's superior atomically bonded crystal structure is what makes it the strongest and stiffest material, nearly 20 times stronger than carbon fiber. CNT displays high mechanical resistance, low-density, and excellent electrical and thermal properties. Studies have demonstrated that CNTs can exhibit good microwave absorption when integrated with polymeric matrices and in multi-layer structures. The aforementioned properties of CNT make it a suitable candidate, both in the microwave and infrared stealth technologies.

The method of production greatly defines the properties of CNT, such as diameter, length, density, and purity. Recent studies show that a higher amount of absorption is observed when CNT with fewer nanotubes and the increased length is considered. Composite is made up of CNT, and polymeric structure presents a RAM with enhanced absorption characteristic. George et al. proposed a nanostructured composite made of small portions of multi-walled CNT (0.086 wt%) in natural rubber. The interconnected network in nanostructured composite gives rise to a high value of

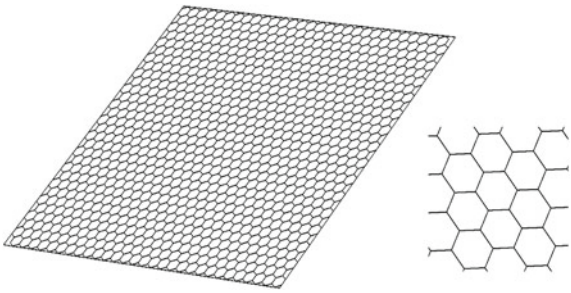

Fig. 2 Illustration of graphene

electrical conductivity and dielectric constant with improved mechanical properties such as elastic modulus and tensile strength [6].

Currently, the CNT coating on an airplane is not feasible due to the limitations in the fabrication processes. One hypothesis to overcome these restrictions is to cover small particles with the nanotubes and suspend them in a medium, for example, paint, which would then be applied to the aircraft.

Graphene

Graphene (G) is a trending material of vast research interest for a wide variety of applications in the field of engineering, especially at microwave and terahertz frequencies. It is a 2D layer of graphite with hexagonal geometry (Fig. 2). It was first observed through an electron microscope in 1962 and was studied only on metal surfaces. It was later rediscovered by Andre Geim and Konstantin Novoselov at the University of Manchester in 2004 [7]. Graphene is a semi-metal which comes under the category of zero bandgap materials; these materials have a small overlap between its valence and conduction band. Graphene possesses some attractive features, such as low density, large specific surface area, high chemical stability, tunable surface conductivity, and outstanding electronic properties.

Developing a composite with distinct morphologies like the ferrite graphene (FG) which consists of magnetic- and carbon-based elements will contribute a lot to the research of RAM. Disperse graphene into magnetic materials like ferrite to introduce free charge carriers in graphene and to improve its absorption effect. Research with a focus on the particle size, shape, concentration, temperature, and so on is going on to improve absorption properties of graphene and its composite materials. The interfacial electronic interactions between ferrite and graphene will lead to a phenomenon of charge transfer, and it alters the electronic properties of graphene. This results in the formation of ferrite graphene heterogeneous nanocomposites with some novel EM properties [8]. Composites with graphene show a significant reduction in weight as well as thickness and hence suitable for high-speed aircraft. The composition and structural integrity of the absorbers are also of great concern. It is necessary to choose the optimal weight fraction of ferrite and graphene and adjust the dielectric, magnetic, and EM wave properties of the composite to obtain the required

absorbing properties. Multi-layering and frequency selective surfaces (FSS) along with proper material selection can play a vital role in the field of research for thin and broadband EM wave absorbers. The radar absorption property of the ferrite graphene-based composites strongly depends on the internal structure, morphology, and its composition [9].

Graphene and graphene-based hybrids are extensively studied over the years while considering its superior electromagnetic absorption and shielding properties. Examples for graphene-based hybrids are G/CNTs, G foams, G/ZnO, and G/magnetic nanoparticle composites [10].

3.1.2 Ferrite-Based RAM

First, RAM that was employed is the iron ball paint consists of carbonyl iron or ferrite. In iron ball paint the alternating magnetic field in the incident electromagnetic wave produces magnetic oscillations, and it leads to conversion of electromagnetic energy into heat and is dissipated.

Ferrite is a metal oxide which comes in the category of a magnetic material, which contains magnetic ions arranged in such a manner that it produces spontaneous magnetization while maintaining good dielectric properties. Ferrites are extensively used for microwave absorption as they use inexpensive raw materials and have simple fabrication methods. Absorbers based on these ferrites are now commercially available under the trade name Eccosorb and are operable at frequencies below 1 GHz. Such absorbers in practice are, however, heavy and brittle and are usually 6–8 mm in thickness.

Among the variants, spinel ferrites are gaining momentum because of their magnetic properties and high electrical resistivity for the broad frequency range. Nickel ferrite ($NiFe_2O_4$) has the highest absorptivity among spinel ferrites leading to its applications as RAM. Spinel ferrites such as nickel–zinc ferrites have also been used as absorber materials [11].

More recently, hexagonal ferrites have entered the scene as they allow better absorption at higher frequencies (X-band) with thinner layers. Absorption mechanism in hexagonal-type ferrite is characterized by its lossy interaction of the magnetic field of the wave with their distinct magnetization. The hexagonal-type ferrite materials exhibit a significant value of permeability (>1), the high value of magnetization, and planar anisotropic behavior in microwave frequencies. Several types of hexagonal ferrites are reported with complex crystal and magnetic structures. The magnetic ions can be replaced by substituting divalent ion and the magnetization increases with increasing amount of non-magnetic substitution [12]. Mostly reported hexaferrites RAM are based on barium. Barium hexaferrite possesses great magnetic properties due to its slightly altered crystal structure and the presence of large barium ions. Through external doping of divalent ions (Zn, Co, Ni, etc.) [13], the magnetization and the anisotropy of barium hexagonal ferrite can be further boosted.

The thickness of the absorber is an imperative criterion in stealth applications, especially for aircraft where weight considerations are very important. Therefore,

maximum absorption with the minimum thickness of absorber is desirable. Absorbers capable of responding to a wide frequency bandwidth of radar signals are required. Large bandwidths are easily achieved by stacking some absorber layers of varying thickness. This increase in bandwidth also increases the absorber thickness. Single-layer absorbers would be more useful in applications where weight is a major consideration.

3.1.3 Silicon Carbide (SiC)

Vast research is going on in the field of carbon and conducting polymer-based absorbers for the last few years. Unfortunately, carbon materials have difficulty in attaining impedance matching because of their significant permittivity and negligible permeability. However, individual conductive polymer materials lack a broad absorption bandwidth. Also, under extreme temperature and stringent working environments, the thermal and chemical resistance of carbon materials and conductive polymer materials is unacceptable, and it restricts their application in the aerospace domain. Nevertheless, SiC stands out for its exceptional properties regarding EM wave absorption and high-temperature stability.

SiC, a semiconductor, consists of silicon and carbon used only as structural ceramic for a long time, and also have high microwave absorption capability. SiC is a high strength and hardness materials. Along with its absorption ability, it possesses good corrosion resistance and excellent dielectric property. Because of its high thermal stability and thermal conductivity properties, it is commonly used in high-temperature environments. Hence for the electromagnetic wave absorption, SiC can be considered as a promising absorber candidate with relatively large bandwidth [14].

Different type of SiC structure is available; it can be zero dimensional (e.g., nanocrystals or particles), 1D (e.g., wires, tubes, and whiskers), 2D (e.g., flakes, platelets), and 3D (e.g., more complex structures). Excellent chemical and thermal properties are achieved in SiC because of its strong covalent bond between Si and C atoms. Si/C atom is surrounded by four C/Si atom to form a tetrahedral sp^3 hybridized bonds. Single intrinsic electric dipolar polarization in SiC reduces the dielectric loss of this material which in turn reduces the electrical conductivity; hence the possibility for its broader applications is limited. This can be overcome by altering the phase, or structural features of SiC to improve its polarization and multi-reflection of the incident EM waves [15].

Modified SiC is used extensively in the design of radar absorbing material and they are SiC modified with carbon-based materials such as CNT, carbon black, and graphene, or with polymeric materials such as PANI, PVDF, or with inorganic materials such as Si_3N_4, SiO_2, or with metal such as Fe, Co, Ni, or their oxides [14, 16].

3.1.4 MXenes

MXenes are a class of attractive compounds which came into the picture in 2011. Material science describes MXenes as a class of two-dimensional inorganic compounds with few atom-thick layers of transition metal carbides, nitrides, or carbonitrides. MXenes are hydrophilic because of their hydroxyl or oxygen-terminated surfaces. MXenes combine its hydrophilic nature and metallic conductivity of transition metal carbides. MXenes are synthesized by etching a layer from MAX phases, and the name "MXenes," MX came from the MAX phases, and "ene" is added to show the similarities of MXene with graphene. MAX phases are a large family (60+ members) of layered hexagonal structure with a composition of $M^{n+1}AX^n$, where M stands for an early transition metal (such as Ti, V, Cr, Nb, etc.), A stands for a group A element (such as Al, Si, Sn, In, etc.), X stands for carbon or nitrogen, and $n = 1$, 2, or 3 [17].

Major attractive applications of MXenes are lithium-ion and sodium-ion energy storage systems, electromagnetic interference (EMI) shielding, and RAM. MXenes are extremely important in electromagnetic field due to their good flexibility, easy processing, and great conductivity with minimal thickness.

Since the discovery of Ti_3C_2 MXenes, it has attracted tremendous attention in the field of fuel cells, lithium-ion batteries, and supercapacitors. In the ordered Ti_3C_2MXene, $(n + 1)$ layers of Ti cover n layers of C. Single or double layers of tip are sandwiched between the layers of a second Ti. EM absorbing materials should have increased polarizations and moderate conductivity for achieving the dielectric loss and impedance match. One can improve the dipole polarization by introducing an intrinsic defect in the structure by using a surface functional group and will result in decreased electrical conductivity. Two-dimensional Ti_3C_2Tx MXenes are extensively studied for its absorption characteristics; an enhanced absorption characteristic is present in this material because of the presence of chemically active surfaces combined with the native defects and its metallic character [18].

3.1.5 Metamaterials

Metamaterials are materials displaying definite properties that are not available in naturally occurring materials, the most important one being the capability to exhibit a negative refractive index. Metamaterial was proposed by Rodger M. Walser of the University of Texas. The name metamaterial comes from the word "meta," which in Greek means beyond, so metamaterial means beyond the material. Even though metamaterials are fairly new, Victor Vesel ago predicted the presence of doubly negative materials in 1968. Doubly negative materials are also known as left-handed materials (LHM). Metamaterials are not naturally occurring material with a negative value of permeability, permittivity, and negative refractive index. Metamaterial structure is fabricated by etching the metallic patterns on a dielectric substrate. Some patterns can be fabricated; such as electric ring resonators with wires, graphene-based films, stacked rings, a combination of FSS, and I-shaped rods.

Electromagnetic absorption characteristics of metamaterial-based RAM depend on its distinct material properties, geometry, and dimensions of the metallic patch and thickness of the substrate. If the cell size is equal to a quarter of a wavelength, then it is called effective-homogeneity limit where refraction dominates scattering/diffraction when the wave propagates through a metamaterial.

Generally, metamaterials are categorized into resonant and non-resonant metamaterials. The material properties such as permeability and permittivity possess a dynamic range adjacent to the resonant frequency, then it is known as a resonant metamaterial. The plot of permittivity versus frequency and permeability versus frequency is seen to follow a Drude–Lorentz relationship as it displays a particular response. The major disadvantage of this kind of metamaterial structure is the narrow bandwidth as well as high loss in the resonant frequency region. Therefore, observing the material parameters, such as ε and μ provides insight into the performance of a metamaterial. But obtaining these material parameters is quite challenging.

Some literature is already available regarding the broadband radar absorbers. Wakatsuchi et al. [19] presented a lossy cut wire pair broadband metamaterial absorber for arbitrary polarization. A periodic unit of lossy cut wire pair with altered lengths is combined and placed adjacent to PEC. The paired cut wire works for both polarizations by exhibiting both electric resonance and magnetic resonance with an absorption peak of 0.76 at 27 GHz [19]. In 2011, Grant et al. presented broadband metamaterial absorber with a stacked metal-insulator layers of different structural parameters in terahertz frequency. The absorption of the structure improved more than 60% with a bandwidth of 1.86 THz [20].

Liu et al. [21] proposed a broadband metamaterial absorber with high absorption capabilities. The proposed structure consists of three layers; the first layer being the ground plane and a dielectric spacer is placed as the second layer and circular metallic patches are etched on the top layer. Broadband resonance characteristics are achieved with the multi-band resonance of each metallic patch, and bandwidth of 2.8 GHz is achieved [21]. Yuan et al. [22] designed and experimentally validated lumped element broadband metamaterial absorber. The designed composite metamaterial behaves as polarization and angle of incidence independent absorber with an improved absorption characteristic in the frequency band of 2.85–5.31 GHz with a relative bandwidth of 60.3% [22].

3.1.6 Conducting Polymer

Conducting polymers are one of the new additions in RAM. They are organic polymers that conduct electricity and such composites may have metallic conductivity or can be semiconductors. Polymer works as a small bandgap semiconductor because of its conjugated π-system. The main drawback of conventional metallic materials, such as copper, steel, and metallic powders is that their conductivity cannot be controlled. Here comes the new conducting material, that is, conducting polymer in which their conductivity can be controlled during its processing phase. The intrinsic conducting polymers with a wide range of electric conductivity can be used as an

EM wave absorbing the material. Along with its ability to control the electrical conductivity, it also has control over its coating thickness, and is transparent, and has a simple and effective surface coating [23].

The thickness and complex permittivity of the material defines the reflection loss of material. Controllability over the electrical conductivity and coating thickness makes conducting polymer a suitable dielectric loss component for RAM. Phonon-assisted hopping between the randomly distributed localized states contributes to the conductivity of a conducting polymer. Conductivity is achieved in a polymer such as polypyrrole (PPy) by the partial oxidation of the polymer (doping), and during the process polarons and bipolarons are formed as the charge carriers along the chains [24, 25].

Polypyrrole–Polymer Composites

Polypyrrole shows high electrical conductivity along with environmental stability and ease of production. However, its practical applications in the aerospace domain are limited due to its mechanical properties, such as high brittleness and low processability. Incorporating PPy within an electrically insulating polymer overcomes the poor mechanical properties and has opened a new door toward the development of conducting polymer composites. Hence most of the useful materials are composites of polypyrrole and other materials such as latex, fibers, or polymer blends. At frequencies above 1 GHz, because of the hopping mechanism of charge transport in the conducting polymer, the conductivity is dominated by the AC conductivity and is dependent on the frequency. Conductivity in the composite does not depend on the material concentration, making it an intrinsic characteristic of the material. Though, processing has a great effect on its material properties such as permittivity, conductivity, and reflectivity. A resonant Dallenbach layer can be easily made from a melt injected polypyrrole/PVC composite, but making a tuned absorber from a compressed sheet of polypyrrole/PVC composite is a difficult task [25].

Polypyrrole Fabric Composites

Polymerizing pyrrole in the presence of fabric or fibers gives rise to different materials which are of interest in the engineering field. By changing the chemical proposition and deposition time, the electrical conductivity of the composite can be tailored. The use of polypyrrole-coated fabrics enables the formation of structural RAM. The properties of the fabric-coated materials were modeled and made used in Salisbury screens and Jaumann layers. By varying its conductivity, it can be used in a wide variety of applications [25].

Polyaniline (PANI)

Polyaniline (PANI) comes under the family of conducting polymers with a 1000 repeat units of polymers and was first reported in 1862. Among conducting polymers, it got attention due to its superior electrical conductivity. Controllability over its electromagnetic parameters and coating thickness improves its EM absorption over a broader bandwidth. Hence it can act as an ideal candidate for radar absorbing material. Polyanilines are produced by oxidative chemical polymerization with three different oxidation states, namely the completely reduced leucoemeraldine base, the completely oxidized pernigraniline base, and the emeraldine base. Different types of polyaniline structure can be produced such as bulk powder, cast films, or fibers and it can also be used in conjunction with glass fiber textiles and PET textiles. Apart from its capabilities, feasibility of low-cost and large-scale production makes it a suitable replacement for a RAM [25].

3.1.7 Hexagonal-BCN (h-BCN)

Graphene discovery has accelerated the research and development of numerous 2D materials, and among them, more studies have been carried out for hexagonal boron nitride (h-BN). h-BN is also having honeycomb structure and contains boron and nitrogen atoms in equal number which are bonded by sp^2 hybridization. Although h-BN and graphene have similar atomic structure, bond strength, and physical properties, h-BN is an insulator due to its wide bandgap of 5.971 eV. Further research has been conducted to identify other possible hexagonal structures similar to graphene and h-BN, and scientists have successfully synthesized structures like graphitic carbon nitride g-$C_3N_{44}C_3N$ and hexagonal graphitic BCN (h-BCN). Properties of these structures are inclined to graphene; for example, h-BCN is more conductive compared to h-BN with a bandgap of 1.5 eV which is greater than gapless graphene and less than insulating h-BN.

Since hexagonal BCN (h-BCN) has exceptional thermal stabilities, chemical stabilities, and adjustable dielectric property, it falls under the promising class of EM wave absorption materials. B and N dopants in h-BCN enhance the lattice polarization and by controlling the N dopant lowest reflection loss can also be achieved, resulting in a highly efficient frequency tunable radar absorber. The mostly used magnetic and dielectric absorbers fail at high temperature, especially above 850 °C. SiC nanomaterials are proposed at high temperature due to its high temperature stability and excellent electromagnetic wave absorption, but its non-tunable complex permittivity and relatively high absorption frequency (in higher GHz) moderates its use in microwave region. In this case h-BCN can replace all these materials due to its extraordinary thermal stability and strong polarization. Also, by adjusting their chemical composition and changing the complex permittivity through the adjustment of B:N:C atom ratio in the hexagonal lattice, we can easily control the dielectric properties of h-BCN materials [26].

Mass production of h-BCN is still a challenging task because matching the theoretical requirement of high thermal stability and low density requires a lot of effort. Precursor pyrolysis, laser ablation hot-filament chemical vapor deposition (CVD), laser vaporization process, aerosol-assisted CVD, and arc discharge using different B, C, and N sources are some of the methods to produce different BCN architectures [27].

3.2 Infrared Stealth

Every object above zero Kelvin radiates energy in the form of electromagnetic waves; these waves are precisely what one needs to look to reveal an object. The important detail to be noted here is that the radiation is distributed non-uniformly across the spectrum, having the maximum intensity within a small band. Detection is effective only when probing for the particular frequency at which radiation has the maximum intensity. For thermal radiation it lies in the band ranging from 1 to 20 μm. This infrared signature is tracked to guide heat-seeking missiles. The countermeasures would require eliminating the thermal signature by either reducing the temperature or by using specialized coatings with low IR emissivity. In a broad sense, stealth requires removing any form of signature going into the surroundings, and on considering the various detection techniques, the most effective and prominent would be radar, sonar, and IR sensing. Microwave stealth is being investigated with the help of RAM and cloaking techniques. This leaves acoustic and thermal signatures as the remaining detection criteria, among which infrared invisibility is more prominent as most of the military detection techniques use IR to locate and identify features of their targets.

The multiple aspects of infrared stealth include absorbing IR waves, reducing IR emissivity, and reducing surface temperature. The infrared band ranges from visible to microwave, but while developing stealth technology one has to narrow it down by taking a few key factors into account. The atmospheric window is the most important factor one has to consider when working on infrared stealth technology. The atmosphere has a composition of materials which ascribe it to its absorption characteristics. Based on this, the infrared sensors should be aiming for the high transmittance regions lying between 3–5 and 8–14 μm. Next, one has to look at are the sources of infrared radiation and find the overlap of bands in the atmospheric window, because any radiation other than this would be absorbed within the atmosphere. The internal sources of IR in an aircraft are mainly the engine, heat exterior surfaces, and the exhaust. Among these sources, the IR signature from the exhaust gases is such that it cannot be mitigated by using any sort of coatings but by using alternative strategies such as mixing cool air with the hot exhaust to reduce the temperature. The ones that has to be considered for coating-related stealth would be the former two. These can also be tackled individually as the different directions of viewing give access to different sources of IR; for example, the rear view will primarily expose the engine parts, and hence its particular IR signature must be considered whereas the signature for other viewing directions would be based on the hot outer surfaces [28].

After this, one can consider the reflection of IR waves that originate from outside the aircraft, which are namely the earthshine, the sky shine, and the sunshine. These sources each have a different distribution with some having peaks in the 3–5 μm range and some intermediately within the 8–14 μm range. These details can be used to make coatings for daytime aircraft specialized in reducing sunshine IR reflectance and the night-time aircraft aiming to reduce the earthshine reflectance. They can also be selectively applied to reduce costs such as the sunshine coating being applied only on the top surfaces of the aircraft and the earthshine coating on the under side [29].

There are some theoretical considerations one can take to narrow down the material choices being investigated for infrared stealth. These can vary from material to material as the mechanism responsible for achieving IR stealth may differ in each case. The following sections list out the materials which have been investigated for their IR stealth properties along with their working mechanisms and performance characteristics.

3.2.1 Carbon Nanotubes (CNTs)

Carbon allotropes have been shown to exhibit some of the most extraordinary properties among materials, and CNTs are no exception to this trend. CNTs exhibit properties such as the strongest and stiffest material, thermal stability up to 750 °C, high thermal conductivity and electrical conductivity tunable from metallic to semiconductor-like. The above-listed properties make this material suitable for a wide range of applications ranging from lightweight fibers for aircraft to tips of atomic force microscopes. There is potential in the material as a stealth coating, given its stability regarding temperature as well as mechanical strength, qualities that are essential in the aerospace domain. The performance of CNTs as a RAM has already been noted [3] and can be explained by considering the proportional dependence of absorption coefficient and electrical conductivity. The problem with RAMs is that they convert the incoming EM waves into heat and on taking into account the natural heating of the aircraft body due to the engine and air friction, the IR signature becomes significant. This is where the excellent thermal conductivity of CNT helps as it can conductively transfer the internal heat to the outside air, thereby reducing the temperature of the material. The thermal conductivity of CNTs is different from normal materials as they exhibit ballistic conduction. It is the process of conduction where the mean free path of carriers is higher than the dimensions of the object, and hence resistance is provided only by colliding with the walls of the object. This leads to CNTs having very high thermal conductivity along the axial direction; this can be ten times as that of copper. The thermal conductivity is thus tunable owing to its ballistic conduction giving different conductivities for different lengths and diameters of the CNT [30]. CNTs also have the option of displaying different properties based on the type of doping and alignment of the nanotubes with respect to the polarization plane. The primary challenge with obtaining the thermal conductivity is to have an axially parallel distribution of nanotubes in the matrix and to avoid aggregation. The surface energy of CNTs being high makes it difficult to disperse them in a matrix, which can

be solved partially by functionalizing them at the cost of decreasing the conductivity. There is an alternative approach to obtain infrared stealth using CNTs and perhaps a more widely used one which is to decrease the emissivity of the surface in the infrared band. This differs from the previous method where decreasing the surface temperature was the contributing factor for stealth. The lower emissivity-based CNT infrared stealth coating uses silver nanoparticles to increase the sheet conductivity and thereby decrease the emissivity.

3.2.2 Photonic Crystals

Photonic crystals (PC) are materials which act as selective filters to light waves, meaning that certain bands of light are not allowed to propagate within the crystal (Fig. 3). They rely on the periodic change in the dielectric material within the crystal causing light to reflect and refract at each boundary. When the reflected light waves of a particular wavelength reinforce each other from multiple layers, they form a standing wave with the incoming wave and lead to destructive interference and prevent further propagation of the wave. The other wavelengths have reflections out of phase and do not reinforce each other, resulting in less attenuation of the wave. This is very similar to the electronic bandgap observed in semiconductors. The alternating dielectrics cause the destructive interference of certain bands of wavelengths and leave the remaining wavelengths largely unhindered with low attenuation. The photonic bandgap can be controlled by various parameters such as the periodicity of the dielectrics, the diameter of holes, the thickness of individual layers, and the doping. The selective nature of photonic crystals allows them to have low emissivity in the atmospheric windows and high emissivity in the non-atmospheric windows. There have been investigations into photonic materials which would give the infrared emissivity needed for stealth applications and the recent developments in that direction have been discussed ahead. The first photonic crystal used for its thermal emission characteristics was the 3D PC made up of tungsten, which had a very detailed structure posing manufacturing challenges. Later a simple 1D PC was investigated which was primarily a metallodielectric material with either silver or tungsten as the metal

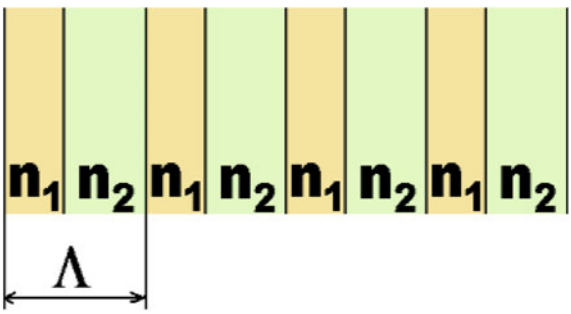

Fig. 3 Schematic of a simple 1D photonic crystal

and it was found to have an emissivity as low as 0.05 for a 10 nm film. These materials were being optimized for their low IR emissivity such that they could be applied in incandescent bulbs with low energy losses. This later expanded the search for similar materials which could be applied in stealth as well because of the similar requirement. One of the PCs investigated has the combination of Ge and ZnS as the two dielectrics. This composition has emissivities as low as 0.05 in the 3–5 μm range and 0.2 in the 8–14 μm range, while showing a good emissivity of 0.6 in the intermediate range. This is exactly the kind of emission characteristics required for stealth coatings as it allows radiative cooling while achieving IR stealth. This PC was prepared by using an optical coating machine where the Ge and ZnS layers were deposited one by one on a quartz substrate. The individual layer thicknesses were optimized to get the best absorption characteristics. In addition to this, there is the option of doping the crystal to obtain holes or valleys for further modification of the emissivity distribution [31].

3.2.3 Cerium(IV) Oxide Co-doped with Calcium and Yttrium

It is possible to relate the electrical conductivity of a material to its emissivity. This predicts that higher conductivity should lead to lower emissivity. This correlation was used to identify materials which can exhibit low infrared emissivities at high temperatures. The general nature of materials is that the conductivity decreases with temperature because there are more collisions. Semiconductors behave differently as they have a different mechanism which allows their conductivity to increase with temperature. One such semiconductor which was investigated for its high-temperature infrared properties is cerium oxide. When doped with lower valency materials oxygen vacancies are created which enhance the electric conductivity significantly. Cerium (IV) oxide was co-doped with calcium (Ca) and yttrium (Y) with varying degrees of concentration. The composites were measured for their electrical conductivities and their infrared emissivities. As objects reach higher temperatures, their emission spectrum peaks at shorter wavelengths and thus the 3–5 μm band is considered for performance measurements of the infrared stealth material. As predicted the particular composition which possessed the highest conductivity also exhibited the least emissivity of 0.241 at 600 °C. The oxygen vacancies which contribute to the high conductivity would benefit more from the Ca doping than the Y doping because of the higher difference in valency, yet co-doping is emphasized to counteract the unintended disadvantages. The perfect balance of the individual components was achieved for $Ce_{0.8}Y_{0.15}Ca_{0.05}O_{2-\delta}$ [32]. The higher yttrium content seems to contradict the valency-based prediction of higher vacancies with higher Ca content. The number of oxygen vacancies is not the only factor affecting the conductivity, considering the transport channel can explain this result. Lattice distortion inhibits the electron transport channels and decreases the conductivity; it is greater with Ca than Y because of the higher difference in size of the ions compared to the cerium ion. The composite is synthesized using a chemical process termed oxalate co-precipitation followed by dry heating the precipitate powder at a high temperature. This material

can especially be used for the hot engine components and the exhaust nozzle area because of the high temperatures they maintain during flight.

3.2.4 Silver (Ag) and Germanium (Ge) Multi-layer Film

The goal for achieving infrared stealth is clear by now; it is to get low emissivities in the atmospheric windows and high emissivities in the non-atmospheric window for radiative cooling. These selective emission properties are attained by a thin multi-layer composite film made up of Ag and Ge. The multi-layer film contains four layers of alternating materials starting with a base Ag layer, next to a Ge layer, followed by an ultrathin Ag layer and a Ge layer on top. The ultrathin Ag layer is responsible for the high emissivity observed, but the layer on its own has a much broader bandwidth for the high emissivity and hence dielectric spacers are added above and below it. They utilize the impedance matching principle, according to this, on matching the wavelength-dependent impedance of a medium to the surrounding medium; in this case, air, by making the imaginary part zero and the real part close to one. The EM waves pass straight into the material and are not reflected [33]. The wavelength dependence of impedance allows for the manipulation of the bands that are allowed. The thicknesses of the dielectric Ge layers are optimized to give maximum transmittance in the 5–8 μm region to facilitate the radiative cooling from the ultrathin Ag layer and also to provide the particular nature by having low values for emissivity in the 3–5 and 8–14 μm bands [33]. The thermal performance measurements show lower temperatures for the coated substrates when compared to the uncoated substrate given equal heating rates. It is made using the thin film deposition process where the material is deposited on a substrate using chemical or physical processes to obtain properties such as corrosion resistance, and thermal resistivity. The process has widespread use in aerospace industry to make coatings that increase durability against atmospheric threats. The physical vapor deposition process used to fabricate the coating is the electron beam evaporation method, which as the name suggests, uses an electron beam to convert the metal atoms into a gas. This forms a thin coating over surfaces in the deposition chamber within its line of sight. There is potential for scalability due to the simplistic nature of the coating and the fabrication process compared to other materials in this field such as CNTs, PCs, and metasurfaces.

3.2.5 Metamaterial Absorber

Metamaterials find their application in infrared stealth as they did with microwaves. There have been multiple investigations of the metal–insulator–metal (MIM) type structures, with the metal layer having various geometries, like square patches, split ring resonators, and so on (Fig. 4). The flexibility of the properties attainable from metamaterials is what places them across the whole range of applications in electromagnetics. Among the combinations studied, one of them used silver as the metal

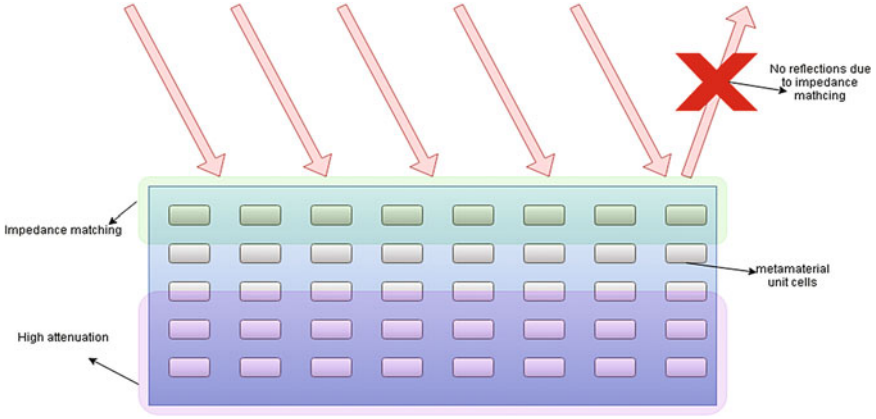

Fig. 4 Schematic of a metamaterial absorber

and polyimide, MgF_2 as the dielectric spacers with a total thickness less than 0.4 μm. This yielded an emissivity distribution having three peaks, all of them in the non-atmospheric windows and very low values in the middle and far atmospheric windows. The metallic pattern used was a simple square patch whose length was modified in each layer to obtain the best result. The intermediate peaks can be explained by magnetic resonances and coupling effects between the metal patches. The layer thickness and the square patch size were optimized using simulations and later experimentally verified. The absorber performs well for temperatures reaching up to 1000 K, making it suitable for the very hot surfaces of aircraft [34].

3.2.6 Aluminum Powder Embedded Resins

It is of utmost importance that both microwave and infrared stealth be achieved in a compatible manner. One of the approaches in this direction is to have the same material exhibit both the properties of high microwave absorptivity and low infrared emissivity. The other approach is to apply the coatings on top of each. The use of resins embedded with aluminum powder is one such example of IR stealth coatings that could be applied on top of RAM surface to achieve dual stealth. In this type of coating, the floating rate is an important factor affecting the emissivity. Given the same content, lower floating rate leads to higher porosity in the substrate which in turn increases absorptivity and emissivity of the material. The opposite is true for the high floating rate variants of the composite which have most of the metal particles aggregated on the surface, leading to low absorbance and thereby lower emissivity. Apart from this, the resin material also plays a role in deciding the emissivity of coating. It does not relate to the emissivity in an obvious manner, a resin with higher absorptivity can lead to lower emissivity when embedded with aluminum powder. This is related to the distribution of the metal powder inside the matrix which shows

a uniform distribution of the particles in the resin with higher absorptivity. The IR emissivity of the polyurethane resin with 90% floating rate and 30% weight content was 0.2, lower than the coatings with lower absorptivity resins. This makes it clear that while selecting materials for the coating the individual components cannot be evaluated in isolation, and the combined performance needs to be considered. These coatings were tested for compatibility with metamaterial-based radar absorbers. The result was that the low IR emissivity is obtained without changing the radar stealth property, that is, the microwave absorptivity [35].

3.2.7 Metal-dielectric Nanostructures

Metal dielectric nanostructure uses a combination of metallic nanowires and nanoparticles to act as scattering and absorbing centers which attenuate the IR waves as they propagate. The nanowires are made with diameter and length randomly varying within a limit which causes most of the incoming waves to scatter and interfere with each other while the nanoparticles act as strong absorption centers that convert EM waves into heat. The dielectric matrix is fully transmitting such that it only serves to hold the composite nanostructures in place. One of the metal–dielectric nanostructures showing good performance for IR stealth consisted of silicon nanowires and silver nanoparticles embedded in a polyimide substrate. The silicon nanowires offer almost zero reflectance because of impedance matching, whereas the silver nanoparticles increase the imaginary part of the refractive index leading to attenuation of EM waves. The effectiveness of the composite varies with the dimensions of the nanowires. The transmissivity decreases with increase in the length of the nanowires but also leads to higher reflections as they are more prone to breaking. The optimum length achieved a transmissivity of 0.02 for the 3–5 and 8–14 μm regions. The absorbed heat is proposed to be dissipated away using cooling air channels which can be incorporated in the sheet [36].

3.3 Visible Spectrum

The visible spectrum of light is what we humans can perceive with our naked eyes. The wavelengths range from 300 to 700 nm. The idea of stealth originated from trying to deceive the visual perception of humans by techniques such as camouflage and flash grenades. The challenge with achieving stealth in the visible spectrum is that our vision works similar to the bistatic radar, as the light that makes an object visible is a diffused source which hits the object from multiple angles and the light scattered is perceived by our eyes. If one attempts at taking a route similar to the ones before, which is to absorb all the light hitting the object, there will be a black spot in the backdrop of the surroundings which will make the location known even though its exact surface details remain hidden. The most promising technique in this aspect is also one of the most ambitious technologies termed the invisibility cloak.

The name might sound familiar as it had been thought of in the fictional realm a long time ago perhaps even inspiring the modern cloak. There have also been proposals of dynamically controlling a screen to match the background and simpler models such as color changing surfaces based on temperature.

3.3.1 Invisibility Cloaking and Metamaterials

Invisibility cloaking in its true form can be considered to be at the epitome of stealth. The concept is to make light bend around the object and pass through to the other side as if there was nothing in the path; similar to how river water diverts around a stone leaving no trail in the downstream. It relies on transformation optics to translate geometrical transformations into material properties based on the form invariance of Maxwell's equations. The geometrical transformation involves mapping the region enclosed by an object onto the annular region outside of it to make all light flow in that same annular region. This transformation is used to derive material properties which would make light follow the mapped space. The two properties which dictate light's interaction with the material are the permittivity and permeability. Generally thought of as scalars, they can be tensors of the second order exhibiting the anisotropy required for cloaking. The properties derived from transformation optics are these permittivity and permeability tensors which on being reproduced in the real world would achieve invisibility. The challenge arises when one tries to look for materials which exhibit the extreme values of anisotropic properties; natural materials do not exhibit these properties. There were two approaches to solve this with the first one being the development of artificial materials called metamaterials whose properties could be tailored at will. The second approach relies on reducing the complexity of the cloak by keeping some variables fixed such that performance is traded off with practical feasibility. The metamaterials approach requires the cell size to be smaller than the wavelength of the EM wave under consideration. This poses a problem in the visible spectrum as the cell size required would be few nanometers long, and such small structures would be tough to manufacture. The cloak also needs 3D structures and corresponding 3D metamaterial cells which require non-conventional fabrication methods such as 3D printing. The current work done with respect to invisibility cloaking using metamaterials is aimed at the microwave frequencies as the cell size required would be in the order of millimeters and is easy to fabricate. The actual materials that the metamaterials are made up of are of two types, one is the conductive material and the other is the dielectric spacer. The materials which would be easy to fabricate while satisfying the conductivities required for behaving as metamaterials need to be investigated such as conductive printing filaments.

4 Conclusion

The advancements in stealth materials have come a long way since the primitive technologies of the past century. The challenge of achieving dual stealth with respect to radars and IR has been addressed with the help of RAMs such as CNT composites with their high thermal conductivity, metamaterials with flexible properties, and IR coatings that can be applied on top of existing RAMs. The limit of narrow bandwidths is overcome by using metamaterials that are tunable to frequencies or by adding thin graphene layers on top of them. Some of the materials like the cerium multi-layer composite have shown high thermal stability, and the carbon composites like the FSFCs can stand up to the structural standards that aircraft require. The advancements in radars such as the bistatic radar can be countered by upcoming technologies like invisibility cloak. The future direction of research for stealth materials needs to take into account the requirement of broadband performance across the entire spectrum. The materials also need to be tested for other application-specific requirements, such as thermal stability, atmospheric durability, and aerodynamic compatibility.

Acknowledgements The author (Ms Bhavya E V) acknowledges the Department of Science and Technology (DST), New Delhi for the INSPIRE Fellowship under which a portion of this work has been carried out.

References

1. Katz D (2017) The 'Magic' behind radar-absorbing materials for stealthy aircraft, part 3, special topic state of stealth, e-book series. Aviation Week & Space Technology
2. Sidiki K (Maj, HAF), Skondras A (2nd Lt, HAF), Tokas C (2nd Lt, HAF) (2014) Low observable principles, stealth aircraft and anti-stealth technologies. J Comput Model 4(1):129–165 (2014). ISSN: 1792-7625 (print), 1792-8850 (online) (Scienpress Ltd)
3. Fang Z, Fang C (2010) Novel radar absorbing materials with broad absorbing band: carbon foams. Appl Mech Mater 26–28:246–249
4. Bhattacharya P, Sahoo S, Das CK (2013) Microwave absorption behavior of MWCNT based nanocomposites in X-band region. eXPRESS Polym Lett 7:212–223
5. Ye W, Sun Q, Zhang GY (2018) Effect of heat treatment conditions on properties of carbon-fiber based electromagnetic-wave-absorbing composites. Ceram Int
6. da Silva VA, Rezende MC (2018) Effect of the morphology and structure on the microwave absorbing properties of multiwalled carbon nanotube filled epoxy resin nanocomposites. Mater Res
7. en.wikipedia.org
8. Panwar R, Puthucheri S, Singh D, Agarwala V (2015) Design of ferrite–graphene-based thin broadband radar wave absorber for stealth application. IEEE Trans Magn 51(11)
9. Chen H, Lu W-B, Liu Z-G, Zhang J, Zhang A-Q, Wu B (2018) Experimental demonstration of microwave absorber using large-area multilayer graphene-based frequency selective surface. IEEE Trans Microw Theory Tech 66(8)
10. Zhou JH, Huo LX, Li WW, You BQ, Li YL, Li HX (2013) A magnetic-controlled detection system for radar absorbing coatings. Adv Mater Res

11. Smitha P, Singh I, Nazism M, Panwar R, Singh D, Agarwala V, das Varma G (2016) Development of thin broadband radar absorbing materials using nanostructured spinel ferrites. J Mater Sci: Mater Electron 27:7731–7737
12. Verma A, Mendiratta RG, Goel TC, Dube DC (2002) Microwave studies on strontium ferrite based absorbers. J Electroceramics 8:203–208
13. Meshrama MR, Agrawala NK, Sinhaa B, Misrab PS (2004) Characterization of M-type barium hexagonal ferrite-based wide band microwave absorber. J Magn Magn Mater 271:207–214
14. Liu C, Yu D, Kirk DW, Xu Y (2017) Electromagnetic wave absorption of silicon carbide-based materials. J R Soc Chem RSC Adv
15. Wu R, Zhou K, Yue CY, Wei J, Pan Y (2015) Recent progress in synthesis, properties and potential applications of SiC nanomaterials. Prog Mater Sci 72:1–60
16. Liang C, Guo Y, Wu L, Zhou J, Kang Z, Shen B, Wang Z (2016) Nature of electromagnetic-transparent SiO_2 shell in hybrid nanostructure enhancing electromagnetic attenuation. J Phys Chem C 120:12967–12973
17. nano.materials.drexel.edu
18. Han M, Yin X, Wu H, Hou Z, Song C, Li X, Zhang L, Cheng L (2016) Ti_3C_2 MXenes with modified surface for high-performance electromagnetic absorption and shielding in the X-band. ACS Appl Mater Interfaces 8:21011–21019
19. Wakatsuchi H, Greedy S, Christopoulos C, Paul J (2010) Customized broadband metamaterial absorbers for arbitrary polarization. Opt Express 18(21):22187–22198
20. Grant J, Ma Y, Saha S, Khalid A, Cumming DRS (2011) Polarization insensitive, broadband terahertz metamaterial absorber. Opt Lett 36(17):3476–3478
21. Liu Y, Gun S, Luo C, Zhao X (2012) Ultra-thin broadband metamaterial absorber. Appl Phys A 108(1):19–24
22. Yuan W, Cheng Y (2014) Low-frequency and broadband metamaterial absorber based on lumped elements: design, characterization and experiment. Appl Phys A 117(4):1915–1921
23. Saville P (2005) Review of radar absorbing materials, Defence R&D Canada, Technical Memorandum DRDC Atlantic TM 2005-003, Jan 2005
24. Truong V-V, Turner BD, Muscat RF, Sarina Russo M (1997) Conducting-polymer-based radar-absorbing materials. In: Proceedings of the SPIE 3241, smart materials, structures, and integrated systems, 14 Nov 1997
25. Huber T, Saville P, Edwards D (2003) Investigations into the polyaniline and polypyrrole families of conducting polymers for application as radar absorbing materials, Defence R&D Canada, Technical Memorandum DRDC Atlantic TM 2003-005, Jan 2003
26. Zhang Y-Y, Pei Q-X, Liu H-Y, Wei N (2017) Thermal conductivity of a h-BCN monolayer. R Soc Chem Phys Chem Chem Phys 19:27326–27331. https://doi.org/10.1039/c7cp04982j
27. Zhang T, Zhang J, Wen G, Zhong B, Xia L, Huang X, Zhao H, Wang H, Qin L () "Ultra-light h-BCN architectures derived from new organic monomer with tunable electromagnetic wave absorption. Carbon 13127
28. Mahulikar SP, Rao GA, Kale PS (2006) Infrared signatures of low-flying aircraft and their rear fuselage skin's emissivity optimization. J Aircr 43(1)
29. Mahulikar SP, Sonawane HR, Arvind Rao G (2007) Infrared signature studies of aerospace vehicles. Prog Aerosp Sci 43(7–8):218–245
30. Kolanowska A, Janas D, Herman AP, Jędrysiak RG, Giżewski T, Boncel S (2018) From blackness to invisibility—carbon nanotubes role in the attenuation of and shielding from radio waves for stealth technology. Carbon N Y 126:31–52
31. Zhang W, Xu G, Zhang J, Wang H, Hou H (2014) Infrared spectrally selective low emissivity from Ge/ZnS one-dimensional heterostructure photonic crystal. Opt Mater (Amst) 37(C):343–346
32. Zhao X (2018) The effects of Ca^{2+} and Y^{3+} ions co-doping on reducing infrared emissivity of ceria at high temperature. Infrared Phys Technol 92:454–458
33. Peng L, Liu D, Cheng H, Zhou S, Zu M (2018) A multilayer film based selective thermal emitter for infrared stealth technology. Adv Opt Mater 1801006:1–8

34. Li Chen X, Hui Tian C, Xin Che Z, Ping Chen T (2018) Selective metamaterial perfect absorber for infrared and 1.54 μm laser compatible stealth technology. Optik (Stuttg) 172:840–846
35. Shi M (2018) Achieving good infrared-radar compatible stealth property on metamaterial-based absorber by controlling the floating rate of Al type infrared coating. J Alloys Compd 764:314–322
36. Moghimi MJ, Lin G, Jiang H (2018) Broadband and ultrathin infrared stealth sheets. Adv Eng Mater 20(11):1–6

Chapter 4
Radar Absorber Design using Two-Dimensional Materials

Delme Winson, P. S. Shibu and Balamati Choudhury

1 Introduction

Stealth is one of the emerging technologies in military aviation platform that makes an aircraft, partially invisible to the radar. This is achieved by reducing the number of waves reaching back to the radar via deflection of an incident wave into some other directions or by absorbing the incoming wave. The goal of stealth technology is to minimize the radar cross section (RCS) of an airplane. Radar absorbers are one of the promising technology toward radar cross section reduction at microwave frequencies. Hence, radar absorber plays a key role in military aviation platform. Modern military application always demands wideband operation but increased thickness is undesirable due to the constraint on the aircraft payload. The conventional wideband radar absorbers include variants of Salisbury screen and Jaumann absorber. However, the bulky thickness of these structures makes them less useful for stealth domain and always there exist a trade-off between thickness and absorption.

The research on radar absorbers is continuing from decades using the concept of metamaterial, the artificial materials which show exotic properties in electromagnetic applications. There must be a proper selection of materials that are used in the aerospace domain regarding the physical, chemical, and thermal properties. Since electromagnetic devices always demand lightweight, low thickness materials for various applications, nanomaterials became one of the focused research areas. Nanometamaterials is widely acceptable in stealth domain, due to its unusual properties. The stealth performance of a radar absorber is tested through radar cross section reduction (RCSR).

Radar signature reduction is the most significant aspect that affects the survivability of aircraft to remain out of sight from the enemy radar vicinity. Low observability minimizes the chance of detection of target. For design of new military platforms,

D. Winson · P. S. Shibu (✉) · B. Choudhury
CSIR-National Aerospace Laboratories (CSIR-NAL), Centre for Electromagnetics (CEM), Bangalore 560017, India

R. Kumari and B. Choudhury (eds.), *Multiscale Modelling of Advanced Materials*, Materials Horizons: From Nature to Nanomaterials,
https://doi.org/10.1007/978-981-15-2267-3_4

radar signature reduction has gained high priority. Radar signature depends on the wavelength of incidence wave, polarization of transmitter section, polarization at receiver portion, relative position of the transmitter/receiver with respect to target, shape, size, orientation, radar absorbing material (RAM), and patterns layered on the target. Ability of a target to scatter back the signals toward radar observer is called radar cross section. It is a ratio of reradiated power propagated toward radar to power density that is captured at the target [1].

$$\sigma = \lim_{R \to \infty} 4\pi R^2 \frac{|E^s|^2}{|E^i|^2}$$

2 Challenges in Conventional Radar Absorber Designs

There are several factors that need to be considered while designing an absorber. The design and development of conventional radar absorber involve certain challenges that are mentioned below.

- ***Electrically large and flexible structures***
  While designing a radar absorber, it must be easily mountable in the aircraft's body. So design consideration of absorbing structure must be electrically large and at the same time, flexible. The reflections from the curved surfaces are more when compared with planar structures. So the design of conformal structures to use in the curved surfaces of a fighter is a big challenge in the stealth platform.
- ***Bandwidth of operation***
  Most of the conventional radar absorbers have narrowband of operation. Modern military application always demands wideband operation. So wide bandwidth requirement is one of the main constraints of design in radar absorbers.
- ***Multiple layers for maximum absorption***
  For wideband operation, conventional structures like Jaumann absorber require multiple layers. The radar absorber will yield maximum absorption through multiple layers.
- ***Thickness***
  As the thickness of the absorber increases, the corresponding absorption may enhance. But at the same time, thickness for the design should not increase beyond the limit. It should not affect the aerodynamic properties of the fighter aircrafts. Due to the constraint on the payload of aircraft, increased thickness is not desirable. These two design parameters conflict with each other and there exists a strong trade-off between thickness and absorption.

- ***Material issues***
  There must be a proper selection of materials that are used in the aerospace domain regarding its physical, chemical, and thermal properties. These factors need to be considered while choosing the appropriate material for the design.

3 RAM Designs based on Nanomaterials

Nanomaterials are becoming the building blocks of radar absorber designs due to their exotic electromagnetic properties. The ultrathin material composition makes them potential candidates in several EM applications.

3.1 Metamaterial-based Radar Absorbers

The metamaterial-based radar absorbers have several advantages over conventional type absorbers. The repeating patterns, ultrathin structures, and improved absorption performance of these absorbers can be used as an alternative for different frequency ranges from microwave to terahertz. These absorbers can be used in numerous practical applications like RCSR, antenna, electromagnetic interference (EMI), and electromagnetic shielding.

Hakla et al. (2016) designed an ultrathin metamaterial absorber for curved surfaces. The structure consists of an array of two concentric rings printed on a dielectric substrate and reflection dips are given at 7.22 and 14 GHz, which are under C band and Ku band, respectively [2]. The designed structure has been tested for TE- and TM-polarized waves. The fine fabrication of the model makes them usable for curved surface application.

Jang et al. (2013) proposed a conformed metamaterial absorber. Three different unit cells have been designed with different angles of incidence (0°, 30°, and 45°) and three of them have different absorption peaks above 90%. The absorption performance of the model has been verified using software simulation and measurement [3]. The structure with 15 cm radius results in an RCS reduction of 11.4 dB.

There exist several metamaterial patterns which are conventionally used in a number of EM applications. Here both Fig. 1a, b are multiple ring-based structures that resonate at different frequencies. Figure 1c is a periodic structure and Fig. 1d is a nonresonant metamaterial structure.

Zhong et al. (2016) designed a perfect metamaterial absorber with multi-material configuration. The structure composed of multi-junction with different materials operating at different frequencies [4]. The absorber design was developed using plasmonic resonant structures and the strong field intensity inside the metallic material resulted in an enhanced absorption. This design was done by using multi-target electron gun evaporator and it has involved parametric sweeping with wave impedance

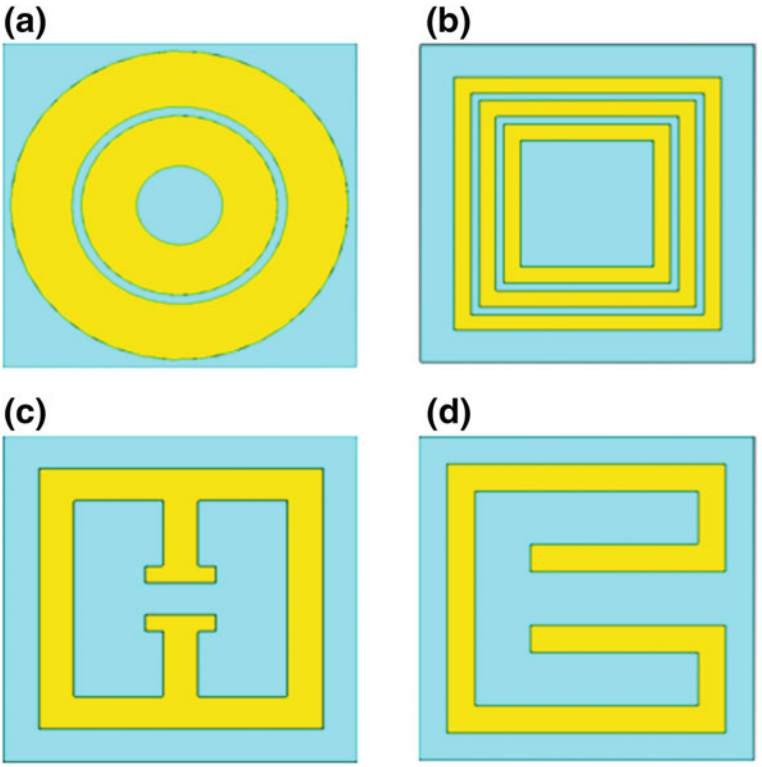

Fig. 1 Schematics of commonly used metamaterial designs **a** multiband circular ring based metamaterial **b** triple-band absorber structure resonator **c** electric ring resonator **d** square ring resonator

matching, for the suitable selection of materials. The proposed design has a dimension of 221 nm for the wavelength of 400–700 nm.

Costa et al. (2014) have performed a study on electromagnetic absorbers based on frequency-selective surfaces. Frequency-selective surfaces are arrays of periodic structures designed for radar absorbing materials [5]. The fabrication of the surfaces has been carried out either by metallic or controlled resistance deposition. By proper selection of the geometrical and electrical properties of the frequency-selective surfaces (FSS) as well as the substrate, several electrically thin absorbing designs can be obtained. Narrowband, wideband, and ultra wideband configurations can also be done for nonconducting FSS.

Zhang et al. (2015) proposed a metamaterial absorber developed on graphene at mid-infrared frequencies. The absorber design consists of a dual-frequency band containing a super cell of cross-shaped metal resonators [6]. This structure exhibits dual-band resonance tuning through the tailoring of conductivity. The proposed model gives an absorption peak of more than 90%. The simulated result of the design demonstrates an efficient dual-band absorber in a wide angle of incidence.

Yuan and Cheng (2014) designed a frequency-selective flexible metamaterial absorber (FFMA) for wideband applications [7]. A single dielectric layer has been used to separate the special metallic layer and metallic pattern. The material Teflon has been adopted as the dielectric layer and the entire structure has octagon geometry. Under the TE polarization, the proposed structure could provide the polarization-insensitivity and wide-angle performance. The simulated results have been shown that the absorber gives the absorption bandwidth between 9.2 and 18 GHz with absorption characteristics of about 65.15%. Since it exhibits a broadband of operation, this design can be opted for several aerospace applications.

Lim et al. (2016) proposed an absorber, based on split-ring resonators for X-band applications. The unit cell consists of a repeating pattern on the top side and completely grounded at the bottom side [8]. In order to measure and analyze the absorption peaks, two horn antennas were used. One has been used for transmitting EM waves with rotated angles, and the other one has been used for receiving the EM waves. The measured absorption of the structure was 99.9% at 11.3 GHz and the simulated absorption was 99.99% at 11.35 GHz.

Xiong et al. (2014) designed a broadband metamaterial absorber. The design consists of an array of resonating structures and thus formed a multilayer absorber. The two metallic layers were separated by a dielectric spacer [9]. The unit cell of the absorber is placed in a waveguide, in such a way that the vertically polarized wave directly impinges on the absorber. The waveguide ports were placed on both the terminations of the waveguide. A genetic algorithm was developed in order to optimize the unit cell parameters for maximum absorption. The peak absorption is more than 90% at 13.5 and 19 GHz.

3.2 Conducting Polymer-based Radar Absorbers

The selection of suitable materials for low observable applications is always a challenging task. Even though conductive materials like steel and copper are easily available for EM applications, their conductivity cannot be controlled [10]. The class of materials known as conducting polymers are widely used in radar absorbing structures. Its conductivity can be controlled; it can be used as shielding or reflective medium to the incident EM waves.

Conducting polymers (CP) are polymeric materials with electronic conductivity. Due to the difficulty of growing, the porous molecular structure can be used either in dry or wet states. Several nonlinear defects are found in conducting polymers, due to the doping in the polymerization. The conjugated molecular bonds induce conductivity in the structure and alternative single and double bonds that exist between the carbon atoms. Every molecular structure in conducting polymer consists of localized sigma and localized pi bonds. In the doping procedure, extra electrons are introduced with dopant ion and impart conductivity to the polymer structure. The unstable state of each polymer molecules are neutralized by the addition of dopant ions [11]. On

the application of electric potential; the free electrons are generated due to the disturbance in a stable backbone. The energy gap is overcome by the dopant ions, hence the conjugated pi electrons are involved in bonding and antibonding, and exhibit conductivity to the polymers. This induces the flow of electrons through the polymer. These conducting polymers are widely acceptable in several engineering applications.

3.2.1 Design and Simulation of Conducting Polymer-based Radar Absorber

A conductive polymer-based radar absorber has been designed and it consists of three layers. An arrow-shaped pattern made of conducting polymer with conductivity 1600 s/m and 0.005 mm thickness has been placed on a dielectric substrate (FR4) of 1.6 mm. The absorber is backed by a perfect electric conductor (PEC). A multilayer absorber of 12-unit cell with size 49.2 mm × 32.4 mm has been designed and it resulted in high absorption. A unit cell of 16.4 mm × 8 mm has been designed and simulated.

Unit cell boundary conditions and normal incidence were given for the simulation. The ports were given in the Z-direction. Figure 2 shows the schematic of a simulation model for conducting polymer-based radar absorber. The absorption characteristics in the frequency range 8–12 GHz were more than 99%.

The simulation has been done for the X band. The absorption characteristic have been plotted for the entire X band. The average absorption measured was more than 99%.

The absorption characteristic shows an enhanced absorption in the X band. Therefore, the designed CP-based absorber can find applications in the field of radar absorbers. Since the absorber is made up of less-weighed conducting polymer, it can reduce the payload of the entire structure. When we design a radar absorber, it should be electrically large and at the same time it is flexible to design.

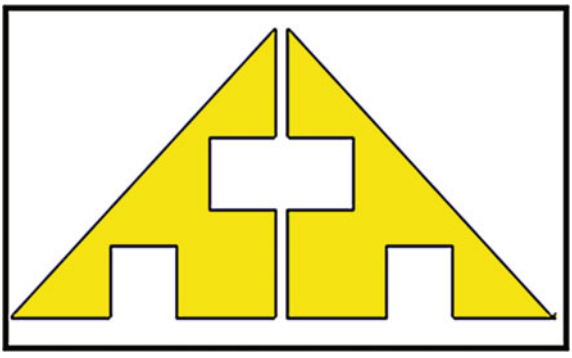

Fig. 2 Schematic unit cell of conducting polymer-based absorber

3.2.2 RCS Analysis of Conducting Polymer-based Radar Absorber

The radar cross section is estimated for a perfect electric conducting plate, and a conducting polymer-based radar absorber layer embedded over a PEC are estimated using commercial software and results are compared. RCS at normal incidence values is used for the comparisons. The perfect electric conductor (PEC) of size 86 mm × 42 mm with thickness 0.017 mm is opted for the backing material. The simulation was performed over a range of 8–12 GHz. The plate is positioned in x-y plane and normal incidence has been considered which is depicted in Fig. 3. The simulated absorption characteristics is plotted in Fig. 4.

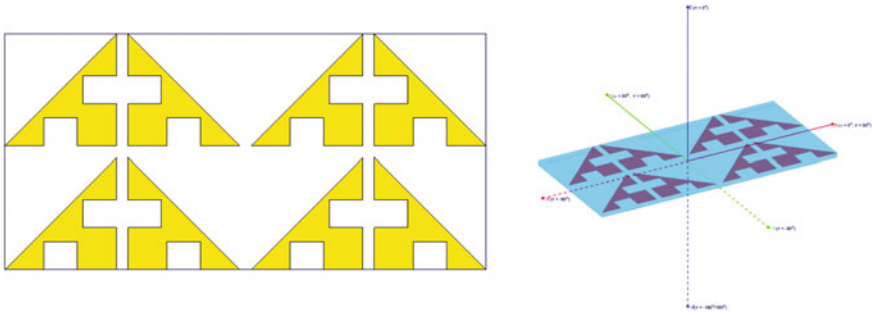

Fig. 3 Schematic of conducting polymer-based radar absorber

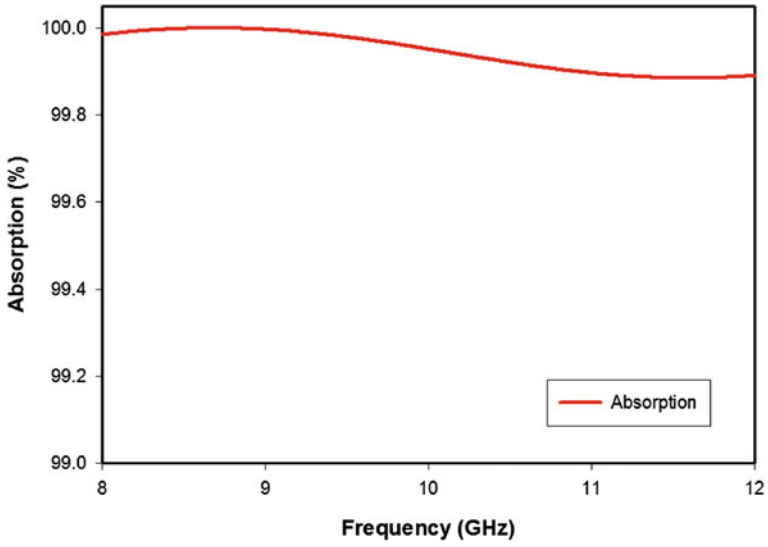

Fig. 4 Absorption characteristics of conducting polymer-based absorber

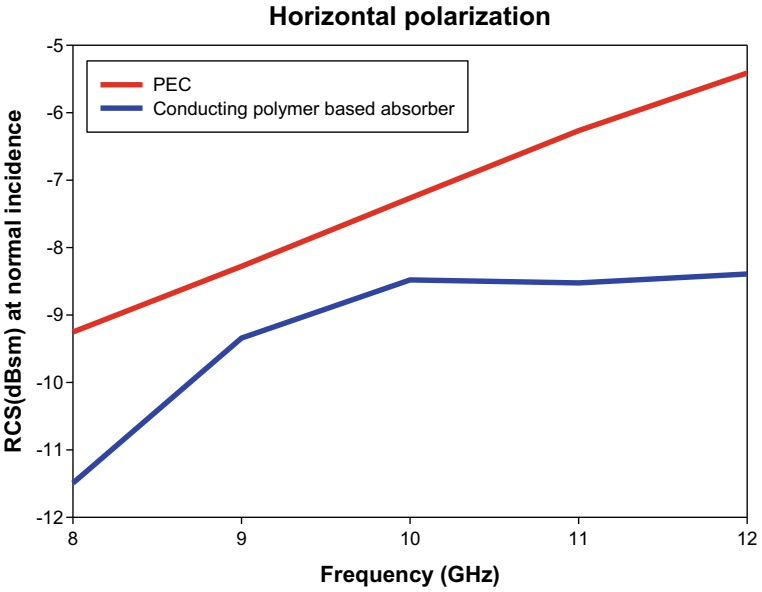

Fig. 5 RCS versus frequency variation at horizontal polarization

The RCS at normal incidence has been estimated for both horizontal and vertical polarization. Radar cross section of PEC and conducting polymer-based absorber over the frequency band at horizontal polarization is shown in Fig. 5. At normal incidence, maximum RCS reduction of 2.98 dBsm has been observed at 12 GHz while minimum RCS reduction of 1.06 dBsm has been observed at 9 GHz. A mean RCS of 1.95 dBsm reduction has been observed over the entire frequency range from 8 to 12 GHz. Figure 6 shows the RCS of PEC and conducting polymer-based absorber for vertical polarization. At normal incidence, maximum RCS reduction of 2.48 dBsm has been observed at 12 GHz while minimum RCS reduction of 0.56 dBsm has been observed at 8 GHz. A mean RCS of 1.92 dBsm reduction has been observed over the entire frequency range from 8 to 12 GHz.

The RCS reduction has been analyzed for conducting polymer-based absorbers. Even though conducting polymer-based designs are thin structures suitable for stealth, the RCSR over a wideband is essential in order to meet EM applications. Two-dimensional nanomaterials with tunable electric potential play a significant role in RCSR.

3.3 Graphene-based Radar Absorbers

Graphene is one of the newly introduced materials, which found applications in various technologies such as THz/optical modulators, transistors, super capacitors, and

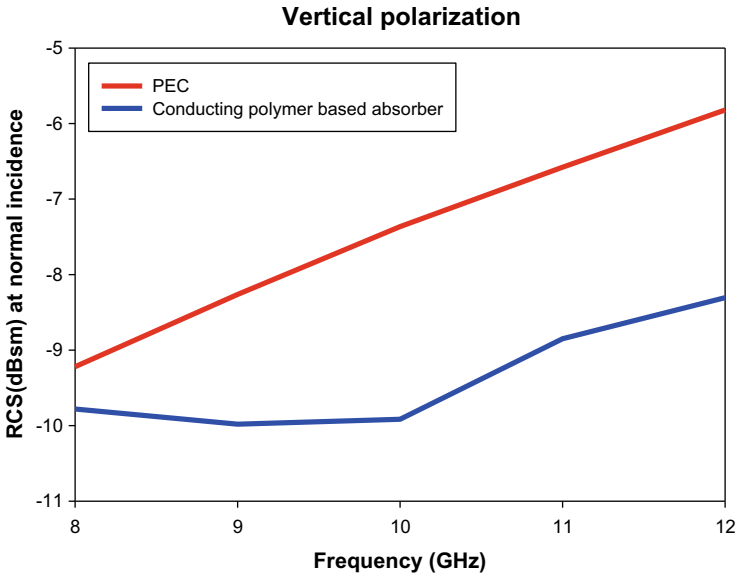

Fig. 6 RCS versus frequency variation at vertical polarization

electronic mixers. Graphene is nothing but a two-dimensional material that comprises carbon atoms, which are arranged hexagonally [12]. The unique optical, electrical, mechanical, and thermal properties make them a cutting-edge technology in the research area. The thickness of graphene is in the order of single carbon atom, but it is stronger than steel and the conductivity reaches up to any other conducting metals. The most interesting feature is its tunable sheet conductivity; the sheet conductivity can be tuned for broad frequency range through shifting the electronic Fermi level either by electronic doping or by chemical doping.

Graphene-based EM absorbers are investigated from lower terahertz to optical frequency spectrum. In the terahertz spectrum, ribbon graphene and periodic-patterned graphene metamaterial structures show improved absorption characteristics as compared to continuous graphene layer structures [13]. Conventional metamaterial structures exhibit narrowband absorption. As in microwave frequency bands, the key application of absorbers achieves stealth through RCS reduction.

Gao et al. (2012) proposed a graphene-based absorbing screen of nonperiodic structure with frequency range from 45 to 160.5 GHz. The electronic properties and impedance tuning of graphene have wide applications, especially in RCS reduction [14]. A planar array with 6×6 element size has been given as the absorbing surface. Simulation and measurement have been carried out for the proposed model and an RCS of 30 dB has been obtained at low frequency.

Deng et al. (2016) have adopted the properties of graphene with THz electromagnetic waves. The designed MM structure composed of patterned metal electric split-ring resonator (eSRR) and graphene reflector spaced by SiO_2/Si layers [15].

The increase in the Fermi level could enhance the conductive properties of graphene. The variation from 0.1 to 1 eV modulates the transmission values in the range of 0.43–0.036.

Kuzmin et al. (2016) proposed a model of graphene-magnetic semiconductor-based structure placed in an external magnetic field. The structure has a periodic stacking of graphene monolayer and magnetic semiconductor layers [16]. Near the cyclotron resonance frequency, the energy of electromagnetic waves actively converses to energy of the electrons rotating around the magnetic field lines. Thus, electromagnetic radiation at these frequencies will also be strongly absorbed by the medium. The resonant frequencies are determined by the value of external magnetic field. At these frequencies, conductivity of graphene sharply increases that leads to an increase in absorption and reflectance (the structure becomes more "metallic") and a decrease in transmittance.

Andryieuski et al. (2013) proposed a graphene-based absorber with effective surface conductivity approach, based on transmission line analogy. The structure consists of a graphene layer placed between two dielectrics. The middle-layer graphene has the property of changing the surface conductivity by reducing the material content through plasmonic resonance [17]. It was observed that the absorption could be enhanced, by using more conductive layers. By this transmission analogy method, the conducting graphene layer has been treated as the load between two transmission lines. The design has been given the maximum absorption at Fermi level energy 5 eV and minimum at 0 eV.

3.3.1 Design and Simulation

A radar absorber has been designed using graphene. The absorber is of size 20 mm × 20 mm, backed with PEC. Graphene layer is sandwiched between the metal pattern and PEC. The metal patches are of the size 2 mm × 2 mm each. The substrate used was FR4 with a thickness of 1.2 mm. The schematic of graphene-based absorber is given in Fig. 7.

The metamaterial pattern with the combination of the graphene layer gives an improved absorption characteristic for the absorber. The proper impedance matching can be done with the surface conductivity tuning of graphene. The ultrasmall thickness of the designed absorber can be used in stealth platform which solves the payload constraints in the aerospace domain. The resulted absorption is more than 85% in the X band.

3.3.2 RCS Analysis of Graphene-based Radar Absorber

PEC of size 20 mm × 20 mm with thickness 0.017 mm is opted for the backing material. The simulation was performed over a range of 8–12 GHz. The plate is positioned in the x-y plane as shown in Fig. 7 and normal plane wave incidence has been adopted (Fig. 8).

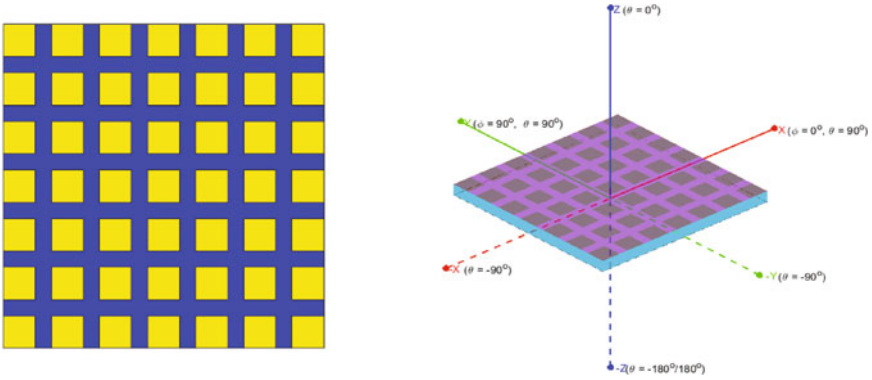

Fig. 7 Schematic of graphene-based radar absorber

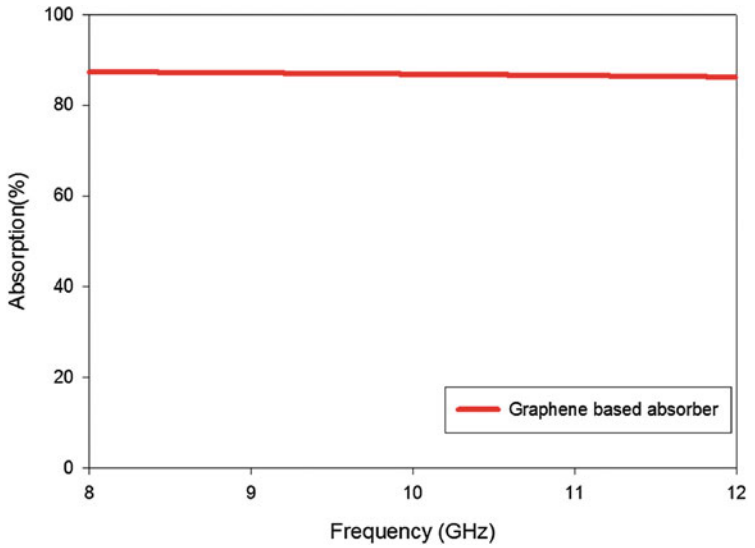

Fig. 8 Absorption characteristics of graphene-based radar absorber

The RCS at normal incidence is estimated for both horizontal and vertical polarization. RCS of PEC and graphene-based absorber over a range of frequency at horizontal polarization is shown in Fig. 9. At normal incidence, maximum RCS reduction of 17.11 dBsm has been observed at 8 GHz while minimum RCS reduction of 11.63 dBsm has been observed at 12 GHz. A mean RCS of 14.30 dBsm reduction has been observed over the entire frequency range of 8–12 GHz. Figure 10 shows the RCS of PEC and graphene-based absorber for vertical polarization. At normal incidence, maximum RCS reduction of 17.11 dBsm has been observed at 8 GHz while minimum RCS reduction of 11.63 dBsm has been observed at 12 GHz.

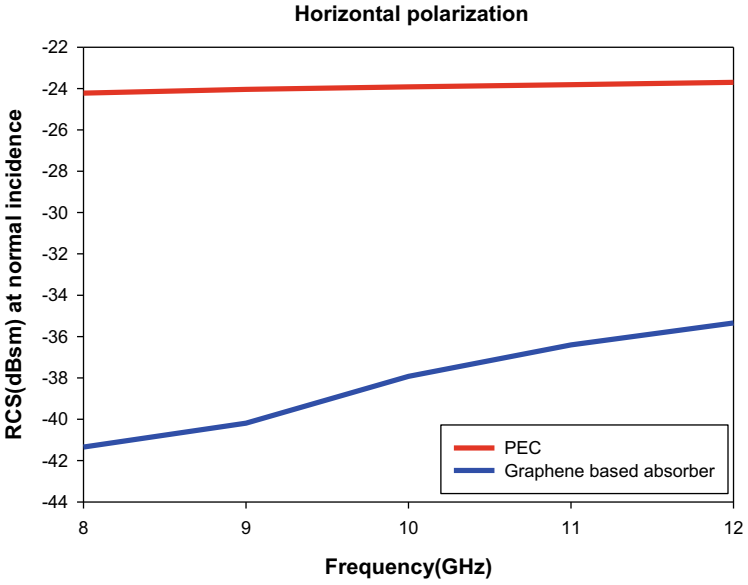

Fig. 9 RCS versus frequency variation at horizontal polarization

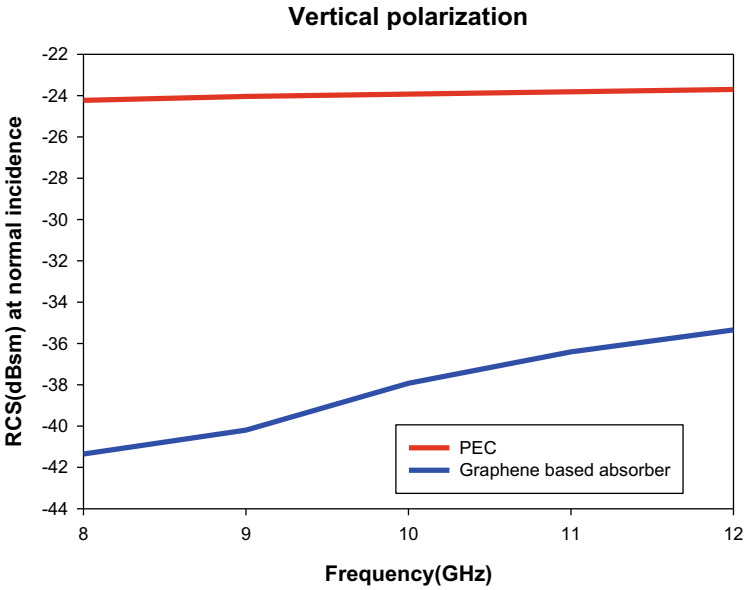

Fig. 10 RCS versus frequency variation at vertical polarization

A mean RCS of 14.30 dBsm reduction has been observed over the entire frequency range of 8–12 GHz.

4 Conclusion

This chapter includes design and RCS estimation of different radar absorbing structures based on nanomaterials. Detailed literature in the field of nano-metamaterials has been carried out. Wideband characteristics and thickness are the primary parameters needs to be addressed while designing radar absorbers. Radar absorber structures using nanomaterials have high potential feasibility in the stealth domain due to their negligible thickness and wideband of operation. The excellent electromagnetic properties of nanomaterials like graphene and conducting polymers give improved performance in EM applications.

A conducting polymer-based radar absorber has been designed and the RCS is estimated. Analysis of RCSR has been carried out for novel design with a reference of PEC. The absorber showed a significant reduction in RCS when it is compared with PEC. Similarly, a graphene-based radar absorber has been designed in the X band. The design has given absorption of more than 85%. Unlike the conventional radar absorber designs, the nanomaterial-based designs showed better performances in broadband frequencies.

References

1. Knott EF (2004) Radar cross section, 2nd edn. SciTech Publishing Inc., Raleigh
2. Hakla N, Ghosh S, Srivastava KV, Shukla A (2016) A dual-band conformal metamaterial absorber for curved surface. In: URSI international symposium on electromagnetic theory, August 2016
3. Jang Y, Yoo M, Lim S (2013) Conformal metamaterial absorber for curved surface. OSA Publ 21(20):24163
4. Zhong YK, Fu SM, Tu MH, Chen BR, Lin A (2016) A multimetal broadband metamaterial perfect absorber with compact dimension. IEEE Photonics J 8(2):1
5. Costa F, Kazemzadeh A, Genovesi S, Monorchio A (2014) Electromagnetic absorbers based on frequency selective surfaces. Forum Electromagn Res Methods Appl Technol
6. Zhang YP, Li TT, Zhang HY, Taylor AJ, Chen HT, Azad AK (2015) Independently tunable polarization-insensitive dual-band metamaterial perfect absorber based on graphene at mid-infrared frequencies. Sci Rep
7. Yuan W, Cheng Y (2014) Low-frequency and broadband metamaterial absorber based on lumped Elements: design, characterization and experiment. Appl Phys A 117(4):1915–1921
8. Lim D, Lee D, Lim S (2016) Angle- and polarization-insensitive metamaterial absorber using via array. Sci Rep
9. Xiong H, Hong JS, Luo CM, Zhong LL (2013) An ultrathin and broadband metamaterial absorber using multi-layer structures. J Appl Phys 114:064109
10. Naishadham K (1993) Shielding effectiveness of conducting polymers. IEEE Trans Electromagn Compat 34(1):47–50

11. Trivedi DC (2002) A new approach for polyaniline synthesis. In: International conference on science and technology of synthetic metals, August 2002
12. Bozzi M, Pierantoni L, Bellucci S (2015) Applications of graphene at microwave frequencies. Radio Eng 24(3)
13. Novoselov KS, Geim AK, Morozov SV, Jiang D, Zhang Y, Dubonos SV, Grigorieva IV, Firsov AA (2004) Electric field effect in atomically thin carbon films. Science 6:666–669
14. Gao C, Jiang Y, Zhang J, Cao W, Gao X, Yu Z, Wang J (2016) Graphene-based wideband absorbing screen with radar cross section reduction. In: 11th international symposium on antennas, propagation and EM theory
15. Deng G, Xia T, Yang J, Yin Z (2017) A graphene-based broadband terahertz metamaterial modulator. J Electromagn Waves Appl 31:2016–2024
16. Kuzmin DA, Bychkovand IV, Shavrov VG (2015) Influence of graphene coating on speckle-pattern rotation of light in gyrotropic optical fiber. Opt Lett 40(6):890–893
17. Andryieuski A, Pizzocchero F, Booth T, Boggild P, Lavrinenko AV (2013) Effective surface conductivity approach for graphene metamaterial based terahertz devices. In: International quantum electronics conference, May 2013

Chapter 5
3D Metamaterial Multilayer Structures

G. Husna Khouser and Yogesh Kumar Choukiker

1 Introduction

The word "Meta" is taken from Greek whose meaning is "beyond". "Metamaterials" have the exotic properties beyond the naturally occurring materials. According to Wikipedia, metamaterial is defined as "a material which gains its properties from its structure rather than directly from its composition" [1]. The first important contributions to the topic of "Metamaterial" was proposed in 1968 by V. G. Veselago. He said that materials with both negative permittivity and negative permeability are theoretically possible [2]. Later the term metamaterial was synthesized by Rodger M. Walser in 1999, which was originally defined as "Macroscopic composites having a synthetic, 3D, periodic cellular architecture designed to produce an optimized combination, not available in nature, of two or more responses to specific excitation" [3]. Metamaterials are also known to be doubly negative materials or left-handed materials (LHM). Again in 1999, John Pendry identified a practical way to make left-handed metamaterials (LHM) which did not follow the conventional right-hand rule [4]. He proposed the design of periodically arranged thin-wire (TW) structure that depicts the negative value of effective permittivity. It was shown that the structure is having a low plasma frequency than the wave in the microwave regime [5].

Figure 1 shows the classification of materials based on electric permittivity "ε" and magnetic permeability "μ". The *permittivity* is a measure of how much a medium changes to absorb electrical energy when subjected to an electric field [6]. *Permeability* is a constant of proportionality that exists between magnetic induction and magnetic field intensity. Both are related to the refractive index "n" given by

$$n = \pm\sqrt{\varepsilon_r \mu_r} \tag{1}$$

G. Husna Khouser · Y. K. Choukiker (✉)
Department of Communication Engineering, School of Electronics Engineering, VIT University, Vellore, India

R. Kumari and B. Choudhury (eds.), *Multiscale Modelling of Advanced Materials*,
Materials Horizons: From Nature to Nanomaterials,
https://doi.org/10.1007/978-981-15-2267-3_5

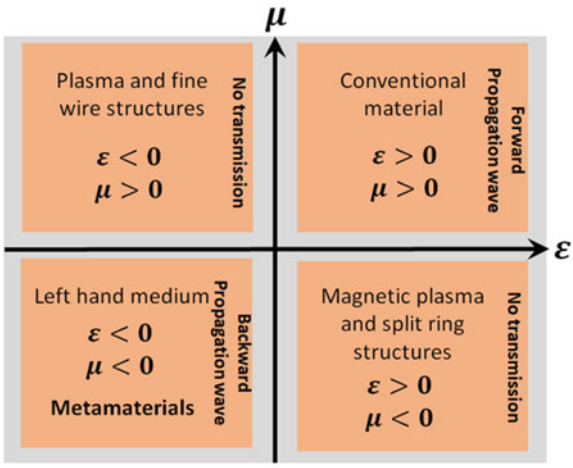

Fig. 1 Material classification according to the sign of electric permittivity "ε" and magnetic permeability "μ"

where ε_r and μ_r are the effective relative permittivity and permeability related to the free space permittivity and permeability by $\varepsilon_0 = \varepsilon/\varepsilon_r = 8.854 \times 10^{-12}$ and $\mu_0 = \mu/\mu_r = 4\pi \times 10^{-7}$, respectively. The metamaterials are categorized into two types: resonant and nonresonant, which is explained with Fig. 1. Metamaterial in first and third quadrant the electromagnetic waves are able to propagate inside the medium and called as nonresonant metamaterial. In the first quadrant the $\varepsilon > 0$ and $\mu > 0$ have a positive velocity, which is a linear function of frequency and is called "*double-positive* (DPS)" media. The third quadrant $\varepsilon < 0$ and $\mu < 0$ has a negative phase velocity; it is known as "*double-negative* (DNG)" and is referred to as left-hand metamaterial (LHM) [7]. Due to the negative phase velocity, the energy is propagated backward in the materials. In the second and fourth quadrant, the electromagnetic wave propagation in no transmission mode and is called resonant metamaterial. The second quadrant $\varepsilon < 0$ and $\mu > 0$, also known as electric plasma, and the propagate wave strongly reflects from the medium. When the metamaterial appears in the fourth quadrant $\varepsilon > 0$ and $\mu < 0$, it is known as magnetic plasma and the propagate wave strongly reflects from the medium. Hence, the material has any one of the parameters (permittivity or permeability) negative; it is known as "*single-negative* (SNG)" and is referred to as "*epsilon-negative* (ENG)" or "*mu-negative* (MNG)" or right-hand metamaterial [8]. From the above explanation, we can conclude that in natural materials such as cold plasma and silver exhibit negative permittivity at microwave and optical frequencies. Similarly, ferromagnetic materials exhibit a negative permeability behavior in the VHF and UHF regimes. However, the negative permittivity and permeability have not been found in nature and hence they must be created artificially (Fig. 2).

Basically, the metamaterial structures (see Fig. 3) are metallic patterns etched/printed on the substrate of dielectric materials which are control the permittivity and permeability. The basic structure of the split-ring resonator (SRR) was

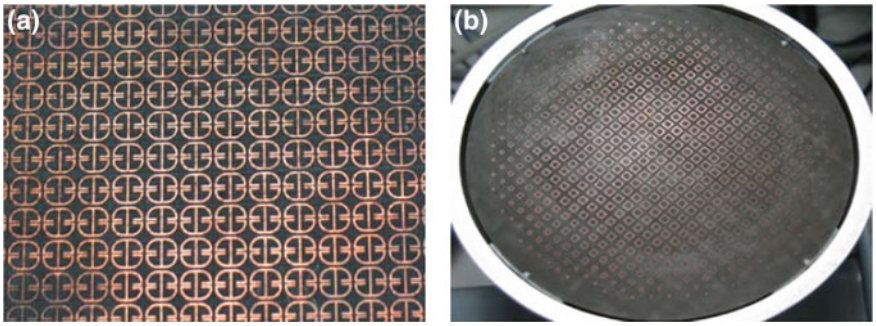

Fig. 2 Planar metamaterial structure [6] **a** periodic structure in homogenous medium **b** aperiodic structure in inhomogeneous medium

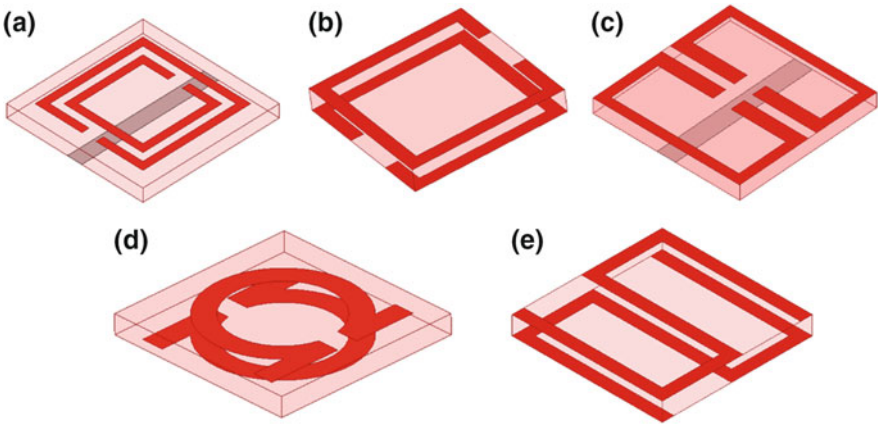

Fig. 3 Overview of 2D Split-ring resonator: **a** edge-coupled SRR [21] **b** broadside SRR [22] **c** axially symmetric SRR [24] **d** omega SRR [15] **e** S-shaped SRR [23]

introduced by Pendry; he extended this study with resonators interacting with electromagnetic waves [9], and metallic wire [10]. Later, Smith and his group realize the LHM, then LHM with wire is to achieve the negative index refraction phenomenon [11]. LHM has attracted attention in both theoretical and experimental studies [12, 13]. Some metamaterial resonators shape such as capacitive loaded loop as tunable metamaterial [14] and omega shaped [15] are lossy and narrow-band. To overcome these issues, the alternate approach is used which is based on transmission line (TL) theory. In the literature, the LHM-based TL approaches are introduced independently [16]. The TL approach describes the metamaterial properties in backward electromagnetic waves [17] and high-pass filter implementation [18] for 1D structure. Similarly, for 2D metamaterial structure properties are investigated [19, 20]. Also, some other 2D metamaterial structures are investigated such as edge and broadside coupled resonator [21, 22], S-shaped SRR [23], and axially symmetric SRR [24].

The concept of 2D/wire metamaterial structures is extended to 3D metamaterial structures. These structures are implemented with the insertion of the metallic vias into the dielectric materials, resulting in changes in the electromagnetic properties [25]. Also, they can reduce the undesired scattering or dispersion of electromagnetic waves and are useful for adding the desired electromagnetic functionality to the overall system. In the literature, the excitation of 3D metamaterials is explored [26–29], 3D-ELC metamaterial [30], 3D metamaterial with LTCC technique [31]. Also, for MIMO environment the mutual coupling reduced investigated by 3D metamaterial structure [32]. Recently, the large explosion of attention is given to 3D metamaterial structures for various applications, and many research journals have been published.

2 3-Dimensional (3D) Metamaterial

The term "3D metamaterial" may be represented as "stereoscopic metamaterials" or "bulk metamaterials". However, there are different terms of the word "3D"; first is the architecture of the metamaterial structure and second is the dimension of the metamaterial shape. In addition to that, the term comes from the degrees of freedom for the functionality of the metamaterial structure [26]. To predict the behavior of the metamaterial, different techniques were used for characterizing the parameters (effective permittivity and permeability) [33]. The NRW method is used to characterize these parameters because it does not involve any such determination of cosine branch index or any other complexity. This method uses the S-parameters for the extraction of effective permittivity and permeability as given below [34].

$$S_{11} = \frac{\Gamma(1 - z^2)}{1 - \Gamma^2 z^2} \tag{2}$$

$$S_{21} = \frac{z(1 - \Gamma^2)}{1 - \Gamma^2 z^2} \tag{3}$$

where Γ is the interface reflection coefficient of the homogeneous medium, $z^2 = e^{-j2\theta}$ and $\theta = k\,d$ are the propagation factor.

The values of z and Γ remain unknown in any medium. Sum and difference properties of S-parameters are implemented as follows:

$$V_1 = S_{21} + S_{11} \tag{4}$$

$$V_2 = S_{21} - S_{11} \tag{5}$$

The product of V_1 and V_2 is

$$V_1 V_2 = (S_{21} + S_{11})(S_{21} - S_{11})$$

$$= \frac{z^2 - \Gamma^2}{1 - \Gamma^2 z^2} \tag{6}$$

The difference between V_1 and V_2 is

$$V_1 - V_2 = (S_{21} + S_{11}) - (S_{21} - S_{11})$$

$$= \frac{2\Gamma(1 - z^2)}{1 - \Gamma^2 z^2} \tag{7}$$

By using Eqs. (6) and (7), X and Y as given below

$$X = \frac{1 + V_1 V_2}{V_1 + V_2} = \frac{1 + z^2}{2z} \tag{8}$$

$$Y = \frac{1 - V_1 V_2}{V_1 - V_2} = \frac{1 + \Gamma^2}{2\Gamma} \tag{9}$$

z is obtained from X and Γ is obtained from Y, using the quadratic equation; it is given below as Eqs. (10) and (11)

$$z = X \pm \sqrt{X^2 - 1} \tag{10}$$

$$\Gamma = Y \pm \sqrt{Y^2 - 1} \tag{11}$$

The choice of the sign is selected to maintain the expected magnitudes of these terms, i.e., $|z| \leq 1$ and $|\Gamma| \leq 1$.

$$z = \frac{V_1 - \Gamma}{1 - \Gamma V_1} \tag{12}$$

$$\Gamma = \frac{z - V_2}{1 - z V_2} \tag{13}$$

From Eqs. (12) and (13), we can obtain the exact equation for propagation constant (z) and wave impedance (η) as follows:

$$1 - z = \frac{(1 - V_1)(1 + \Gamma)}{1 - \Gamma V_1} \tag{14}$$

$$\eta = \frac{1 + \Gamma}{1 - \Gamma} = \frac{(1 + z)(1 - V_2)}{(1 - z)(1 + V_2)} \tag{15}$$

Next, assuming the thinness "d" of any unknown finite material, i.e., $k_{real}\, d \leq 1$ and complex wave number $k = \omega\sqrt{\mu_r \varepsilon_r}/c \; = k_0\sqrt{\mu_r \varepsilon_r}$.

To simplify the equation for propagation factor (z), the Taylor expansion can be used and given as follows [35]:

$$z = 1 - jkd \tag{16}$$

Using Eqs. (13) and (15), permeability (μ_r) can be obtained as

$$\mu_r = \frac{2}{jk_o d}\left[\frac{1 - V_2}{1 + V_2}\right] \tag{17}$$

The permittivity (ε_r) and refractive index (n) can then be obtained simply as

$$\varepsilon_r = \frac{2}{jk_o d}\left[\frac{1 - V_1}{1 + V_1}\right] \tag{18}$$

$$n^2 = \sqrt{\mu_r \varepsilon_r} \tag{19}$$

The extraction of the above formulas was applied to validate the structure as a 3D metamaterial. Also, the resulting effective permittivities and permeabilities are to be interpreted in terms of how the 3D metamaterial acts in reflection and transmission under normal incident plane wave illumination.

2.1 Basic Model of 3D Circular Split-Ring Resonator (3D-CSRR)

The 3D Circular Split-Ring Resonator (CSRR) structure is formed with two split metallic open rings, positioned with conducting metal vias. Figure 4a–c shows the schematic 3D view, closed boundary excitation, and equivalent circuit model of the 3D-CSRR, respectively. The 3D structure contains split inner and outer ring of width (d), gap (g), radius (r_1) and (r_2), substrate height (h), and conducting metallic vias height (h_1) as shown in Fig. 4a. The split inner ring (r_1) and outer ring (r_2) are placed on top of the conducting metal vias and bottom of the substrate, respectively. The air gap (h) is used between the top of the substrate and inner ring for the proposed structure. Figure 4b shows the 3D-CSRR closed boundary excitation, when an external field is applied along the E-plane or H-plane. The 3D-CSRR structure can lead to both electric and magnetic resonances. When the axis of the ring is parallel to the H-field, the H-field generates a current in the 3D-CSRR, which gives rise to a strong magnetic dipole and hence a magnetic resonance. If the gap of the 3D-CSRR is parallel to the E-field, the E-field generates a voltage variation at the gap, leading to a strong electric dipole, and this gives rise to an electric resonance. Figure 4c shows the equivalent circuit model of the 3D-CSRR

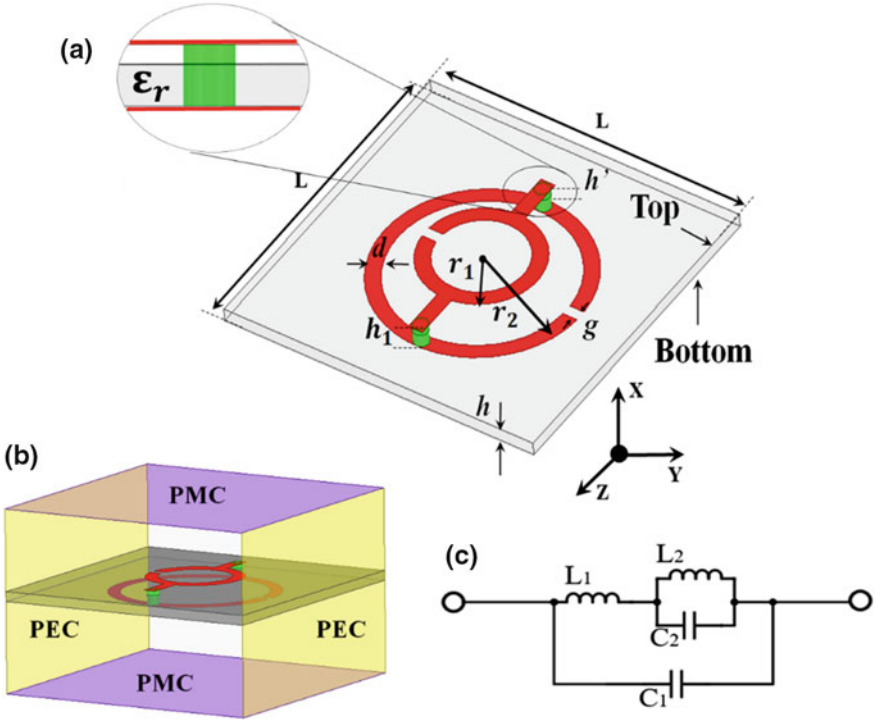

Fig. 4 3D metamaterial structure of circular split-ring resonator **a** 3D geometry **b** schematic view of closed boundary simulation setup **c** equivalent circuit model

geometry. It behaves like an LC resonator that can be excited by an external magnetic flux, and the resonant frequency can be obtained [36]

$$f = \frac{1}{2\pi\sqrt{L_1 C_1}} \tag{20}$$

where

C_1 is equivalent capacitance and
L_1 is equivalent inductance of both the rings

The total capacitance C_1 of 3D-CSRR is given by

$$C_1 = (\pi\, r_a - g)\, C_p \tag{21}$$

where r_a is the average radius of the rings, g is the split-ring gap, C_p is the per-unit-length capacitance between the rings which is given as below

$$r_a = \frac{r_2 - r_1}{2} \tag{22}$$

Here, r_1 is the split inner ring and r_2 is the outer ring radius

$$C_p = \frac{\sqrt{\varepsilon_{eff}}}{cZ_0} \tag{23}$$

where $\mathfrak{E}_{eff}$ is effective permittivity of the medium, $c = 3\times10^8$ m/s is the velocity of light in free space, and Z_0 is the characteristics impedance.

The effective inductance L_1 of 3D-CSRR is given by

$$L_1 = \mu_0 r_2\left[\ln\frac{8r_2}{d} - 1.75\right] \tag{24}$$

where μ_0 is the free space permeability, r_2 is the outer ring radius, and d is the width of the ring.

To make the CSRR structure a 3D structure, a metallic via is used. The metallic via also acts as an LC tank circuit. As seen from the equivalent circuit model, parallel connection of inductance L_2 and capacitance C_2 is serially connected to the equivalent inductance L_1. The inductance L_2 and capacitance C_2 can be written as [37]

$$L_2 \approx \frac{\mu_o\mu_r}{\pi}\cosh^{-1}\left(\frac{g_v}{2r_v}\right)h \tag{25}$$

$$C_2 = \frac{\varepsilon_o\varepsilon_r A}{g_v} \tag{26}$$

where μ_0 is the free space permeability, μ_r is the substrate permeability, g_v is the distance between the center of metallic vias, r_v is the radius of metallic via, h is the height of the substrate, and $A = 2r_v h$ is the area of cross section of the metallic via.

Figure 5a, b shows the simulated S-parameters of the equivalent circuit model and EM simulation for the 3D-CSRR structure. The dips of S_{11} (reflection) and S_{21} (transmission) indicate the points of resonant frequencies. Either S_{11} or S_{21} could be used to define the resonant frequency. From Fig. 5a, it is observed that S_{11} is the resonant frequency for the 3D-CSRR equivalent circuit model. Here, the reflection is minimum, therefore, maximum power is transmitted to the other end. The transmission acts as a passband and the dip is shifted toward the higher resonance due to the inductive effect which exists in the 3D-CSRR.

Based on the equivalent circuit model, the 3D-CSRR structure is designed for the resonant frequency of 3.63 GHz using the EM simulator. It is printed on the RT–Duroid 5880 substrate ($\varepsilon_r = 2.2$) of dimensions L × L and height ($h = 0.8$ mm). All the dimensions of 3D-CSRR are listed in Table 1. Figure 5b shows the simulated S-parameters of the 3D-CSRR structure. Here, S_{21} parameter is used to define the resonant frequency. S_{11} acts as a stopband and the dip is shifted toward the lower resonance due to the capacitive effect which exists in the 3D-CSRR structure.

To validate the structure, effective permittivity and permeability of a particular 3D metamaterial structure can be extracted and analyzed. Thus, we can achieve the

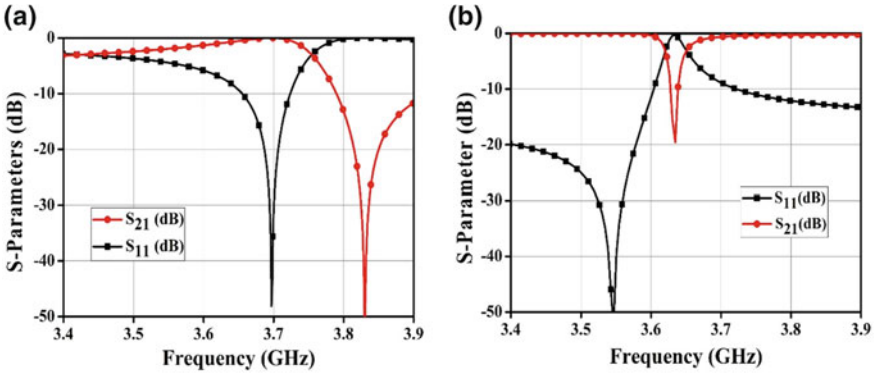

Fig. 5 Simulated S-parameters of 3D-CSRR metamaterial structure **a** circuit simulation, [L_1 = 0.03609 μH, C_1 = 338.2 pF, L_2 = 0.02879 μH, and C_2 = 115.7 pF] **b** EM simulation results (HFSS)

Table 1 Dimensions of 3D split-ring resonator (all the dimensions are in mm)

L	r_1	r_2	h'	d	g
33	4	7	0.4	1	0.75

typical response of a practical 3D-CSRR structure via such full-wave simulation analysis, as shown in Fig. 6a, b. Effective permittivity (ε_r) of the 3D-CSRR structure is shown in Fig. 6a. It exhibits the large peak positive value at the resonant frequency (3.63 GHz) and no dispersion of energy in other ranges. Effective permeability (μ_r) of the 3D-CSRR structure is shown in Fig. 6b. It is observed that the permeability is low and negative at the resonant frequency around 3.63 GHz. The permittivity and permeability are highly dispersive around the resonance frequencies. Based on

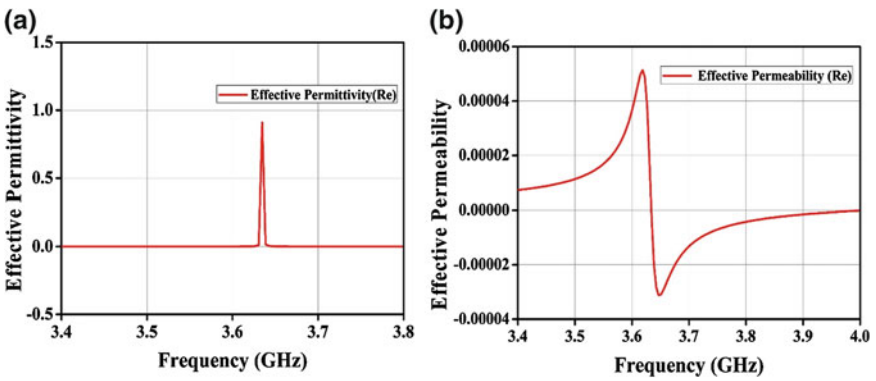

Fig. 6 Extracted effective parameters (real) of 3D-CSRR metamaterial structure **a** permittivity (ε_r) **b** permeability (μ_r)

the permittivity and permeability, the next parameter to validate the 3D metamaterial is the refractive index (n) as shown in Fig. 7. It is observed that the values of refractive index are negative (<0) and fall under the μ-*negative* category. Hence, the complex index of reflection is purely imaginary. In conclusion, from the calculated metamaterial parameters we can validate our proposed 3D-CSRR structure as a metamaterial.

The surface charge distribution and current direction on the surface of the 3D-CSRR metamaterial at 3.63 GHz is shown in Fig. 8. The direction of current is represented with arrow marks for clear understanding. The flow of current in the 3D-CSRR metamaterial has two paths. First, the current flows from outer ring to inner ring through metallic vias (black arrows). Second, the path is opposite to the first path (i.e., inner ring to outer ring through the metallic vias). It is noted that the current flows anticlockwise (black arrows) in outer ring, vertical up/down direction in metallic vias, and clockwise (black arrows) direction in inner ring. Here, we assume the E-field is applied to the boundary of the designed 3D-CSRR structure. The current is induced in outer ring and parallel current is distributed in 3D-CSRR

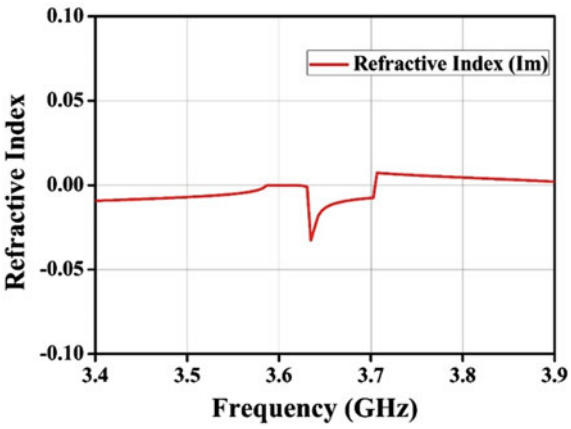

Fig. 7 Refractive Index (imaginary) of 3D-CSRR metamaterial structure

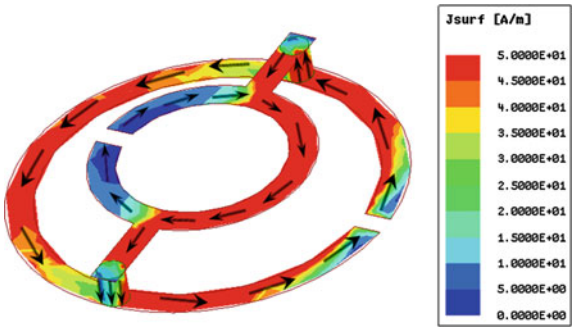

Fig. 8 Surface current density of 3D-CSRR metamaterial structure with current direction

structure, resulting in electric response, whereas the circulating current in the metallic vias leads to the magnetic response.

2.2 3D-Square Split-Ring Resonator (3D-SRR) Metamaterial Structure

The 3D-Square Split-Ring Resonator (3D-SSRR) structure is formed with two split metallic square loops and metallic vias. It is printed on an FR-4 substrate ($\varepsilon_r = 4.4$) of square dimension L × L and height (h). The coupling element for the 3D-SSRR structure, transmission line, is used and placed on top of the substrate. The 3D-SSRR metamaterial structure contains split inner square loop of length l_1, outer square loop (l'), square loops width (d), gap (g), and metallic vias height (h_1) which are shown in Fig. 9. The split inner square loop (l_1) is placed on top of the conducting metal vias and outer square loop (l') is on the bottom of the substrate. The air gap (h') is used between the top of the substrate and inner square loop. The air gap and metallic vias play a pivotal role in making the structure a 3D-SSRR metamaterial. The proposed structure is designed at a resonant frequency of 1.34 GHz using an EM simulator. All the dimensions of 3D-SSRR are listed in Table 2.

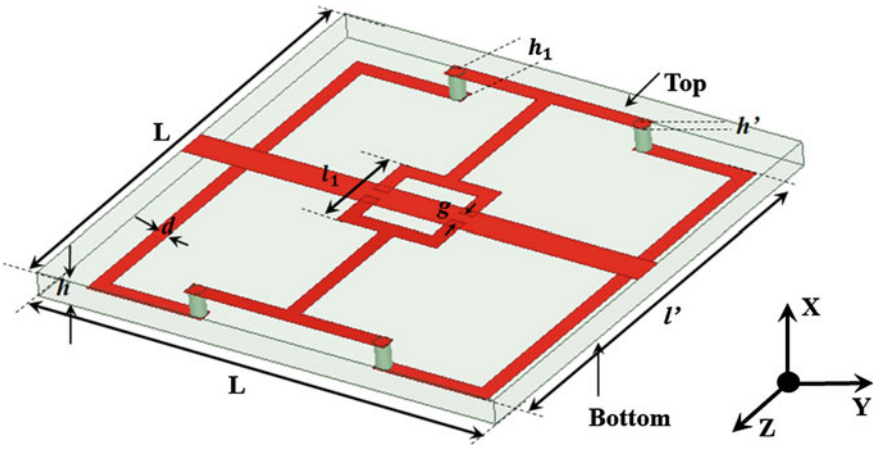

Fig. 9 Schematic view of 3D-Square split-ring resonator (3D-SSRR) metamaterial structure

Table 2 Dimensions of 3D-square split-ring resonator (all dimension are in mm)

L	l'	l_1	h'	H	D	G
32	28	7	0.5	1.6	2	0.8

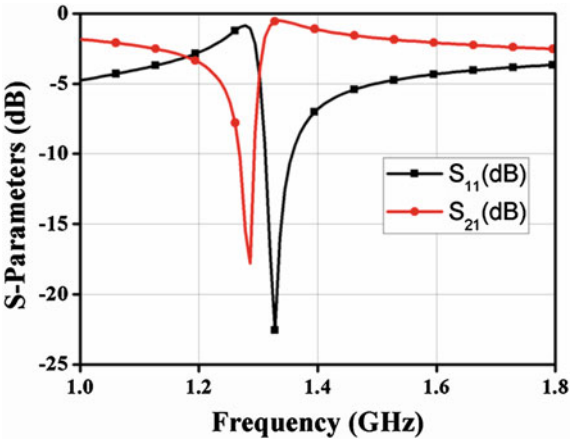

Fig. 10 Simulated S-parameters of 3D-SSRR metamaterial structure

Figure 10 shows the simulated S-parameters (S_{11} and S_{21}) of 3D-SSRR metamaterial structure using EM simulation. It is observed that the structure shows the pass-band characteristics. The transmission coefficient (S_{21}) has a peak notched and shows good rejection level at resonant frequency (1.34 GHz). The reflection coefficient (S_{11}) attained almost zero at the resonant frequency.

To examine the 3D-SSRR structure as a metamaterial, the effective parameters (permittivity and permeability) are calculated from the simulated S-parameters as shown in Fig. 11a, b. Effective permittivity (ε_r) of the 3D-SSRR structure is shown in Fig. 11a. It exhibits positive value with spatial dispersion of low energy at the resonant frequency (1.34 GHz). The effective permittivity (μ_r) of the 3D-SSRR structure is shown in Fig. 11b. It exhibits high negative peak value at the resonant frequency. Therefore, a strong magnetic response is produced for negative permeability. The effective parameters $\varepsilon > 0$ and $\mu < 0$ result in 3D-SSRR as MNG metamaterial. The refractive index for 3D-SSRR is negative as shown in Fig. 12. It defines whether the

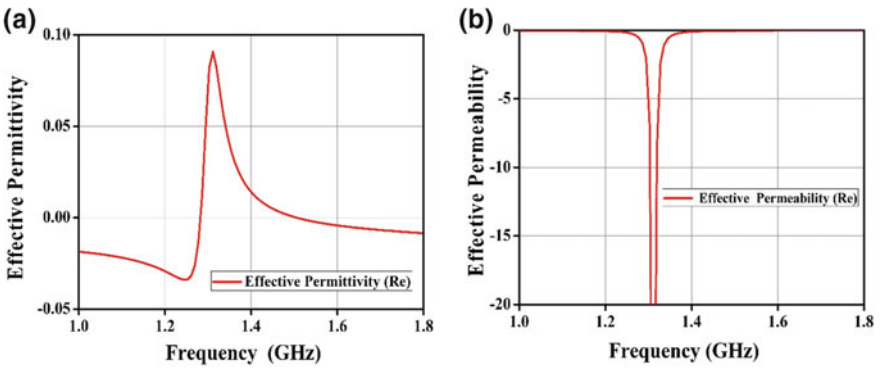

Fig. 11 Effective parameters (real) 3D-SSRR metamaterial structure **a** permittivity (ε_r) **b** permeability (μ_r)

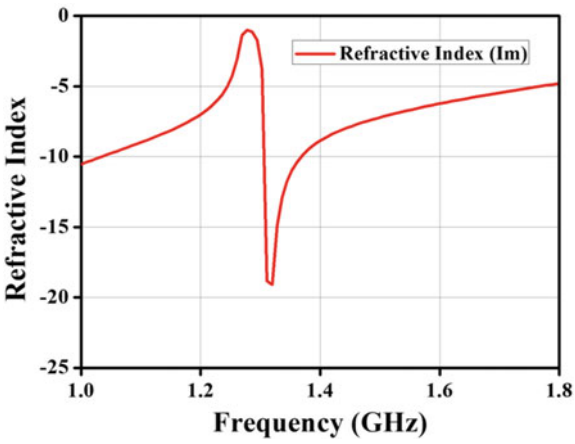

Fig. 12 Refractive index (imaginary) of 3D-SSRR metamaterial structure

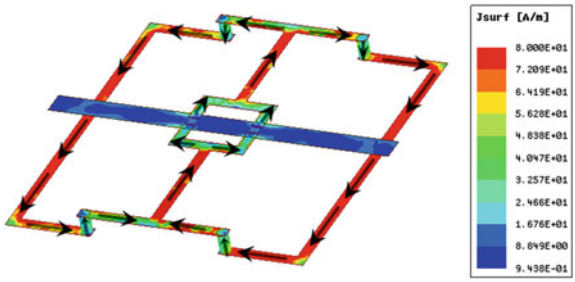

Fig. 13 Surface current density of 3D-SSRR metamaterial structure with current direction

impedance of the 3D-SSRR structure is matched. Hence, the coupling is strong with electromagnetic waves.

Figure 13 shows the surface charge distribution and current direction of a 3D-SSRR metamaterial structure at 1.34 GHz. The E-field is applied to the boundary of the designed 3D-SSRR. Initially, the current in the transmission line and coupled with the inner square loop. The flow of current (arrow marks) from split inner square loop to outer square loop through metallic vias are in clockwise and anticlockwise direction.

2.3 3D Dual Circular Split-Ring Resonator (3D-DCSRR) Metamaterial Structure

The 3D Dual Circular Split-Ring Resonator (3D-DCSRR) structure is formed with outer ring, two dual inner rings, and metallic vias. It is printed on an RT–Duroid substrate ($\varepsilon_r = 2.2$) of dimension L × L and height (h). The 3D structure contains inner and dual outer rings of radius (r_1) and (r_2), width (d), gap (g), substrate height

(h) and metallic vias height (h_1), and air gap (h') as shown in Fig. 14. The transmission line and outer rings of radius (r_1) are placed on the top and bottom of the substrate, respectively. The two dual inner rings of the same radius (r_2) are placed on top of the metallic vias (h_1). The air gap (h') acts as a coupling gap between dual inner ring and transmission line for the 3D-DCSRR structure. The proposed structure is designed at a resonant frequency of 2.75 GHz using an EM simulator. All the dimensions of 3D-DCSRR are listed in Table 3.

Figure 15 shows the simulated S-parameters of the 3D-DCSRR structure using EM simulation. At resonant frequency (2.75 GHz), impedance is matched and passband is observed, where reflection attains zero. Figure 16a, b shows the effective electric permittivity and effective magnetic permeability of the 3D-DCSRR extracted from the simulated S-parameters. The effective permittivity (ε_r) and permeability (μ_r) are observed as positive and negative values, respectively, at the resonant frequency. The 3D-DCSRR structure has ($\varepsilon_r > 0$, $\mu_r < 0$) the corresponding refractive index (n) is negative, hence MNG metamaterial shown in Fig. 17.

The surface current distribution is shown in Fig. 18. We assume an electric field is applied parallel to the axis of the dual inner ring (r_2), current is induced, and magnetic field is produced. There is strong coupling between the transmission line and dual inner rings through the air gap. The current is split and flows from dual inner ring (r_2) to outer ring (r_1) through metallic vias in both anticlockwise and clockwise direction.

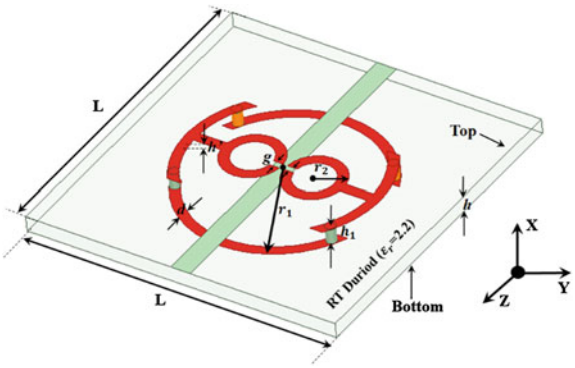

Fig. 14 Schematic view of 3D-DCSRR metamaterial structure

Table 3 Dimensions of 3D dual circular split-ring resonator (3D-DCSRR) (all dimensions are in mm)

L	r_1	r_2	D	h'	h	g
32	10	3	1	0.1	1.524	1

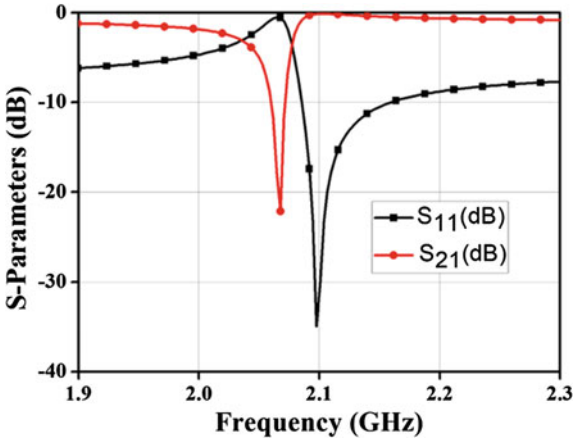

Fig. 15 Simulated S-parameters of 3D-DCSRR metamaterial structure

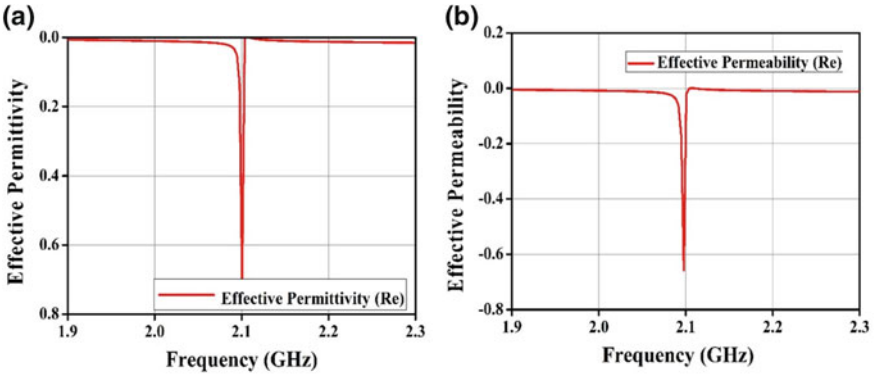

Fig. 16 Extracted effective parameters (real) of 3D-DCSRR metamaterial structure **a** permittivity (ε_r) **b** permeability (μ_r)

3 Conclusion

In this chapter, an extended study was conducted on 3D metamaterial multilayer structures with circuit and EM simulation for validating the geometry as metamaterial structure. The S-parameters were analyzed for these 3D structures to calculate the effective material parameters such as permittivity (ε_r), permeability (μ_r), and refractive index (n). The conducted analysis for 3D metamaterial structures exhibits negative material characteristics that are suitable for various high-frequency wireless applications. The 3D metamaterial structure can be used to control electromagnetic interference and provide isolation and compartmentalization of high-frequency elements internally and external interference sources. In addition, the 3D metamaterial

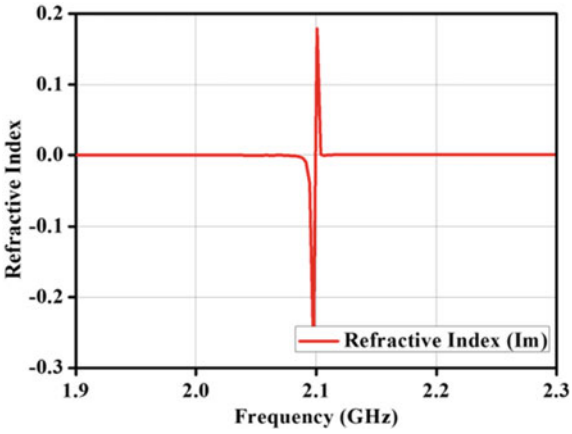

Fig. 17 Refractive index (imaginary) of 3D-DCSRR metamaterial structure

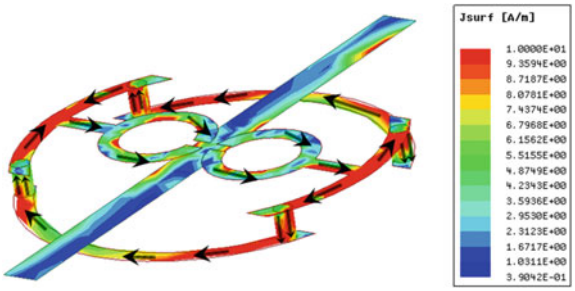

Fig. 18 Surface current density of 3D-DCSRR metamaterial structure with current direction

structures are used as metamaterial antennas, passive substrate elements for MMICs such as filters and phase shifter, and radar signature of antenna arrays.

References

1. http://en.wikipedia.org/wiki/Metamaterial,2019
2. Vesalogo VG (1968) The electrodynamics of substances with simultaneously negative values of permittivity and magnetic permeability. Soviet Phys 10:509–514
3. Walser RM (2001) Electromagnetic metamaterial. In: Proceedings of SPIE 4467, pp 1–15
4. Pendry JB, Holden AJ, Robbins DJ, Stewart WJ (1998) Low frequency plasmons for thin-wire structure. J Phys Condens Matter 10:4785–4809
5. Pendry JB, Holden AJ, Robbins DJ, Stewart WJ (1999) Magnetism from conductors and enhanced nonlinear phenomena. IEEE Trans Microw Theor Techniques 47(11):2075–2084
6. Cui TJ, Smith DR, Liu R (2010) Metamaterial theory design and application. Springer New York Dordrecht Heidelberg London. https://doi.org/10.1007/978-1-4419-0573-4
7. Ziolkowski RW, Heyman E (2001) Wave propagation in media having negative permittivity and permeability. Phys Rev E 64

8. Alù A, Engheta N (2003) Pairing an epsilon-negative slab with a mu-negative slab: resonance, tunneling and transparency. IEEE Trans Antennas Propag Special issue on metamaterials 51, 10:2558–2571
9. Pendry JB, Holden AJ, Stewart WJ, Youngs I (1996) Extremely low frequency plasmas in metallic microstructures. Phys Rev Lett 76:4773–4776
10. Pendry JB, Holden AJ, Robbins DJ, Stewart WJ (1999) Magnetism from conductors and enhanced nonlinear phenomena. IEEE Trans Microw Theor Techniq 47(11):2075–2084
11. Smith DR, Padilla WJ, Vier DC, Nemat-Nasser SC, Schultz S (2000) Composite medium with simultaneously negative permeability and permittivity. Phys Rev Lett 84, 18:4184–4187
12. Shelby RA, Smith DR, Schultz S (2001) Experimental verification of negative index of refraction. Science 292:5514
13. Cui TJ, Kong JA (2004) Time-domain electromagnetic energy in a frequency-dispersive left handed medium. Phys Rev B 70:205106
14. Aydina K, Ozbay E (2007) Capacitor-loaded split ring resonators as tunable metamaterial components. J Appl Phys 101:024911
15. Simovski CR, He S (2003) Frequency range and explicit expressions for negative permittivity and permeability for an isotropic medium formed for lattice of perfectly conducting Ω-particle. Phys Lett A 311:254 (2003)
16. Caloz C, Itoh T (2002) Application of the transmission line theory of left-handed (LH) materials to the realization of a microstrip LH transmission line. IEEE-AP-S Digest 2, 412–415, San Antonio, TX
17. Caloz C, Itoh T (2006) Electromagnetic metamaterials: transmission line theory and microwave applications. Wiley. IEEE Press
18. Caloz C, Itoh T (2004) Transmission line approach of left-handed (LH) structures and microstrip realization of a low-loss broadband LH filter. IEEE Trans Antennas Propagat 52:1159–1166
19. Iyer AK, Eleftheriades GV (2002) Negative refractive index metamaterials supporting 2-D waves. In: Proceedings of IEEE international symposium on microwave theory and technology 2:1067–1070. Seattle, WA
20. Ruvio G, Leone G (2014) State-of-the-art of metamaterials: characterization, realization and applications. Stud Eng Technol 1(2). https://doi.org/10.11114/set.v1i2.456
21. Marqués R, Mesa F, Martel J, Medina F (2003) Comparative analysis of edge- and broadside coupled split ring resonators for metamaterial design—theory and experiments. IEEE Trans Antennas Propag 51:10
22. Aznar F, Gil M, Bonache J, Garcia-Garcia J, Martin F (2007) Metamaterial transmission lines based on broad-side coupled spiral resonators. Electron Lett 43:9
23. Chen H, Ran L, Huangfu J, Zhang X, Chen K (2004) Left-handed materials composed of only S-shaped resonators. Phys Rev E 70:1–4
24. O'brien S, Pendry JB (2002) Magnetic activity at infrared frequencies in structured metallic photonic crystals. J Phys Condens Matter 14:6383–6394
25. Noginov MA, Podolskiy VA (2012) Tutorials in metamaterial. Series in nano optics and nanophotonic. Taylor and Francis
26. Tanaka T, Ishikawa A (2017) Towards three-dimensional optical metamaterial. Nano Convergence 4:1–6
27. Iyer AK, Eleftheriades GV (2008) Three-dimensional isotropic transmission-line metamaterial topology for free-space excitation. J Appl Phys 92:106–261
28. Baena JD, Jelinek L, Marques R, Zehentner J (2006) Electrically small isotropic three-dimensional magnetic resonators for metamaterial design. Appl Phys Lett 88:13, 134108
29. Silveirinha MG, Fernandes CA (2005) Homogenization of 3-d-connected and nonconnected wire metamaterials. IEEE Trans Microw Theor Tech 53(4):1418–1430
30. Sajuyigbe S, Justice BJ, Starr AF, Smith DR (2009) Design and analysis of three dimensionalized ELC metamaterial Unit Cell. IEEE Antennas Wireless Propag Lett 8:1268–1271
31. Varadan VV, Kim IK (2012) Fabrication of 3-D metamaterials using LTCC techniques for high-frequency application. IEEE Trans Components Packaging Manufact Technol 2:410–417

32. Yu K, Li Y, Liu X (2018) Mutual coupling reduction of a MIMO antenna array using 3-D novel meta-material structures. Appl Comput Electromag Soc J 33:758–762
33. Islam SS, Faruque MR, Islam MT (2015) A new direct retrieval method of refractive index for the metamaterial. Curr Sci 109:337–342
34. Nicolson AM, Ross GF (1970) Measurement of the intrinsic properties of materials by time-domain techniques. IEEE Trans Instrument Measure 19:377–382
35. Morse PM, Feshbach H (1953) Derivatives of analytic functions, Taylor and Laurent series. Methods Theor Phys Part I 374–398
36. Baena JD, Bonache J, Martin F et al (2005) Equivalent-circuit models for split-ring resonators and complementary split-ring resonators coupled to planar transmission line. IEEE Trans Microw Theor Techniques 53:1451–1461
37. Can S, Yılmaz AE, Kapusuz KY (2017) An equivalent-circuit model of miniaturized split-ring resonator. In: IEEE international symposium on antenna and propagation & UNSC/URSI. IEEE Press, CA, USA. https://doi.org/10.1109/APUSNCURSINRSM

Chapter 6
Metamaterial-Inspired Planar Cells for Miniaturized Filtering Applications

Asit K. Panda

1 Introduction

With the rapid advancement in the using of next-generation wireless communication systems, the demand for high-throughput microwave planar filters with miniaturized size and high selectivity increased exponentially [1, 2]. To meet the requisites, RF designers are looking for innovative miniaturization approaches to synthesize compact planar microwave filters for RF front end. These approaches are based on resonant type artificial metamaterial transmission line structures. Metamaterial (MTM) transmission lines (TLs) composed of host resonant TL (CPW line or microstrip line) loaded with sub-wavelength metamaterial resonators turns out to be an adequate approach for the miniaturization of planar microwave filters [3–5]. Furthermore, the eccentric and alluring electromagnetic band-gap characteristics of these artificial TLs can be engineered to enhance the performance of such filters. Hence, by using MTM TLs, size reduction can be accomplished by the miniaturizing of each resonant element with expanded functionalist.

The sub-wavelength, frequency-selective and self-resonant properties allow the metamaterial structures for designing miniaturized planar filters, by loading different combinations of electrically small resonators with the host transmission line configured as left-handed material with negative permittivity or permeability material [4, 5]. By varying the size, resonator geometry, relative location of the small metamaterial electrical resonators loaded on the host line, the metamaterial filer can also be tuned. This convenient handling of electrical characteristics makes the metamaterial filters alternatives to the usual planar miniaturized filter designs. In the first meta-filter design method, an improved LPF for out-of-band rejection was proposed. In this design, SRRs unit cells are inserted into the LPF [6, 7]. Without increasing the considerable size in conventional couple-line LPF, the out-of-band rejection level is

A. K. Panda (✉)
National Institute of Science & Technology (NIST), Berhampur, India

R. Kumari and B. Choudhury (eds.), *Multiscale Modelling of Advanced Materials*,
Materials Horizons: From Nature to Nanomaterials,
https://doi.org/10.1007/978-981-15-2267-3_6

improved. Later, narrowband left-handed (LH) BPFs were investigated [3, 8, 9]. In this design, periodic SRRs are loaded on the host CPW line. The position of SRRs with respect to CPW line is an important design parameter for realizing filter. The inductive CPW line and the loaded capacitive SRRs make wave transmission medium as narrow LH passband. Afterwards Bonache et al. used this approach in other meta-filters realization [10, 11]. The BPF alternatively realized by loading complementary split-ring resonators (CSRRs) on the microstrip line. The CSRRs are etched on the ground plane and capacitive gaps are etched in the microstrip transmission line. There are similar design approaches for realizing narrowband filter meta-filters that are addressed based on the alternating arrangement of RH and LH cells along the wave propagation direction [12, 13]. The series arrangement of LH and RH unit cells enhances the selectivity of miniaturized planar meta-filters. Garcia et al. [10] exhibited the outline of highly miniaturized planar filters in the microwave frequency band based on electrically small resonators. They have analyzed the magnetic and electric coupling coefficients and have proposed that an increase in the coupling can be accomplished by carving in the ground plane of microstrip innovation and metallic layers in 1D CPW configuration. Gill et al. [11] demonstrated the tenability of metamaterial transmission line by loading split-ring resonators with varactors that have been coupled to microstrip lines. They also derived a lumped equivalent model for the structure. A planar MTM unit cell in microstrip technology was investigated by Jiusheng and Tieying [14]. It composed of microstrip line and vias whose equivalent model act as a series of capacitances and shunt inductors. A novel BPF was based on the chamfered structure using th microstrip MTM resonant cells.

In this chapter, a potential application of metamaterial to the design of compact planar filters is explained. The aim of this chapter is to design and develop compact metamaterial-inspired microstrip filters, in particular, printed bandpass filters (BPFs) and bandpass filters (BSFs) by utilizing planar resonant transmission line by loading with an array with electrically small metamaterial resonators, namely, split-ring resonator (SRR) and complementary split-ring resonator (CSRR) as a basic building element of filters. These approaches are based on resonant type artificial metamaterial transmission line structures. Metamaterial transmission lines composed of host resonant TL (CPW line or microstrip line) loaded with sub-wavelength metamaterial resonators turn out to be an adequate approach for the miniaturization of planar microwave filters. We examine different metamaterial-inspired filter configurations. The first design takes up comparative investigations of different SRRs-based CPW bandpass filter configurations, and loading of CPW lines with SRRs in a series of gaps results in such BPFs. The second model deals with a microstrip line loaded with hex-omega MTM resonator cell to design a compact narrow-band BPF and BSF configurations.

2 Compact CPW Metamaterial-Inspired Lines and Its Use in Bandpass Filter

The demand of wideband bandpass filters (BPFs) with compact size, high selectivity and low insertion loss in passband greatly stimulates modern wireless communication which needs high data transmission rates. Planar BPFs have been widely studied and used as basic circuit elements in RF and microwave communication systems to remove and suppress signals from an undesired frequency band with the function of in-band transmission and out-of-band rejection. To meet the necessities in modern wireless system, many efforts have been proposed recently to develop multiplicity of compact BPF with jagged and deep rejection level inside the stopband by generating transmission zeros or attenuation poles. However, most of conventional bandpass filters are unsuitable for miniaturized realization demand of communication system.

Recently, design of filters using split-ring resonator (SRR) and complementary SRR (CSRR) with different geometrical shapes in a widespread way were studied by different researchers for designing of planar antennas, filters to achieve miniaturization. One-dimensional (1D) filtering structures using artificial media supporting LH propagation were first proposed by Martin et al. in 2003 [3] by magnetically coupling a coplanar waveguide (CPW) and sets of SRRs. After this first contribution, several designs have been presented [4–8, 15–18] in order to improve the initial performance and broaden the range of applications. In this implementation, the SRRs are carved on the posterior of the substrate, underneath the slots, to accomplish high magnetic coupling among the line and rings at resonance. The nearness of the rings prompts an effective permeability to turn into negative value in a narrow band, and by including shunt metallic strips between the central conductor and ground planes negative permittivity is achieved. The cited structure generates a passband frequency response near the resonant frequency of SRR, where the LH medium condition is satisfied. The frequency response of these structures, in general, presents a high rejection level just underneath the passband; however, poor selectivity and transmission band edges in the upper band. The previous impact can be clarified by the Split-ring resonator resonance, while the latter is ascribed to the smooth change of the split-ring resonator permeability from negative to positive values around the magnetic plasma frequency. Thus, differing approaches have been proposed to overcome this asymmetric response and its related disadvantages.

This section of the chapter presents an investigation of the CPW line loaded with concentric triangular SRR (TSRR) to acquire the bandpass characteristics. The compact structure provides high-frequency selectivity and low insertion loss depending upon the parameter variation of the TSRR and CPW transmission line (CPW TL). In this project, two types of triangular SRR (TSRR) are used as a unit cell of LHM.

2.1 Base Slit Triangular SRR—CPW TL

The typical layout of the TSRR is designed to resonate at 3.4 GHz as shown in Fig. 1a, b are loaded on a coplanar waveguide (CPW) line as shown in Fig. 2 in chapter 3. It comprises of a CPW line on the top of the substrate loaded with a pair of triangular SRRs (TSRRs). TSRRs are symmetrically placed on the rear of the substrate. Table 1 defines the geometrical configuration of CPW TL-based BSF. Here, the signal line is width (W_t), (G) is the gap between ground and the signal line, (h) is unit cell's outer ring height, the separation between each TSRR(c) was 0.45 mm and substrate thickness is (t), permittivity is (ε_r) and loss tangent is (tan δ). Copper metallization is used with a thickness (d), and conductivity (σ). By placing the triangular SRRs (TSRRs) parallel to the CPW transmission line, the electric field in the triangular rings is horizontal to the ring plane, while the magnetic field is polarized normal to the triangular ring along the ring alignment. This will achieve a negative effective permeability. On the other hand, connecting wires provide the effective negative permittivity which is needed to get LHM wave propagation in the CPW line.

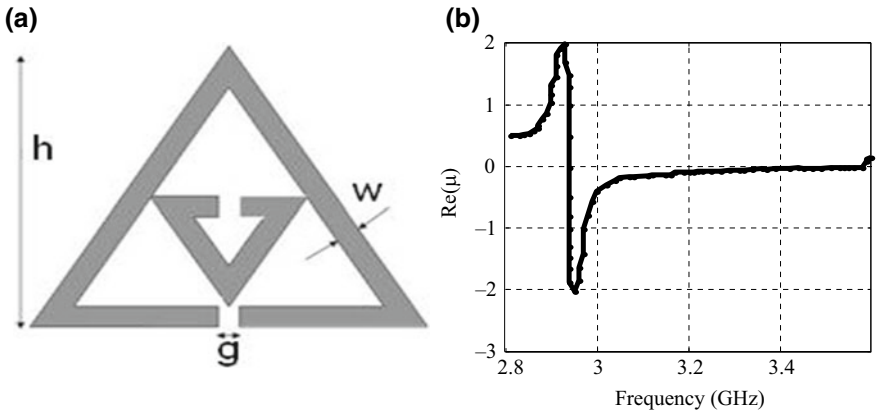

Fig. 1 **a** TSRR LHM unit cell, **b** negative permeability of TSRR

Table 1 Parameter values for the CPW geometry, unit cell characteristic

W_t (mm)	L_s (mm)	G (mm)	t (mm)	ε_r	tan δ
8.8	16.9	0.5	0.5	4.4	0.019

h (mm)	w (mm)	g (mm)	c (mm)	g_{srr} (mm)	d (mm)
6.75	0.6	0.4	0.15	0.5	0.02

2.2 Base-Coupled TSRR-Loaded CPW

The MTM unit cell and the proposed SRR-loaded CPW filter were designed and simulated using FDTD-based CST MWS electromagnetic simulator [19]. The transmission (S_{21}) and reflection (S_{11}) response of the proposed filter are depicted in Fig. 2.

As shown in Fig. 3, the structure exhibits a transmission zero at the resonant frequency of the coupled TSRRs. The examination of these transmission characteristics is performed by the extraction of the effective medium parameters of the unit-dimensional propagation structure as shown in Fig. 1a. The extraction depends on the (NRW) methods [20, 21], where the effective values of permittivity and permeability are retrieved from the simulated S-parameters. The results obtained from simulation confirm the existence of a transmission passband region between 3.06 and 3.95 GHz, corresponding to an SNG frequency band as it is predictable. The result

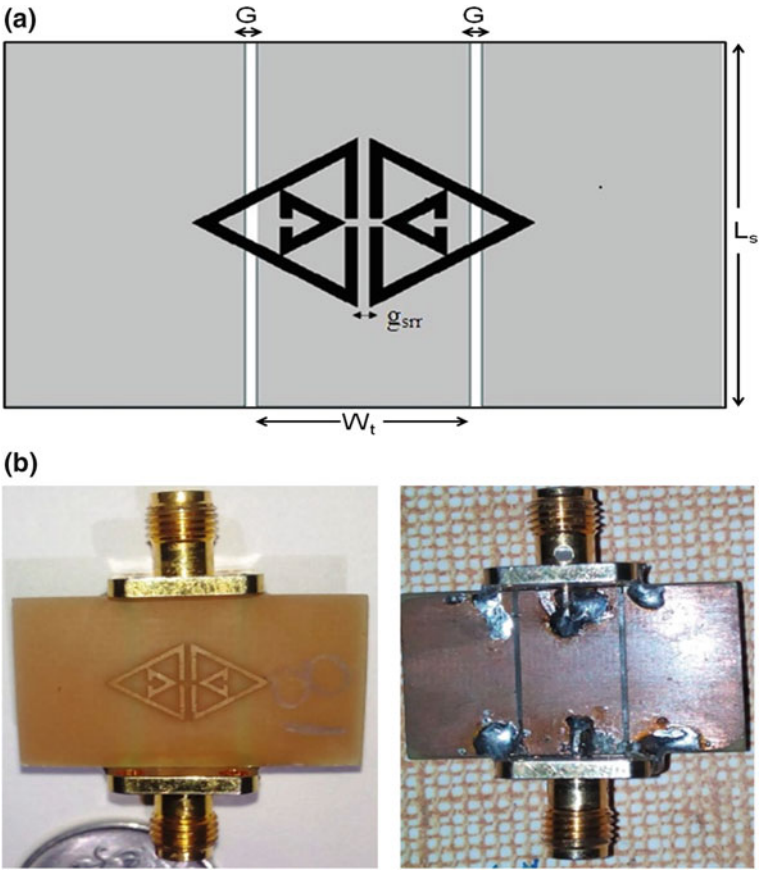

Fig. 2 TSRR-loaded CPW (base coupled) BPF: **a** configuration and **b** fabrication prototype

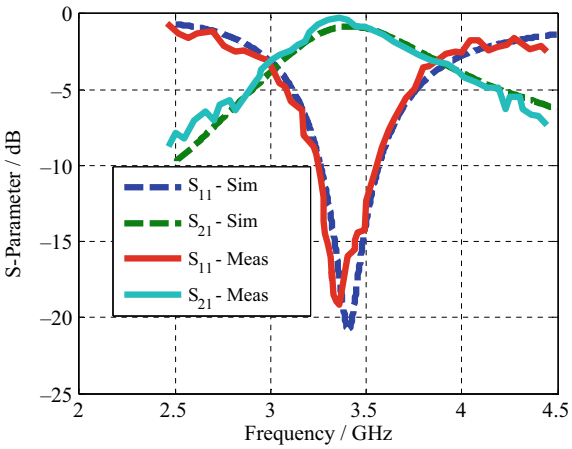

Fig. 3 S-parameter of TSRR-loaded CPW (base coupled) BPF

shown in Fig. 3 confirms the presence of passband in the vicinity of the resonant frequency of the TSRRs.

2.3 Vertex-Coupled TSRR-Loaded CPW

In this configuration the purposed TSRR is loaded in the CPW is different, i.e. the TSRR is loaded with coupling to the vertex of the unit cell as shown in Fig. 4a. As a result, there is no enough coupling between SRR's but strong coupling between SRR and transmission line and the capacitive effect is high due to which the resonating frequency shift towards lower value. The transmission (S_{21}) and reflection (S_{11}) response of the filter were shown in Fig. 5. This configuration also shows the bandpass characteristics as expected.

2.4 Parametric Study of Base-Coupled SRR-Loaded CPW

In this section, a detailed parametric study on the passband characteristics of TSRR-loaded CPW line based on split gap, strip width, the gap between two SRRs and with different substrates is done. It is very useful for designing sub-wavelength resonator-based planar filter at the desired frequency.

2.4.1 With the Effect of Different Split Gap (g) of SRR

The resonant frequency is directly proportional to the split gap of the resonator. To verify this effect we have verified four different split gaps (g = 0.25, 0.5, 1 mm) and

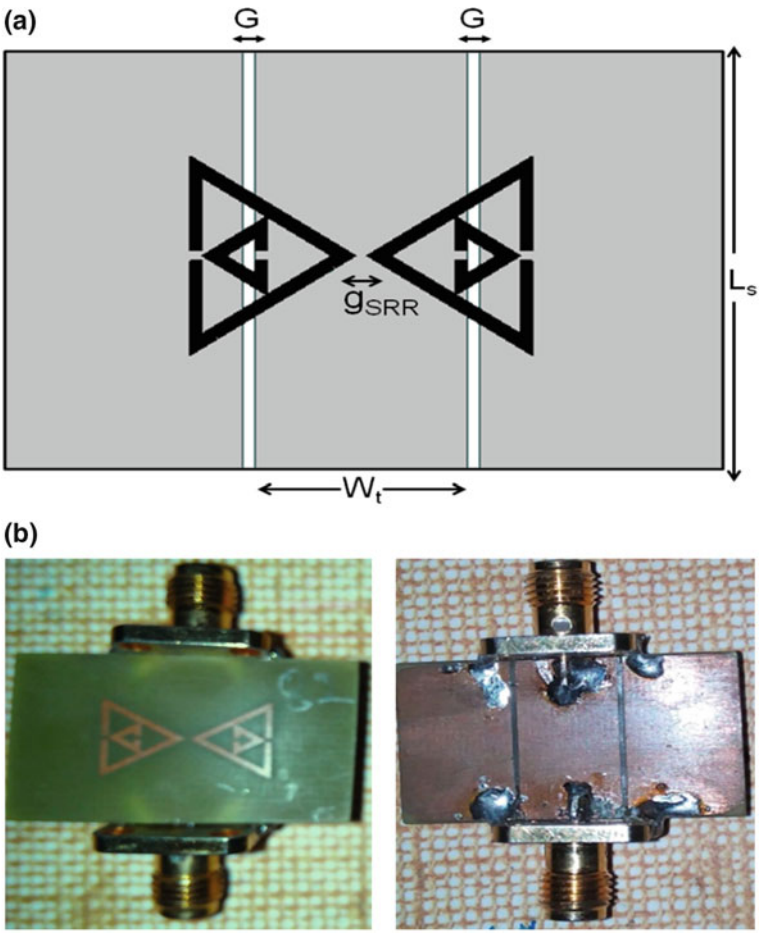

Fig. 4 TSRR-loaded CPW (vertex coupled) BPF2: **a** configuration, **b** prototype

the comparison result is shown in Fig. 6a. As the split gap increases the effective capacitance diminishes and consequently the transmission zero moves to minimal higher frequencies.

2.4.2 With the Effect of Different Substrate Permittivity

The resonance point scale as inversely proportional to the dielectric constant of the substrate (ε_r) modifies the substrate dielectric constant and the resonant peak shift accordingly. To demonstrate this effect we have simulated the SRR with three different substrates having different dielectric constant value and the result is shown in Fig. 7. As the effective dielectric constant increases, the capacitance effect of the

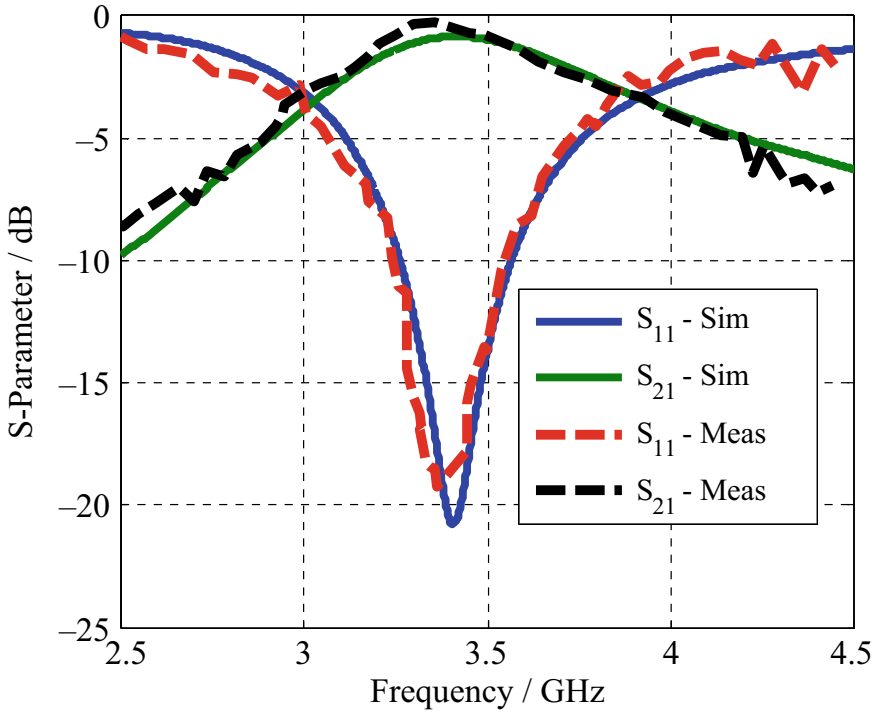

Fig. 5 Measured and simulated S-parameter of loaded CPW (vertex coupled) BPF

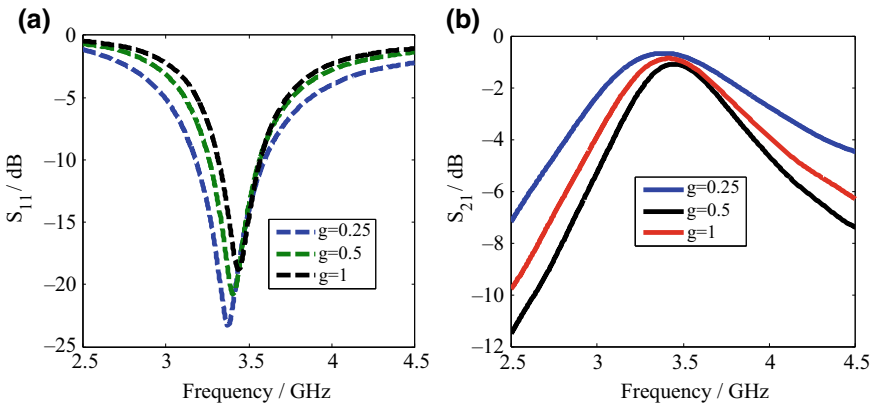

Fig. 6 With the effect of different split gap (g) of TSRR **a** S_{11}, **b** S_{21}

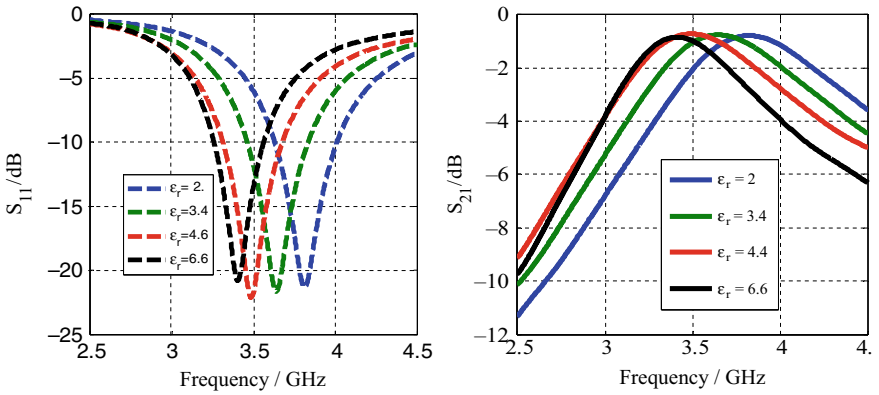

Fig. 7 With the effect of different substrate permittivity (ε_r) **a** S_{11}, **b** S_{21}

SRR loaded with CPW also increases, hence there is shift in the resonance frequency towards lower value.

2.4.3 With the Effect of Difference Between Two SRR (g_{SRR})

The resonance point scale as inversely proportional to the device having high selectivity and wide BW exhibits low value of insertion loss with high return loss, as compared to the device having moderate or high insertion loss which does not exhibit high selective response. The key aspect to achieve wideband BPF is the necessity to avoid this tread off, when distance between two unit cells is adjusted carefully. To demonstrate this effect and to achieve high selectivity BPF, we have parameterized the distance between two SRRs for different values. As shown in Fig. 8a, with increase in gap between two SRR, there is decrease in insertion loss with increase

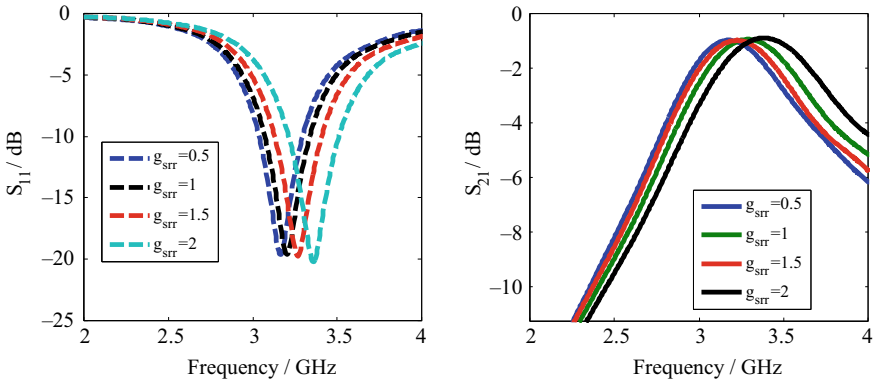

Fig. 8 With the effect of distance between two SRR (g_{srr}) **a** S_{11}, **b** S_{21}

in selectivity response of the purposed filter. This is due to strong coupling between SRR and CPW line.

3 Metamaterial Microstrip Line for Miniaturized Band-Stop and Bandpass Filter

Microstrip filter with miniaturized size plays an important role in wireless communication systems. High selectivity bandpass and band-stop filters (BPF and BSF) are used as a basic circuit element in RF communication system to prevent the emission of signals with unwanted frequency. Rapid growth of modern communication systems demands miniaturized size and high-performance planar filters [22, 23]. In the last decade, electromagnetic metamaterial brought revolution in the microwave community and communication for the design of microwave components like band-stop and bandpass filters [24–27]. In the literature, there are various metamaterial resonator structures like square, circular, omega, triangular and fractal which are reported to design compact microwave filters.

Planar metamaterial structure formed by loading the capacitor in series and inductors in shunt on a host microstrip transmission line has also been investigated both theoretically and experimentally [14]. Furthermore, it is impractical to integrate it into a common IC due to large size and more power consumption. Also, lumped element-based microwave filters are difficult to implement for the susceptibility to parasitic effects in millimetre and microwave frequency range. In recent years, composite right and left-handed transmission lines-based microwave components have been reported [27].

Engheta et al. [28] demonstrated first the omega resonator offering both negative permittivity and permeability for certain range of frequencies. This resonator has been used as lowpass filters. Authors in [26] demonstrated the improvement of the selectivity of the planar filters by loading the complementary Hex-omega resonator (HOR) array in the ground plane of the microstrip line structure. Some authors have adapted the customary state of the omega resonators to configuration planar filters [29, 30]. For the design of compact high selective microwave planar filters, the hex-omega metamaterial resonator structure proposed by Sahu et al. [26] has been an alluring option structure because of its scaled downsize and negative magnetic permeability behaviour.

This section of this chapter deals with a new kind of microstrip transmission line based on hex-omega metamaterial resonator cell that has been investigated to design a novel narrow-band bandpass and band-stop filter configurations. The metamaterial resonators placed on either side of the microstrip line contributes to the capacitive gap for the realization of series capacitor and a vias hole on the microstrip line to realize shunt inductor. The proposed bandpass and band-stop filter based on HOR MTM unit cell structure exhibits the same EM characteristics as the regular ones. The

performance of the filters has been validated using both numerical and measurement results.

3.1 Hex-Omega-Shaped Metamaterial Resonator

The layout of the proposed hex-omega metamaterial resonator (HOR) is shown in Fig. 9a, b to realize as band-stop filter and bandpass filter. The unit cell structure is constituted by two symmetrically Hex-Omega-shaped metallic inclusions on both sides of the microwave laminator by using 0.02 mm thick copper clad. Here, we have used a low loss glass epoxy substrate with dielectric constant ($\varepsilon_r = 4.4$), loss tangent ($\tan \delta = 0.002$) and substrate thickness ($t = 1.6$ mm), respectively. The geometrical dimensions of unit cell are set as to be (in mm): L =, W = 0.5, $a_x = 7$, $a_y = 8$.

The unit cell structure was simulated in the frequency range 3–5.5 GHz to obtain the S-parameters. These S-parameters were exported to MATLAB. Then, Nicolson–Ross–Weir approach [20, 21] was implemented in MATLAB to characterize the effective medium parameter.

It can be seen from Fig. 10 that the HOR has magnetic resonance appeared at 4.4 GHz in the EM simulation. Its relative permeability is truly negative from 4.4 to 5.3 GHz and behaves as a single negative medium in this region. The relative permeability structure which clarifies that designed MTM resonator exhibits negative behaves as single negative material.

Based on the electromagnetic characteristics of hex-omega metamaterial resonator, the synthesis of narrow band-stop (BSF) and bandpass filter (BPF) configurations in the range of same resonant frequency (4.29 GHz) are presented in the following section.

The BSF is constructed using the cascaded coupled hex-omega resonators excited by a 50 Ω transmission line. The BSF can be altered into BPF by the insertion of metallic via on the microstrip line. The bandpass structure is realized by changing the excitation microstrip line with a series of via holes. Via conductor on the microstrip

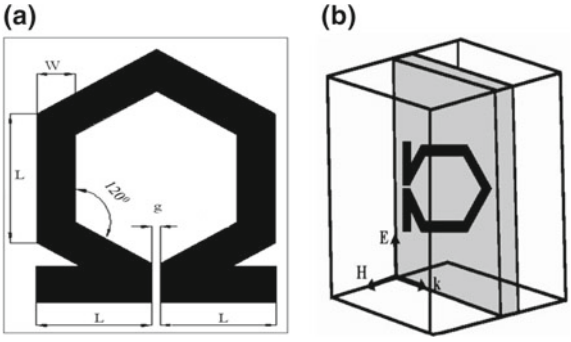

Fig. 9 **a** Hex-omega unit, **b** HFSS simulation model of the unit cell with the polarization direction

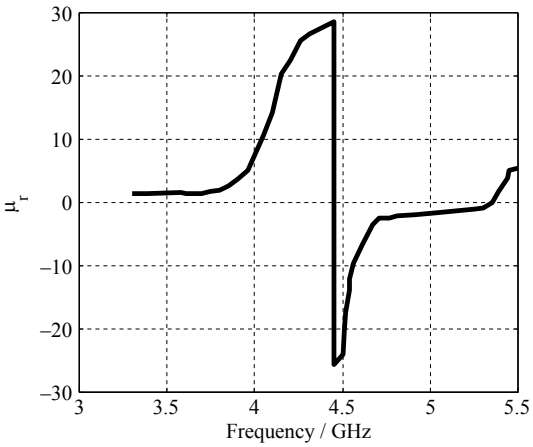

Fig. 10 Electromagnetic characteristics of Hex-omega structure

line realizes as shunt inductor and the gap between the hexagonal omega resonator and microstrip line offers series capacitance.

3.2 Metamaterial-Inspired Filter Implementation

1. Narrow-Band Bandpass Filter Implementation

Figure 11a, b show the design geometry configuration and photograph of the prototype fabrication of the high selectivity bandpass filter, respectively. It consists of microstrip line loaded with four cascaded hex-omega resonators adjacent to the central conductor of a microstrip transmission line and four cascaded arrangements of

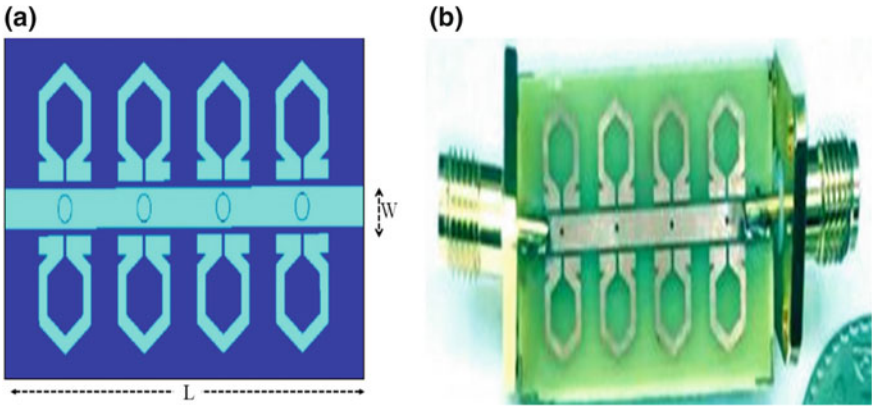

Fig. 11 **a** Configuration of BPF, **b** prototype of BPF

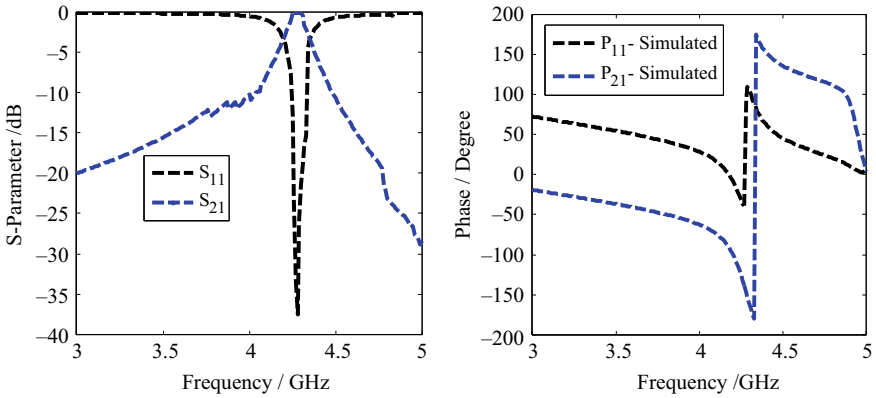

Fig. 12 **a** S-parameter of BPF **b** phase of BPF

metallic vias extending from the central conductor (microstrip line) to the ground plane are introduced. The introduction of periodic metallic vias acts as microwave plasma with effective permittivity (ε) that negatively varies from magnetic cut-off frequency to the plasma frequency. When the resonant frequency of the HOR is tuned below this place frequency, LH wave propagation is experienced over a precise band in the proximity of the resonant frequency of the hex-omega resonator. This architecture can be used as a high selectivity BPF with negative phase (Fig. 12).

The periodicity (p) between two cascaded resonators has been set to 3.7 mm. In this work, the gap between microstrip line and Hex-omega cells of 1 mm is maintained, by which the characteristic inductive and capacitive coupling between the microstrip line and the resonators is enhanced. The total dimension of the substrate is 14.8 mm × 7.38 mm. The filter is designed at 4.7 GHz, the optimized dimension of the resonator for 4.7 GHz is W = 0.7 mm, R = 2.7 mm (Fig. 11a). The microstrip line length (L) and width (W) are 14.8 mm and 1.44 mm for a characteristic impedance of 50 Ω. Via conductor on the microstrip line realizes as shunt inductor and the gap between the hexagonal omega resonator and microstrip line offers series capacitance. Also, the split in each hex-omega resonator offers series capacitance. These two dominant capacitive effects contribute to electrical energy storage in the geometry of the bandpass filter. The BPF based on hex-omega metamaterial resonators was build up using planar microstrip technology on a low-cost FR4 substrate with dielectric constant 4.4 and dielectric thickness of h = 1.6 mm. The simulation and optimization are performed using CST MWS [19]. The experimental study for S-parameters was performed using Agilent 8719ES VNA.

The simulated and measured S-parameter results of bandpass filter are shown in Fig. 13. The two results match very well with a very little frequency offset of 0.1 GHz. It exhibits a transmission band cantered around 4.4 GHz The bandpass filter shows 0.25 dB in-band attenuation both in simulation and measurement. This attenuation loss may be originated from dielectric loss due to high electric fields in the gap. Further, from this figure one can observe that return loss and insertion loss of the

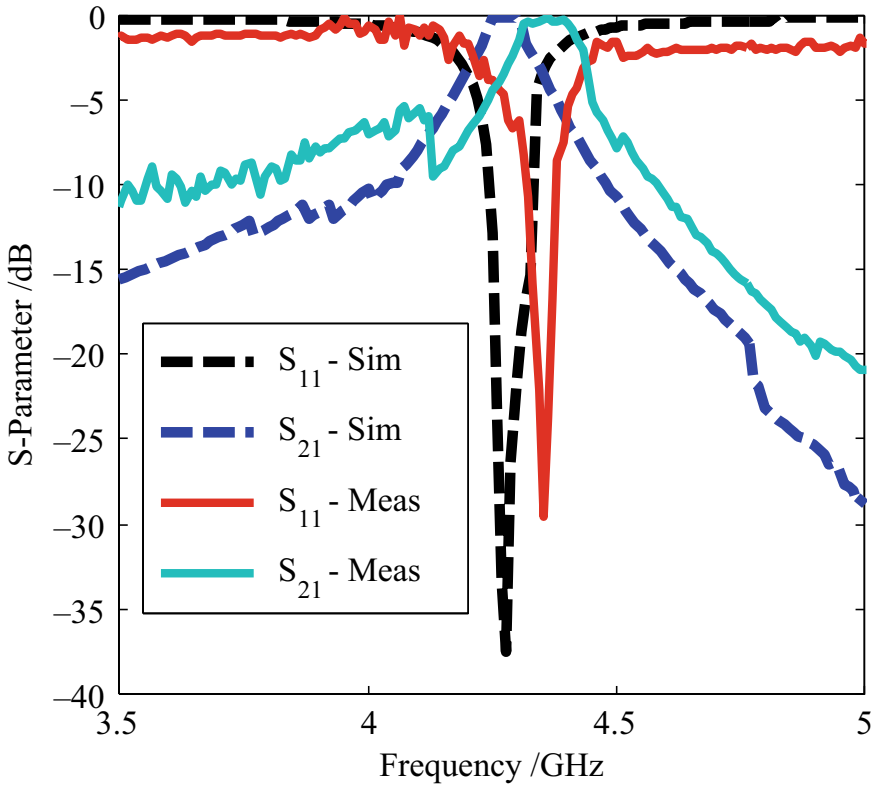

Fig. 13 Simulated and measured S-parameters results

designed bandpass filter at the centre frequency (4.4 GHz) are better than −30 dB and 0.25 dB in the passband, respectively. The simulation and measurement agree well with the exception of the frequency deviation around the outline frequency at 4.38 GHz. This discrepancy may be due to the use of the lossy FR4 substrate and the fabrication error. Figure 12b shows the simulated phase variation from HFSS simulation, where a clear phase reversal for S_{11} near the resonant frequency 4.38 GHz indicating metamaterial characteristics.

2. Narrow-Band Band-stop Filter Implementation

The geometry of the narrow-band band-stop filter (BSF) filter model is shown in Fig. 14. In this model, a highly compact BSF, based on metamaterial transmission line is presented. It consists of a microstrip transmission line loaded with 4 HORs on both sides of the microstrip line that has been examined to improve the propagation characteristics. Generally a small gap between the MTM transmission line and resonators enhance the magnetic coupling which creates negative permeability around the resonant frequency. This phenomenon will give rise to stopband filtering transmission behaviour around that resonant frequency.

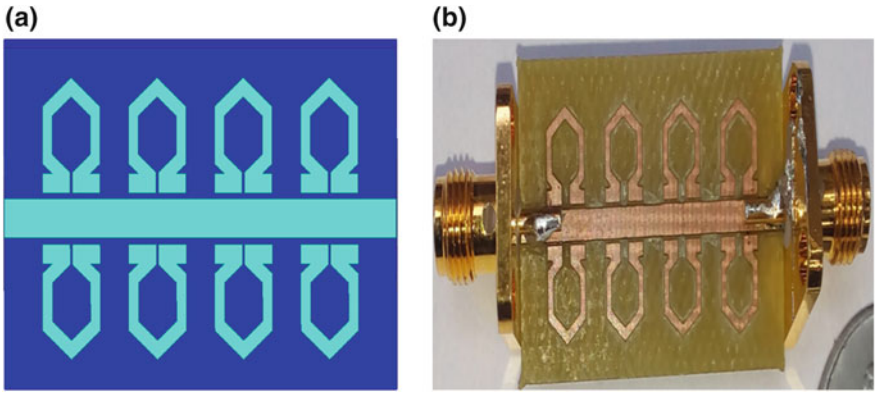

Fig. 14 **a** Configuration of BSF, **b** prototype fabrication of the BSF

The frequency response for designed BSF is depicted in Fig. 15. It confirms the presence of a stopband in the vicinity of the resonant frequency (at 4.4 GHz) of the Hex-omega resonator. For the BSF structure of Fig. 15a, a high selectivity stopband appears cantered at 4.3 GHz. with rejection level greater than −25 dB at the centre frequency with very sharp transition bands. This structure has been fabricated and the frequency response was measured by using Agilent 8722ES. The two simulated and measurement results match very well except the measured frequency shift of around 60 MHz (4.29–4.35 GHz). The phase variation of BSF is depicted in Fig. 15b. The band-stop filter shows around −28 dB in band attenuation. The hex-omega array band-stop filter shows a narrow bandwidth of roughly 2% in light of the fact that the resonance is reliant on the hex-omega resonator's innate resonance.

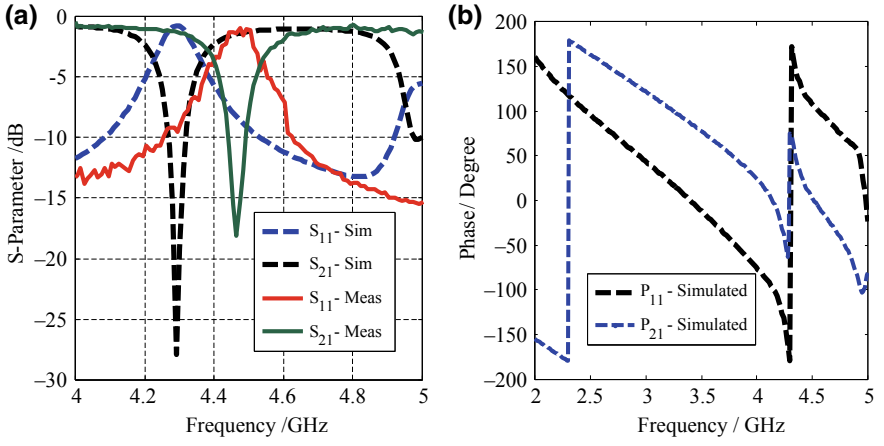

Fig. 15 **a** Simulated and measured S-parameter results; **b** simulated phase variation

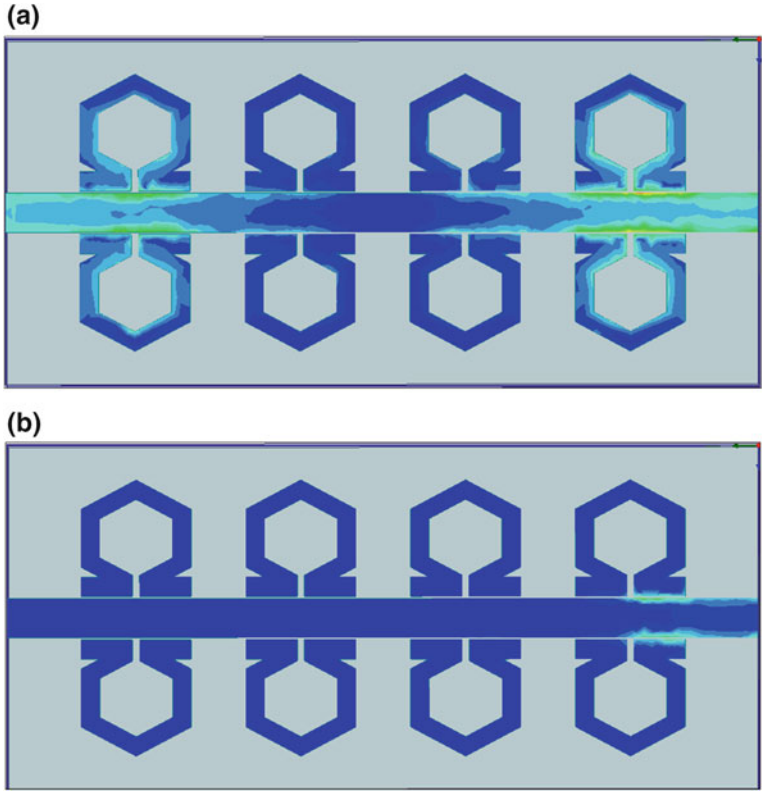

Fig. 16 Magnitude of surface current distribution at **a** 4.28 GHz **b** 3 GHz of bandpass filter

Figure 16 shows the surface current distribution inside the bandpass frequency region at 4.38 GHz and outside the bandpass frequency region of the proposed metamaterial-inspired BPF filter at 3 GHz. It is clearly observed from Fig. 16a that maximum power is transmitted from port 1 to port 2 within the bandpass region. Figure 16b shows that no power is transmitted within the band-stop region of the proposed filter within the band-stop region 4.28 GHz.

3.3 Parametric Study

The effects of the dimensions on the resonant frequency and 3 dB fractional bandwidth are investigated to achieve a better understanding of the operating principle for the composite-shaped hex-omega resonator with microstrip line. By varying 'g' keeping other design parameters fixed of bandpass filter, variations of the simulated resonant frequency with rejections are reported in Table 2.

Table 2 $g_1 = 0.1$ mm, g is varied of bandpass filter of Fig. 11a

Sl. no.	g	f_0	S_{11} (dB)	S_{21} (dB)
1	0.2	4.2688	−34	−0.6628
2	0.3	4.2711	−35	−0.8406
3	0.4	4.2674	−34.1	−0.5349
4	0.6	4.2737	−37	−0.4913
5	0.8	4.2768	−34.5415	−0.5349
6	1.0	4.2788	−40.78	−0.5273

Table 3 g1 = 0.1 mm, g is varied of band-stop filter of Fig. 14a

Sl. no.	g	f_0	S_{21} (dB)	S_{11} (dB)
1	0.2	4.2787	−27.0909	−0.5455
2	0.3	4.2787	−31.9091	−0.4545
3	0.4	4.2787	−31.7273	−0.3636
4	0.6	4.2787	−28.3636	−0.5455
5	0.8	4.2816	−29.0909	−0.4545
6	1.0	4.2816	−30.1818	−0.4545

Keeping g_1 fixed, with variation of g of band-stop filter different observations are obtained which are depicted in Table 3 with corresponding transmission and reflection parameter.

Table 3 demonstrates the simulated insertion loss (IL) of BSF as a function of capacitive gap disparity 'g'. For gap of 0.3 and 0.4 mm the better IL performance for stopband could be gotten with an improved electromagnetic coupling between the transmission line and hex-omega resonators. For a gap of 0.3 mm, maximum IL of −31.9 dB is uncovered.

4 Summary

In this chapter, different approaches for designing and miniaturization methods of metamaterial-inspired planar filters for both bandpass and band-stop characteristics by loading the different SRRs and CSRRs on CPW line and microstrip line have been studied.

This chapter outlines and develops compact metamaterial-inspired microstrip filters, in particular, printed bandpass filters (BPFs) and bandpass filters (BSFs) by utilizing planar resonant transmission line by loading with an array with electrically small metamaterial resonators. In the first section, comparative investigations of different SRRs-based CPW bandpass filter configurations are performed. These BPFs are obtained by loading the CPW lines with TSRRs in a series of gaps. In the second

model, a microstrip transmission line based on hex-omega metamaterial resonator cell has been investigated to design a novel narrow-band bandpass and band-stop filter configurations.

References

1. Pendry JB, Holden AJ, Robbins DJ, Tewart WJ (1999) Magnetism from conductors and enhanced nonlinear phenomena. IEEE Trans Microw Theory Tech 47:2075–2084
2. Gay-Balmazando P, Martin JF (2004) Electromagnetic resonance in individual and coupled split ring resonator. Microwave Opt Tech Lett 40:3–6
3. Martin F, Bonache J, Falcone F, Sorolla M, Marques R (2003) Split ring resonator-based left-handed coplanar waveguide. Appl Phys Lett 83(22):4652–4654
4. Martin F, Falcone F, Bonache J, Marques R, Sorolla M (2003) Miniaturized coplanar waveguide stop band filters based on multiple tuned split ring resonators. IEEE Microw Wirel Compon Lett 13(12):511–513
5. Falcone F, Martin F, Bonache J, Marques R, Lopetegi T, Sorolla M (2004) Left handed coplanar waveguide band pass filters based on bi-layer split ring resonators. IEEE Microw Wirel Compon Lett 14(1):10–12
6. García JG, Bonache J, Falcone F, Baena JD, Martín F, Gil I, Lopetegi T, Laso MAG, Marcotegui A, Marqués R, Sorolla M (2004) Stepped-impedance low pass filters with spurious passband suppression. Electron Lett 40:881–883
7. Ali A, Khan MA, Hu Z (2007) High selectivity lowpass filter using negative-epsilon metamaterial resonators. Electron Lett 43:528–530
8. Marqués R, Martín F, Sorolla M (2011) Metamaterials with negative parameters: theory, design and microwave applications. In: Wiley series in microwave and optical engineering, vol. 183. Wiley
9. Gil M, Bonache J, Martín F (2008) Metamaterial filters: a review. Metamaterials 2(4):186–197
10. Garcia JG, Bonache J, Gil I, Martin F, Ahumada MCV, Martel J (2006) Miniaturized microstrip and CPW filters using coupled metamaterial resonators. IEEE Trans Microw Theory Techn 54(6):2628–2634
11. Gil I, Martín F, Bonache J, García-García J (2006) Tunable metamaterial transmission lines based on varactor loaded split rings resonators. IEEE Trans Microw Theory Tech 54(6):2665–2674
12. Bonache J, Martín F, Falcone F, García J, Gil I, Lopetegi T, Laso MAG, Marqués R, Medina F, Sorolla M (2004) Super compact split ring resonators CPW band pass filters. In: Proceedings of the IEEE-MTT international microwave symposium digest, FortWorth, TX, USA, June 2004, pp 1483–1486
13. Mondal P, Mandal MK, Chaktabarty A, Sanyal S (2006) Compact bandpass filters with wide controllable fractional bandwidth. IEEE Microw Wirel Compon Lett 16:540–542
14. Jiusheng L, Tieying D (2007) Application of metamaterial unit cell in bandpass filter. Microw Opt Technol Lett 49(9)
15. Falcone F, Lopetegi T, Laso MAG, Baena JD, Bonache J, Beruete M, Marques R, Martın F, Sorolla M (2004) Babinet principle applied to the design of metasurfaces and metamaterials. Phys Rev Lett 93(19):197401
16. Baena JD, Bonache J, Martin F, Sillero RM, Falcone F, Lopetegi T, Laso MAG, Garcia-Garcia J, Gil I, Portillo MF, Sorolla M (2005) Equivalent-circuit models for split-ring resonators and complementary split-ring resonators coupled to planar transmission lines. IEEE Trans Microw Theory Tech 53(4):1451–1461
17. Rogla LJ, Carbonell J, Boria VE (2007) Study of equivalent circuits for open ring and split-ring resonators in coplanar waveguide technology. IET Microw Antennas Propag 1(1):170–176

18. Aznar F, Bonache J, Martin F (2008) Improved circuit model for left-handed lines loaded with split ring resonators. Appl Phys Lett 92(4):043512
19. CST Microwave Studio Suit, @ 2015 CST: Computer Simulation Technology, AG
20. Nicolson AM, Ross GF (1970) Measurement of the intrinsic properties of materials by time domain techniques. IEEE Trans Instrum Meas 19:377–382
21. Weir WB (1974) Automatic measurement of complex dielectric constant and permeability at microwave frequencies. Proc IEEE 62:33–36
22. Hong JSG, Lancaster MJ (2004) Microstrip filters for RF/ microwave applications. Wiley, New York
23. Pozar DM (2005) Microwave engineering. Wiley
24. Garcia-Garcia J, Bonache J et al (2006) Comparison of electromagnetic bandgap and split ring resonator microstrip line as stop band structures. Microw Opt Technol Lett 44(4)
25. Saasi I, Talbi L, Hettak K (2016) Compact band pass filters based on linked hexagonal-omega resonators. Microw Opt Technol Lett 58(5)
26. Sahu S, Kishore Mishra R, Ranjan Poddar D (2011) Compact metamaterial microstrip low-pass filter. J Electromagn Anal Appl 3(10):399–405
27. Gill I, Bonache J, Gracia-Gracia J, Falcone F, Martin F (2005) Metamaterials in microstrip technology for filter applications. IEEE Antenna Propag Soc Int Symp 2005:668–671
28. Saadoum MMI, Engheta N (1992) A reciprocal phase shifter using novel pseudochiral or Ω medium. Microw Opt Technol Lett 5:184–188
29. Engheta N, Ziolkowski RW (2006) Metamaterials: physics and engineering explorations. IEEE Press, New York, NY
30. Bassirian Jahromi P, Rashed-Mohassel J (2015) Deformed omega resonator and its application to microwave filters. Micro Opt Technol Lett 57:1447–1451

Chapter 7
Conducting Polymer-based Antennas

Laya Varghese and Balamati Choudhury

1 Introduction

Global positioning system has become one of the most commonly used Global Navigation and Satellite System (GNSS) in current years, as it is the only space-based satellite navigation system having worldwide coverage for commercial, civil and defense applications. Wireless applications widely use microstrip patch antennas (MPA) because of their higher bandwidth and compact size. Microstrip patch antennas had been proved acceptable in the production of miniature elements because of its planar structure. Fractal is a recursively created structure containing self-similar shape, which indicates that some of the parts are having same shape as the complete object but at different scale. Fractal shows another space-filling properties and has self-similarity. Fractals are multiband and compact antennas. Certain unique characteristics shown by fractal-shaped antennas help in improving their performance without degrading the properties shown by them [1].

Recent researches are focused on exploring a new effective material in MPA designing. Application of conductive polymers like PPy (Polypyrrole) or PEDOT (Poly (3, 4-ethylenedioxythiophene)) for microwave applications is being topic for current studies due to advantage in processability, flexibility and low cost. They can be even used as an alternative to copper in planar antennas. A comparative analysis between performance characteristics of Cu, PEDOT and PPy material is done in this study. The obtained results confirm that use of polymer materials in microwave applications is more advantageous as compared to generally used copper. The acceptable antenna efficiency achieved by the use of polymer materials is due to the presence of sufficiently thick layer of conductive material along with adequately high conductivity [2].

L. Varghese (✉) · B. Choudhury
Centre for Electromagnetics (CEM), CSIR-National Aerospace Laboratories (CSIR-NAL), Bangalore 560017, India

R. Kumari and B. Choudhury (eds.), *Multiscale Modelling of Advanced Materials*,
Materials Horizons: From Nature to Nanomaterials,
https://doi.org/10.1007/978-981-15-2267-3_7

2 Materials

Advanced material is a material which has engineered properties produced through the development of synthesis technology and specialized process, in other words, they are materials used in high-technology applications. They are either conventional materials with improved properties or newly bent materials having capabilities for high performance, which make them relatively expensive. High-Tech devices use these materials which operate depending on relatively complex principles (e.g. air-crafts, space-crafts, computers, electronic gadgets, etc.). Integrated circuits (ICs), lasers, LCDs, fibre optics, thermal protection for space shuttle, etc. are the typical applications. Examples for advanced materials include inter-metallic compounds, multi-component alloys, metallic foams, special ceramics, high-temperature materials and magnetic alloys and so on.

Advanced materials can be described in many ways. The widely used definition refers it as all the materials which represent advancements over the traditional materials which are being used for centuries. This way, advanced materials can be used to refer all new and modified materials to achieve high-characteristics performances that are crucial for applications of interest.

These materials show entirely new properties. Typically, advanced materials exhibit superior properties due to which they outperform traditional materials in applications. The arrival of new technologies and intellectual properties (IP) paved way for the development of these advanced materials. The developments in advanced materials may even result in the design of entirely new products. Advanced materials can be even remarkably adaptable.

More focused and insightful approach in advanced materials are considered for the materials which are in the early stage of their technology and/or product lifecycle. Hence, there is substantial space for progress in performance characteristics (technology lifecycle) and sales volume (product lifecycle) of these materials. Ceramics, metals, glass, composites, polymers and semiconductors are some of the examples of these leading materials. Advanced materials along with the process technologies associating with them have the potential to be highly applicable in the field of high-value added products. Hence, it forms a multidisciplinary area within itself and also cross-cutting over market sectors and technology areas.

2.1 Conducting Polymers and RF Antennas

Polymer materials that exhibit both electrical and thermal conductivity are called conducting polymers. The polymer backbone (chain) of these materials being impregnated with highly conductive metals or carbon particles forms the reason for electrical and thermal conduction property. Conductivity in Conducting polymers (CPs) is obtained from oxidation and reduction reactions along the polymer backbone. The reduction and oxidation reactions also called ‘Redox’ reactions are usually conducted

electrochemically. Certain cationic or anionic species (or ions) are embedded into the polymeric chain as 'dopants'. The oxidation or reduction of the polymeric chain and formation of charge centres are caused by the insertion of these impurities, which is the reason for observed conductivity in CPs.

A number of CPs are now popular and have been studied in detail for their properties and possible applications in very diverse engineering disciplines. Some of the CPs are polyacetylene, polythiophenes, polyaniline (PANi), polypyrrole (PPy), Poly (3, 4-ethylenedioxythiophene), (PMT) or PEDOT.

Since the discovery of conductive polymers (CPs), they have found numerous applications. Fast-growing developments in conductive polymer science have largely inspired to utilize these materials as a substitute to classic conducting metals like gold and copper in the design and manufacturing of electromagnetic gadgets. Even though polymers show less conductivity as compared to metals, it is being considered acceptable for antenna production.

Excellent improvements in stability as well as continuous enhancements in the electrical conductivity make conducting polymers an exceptionally good choice for replacing copper (Cu) in planar antennas. These are widely utilized in lightweight applications. Low cost, wearable or conformal antennas are of high consideration. Isolation or very few efforts were done in the past for exploiting CPs for designing antenna.

A conducting polymer (CP) composite was specifically utilized by Solberg et al. [3] to construct a direction finding non-planar antenna which operated in 30 MHz to 1 GHz range of frequency. Design of low-cost RFID coil antennas utilizing polymeric film having silver chips was tried [4].

Rmili et al. [5] proposed a created rectangular microstrip patch antenna wire which had transmitting component made of polyaniline (PANI) which is a conducting polymer with mass 6000 S/m DC conductivity.

PEDOT: PSS developed and patented by Bayer A. G is the most popular. PEDOT: PSS and its derivatives that combine optical, electronic and mechanical properties are technologically valuable with scientific interest. An aesthetic broadband RFID UHF antenna was earlier shown by the authors for traceability through interoperability worldwide; however, this proposed antenna was not set on recyclable or optically transparent materials [6]. Applications of optically transparent and aesthetic antennas in construction of solar cells, windows, decoration and vehicles have gained attraction for great concern latterly. Indium tin oxide (ITO), silver-coated polyester film (AgHT) and fluorine-doped tin oxide (FTO) were some of the transparent conductive films explored earlier. In 2015 labels which were more than 8.9 billion were sold, which was 14% more compared to 2014, and proceeds with similar development along the comparative rates in coming years. As a result, many of these tags can be seen as an unrequired impurity causing environmental pollution in a recycle chain of glass, paper or plastic at the finish of value chain.

RFID UHF broadband antenna in PEDOT: PSS material identified for biocompatibility and biodegradability property was proposed by Kamel et al. Properties such as higher stability level with medium conductivity, time and capability to be removed on a substrate by the inkjet complaint or serigraphic process with industrial

production make these polymers an economical solution [7]. These characteristics motivate growing interest for contactless technologies in the field of health and environmental safety. This chapter proposes a low-cost conducting polymer and a novel RFID antenna exhibiting broadband characteristics required to cover all UHF frequency bands, resulting in an efficient combination of UHF RFID and transparency. In order to measure the execution of the proposed antenna design using CPs, a copper antenna with comparable geometry was optimized and furthermore developed to do a comparison in their performances and to validate these antenna simulations and to consider about their execution.

3 Antenna Design using Materials

The identical three MPAs are designed and simulated using FR4 as substrate of 1.6 mm, dielectric constant of 4.3 and loss tangent of 0. 025. The first MPA is designed with 0.018 mm Cu thickness. An identical two more MPAs are designed using PEDOT and PPy on FR4 substrate having thickness of 0.018 mm for the direct comparison of relative performances. These antennas are microstrip line fed with characteristic impedance of 50 Ω. These antennas were designed for operations at 1.5754 GHz.

3.1 Design and Analysis of Fractal Antenna using Copper Patch

Fractal antennas are compact, multiband antennas. The fractal-shaped antennas have their own unique characteristics, which enhances the antenna performance characteristics without degrading their performances [8]. Some properties of fractal geometry are useful in designing small size and multi-frequency antennas [9]. Various fractal geometries such as the Minkowski [10], Sierpiski [10], Koch curves [11] and the tree structures [12] have been explored for different antenna designs.

The proposed antenna consists of a conducting patch of fractal geometry on one side of the dielectric substrate with a ground plane on the other side. The patch is made of conducting material copper of fractal shape. The radiating patch and feed lines are usually photo etched on the dielectric substrate. Microstrip line feeding techniques have been used for the fractal patch antenna.

MPA consists of a patch, substrate and ground plane. Patch and ground are on the opposite faces of the substrate as shown in Fig. 1 and fringing fields which take place between ground plane and patches results in the radiation mechanism in microstrip patch antenna (MPA). This design uses highly conducting materials like copper to make patch, ground plane and the feed line of MPA. Patch is made rectangular shaped

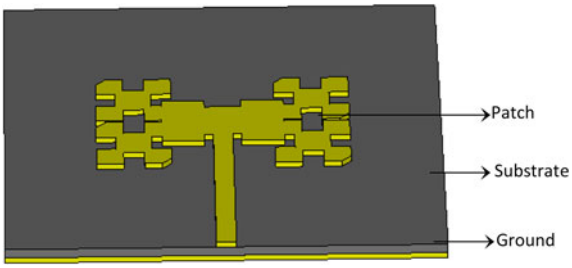

Fig. 1 Basic rectangular microstrip patch antenna

in this design for easy analysis and calculation. Figure 1 shows the rectangular fractal microstrip patch antenna.

The dimensions of the MPA can be determined using the design equations through 1 to 2 as given below. The proposed antenna structure is fed by a microstrip line. The microstrip feed line dimensions have been taken for a characteristic impedance of 50 Ω. It can be determined from Eqs. (1) and (2) which is equal to w = 3.136789 mm.

When w/h > 1

$$\varepsilon_{\text{reff}} = \frac{\varepsilon_r + 1}{2}\left[\frac{\varepsilon_r - 1}{2\sqrt{1 + 12\left(\frac{h}{w}\right)}}\right] \tag{1}$$

$$z_0 = \frac{120\pi}{\sqrt{\varepsilon_{\text{reff}}\left[\frac{w}{h} + 1.393 + \frac{2}{3}\ln\left(\frac{w}{h} + 1.444\right)\right]}} \tag{2}$$

$\varepsilon_{\text{reff}}$ Effective dielectric constant
ε_r Relative dielectric constant of substrate
w Width of stripline feed
h Thickness of dielectric substrate.

3.1.1 Design and Simulation of Fractal GPS Antenna using Cu Patch

The proposed antenna consists of conducting patch of fractal geometry on FR4 substrate backed by a defected ground plane. The designed antenna has an operating frequency of 1.57542 GHz (GPS L1 band) with enhanced gain, efficiency and wide angle coverage to ensure a stable wireless link.

Design of Fractal Geometry

The proposed fractal antenna design is based on the progress from the square microstrip antenna for GPS frequency. To reduce the size of the square patch microstrip antenna we use second iterations of fractal. Because with increasing the

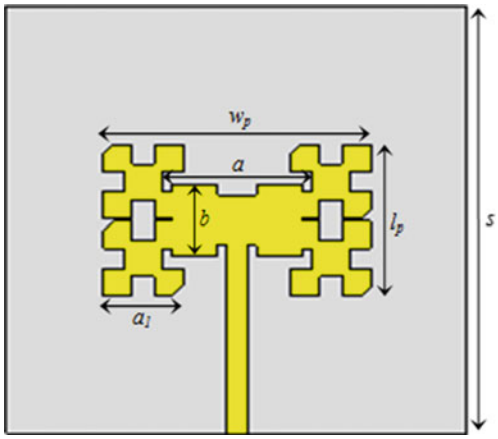

Fig. 2 Fractal patch antenna geometry

number of iterations we get long antenna on the same surface which reduces the resonance frequency.

The design of the structure of the fractal antenna started with a rectangular shape and was iterated twice over substrate. The ground plane material and thickness is same as that of patch.

Geometric construction of the second iterated fractal reference antenna is shown in Fig. 2. In which each side of the basic rectangular patch is divided into three equal parts and the first iterated part of each side is replaced by a projection inwards with two vertical and two horizontal segment of equal length.

Design of Defected Ground Structure (DGS)

Planar transmission line ground planes contain intentionally imprinted non-periodic or periodic cascaded configuration imperfection called as DGS [13]. This causes disturbance in the distribution of shield current in the ground plane which causes transmission line characteristics such as line conductance and capacitance to change eventually.

The development of the defected ground structure in microstrip patch antennas helps the microstrip patch antenna's size reductions, harmonics reduction, cross-polarization reduction, mutual coupling reduction, broadband RCS reduction and radiation properties enhancement.

The consequences of fractal slots in the printed antenna characterization are examined using the defects on the ground plane with the optimized patch antenna in order to get better performance [14]. Test and verification of ground plane were done using different shaped slots. But fractal-shaped printed slot on ground plane gives better performance. Geometric construction of the first iterated FDGS of reference antenna is shown in Fig. 3.

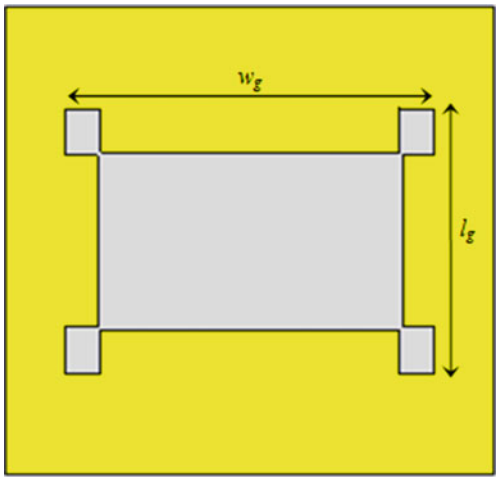

Fig. 3 Fractal defected ground structure (FDGS) geometry

Table 1 Dimensions of fractal GPS antenna

Symbol	Parameter	Dimensions (mm)
w_p	Width of patch	24.38
l_p	Length of patch	40.38
a	Width of centre patch	25.06
b	Length of centre patch	11.6
a_1	Size of scale down design	11.99
w_g	Width of FDGS	52.38
l_g	Length of FDGS	39.38
s	Size of substrate	69.55
h	Height of substrate	1.6

The planar fractal GPS antenna operating at 1.5754 GHz (L1 band) is designed and then simulated in FEM-based simulation tool. The design parameters of the patch antenna are given in Table 1.

3.1.2 Simulation of Fractal GPS Antenna using Cu Patch

The designed fractal GPS antenna using Cu patch is simulated and its characteristics are studied. The characteristics like return loss, bandwidth, gain and directivity are analyzed.

From Figs. 4 and 5 the performance of the designed fractal GPS antenna can be analyzed. From Fig. 4 it is observed that the designed antenna gives a return loss of –22.96 dB at a resonating frequency of 1.5754 GHz.

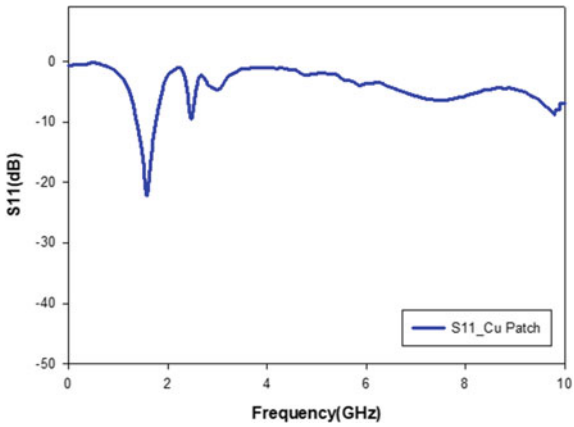

Fig. 4 Return loss characteristics of planar fractal GPS antenna using Cu patch

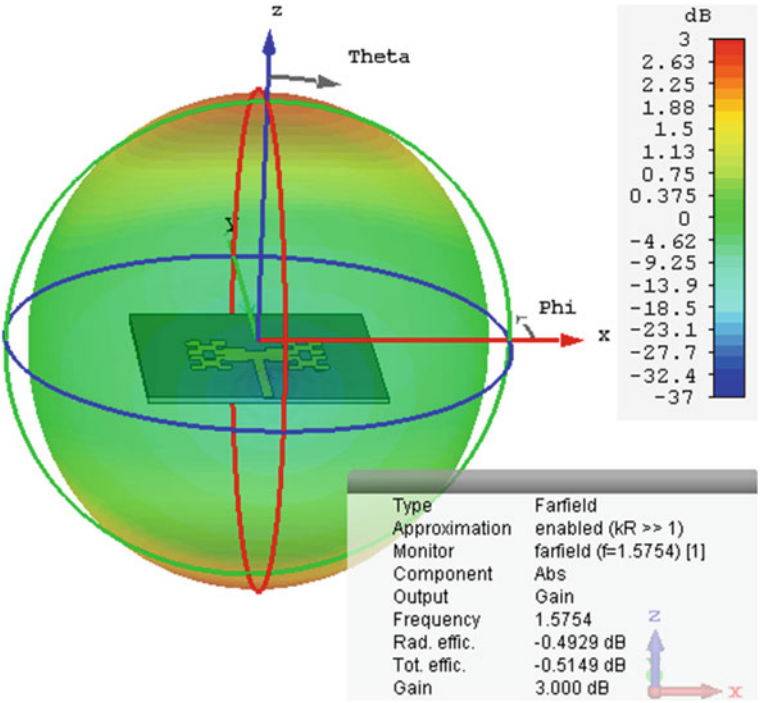

Fig. 5 Gain of planar fractal GPS antenna using Cu patch

The gain and directivity obtained at 1.5754 GHz are 3 dB and 3.493dBi, respectively. The summary of the performance parameters is given in Table 2.

Table 2 Performance parameters of fractal GPS antenna using Cu patch

Frequency	1.5754 GHz
Return loss	– 22.96 dB
Realized gain	3 dB
Directivity	3.493 dBi

3.2 Design and Analysis of Fractal Antenna using PEDOT Patch

The second MPA has been designed using PEDOT as patch. The bulk conductivity level of the PEDOT patch is 9532 S/m and its thickness is 0.018 mm. The antenna is designed to operate in the 1.5754 GHz region. The results show that a microstrip antenna with PEDOT as the patch provides a gain of 5.35 dB at 1.5754 GHz as against 3 dB for the copper patch at 1.5754 GHz.

3.2.1 Simulation of Fractal GPS Antenna using PEDOT Patch

The designed fractal GPS antenna using PEDOT patch is simulated and its characteristics are studied. The characteristics like return loss, bandwidth, gain and directivity are analyzed.

From Figs. 6 and 7 the performance of designed patch antenna can be analyzed. From Fig. 6 it is observed that the designed antenna gives a return loss of –16.84 dB at a resonating frequency of 1.5754 GHz.

The gain and directivity obtained at 1.5754 GHz are 5.356 dB and 6.977 dBi, respectively. The summary of the performance parameters is given in Table 3.

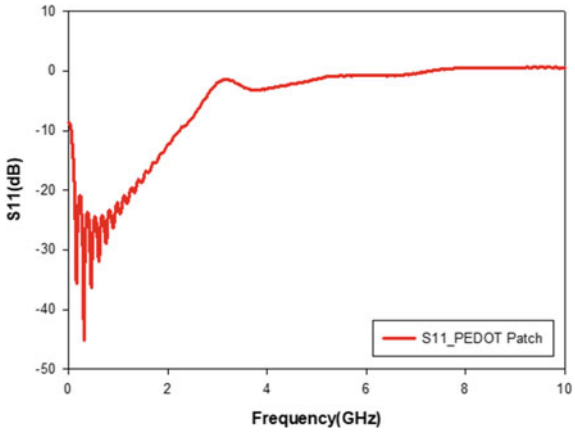

Fig. 6 Return loss characteristics of planar fractal GPS antenna using PEDOT patch

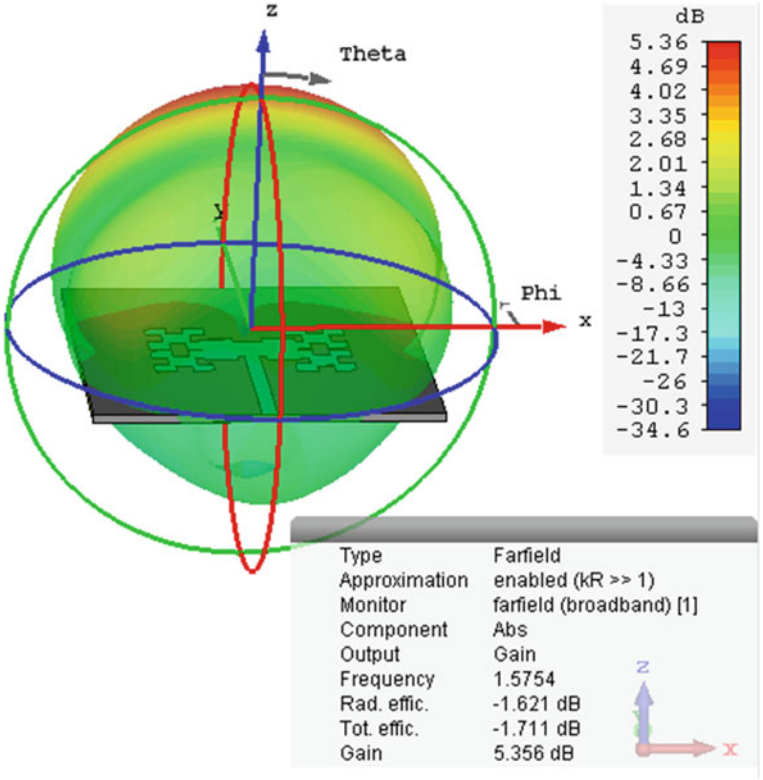

Fig. 7 Gain of planar fractal GPS antenna using PEDOT patch

Table 3 Performance parameters of fractal GPS antenna using PEDOT patch

Frequency	1.5754 GHz
Return loss	– 16.84 dB
Realized gain	5.356 dB
Directivity	6.97 dBi

3.3 Design and Analysis of Fractal Antenna using Polypyrrole Patch

The third MPA has been designed using Polypyrrole (PPy) as patch. The bulk conductivity level of the PPy patch is 2000 S/m and its thickness is 0.018 mm. The antenna is designed to operate in the 6.67 GHz region. The results show that a microstrip antenna with PPy as the patch provides a gain of 5.31 dB at 6.67 GHz.

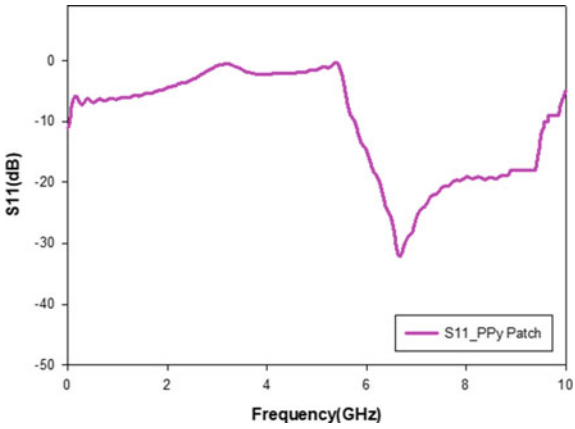

Fig. 8 Return loss characteristics of planar fractal GPS antenna using PPy patch

3.3.1 Simulation of Planar Fractal GPS Antenna using Polypyrrole Patch

The designed fractal GPS antenna using Cu patch is simulated and its characteristics are studied. The characteristics like return loss, bandwidth, gain and directivity are analyzed.

From Figs. 8 and 9, the performance of designed patch antenna can be analyzed. From Fig. 8, it is observed that the designed antenna gives a return loss of –32 dB at a resonating frequency of 6.67 GHz.

The gain and directivity obtained at 6.67 GHz are 5.310 dB and 9.152 dBi, respectively. The summary of the performance parameters is given in Table 4.

3.4 Comparison of Fractal GPS Antennas using Materials

For the comparison of three microstrip patch antenna, these antennas on identically thicker (1.6 mm) FR4 substrate with Cu, PEDOT and PPy patches have been simulated under the same conditions in FEM-based software.

Figure 10 shows the comparison simulation result of the return loss of the fractal GPS planar and conformal antennas.

A comparison study of these three antennas for an operating frequency of 1.574 GHz was carried out and represented in tabular form in Table 5. It can be observed from tabular data that at 1.5754 GHz frequency antenna with Cu patch is having a gain of 3 dB and a directivity of 3.493 dBi while PEDOT patch antenna provided 5.356 dB gain and 6.977 dBi directivity. On the other hand, PPy patch antenna showed a gain of 5.310 dB with 9.152 dBi directivity at a frequency of 6.67 GHz. From these observations, it can be inferred that the performance characteristics of the antenna with PEDOT patch become a better alternative for conventional antennas.

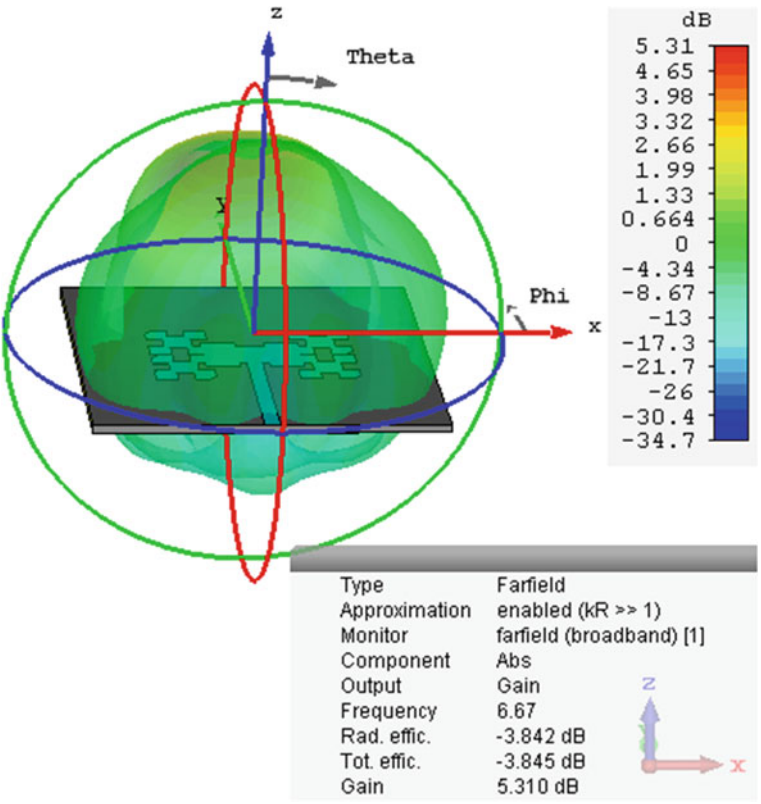

Fig. 9 Gain of planar fractal GPS antenna using PPy patch

Table 4 Performance parameters of fractal GPS antenna using PPy patch

Frequency	6.67 GHz
Return loss	– 32 dB
Realized gain	5.310 dB
Directivity	9.152 dBi

4 Conclusion

In this chapter, a GPS fractal antenna made from a PEDOT polymer and a PPy conductor with patches on FR4 substrate have been modelled. A reference structure with copper patch has also been designed for the comparative analysis. The performance of CP-based microstrip patch antennas at 1.5754 GHz was compared with an equivalent Cu patch antenna. It shows that the proposed structures of PEDOT patch on FR4 substrate have analogous applications to copper patch in microwave applications. However, the MPA with PPy patch design showed a change in the frequency

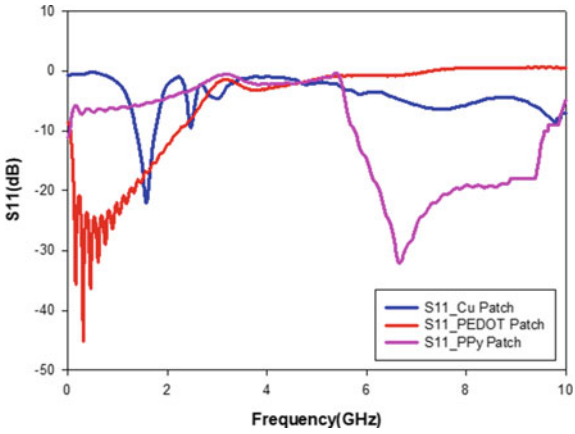

Fig. 10 Return loss characteristics Comparison of planar fractal GPS antenna using Cu, PEDOT and PPy patches

Table 5 Comparative analysis of fractal GPS antennas

Antenna performance parameters	Results		
	Cu_Ground plane	PEDOT_Ground plane	PPy_Ground plane
Operating frequency (GHz)	1.5754	1.5754	6.67
Return loss (dB)	– 22.96	– 16.84	– 32.07
Gain (dB)	3	5.356	5.310
Directivity (dBi)	3.493	6.977	9.152
Impedance (Ω)	50	50	50
VSWR	1.15313	1.33	1.05

band. In this way, the use of PEDOT patch can bring a new era of advancements in antenna designing. From the comparison between three designs, it can be easily concluded that PEDOT and PPy material gives a good competition to copper with the comparative values for gain and return loss, respectively. This structure in future can be used as a resonant one in antenna deployment. The array design of PEDOT and PPy MPAs results in high directivity and radiation intensity. Conducting polymers have now become an area of interest for researchers to obtain much better results for electronics communication system.

Acknowledgements The author (Ms Laya Varghese, MTech, CUSAT) acknowledges Prof. C K Aanandan, Professor, Department of Electronics, CUSAT, Kochi, for providing the facility for simulation and measurement.

References

1. Murad NA, Esa M, Yusof SK, Fisaf N (2003) Fractal patch antenna for GPS application. In: Student conference on research and development (SCOReD) Proceedings, pp 102–104
2. Kaufmann T, Shepherd R, Fumeaux C (2012) Modeling conductive polymer antennas in the microwave region. In: IEEE international conference on wireless information technology and systems (ICWITS)
3. Solberg RF, Siemsen PJ (1999) Development of a conductive polymer composite direction finding antenna. Antennas Propag Soc Int Symp 3:1966–1969
4. Cichos S, Haberland J, Reichl H (2002) Performance analysis of polymer based antenna-coils for RFID. In: Conference on polytronic
5. Rmili H, Miane JL, Zangar H, Olinga T (2006) Design of Microstrip fed proximity-coupled conducting polymer patch antenna. Microw Opt Technol Lett 48:655–660
6. Guerchouche K, Rolland N, Loyez C (2012) A folded compact antenna for broadband RFID UHF application. In: Conference on antenna measurements applications (CAMA), pp 1–4
7. Guerchouche K, Herth E, Calvet LE, Roland N, Loyez C (2017) Conductive polymer based antenna for wireless green sensors applications. Microelectron Eng
8. Krzysztofik W, Nartowski L (2015) Modified minkowski fractal patch antenna for multiband GPS receiver. In: 9th European conference on antennas and propagation (EuCAP)
9. Balanis CA (1982) Theory analysis and design, harper and row. New York. ISBN 8126508191
10. Caoand TN, Krzysztofik WJ (2016) Hybrid minkowski fractal island antenna operating in two bands of GPS satellite system. IEEE Int Symp Antennas Propag 211–212
11. Krzysztofik WJ (2009) Modified Sierpinski fractal monopole for ISM-bands handset applications. IEEE Trans Antennas Propag 57(3):606–615
12. Rmili H, El Mrabet O, Floc'h JM Mian JL (2007) Study of an electrochemically-deposited 3-d random fractal tree-monopole antenna. IEEE Trans Antennas Propag 55(4):1045–1050
13. Garg C, Kaur M (2014) A review of defected ground structure (DGS) in microwave design. Int J Innov Res Electr Electron Instrum Control Eng 2(3):1285–1290. ISSN 2321–2004
14. Vinoy KJ, Abraham JK, Varadan VK (2012) A Koch-like sided fractal bow-tie dipole antenna. IEEE Trans Antennas Propag 60(5)

Chapter 8
Metamaterial Resonator Antennas

Sandeep Kumar and Runa Kumari

1 Introduction

Metamaterials (MTMs) are the synthetic materials engineered to have electromagnetic properties that are not usually found in nature. They may have negative values of permittivity or permeability or both of these over a specific range of frequencies. There are two types of metamaterials: single-negative (SNG) and double-negative (DNG) metamaterials. An SNG metamaterial has either negative permittivity or negative permeability. Accordingly, it is named as epsilon-negative (ENG) or mu-negative (MNG) metamaterial. The DNG metamaterial possesses simultaneous negative values of permittivity and permeability. Such a material has a negative value of refractive index and termed as negative-index metamaterial (NIM). When a plane electromagnetic wave passes through a DNG material, the Poynting vector is antiparallel to wave vector leading to backward wave propagation, which is known as the left-handed material (LHM) in contrast to the conventional right-handed material (RHM) for which Poynting vector and wave vector point in the same direction.

In the 1960s, Veselago [1] theoretically found that when light falls at the interface between two materials one having positive refractive index and other having negative refractive index, it gets refracted in reverse (negative) direction as shown in Fig. 1. Such an extraordinary material having a negative refractive index with simultaneous negative values of permeability and permittivity was termed as NIM or DNG material.

In 1999, Pendry et al. [2] designed a periodic medium by combining a number of split-ring resonators (SRRs) with a strong magnetic coupling between them. When a time-varying magnetic field was applied parallel to the axis of the SRRs, the medium was demonstrated to have a negative permeability.

S. Kumar (✉) · R. Kumari
BITS-Pilani Hyderabad Campus, Hyderabad, India
e-mail: skverma@hyderabad.bits-pilani.ac.in

R. Kumari and B. Choudhury (eds.), *Multiscale Modelling of Advanced Materials*,
Materials Horizons: From Nature to Nanomaterials,
https://doi.org/10.1007/978-981-15-2267-3_8

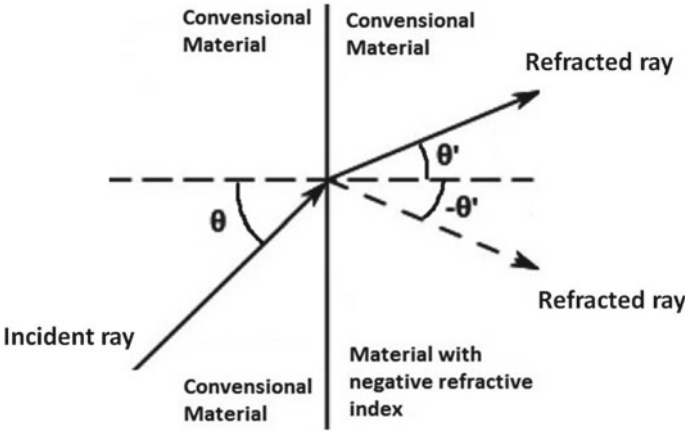

Fig. 1 Refraction of light at the interface of two media

In 2000, Smith et al. [3] proposed a medium of parallel thin metallic wires (radius ~ 0.8 mm) aligned in a direction parallel to the incident electric field, which could provide a negative permittivity. They combined their work with that of Pendry et al. [2] and came up with a composite medium (wire/SRR configuration) having simultaneous negative values of permittivity and permeability over a common frequency range which was the first experimental demonstration of a left-handed medium (LHM).

In 2002, a group of researchers came up with an idea of LC loaded transmission line (T/L) to overcome the narrow bandwidth limitation of wire/SRR configuration [4]. They designed a pure left-handed micro-strip T/L which is called as artificial T/L media in MTM literature. It added the advantages of being more compact, scalable, and tunable. The left-handed T/L along with its right-handed counterpart is shown in Fig. 2.

The class of antennas designed using MTMs is called MTM-based antennas. They are widely used in microwave devices, circuits, and antenna design applications due to their unique electromagnetic properties such as backward wave propagation and zero propagation constant [5, 6]. The MTM-based antennas can be divided into following two broad categories: leaky-wave antennas (LWAs) and MTM resonator type antennas. In LWAs, the guided power gradually leaks away in the form of radiation. They are designed using the MTMs having both positive and negative phase velocities that allow beam steering in forward as well as backward directions.

Such LWAs along with circular polarization feature are used for wireless applications under dynamic motion such as satellite communications. The MTM resonator antennas are the dispersion engineered antennas that can support negative-order, zeroth-order, and positive-order resonances. They are designed using MTM transmission lines and offer compact size with good radiation characteristics. They are further divided into following three categories:

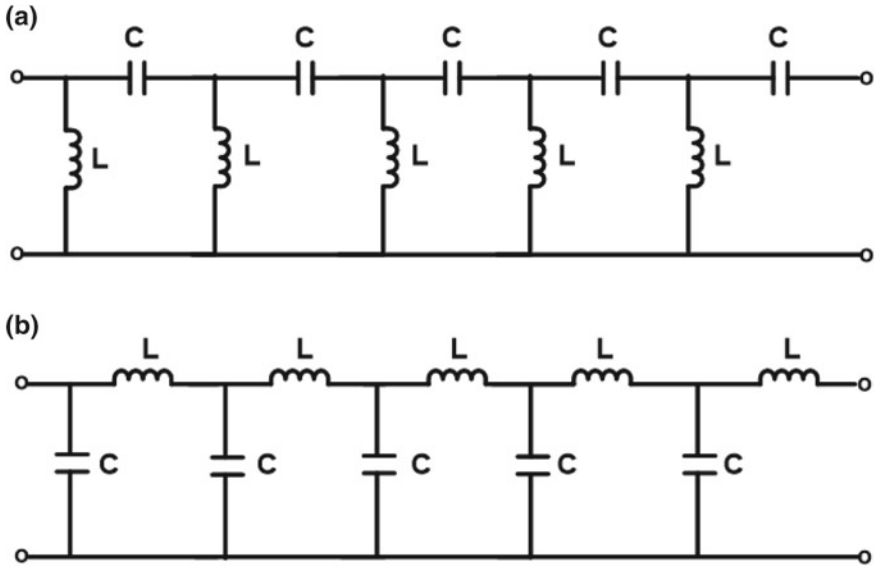

Fig. 2 **a** Pure left-handed T/L. **b** Pure right-handed T/L

(i) Composite right/left-handed transmission line (CRLH T/L)-based antennas
(ii) Epsilon-negative transmission line (ENG T/L)-based antennas
(iii) Mu-negative transmission line (MNG T/L)-based antennas.

In this chapter, all three types of MTM resonator antennas have been discussed.

2 CRLH T/L-Based MTM Antenna

This section deals with CRLH T/L theory followed by an antenna design example. The CRLH T/L theory will explain the basic unit cell structures, zeroth-order resonance (ZOR) condition, and simultaneous occurrence of negative and positive-order resonance modes. The antenna design part will describe the design and simulation of CRLH antenna along with reflection coefficient analysis to find the bandwidth response.

2.1 CRLH T/L Theory

The equivalent circuit models of symmetrical CRLH unit cells are shown in Fig. 3. Figure 3a shows the T-type model whereas the Fig. 3b shows the π-type model [7]. In both of these models, the series capacitor and shunt inductor contribute to left-handed

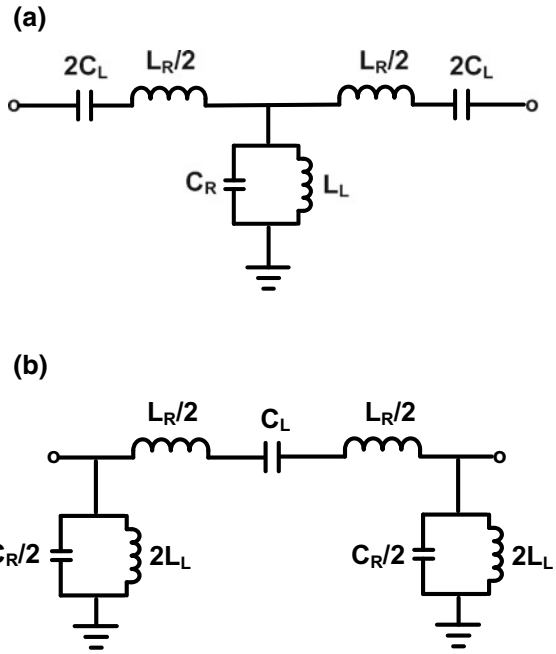

Fig. 3 Equivalent circuit models of symmetrical CRLH unit cells. **a** T-type model. **b** π-type model

property whereas the series inductor and shunt capacitor contribute to right-handed property. On applying Bloch Floquet theory [8] with periodic boundary conditions, the *T*-type and π-type unit cells become essentially identical, giving the same results. The dispersion relation of the unit cell is given by [7]:

$$\cos^{-1}\left(1-\frac{1}{2}\left(\frac{\omega_L^2}{\omega^2}+\frac{\omega^2}{\omega_R^2}-\frac{\omega_L^2}{\omega_{se}^2}-\frac{\omega_L^2}{\omega_{sh}^2}\right)\right)=\beta(\omega)\cdot d \tag{1}$$

where $\omega_L = \frac{1}{\sqrt{C_L L_L}}$, $\omega_R = \frac{1}{\sqrt{C_R L_R}}$, $\omega_{se} = \frac{1}{\sqrt{C_L L_R}}$, $\omega_{sh} = \frac{1}{\sqrt{C_R L_L}}$, β is the phase constant, and d is the length of a unit cell. From Eq. (1), two resonant frequencies are identified with zero phase constant (β) and a band-gap in between them. These are ω_{se} and ω_{sh}, respectively. They are called the ZOR frequencies. The band-gap vanishes if CRLH T/L is balanced (i.e., $\omega_{se} = \omega_{sh}$). Generally, only one particular ZOR is excited which depends upon the boundary conditions and the circuit parameter values. For an open-ended CRLH T/L, ZOR frequency is determined by ω_{sh}, whereas for the short-ended case, it is determined by ω_{se}.

If N unit cells are cascaded to make N-Stage CRLH T/L, then more than one resonance including negative-, zeroth-, and positive-order resonances are excited which can be located on the dispersion curve based on the following relationship [9]:

$$\beta_n d = \frac{n\pi}{N}\begin{cases} n = 0, \pm 1, \ldots, \pm(N-1) & \text{for T}-\text{type unit cell.} \\ n = 0, \pm 1, \ldots, \pm N & \text{for } \pi-\text{type unit cell.} \end{cases} \tag{2}$$

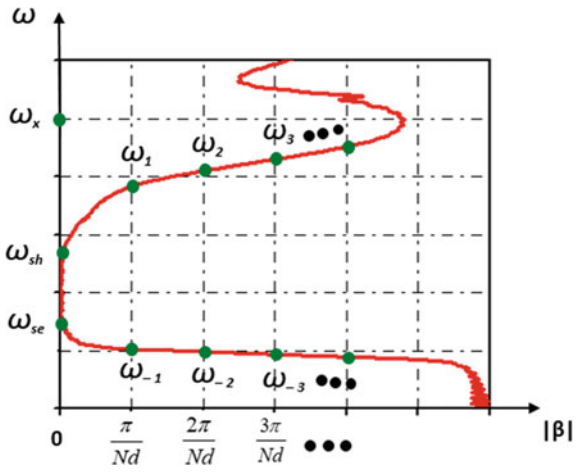

Fig. 4 Dispersion diagram of CRLH T/L

In Eq. (2), n is the resonance mode number. The dispersion diagram which indicates the locations of negative-, zeroth-, and positive-order resonances is shown in Fig. 4 [9].

In this figure, the ZOR frequency can be either ω_{se} or ω_{sh} depending upon the open-ended or short-ended boundary conditions, respectively. The frequency points indicated by positive subscripts (e.g., ω_1, ω_2, ω_3, etc.) are the positive-order resonances. Similarly, the frequency points indicated by negative subscripts (e.g., ω_{-1}, ω_{-2}, ω_{-3}, etc.) are the negative-order resonances.

The region with a frequency range from 0 to ω_{se} is called as the left-handed region whereas the region with frequency range from ω_{sh} to ω_x is called as the right-handed region.

2.2 CRLH Antenna Design

The antenna configuration is shown in Fig. 5 [10]. A coplanar waveguide (CPW) is used as a host transmission line with input impedance close to 50 Ω. The antenna consists of three unit cells of CRLH T/L. In each unit cell, the central feed line provides the series inductor, the interdigital gap provides the series capacitor, the meander line provides the shunt inductor, and the gap between central feed line and CPW ground plane provides the shunt capacitor. The CRLH antenna is designed on a single layer FR4 substrate having dielectric constant of 4.4, loss tangent of 0.025, and thickness of 1.6 mm. The CST Microwave Studio is used for antenna simulation.

The simulated reflection coefficient is shown in Fig. 6 [10]. From Fig. 6, it can be observed that the CRLH antenna provides negative-order, zeroth-order, and positive-order resonances. The simulated-10 dB impedance bandwidth is 1900 MHz (2.1–4 GHz) which covers zeroth-order resonance and first positive-order resonance at

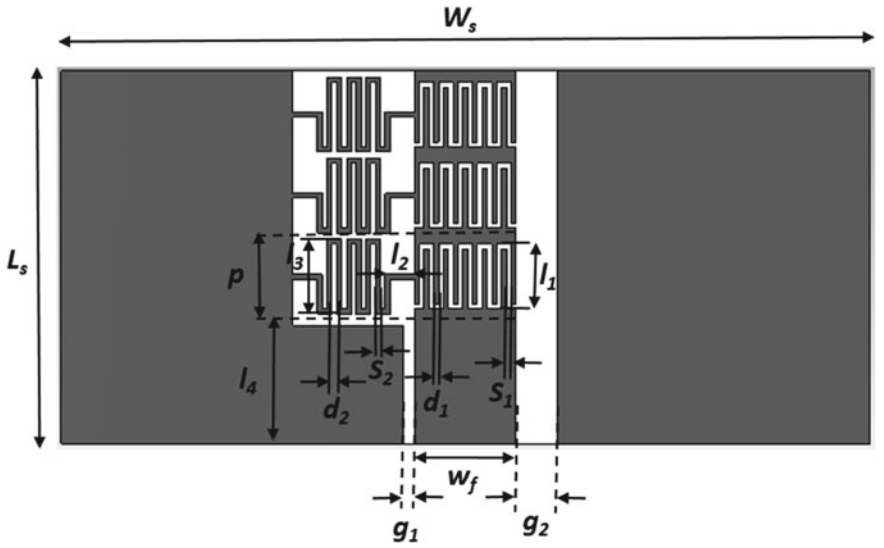

Fig. 5 Configuration of CRLH antenna ($L_s = 23$ mm, $W_s = 50$ mm, $w_f = 6.3$ mm, $g_1 = 0.7$ mm, $g_2 = 2.5$ mm, $l_1 = 4.0$ mm, $l_2 = 1.8$ mm, $l_3 = 4.6$ mm, $l_4 = 7.5$ mm, $p = 5$ mm, $d_1 = d_2 = 0.3$ mm, $S_1 = S_2 = 0.3$ mm)

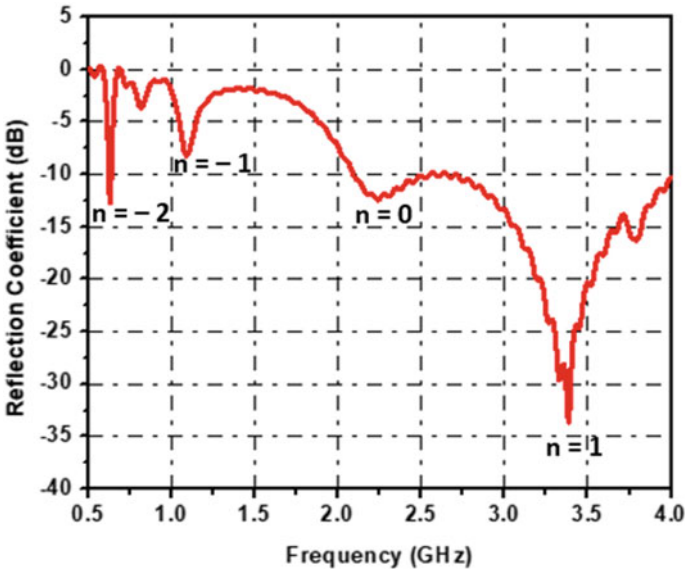

Fig. 6 Simulated reflection coefficient of CRLH antenna

2.25 GHz and 3.4 GHz, respectively. The CRLH antenna can be used in modern wireless communication systems such as LTE, WLAN, and WiMAX.

3 ENG T/L-Based MTM Antenna

This section deals with ENG T/L theory followed by an antenna design. The ENG T/L theory will explain the basic unit cell structure, zeroth-order resonance (ZOR) condition, and occurrence of the multiple resonances due to cascading of unit cells. The antenna design subsection will describe the design and simulation of three-unit cell ENG antenna. The reflection coefficient will be analyzed to find the bandwidth response.

3.1 ENG T/L Theory

The equivalent circuit of the unit cell of a ENG T/L is shown in Fig. 7 [11]. The shunt conductance (G) represents the losses and p is the length of unit cell. On applying Bloch Floquet theory with periodic boundary conditions, the dispersion relation is given by [11]:

$$\cos^{-1}\left(1 - \frac{\omega^2}{2\omega_R^2} + \frac{\omega_E^2}{2\omega_R^2}\right) = \beta(\omega) \cdot p \tag{3}$$

where $\omega_R = \frac{1}{\sqrt{C_R L_R}}$, $\omega_E = \frac{1}{\sqrt{C_R L_L}}$ and β is the phase constant.

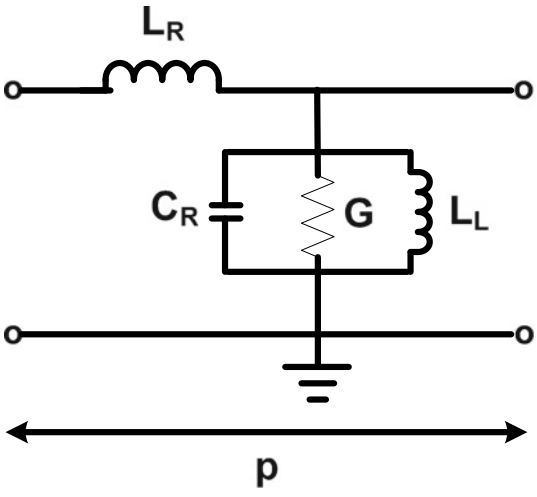

Fig. 7 Equivalent circuit model of ENG T/L unit cell

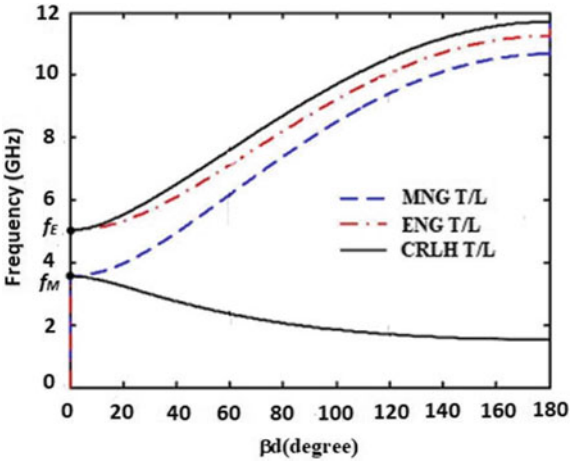

Fig. 8 Dispersion diagrams of metamaterial transmission lines

From Eq. (3), a resonant frequency can be identified with a zero-phase constant (β), which is referred as the ZOR frequency. In an ENG T/L, ZOR frequency is determined by the shunt admittance. So, it is always operated in open-ended condition and ZOR frequency is given by ω_E.

If N unit cells are cascaded to make N-Stage ENG T/L, more than one resonance including zeroth- and positive-order resonances can be excited which can be located on the dispersion curve based on the following relationship [11].

$$\beta_n p = \frac{n\pi}{N}, n = 0, 1, \ldots, (N-1), \tag{4}$$

The dispersion diagram for ENG T/L is shown in Fig. 8 [12]. From Fig. 8, it can be perceived that in low-frequency region (frequency less than f_E), ENG T/L provides a rejection band and in high-frequency region (frequency greater than f_E), it provides a right-handed pass-band. This is due to the negative effective permittivity in low-frequency band and positive effective permittivity in high-frequency band. The frequency point f_E is the transition point where the effective permittivity becomes zero. Therefore, f_E is called the ZOR frequency of ENG T/L.

3.2 ENG Antenna Design

The antenna configuration is shown in Fig. 9 with all dimensions in the figure caption [11]. An asymmetric coplanar waveguide (ACPW) is used as a host transmission line with input impedance close to 50 Ω. The antenna consists of three unit cells of ENG T/L. In each unit cell, the central feed line provides the series inductor, the meander line provides the shunt inductor, and the gap between central feed line and ACPW ground plane provides the shunt capacitor. The ENG antenna is designed on a single

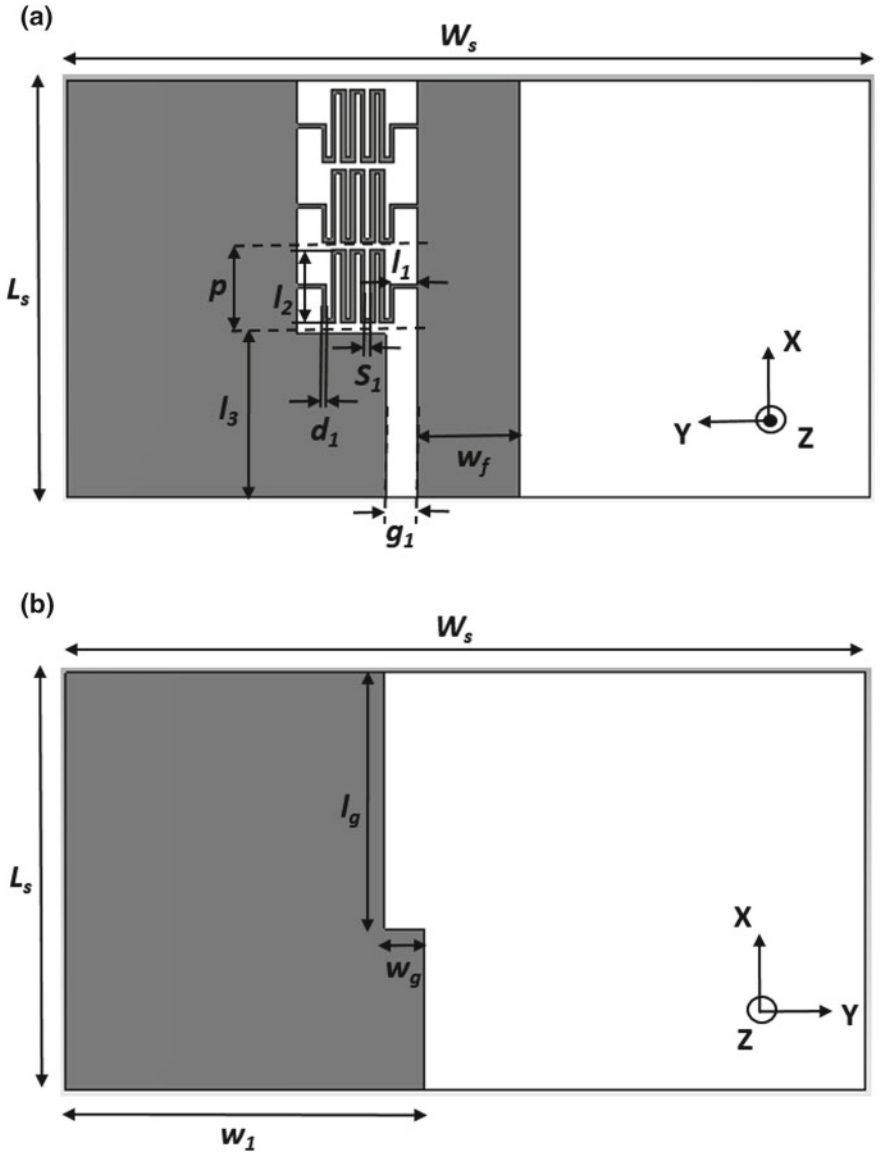

Fig. 9 Configuration of ENG antenna. **a** Top view. **b** Bottom view (All dimensions in mm: $L_s = 26$, $W_s = 50$, $w_f = 6.3$, $w_g = 2.6$, $w_1 = 22.45$, $g_1 = 2$, $g_2 = 0.6$, $l_1 = 1.8$, $l_2 = 4.6$, $l_3 = 10.5$, $l_g = 16$, $p = 5$, $d_1 = 0.3$, $S_1 = 0.3$)

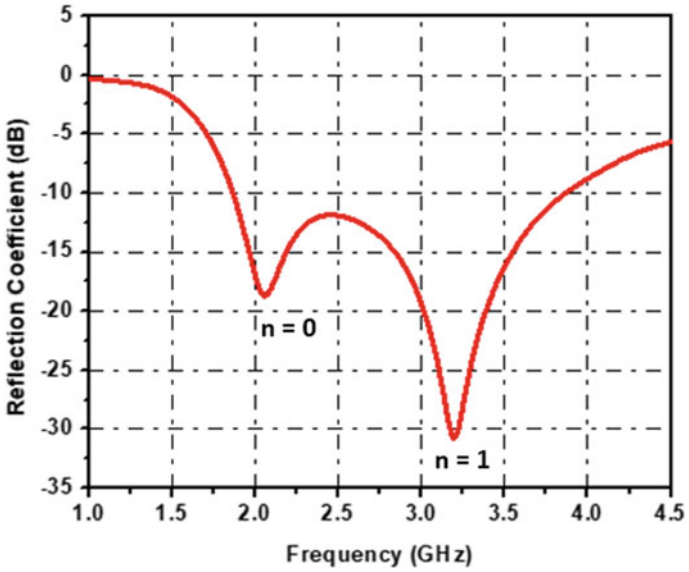

Fig. 10 Simulated reflection coefficient of ENG antenna

layer F4B2 substrate having dielectric constant of 2.65 and thickness of 1.6 mm. The CST Microwave Studio is used for antenna simulation. The simulated reflection coefficient of ENG antenna is shown in Fig. 10 [11].

From Fig. 10, it can be observed that the ENG antenna provides zeroth-order and positive-order resonances. The simulated-10 dB impedance bandwidth is 2000 MHz (1.8–3.8 GHz) which covers zeroth-order resonance and first positive-order resonance at 2.1 GHz and 3.25 GHz, respectively. The ENG antenna can be used for GSM, UMTS, LTE, WLAN, and WiMAX applications.

4 MNG T/L-Based MTM Antenna

This section deals with MNG T/L theory followed by an antenna design example. The MNG T/L theory will explain the basic unit cell structure, zeroth-order resonance (ZOR) condition, and occurrence of the multiple resonances due to cascading of unit cells. The antenna design part will describe the design and simulation of three-unit cell MNG antenna. The reflection coefficient will be analyzed to find the bandwidth response.

4.1 MNG T/L Theory

The equivalent circuit of the unit cell of a lossless MNG T/L is shown in Fig. 11 [12]. In this figure, L_R, C_L, and C_R are the per unit length series inductance, times unit length series capacitance, and per unit length shunt capacitance, respectively. The parameter d is the length of unit cell. On applying Bloch Floquet theory with periodic boundary conditions, the dispersion relation is given by [12]:

$$\cos^{-1}\left(1-\frac{\omega^2}{2\omega_R^2}+\frac{\omega_M^2}{2\omega_R^2}\right)=\beta(\omega)\cdot d \tag{5}$$

where $\omega_R=\frac{1}{\sqrt{C_R L_R}}$, $\omega_M=\frac{1}{\sqrt{L_R C_L}}$ and β is the phase constant.

Also, $C_L=C_L^{'}/d$, $C_R=C_R^{'}.d$ *and* $L_R=L_R^{'}\cdot d$.

From Eq. (5), a resonant frequency can be identified where the phase constant (β) will be zero. This is referred as the ZOR frequency. In an MNG T/L, ZOR frequency is determined by the series impedance. So, it is always operated in short-ended condition and ZOR frequency is given by ω_M. If N unit cells are cascaded to make N-Stage MNG T/L then, more than one resonance including zeroth- and positive-order resonances can be excited which can be located on the dispersion curve based on the following relationship [12]:

$$\beta_n d=\frac{n\pi}{N}, n=0,1,\ldots,(N-1), \tag{6}$$

The dispersion relation of MNG T/L is shown in Fig. 8 [12]. It can be seen that in low-frequency region (frequency less than f_M), the MNG T/L provides a rejection

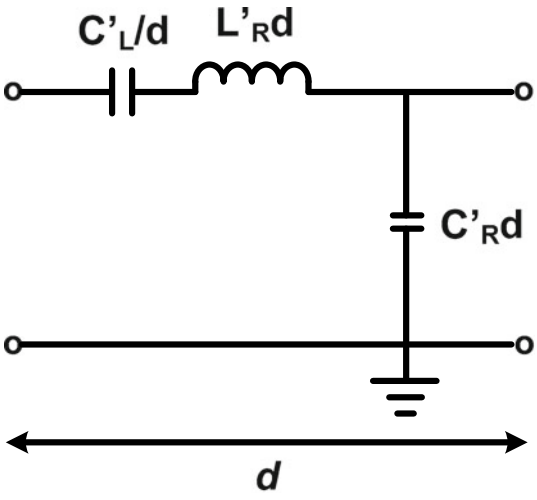

Fig. 11 Equivalent circuit model of MNG T/L unit cell

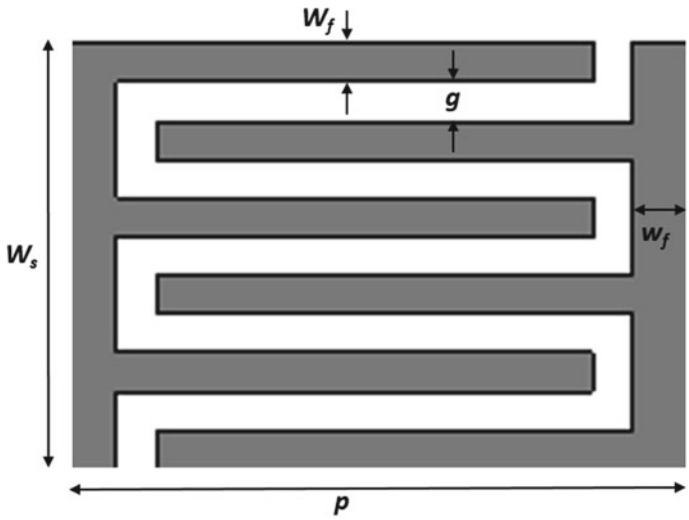

Fig. 12 Unit cell of MNG T/L ($g = 0.1$ mm, $w_f = 0.15$ mm, $p = 3$ mm)

band and in high-frequency region (frequency greater than f_M), it provides a right-handed pass-band. This is due to the negative effective permeability in low-frequency band and positive effective permeability in high-frequency band. The frequency point f_M is the transition point where the effective permeability becomes zero. Therefore, f_M is called the ZOR frequency of MNG T/L.

4.2 MNG Antenna Design

Figure 12 shows the MNG unit cell with all parameters in the caption [12]. The substrate used is double layered Rogers RT/Duroid 5880 with dielectric constant of 2.2 and thickness of 1.57 mm. In this unit cell, the patch on top side provides the series inductor, the interdigital gap provides the series capacitor, and the gap between top-sided patch and bottom-sided ground plane provides the shunt capacitor. Using this unit cell, an N-unit cell MNG antenna can be designed as shown in Fig. 13 [12]. In this antenna, both of the ends are connected to ground by using metallic vias to provide short-ended boundary conditions. A quarter-wave feed line is used at mu-zero resonance frequency to provide an efficient magnetic coupling. The software tool Ansoft's HFSS is used for the antenna simulation.

Figure 14 shows the simulated reflection coefficient for three-unit cell MNG antenna [12]. It is observed that the ZOR occurs at 7.5 GHz. The simulated-10 dB fractional bandwidth is found to be 450 MHz (7.25–7.7 GHz).

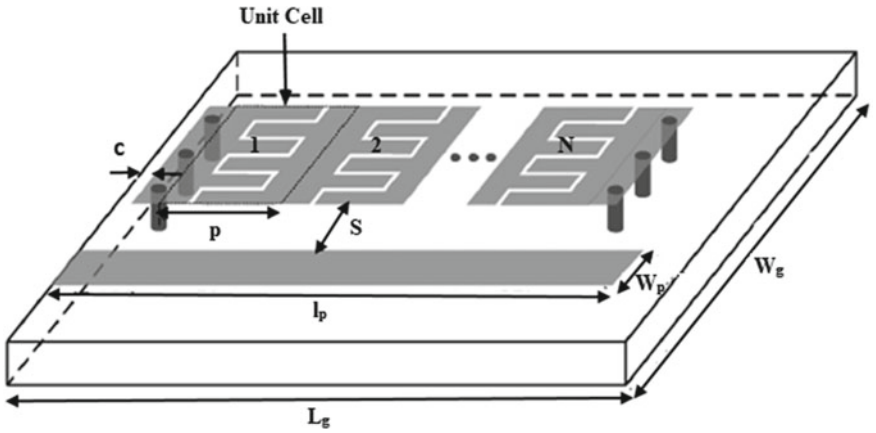

Fig. 13 Configuration of N-unit cell MNG antenna ($S = 2.5$ mm, $l_p = 7.9$ mm, $w_p = 1$ mm, $c = 0.55$ mm)

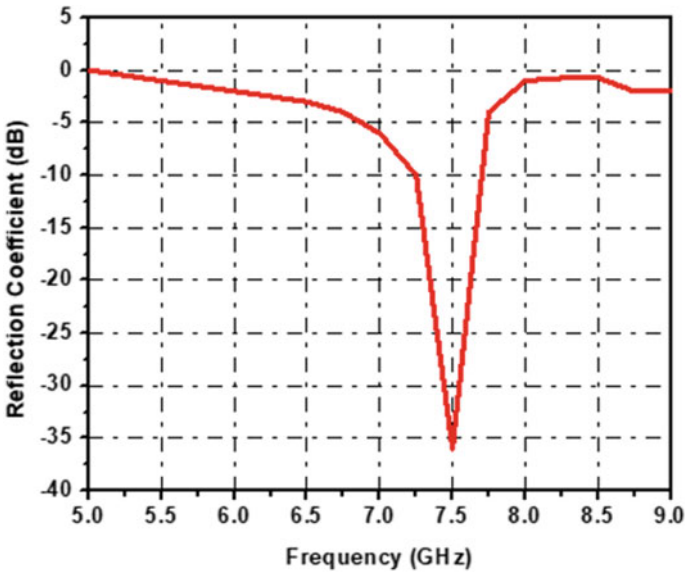

Fig. 14 Simulated reflection coefficient of three-unit cell MNG antenna

5 Conclusion

This chapter presents a comprehensive review of MTM resonator antennas. The theories and designs of various MTM resonator antennas have been described in detail. In theory part, the MTM unit cell structures, their mathematical analysis, and basic operating principles are discussed whereas the design part covers the specific

examples of MTM antennas. In these examples, all design aspects have been revealed along with the analysis of simulated reflection coefficients to find the bandwidth responses.

References

1. Veselago VG (1968) The electrodynamics of substances with simultaneously negative values of ϵ and μ. Sov Phys Uspekhi 10(4):509–514
2. Pendry JB, Holden AJ, Robbins DJ, Stewart WJ (1999) Magnetism from conductors and enhanced nonlinear phenomena. IEEE Trans Microw Theory Tech 47(11):2075–2084
3. Smith DR, Padilla WJ, Vier DC, Nemat-Nasser SC, Schultz S (2000) Composite medium with simultaneously negative permeability and permittivity. Phys Rev Lett 84(18):4184–4187
4. Ramo S, Whinnery JR, Duzer TV (1994) Fields and waves in communication electronics. Third edn. Wiley (1994)
5. Caloz C, Itoh T (2006) Electromagnetic metamaterials: transmission line theory and microwave applications. Wiley, pp 59–125
6. Lai A, Caloz C, Itoh T (2004) Composite right/left-handed transmission line metamaterials. IEEE Microw Mag 5:34–50
7. Dong Y, Itoh T (2012) Metamaterial-based antennas. Proc IEEE 100(7):2271–2285
8. Garcia PG, Alvarez JPF (2015) Floquet-bloch theory and its application to the dispersion curves of nonperiodic layered systems. In: Hindawi Publishing Corporation: mathematical problems in engineering, vol 2015, pp 1–12
9. Sanada A, Caloz C, Itoh T (2003) Novel zeroth-order resonance in composite right/left handed transmission line resonators. In: Asia-pacific microwave conference, vol 3, pp 1588–1591
10. Niu BJ, Feng QY (2013) Bandwidth enhancement of asymmetric coplanar waveguide (ACPW)-fed antenna based on composite right/left-handed transmission line. IEEE Antennas Wirel Propag Lett 12:563–566
11. Niu BJ, Feng QY, Shu PL (2013) Epsilon negative zeroth- and first-order resonant antennas with extended bandwidth and high efficiency. IEEE Trans Antennas Propag 61(12):5878–5884
12. Park JH, Ryu YH, Lee JH (2010) Mu-zero resonance antenna. IEEE Trans Antennas Propag 58(6):1865–1875

Chapter 9
Antenna Performance Enhancement using Metasurface

V. V. Akshaya and Balamati Choudhury

1 Introduction

Advanced materials can be defined as the materials that show superior performance over the conventional or traditional materials that have been utilized for the past hundreds of years. It includes all the novel materials that are realized by modifying the existing materials to yield certain superior characteristics for any particular application. The foremost contributor to the advanced materials domain is composites material. Composites are the combination of two or more constituent materials with different properties that show characteristics different from the individual components. Unlike in solid solutions and mixtures, the individual materials of the composites remain distinct in the final structure. The composite materials are heterogeneous in nature where the scatterers or inclusions are termed as guest and the environment to which the scatterers are placed is termed as host. Even period structures such as conventional photonic band gap (PBG), electromagnetic band-gap (EBG), frequency-selective surface (FSS) and metamaterials come under the composites. The electromagnetic behaviour of these periodic composite materials is quite confusing. Hence the composite material is divided into three characteristic regions depending on the frequency or wavelength as shown in Fig. 1 [1].

Region 1 in Fig. 1 corresponds to low frequencies where the wavelength is much larger than the periodicity of scatterers of the composite medium. These scatterers are positioned in a host matrix similar to molecules in a classical material and may not have a specific shape. To model certain electromagnetic behaviour, such man-made composites can be created and the effective material parameters can be obtained using classical mixing formulas.

Region 3 in Fig. 1 corresponds to high frequencies where the wavelength is comparable or smaller than the periodicity of scatterers of the composite medium. At high

V. V. Akshaya (✉) · B. Choudhury
Centre for Electromagnetics (CEM), CSIR-National Aerospace Laboratories (CSIR-NAL), Bangalore 560017, India

R. Kumari and B. Choudhury (eds.), *Multiscale Modelling of Advanced Materials*,
Materials Horizons: From Nature to Nanomaterials,
https://doi.org/10.1007/978-981-15-2267-3_9

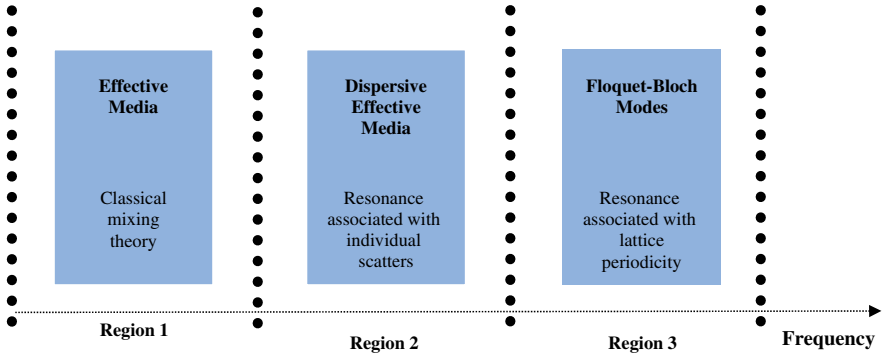

Fig. 1 Characteristics region of a composite material

frequencies, the electromagnetic behaviour analysis is more complex and Floquet–Bloch approach is utilized. Floquet–Bloch theorem provides a solution of Maxwell's equations for the wave propagation in a periodic structure, and the modes in the periodic medium are called as Floquet–Bloch modes. In the region, the higher order Floquet–Bloch modes are considered which interferes with fundamental wave. In this region the composite is called as photonic band gap or electromagnetic band-gap structures. These structures act like bandpass filter, which blocks the electromagnetic wave propagation in certain frequencies called stopband and allows wave propagation in passbands.

Region 2 in Fig. 1 corresponds to the region where wavelength is still larger compared to the structure periodicity. Unlike the other regions, the individual scatterers in region 2 resonates themselves and it opens a new medium called metamaterials. These metamaterial exhibits unique behaviour that is not common in nature occurring materials. In this region also the composite behaves as an effective medium similar to Region 1, but with a frequency-dependent material parameters. This region occurrence is rare and the scatterer design is little complex. The scatterers have to be designed in such a way that it should resonate at a particular frequency below the higher order Floquet–Bloch modes region. Otherwise the resonance region will be pushed to Floquet–Bloch modes region and the behaviour cannot be described using effective-medium model.

1.1 Metamaterial

Metamaterials are artificially engineered materials, consisting of periodically patterned sub-wavelength inclusions, which shows an unusual and exotic behaviour at the designed frequency [1]. The word metamaterial was coined by Rodger M. Wasler, from the University of Texas. The root word '*meta*' is a Greek word, which means

beyond. In other words, the metamaterial implies the materials that behaves beyond the naturally occurring materials.

The most commonly used definition for metamaterial is given as '*A metamaterial is a macroscopic composite of periodic/non-periodic structure, whose function is due to both cellular architecture and chemical composition*' [2]. It indicates that the electromagnetic behaviour of the metamaterial is determined by material properties as well as structural dimensions. The unusual properties of the metamaterials are gained from the inclusion of structures rather than its composition. Since metamaterials are frequency dependent, the cellular size has to be maintained less than sub-wavelength. The control over its bulk material properties is generally achieved by suitable tailoring of dimensions and arrangement of microscopic inclusions, which in turn can lead towards realization of the macroscopic extraordinary electromagnetic properties. One of the most exciting properties is the ability to exhibit negative refractive index. Though the metamaterial science domain is relatively new, in 1968 itself Victor Veselago has predicted the doubly negative materials existence [3]. Metamaterials could exhibit unusual values of permittivity or permeability to the incident fields, which permits its potential applications such as superlens, invisibility cloaking and many other novel applications.

1.2 Metamaterial to Metasurface

Most of the materials exhibit similar electromagnetic behaviour in its two-dimensional form. The two-dimensional scatterer lattice in region 1, region 2 and region 3 corresponds to classical thin-film materials, metasurfaces and conventional frequency selective surfaces.

Although three-dimensional metamaterials are quite appealing for several electromagnetic applications, the design and fabrication of metamaterials are still challenging. Due to the remarkable thickness of bulk metamaterials, their realization is limited by some nanofabrication tools and techniques, which are generally better established in two-dimensional structures. Consequently, a great interest in two-dimensional patterned thin films has arisen in the metamaterial field. The interest was to extend the three-dimensional metamaterials to its two-dimensional scenarios by retaining their exotic properties. As a result, the two dimensional or planar metamaterials have been realized by placing electrically small scatters at the surface or interface, which results in surface version of metamaterial, termed as metasurfaces. Since these metasurfaces are the two-dimensional version of the bulk metamaterials, it will take up less physical space. Hence, the transmission path in the materials can be reduced, besides it provides an alternative for loss reduction. If the phase continuities are fashioned in such a monolayer of metamaterial, where the reflected and refracted light flow can be manipulated completely, then an advanced control over electromagnetic wave propagation can be accomplished. Such ultrathin metamaterials offer a fascinating possibility of shaping the outgoing light wavefront and

improves metamaterial capabilities. The two-dimensional version of metamaterial called metasurface finds its application in entire electromagnetic spectrum.

1.3 Metasurface

Originally metasurface was given a tag called metafilm, since those comprise of the surface distribution of tiny scatterers [4]. Even though metasurfaces are called as a single-layer metamaterials or a 2D-version of metamaterials, the physical thickness of the scatterers are not zero, but it should be maintained smaller than the wavelength in the surrounding medium [5].

The two important subclasses for the metasurface are metafilm and metascreen [1]. Metasurfaces with cermet topology as shown in Fig. 2 are called as metafilm and metasurfaces with fishnet structure as shown in Fig. 3 are called as metascreen. Other types of metasurfaces lie somewhere in between metascreen and metafilms. For instance, a parallel conducting wires grating behaves like a metafilm in the direction perpendicular to the wire axes and it behaves like a metascreen in the direction along axes.

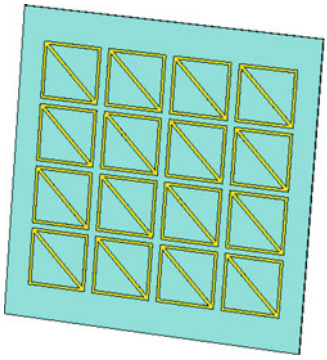

Fig. 2 A typical metafilm

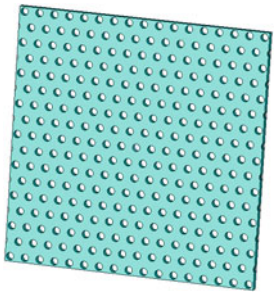

Fig. 3 A typical metascreen

Metasurfaces are recent research hotspot of metamaterials, since it reduces the fabrication challenges and significant losses in bulk metamaterials. Metasurface takes less space compared to three-dimensional metamaterials, and it offers low-lossy structures. Because of all these advantages the metamaterials have been replaced by metasurface in several applications such as controllable smart surfaces, novel waveguiding structures, miniaturized cavity resonators, compact wide-angle absorbers, impedance-matching surfaces, biomedical devices, etc. It is evident that the metasurface invention was a cross-cutting technology to the metamaterial field for several electromagnetic applications.

2 Challenges of Metasurface

Even though the metasurfaces are replacing the bulk metamaterials in various electromagnetic applications, the design and development of metasurfaces are still challenging. Several challenges in metasurface design and development are mentioned below.

- ***Materials issue***

Since the naturally occurring materials exhibit ordinary properties, a need for artificially engineered materials called metamaterials arose for various electromagnetic applications. These materials are capable of parading some extraordinary properties like negative values of permittivity and permeability. The planar version of these metamaterials called metasurfaces are also capable of exhibiting these unusual properties. The designer could engineer the material properties like dielectric constant and frequency of operation according to the desired applications. The challenging part is the selection of the materials to suit the design requirement.

- ***Design issues***

As previously mentioned in the introduction, metasurfaces are used for several electromagnetic applications from microwave to optical range of frequencies. These metasurfaces are sub-wavelength structures whose analysis are carried out using advanced electromagnetic concepts such as finite division time domain (FDTD), equivalent circuit analysis (ECA), etc. But currently no mathematical relationships are available in literatures for the prediction of metasurface resonant frequency as a function of its dimensions. Hence, the task of finding the exact dimension of the structures satisfying the desired frequency range is done in an iterative manner. As a result, metasurface designing is considered as cumbersome task.

- ***Fabrication issues***

Since metasurfaces are surface versions of 3D metamaterials, it deals with micro- and nano- featured patterns. The fabrication methods for such sub-wavelength features are seem to be very expensive. The two issues regarding the fabrication of metasurfaces are: (1) selection of suitable fabrication technique from the available

methods according to the desired application and frequency range of operation, and (2) alterations on fabrication technique in such a way to yield mass production in less cost. Most of the metasurface fabrication techniques are very expensive and require highly sophisticated equipments.

3 Antenna Performance Enhancement

The emerging wireless communication system targets on miniaturized terminal arrangements with high-performance antenna so as to maintain performance stability and link budget, which raises challenges on novel material antenna design technology. Recently, metamaterial finds several applications in electromagnetic devices, due to the ability of arbitrarily manipulating the electromagnetic wave propagation. Metamaterials with near-zero-index (NZM) have been employed to achieve high gain antennas with narrow operational bandwidth. Gradually, metasurface with sub-wavelength thickness also emerged for the antenna performance improvement. Metasurface with periodic patterns on dielectric substrate suspended above the planar antennas enhances the performance by maintaining advantages of planar antenna.

3.1 Gain and Bandwidth Enhancement

Planar patch antennas possess many attractive features like small size, low cost, low profile, easy fabrication, etc. But the major two drawbacks associated with patch antenna are narrow bandwidth and low gain, which limit its applications. Conventional method for improving gain is through the antenna array concept. But the array feeding mechanisms that encounter phase delays cause the whole structure more complicated and even lead signal losses. Another method to enhance antenna performance is by keeping a superstrate with high relative permittivity or permeability. It is also possible to place a partially reflective surface (PRS) on top of the metallic ground, which allows high directivity, but with narrow bandwidth. The spacing between ground and PRS is also a limiting factor for this approach. An alternative method for obtaining directive antenna is by using metamaterials as superstrate because of its unusual electromagnetic property. Instead of metamaterials, it is better to consider metasurfaces that take the mechanical advantages of ease of fabrication and requirement of less space compared to 3D metamaterial structures. The use of metasurface as superstrate results in reduction of mutual coupling along with increased gain and bandwidth.

Chaimool et al. (2010) designed a reflective metasurface as a superstrate for the gain and bandwidth enhancement of a microstrip patch antenna with centre frequency at 2.45 GHz [6]. A double split ring (DSR) resonator and double closed ring (DCR) resonators were considered as the unit cells for the analysis. Mu-near-zero metasurface and proximity electromagnetic (EM) coupling were employed for the gain and

bandwidth improvement, respectively. The maximum gain of the patch antenna has been increased from 2.31 to 9.16 dBi for DSR superstrate and to 9.77 dBi for DCR superstrate. Also the 3 dB bandwidth is extended from 60 to 130 MHz for DSR and to 320 MHz for DCR.

The out of phase emission from a normal patch antenna can also be compensated by using phase compensation metasurfaces. Chen et al. (2015) designed a phase compensation metasurface for improving impedance matching, bandwidth and gain of a microstrip patch antenna on the basis of Huygens principle [7]. The spherical-like phase profile of the patch antenna was compensated by the metasurface and an in-phase radiation has been produced. Side lobe suppression and squeezing of radiation pattern into narrow lobe resulted in the antenna gain improvement and bandwidth doubling. A comparison of patch antenna with and without the presence of metasurface was presented for performance enhancement analysis. The proposed antenna extends the application of patch antenna into the point to point wireless communication systems around a frequency of 5.7 GHz.

Nowadays, eco-friendly bio-based plastic materials find its application in microwave circuitry due to its durability. Islam et al. (2013) designed a metasurface as a superstrate for a dual-band microstrip patch antenna which resonate at 0.9 and 2.5 GHz [8]. The proposed antenna uses a ceramic-filled bio-plastic sandwich-material substrate that havs high permittivity for improving the operating bandwidth as well as gain. The loaded metasurface structure extended the operating bandwidth for both lower and upper band of patch antenna from 120 MHz to 170 MHz and from 370 MHz to 580 MHz, respectively. The gain has been improved in the lower band from 2.12 to 3.02 dBi and in the upper band from 4.10 to 5.28 dBi. The proposed design ends up with a more directive antenna pattern and it extends the application of the patch antenna to radio-frequency identification (RFID) and wireless local area network (WLAN).

3.2 Reconfigurable Antennas

Metasurfaces also find its application in reconfigurable antennas. Generally, the main three characteristics in antenna design are its frequency of operation, polarization and radiation pattern. If any of the fore-mentioned antenna characteristic S-parameters are made to reconfigure, it will result a move from multiple wireless standard integration into a single wireless platform.

Research works have been carried out for the reconfigurability of these antenna characteristics and the two general mechanisms used for reconfiguring are electrical and mechanical. Electrically reconfigurable antennas use PIN diode or varactor diode, which are biased using direct-current sources and biasing circuits. Biasing elements adversely affect the antenna parameters such as efficiency and radiation pattern. Even though electrically reconfigurable antennas are popular, the performance of antenna depends on the reliability of the electronic components used. Mechanically reconfigurable antennas usually achieve the reconfigurability by the adjustment of its

movable parts. The mechanical movements produced by the actuator makes the entire antenna structure bulkier. Since the actuator is very complicated and usually occupies more space, mechanical reconfigurable antennas are expensive and look bulky. The size or shape change is also a limitation for mechanically tunable antennas.

To overcome this, metasurfaces are used in the reconfigurable antenna design. Since metasurfaces are the two-dimensional equivalent of metamaterials with surface distribution of small scatterers, it makes mechanical movement easier. Due to the low cost and easy integration of metasurfaces with planar antennas, metasurface reconfigurable antenna is the best option.

Zhu et al. (2014) designed a tunable antenna called frequency reconfigurable metasurface antenna which is having a tuning range around 5 GHz [9]. This metasurface antenna includes a circular patch antenna that acts as a source antenna, above which the designed metasurface is placed. This arrangement makes the whole structure more compact. The metasurface simply tunes the resonant frequency without affecting the radiation pattern and polarization. Zhu et al. not only presents performance enhancement in terms of frequency reconfigurability but also considered parameters like efficiency realized gain and radiation pattern.

Zhu et al. (2014) designed a frequency reconfigurable slot antenna using metasurface comprising of various rectangular loop unit cells, which was kept above source antenna in direct contact to eliminate the air gap [10]. The paper also presented the observations on efficiency and radiation pattern. Instead of a bidirectional pattern, the simulated radiation showed a unidirectional pattern making the proposed antenna more directional.

Zhu et al. (2014) presented a novel design of compact and low profile polarization reconfigurable metasurface antenna [11]. The results showed that, by the metasurface rotation, the polarization of the metasurface antenna can be reconfigured to linear polarization, right-hand circular polarization as well as left-hand circular polarization. The polarization reconfigurable antenna performance is studied around the operating range of 3.5 GHz, since simulation results showed an axial ratio less than 3 dB from 3.3 to 3.7 GHz.

Zhu et al. (2015) presented the design and simulation of pattern reconfigurable metasurface antenna operating around 5.5 GHz [12]. The proposed antenna showed that continuous steering of the main beam can be achieved by rotating the planar metasurface above source antenna. Here metasurface acts as a refractor, that receives the radiation from the source antenna and re-radiates it to the other sides. Measured results showed that the peak realized gain of main beam reaches a value of 7.2 dBi with half power beam width of 50°.

3.3 Polarizer

Metasurfaces have the ability to manipulate electromagnetic waves and produce effects like polarization conversion, polarization rotation, wave re-direction, etc.

Metasurfaces can also be used as polarizer to convert linear polarization to circular polarization.

In circular polarization, the polarization plane is rotating in a corkscrew pattern, which completes one revolution in each wavelength. Depending on the propagation direction, circular polarization is of two types, right-hand circular polarization (RHCP), which follows a clockwise direction and left-hand circular polarization (LHCP), which follow a counterclockwise direction. Circular polarizations have some advantages over linear polarizations. Circular polarized signals are resistant to Faraday effect that are severe in low-frequency bands, so the interference or cross polarization is less concerned. Some atmospheric conditions cause signal degradation by signal rotation. Circular polarization resists such atmospheric conditions along with higher link reliability and allows easy installation. Circularly polarized antennas perform vital roles in RADAR, RFID, WLAN and satellite communication due to the signal reception stability and smashing mobility.

Huang et al. (2016) proposed an approach by using metasurface for the realization of a circular polarized slot antenna with high radiation gain and wide bandwidth [13]. The proposed metasurface consists of corner cut square patterns, whose cut size affects the axial ratio which changes the polarization nature. The parameter studies show the influence of patch size and unit cell spacing on axial ratio performance. The proposed metasurface and slot antenna have same ground plane so that the air gap in overall antenna structure that affects aerodynamic performance was eliminated.

Circular polarization (CP) conversions are designed based on patch antenna, slot antenna or dipole antenna. To make CP antennas more compact, even monopole antennas are proposed for polarization conversion. But the limitation faced by monopole based CP antenna was their low-gain performance. Cao et al. (2015) proposed high-gain circular polarized monopole antenna using metasurface [14]. Here, the metasurface acts as a reflector, which was placed at a sub-wavelength distance from the monopole radiators. This monopole CP antenna offers a lower backside radiation with an increased bore-sight gain from 5 to 6.92 dBi at 1.55 GHz. Hence the proposed antenna can be considered as a suitable candidate for Global Navigation Satellite System (GNSS).

Chen et al. (2015) designed a circular polarized metasurface antenna with wide axial ratio beamwidth and RCS reduction [15]. A dipole antenna was designed as a source antenna for reference. The metasurface unit cells were double head arrow resonator and the geometrical parameters were designed in such a way that the antenna should work in C-band especially for satellite communication. In C-band, the co-polarization reflection and cross-polarization reflections are maintained below −15 dB and 0 dB, respectively, to make efficient linear polarization conversion. On comparing with traditional dipole antenna, the proposed metasurface based dipole antenna showed a reduction in RCS of more than 7 dB throughout the entire operating range, which reveals its great possibilities in microwave application.

4 Metascreen-based Antenna

Planar patch antennas are the most versatile solutions to several systems that require a radiating element. Microstrip patch antennas are the most popular and adaptable antennas among the other printed antennas due to their salient features such as ease of integration, good radiation control and low cost of production. The two main drawbacks of patch antennas that would prohibit its use in variety of applications are narrow bandwidth and low gain.

Sections 4 and 5 discuss a possible solution to overcome these limitations. Two types of metasurfaces have been investigated, via metascreen and metafilm. In both the sections, a microstrip patch antenna is designed as a source antenna whose performance has to be improved. Then a metascreen and a metafilm are kept as superstrate at a particular distance above the designed patch antenna and the antenna characteristics like bandwidth and gain have been studied.

Section 4 discusses the design of metascreen-loaded patch antenna along with the simulation results and plots. As mentioned, patch antennas are not preferable in wide-band applications due to its narrow bandwidth characteristics; it is desirable to extend the applications by improving the operating bandwidth. This section includes the design and simulation of metascreen-loaded patch antenna to improve bandwidth without affecting the gain.

4.1 Design of Source Antenna

A microstrip patch antenna has been designed as a source antenna. A microstrip patch antenna consists of a patch, substrate and ground plane, where the patch and ground are on the opposite faces of the substrate as shown in Fig. 4. The patch and ground should be highly conducting material; hence copper is commonly used in designs. The patch design is made rectangular to yield easy analysis and simple calculations.

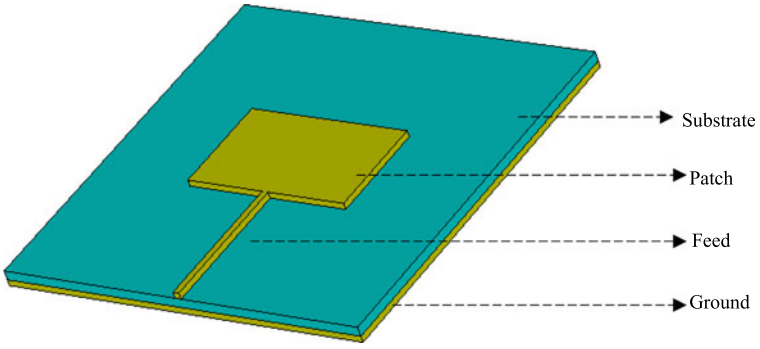

Fig. 4 Rectangular microstrip patch antenna

The fringing fields between this patch and ground are the reason behind the patch antenna radiations. The dimensions of the patch antenna can be determined using the design equations as given below.

Width of the patch:

Width of patch (W_p) that affects the antenna bandwidth is given by

$$W_p = \frac{c}{2f_r\sqrt{\frac{\varepsilon_r+1}{2}}} \tag{1}$$

where c is the velocity of light, f_r is the resonant frequency and ε_r is the dielectric constant of the substrate.

Effective dielectric constant of the patch antenna:

Effective dielectric constant ($\varepsilon_{\text{reff}}$) is calculated due to fringing fields effect outside the radiating patch

$$\varepsilon_{\text{reff}} = \frac{\varepsilon_r + 1}{2} + \frac{\varepsilon_r - 1}{2}\left(1 + \frac{12 \times h}{W_p}\right) \tag{2}$$

where h is the thickness of the substrate.

Actual length of the patch:

The patch appears longer than the actual length due to the effect of the fringing fields. Hence the actual length of the patch is considered by including the effect of fringing fields. The actual length of the patch (L_p) is given as

$$L_p = L_{\text{eff}} - (2 \times \Delta L) \tag{3}$$

where L_{eff} is the effective length of the patch given by

$$\mathrm{L}_{\text{eff}} = \frac{c}{2f_r\sqrt{\varepsilon_{\text{reff}}}} \tag{4}$$

$$\Delta L = 0.412h\left(\frac{\varepsilon_{\text{reff}} + 0.3}{\varepsilon_{\text{reff}} - 0.258}\right)\left(\frac{\frac{W_p}{h} + 0.264}{\frac{W_p}{h} + 0.8}\right) \tag{5}$$

Here, a patch antenna has been designed as a source antenna operating at 2.45 GHz. The substrate for the antenna design is taken as RT duroid of thickness 2.54 mm with dielectric constant 10.2 and loss tangent 0. 0023. According to the desired operating frequency, the length and width of the patch have been calculated as 18.6 mm and 25.9 mm, respectively. A microstrip feeding mechanism has been used in this design, which helps to maintain the planar structure of the antenna. This mechanism provides simplicity and ease of fabrication since the feed can also be etched on same substrate.

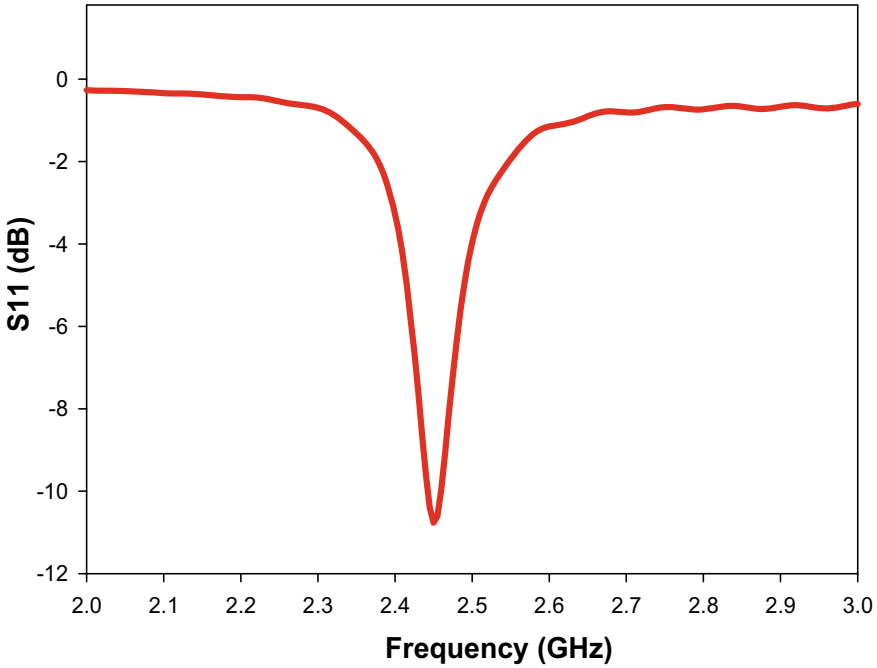

Fig. 5 Return loss characteristics of patch antenna

The designed microstrip patch antenna is simulated in CST Microwave Studio and the characteristics like return loss, 3-dB bandwidth, gain and directivity have been analyzed. Figure 5 shows the return loss characteristics and Fig. 6 shows the 3D-radiation pattern along with gain for the designed microstrip patch antenna.

The performance of the designed microstrip patch antenna has been analyzed from the above simulation results. Figure 5 shows that the designed antenna is resonating at 2.45 GHz with a return loss value of −10.76 dB and the 3 dB bandwidth is obtained as 120 MHz. The gain and directivity obtained at 2.45 GHz are 5.028 dB and 6.765 dBi, respectively. The summary of the performance parameters is given in Table 1.

4.2 Design of Metascreen-Loaded Antenna

A metascreen-loaded antenna is designed by placing a metascreen on the source antenna as a superstrate. The previously designed patch antenna is taken as the source antenna. The material considered for the metascreen superstrate is the same as of the patch antenna substrate to maintain a high dielectric constant. The metascreen superstrate is designed by implanting dielectric air cylinders of radius 1 mm on the material. The centre to centre distance between each air gap, called periodicity is

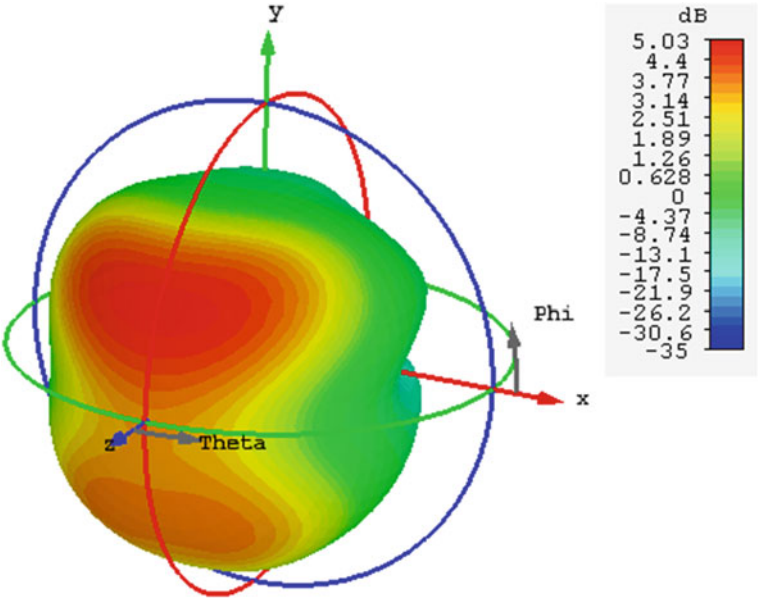

Fig. 6 3D-radiation pattern (gain) of patch antenna

Table 1 Performance parameters of microstrip patch antenna

Frequency	2.45 GHz
Return loss	−10.76 dB
Bandwidth	120 MHz
Realized gain	5.028 dB
Directivity	6.765 dBi

taken as 7 mm. This metascreen superstrate is placed at a distance of 12 mm above the antenna as shown in Fig. 7.

Fig. 7 Proposed metascreen-loaded patch antenna

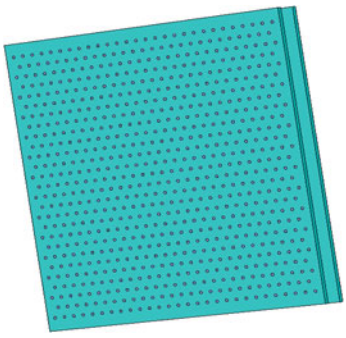

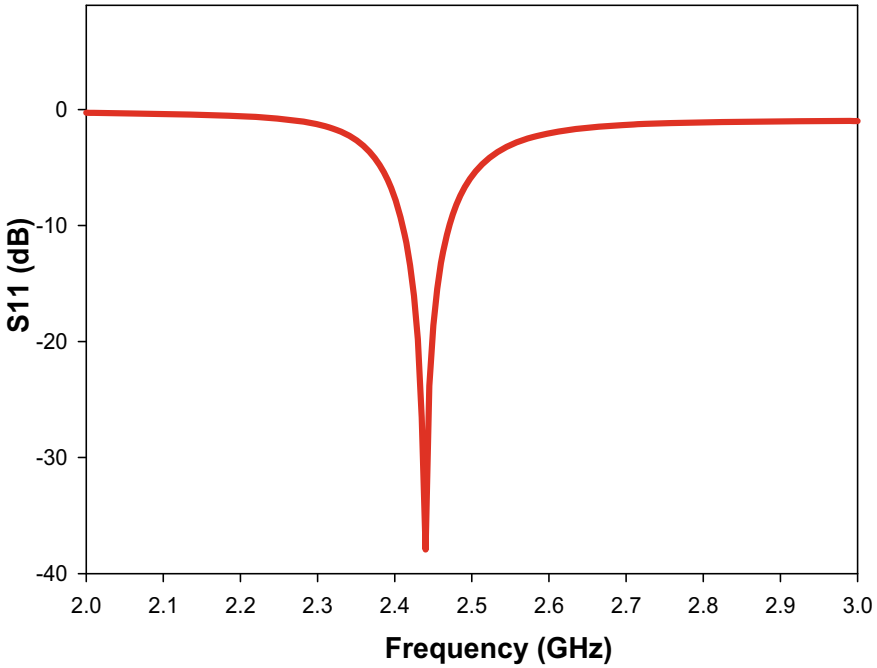

Fig. 8 Return loss characteristics of metascreen-loaded antenna

The designed metascreen-loaded microstrip patch antenna is simulated and the characteristics like return loss, bandwidth, gain and directivity are analyzed for observing the enhancements. Figure 8 shows the return loss characteristics and Fig. 9 shows the 3D-radiation pattern along with gain for the designed metascreen-loaded antenna.

Figure 8 shows that the resonant frequency of metascreen-loaded antenna is almost the same as that of the source antenna. The designed metascreen-loaded antenna is resonating at 2.44 GHz with a return loss value of −37.93 dB and the 3 dB bandwidth is obtained as 195 MHz. The gain and directivity obtained at 2.44 GHz are 5.511 dB and 6.229 dBi, respectively. The summary of the performance parameters is given in Table 2.

It has been found that the potential parameters of metascreen-loaded patch antenna has improved significantly in comparison to patch antenna alone. From Figs. 5 and 8, it is evident that the return loss is reduced from −10.76 to −37.93 dB at 2.45 GHz. The designed metascreen superstrate gives a 27.17 dB reduction in return loss characteristics at the resonating frequency. The 3-dB bandwidth is increased from 120 to 195 MHz, which showed a 75 MHz improvement in metascreen-loaded antenna. Hence, the designed metascreen structure acts as a superstrate on the source antenna to enhance the bandwidth without affecting its gain and directivity.

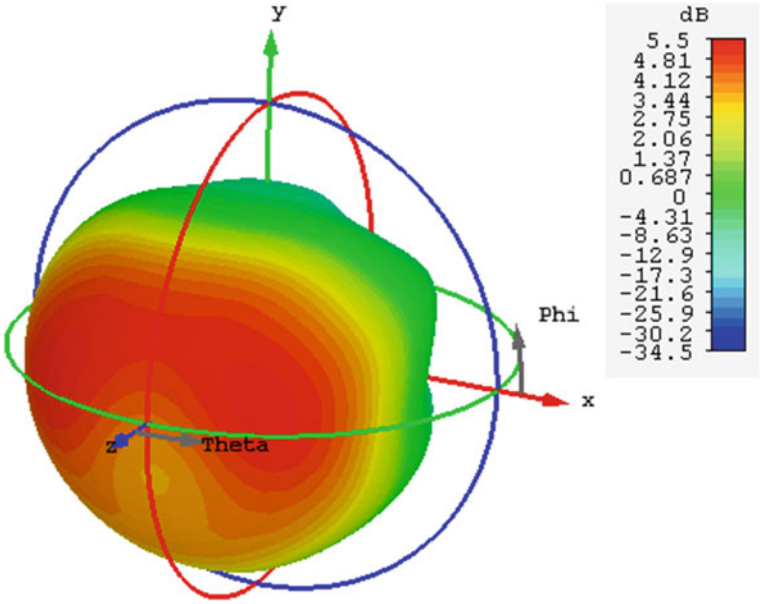

Fig. 9 3D-radiation pattern (gain) of metascreen-loaded antenna

Table 2 Performance parameters of metascreen-loaded antenna

Frequency	2.44 GHz
Return loss	−37.93 dB
Bandwidth	195 MHz
Realized gain	5.511 dB
Directivity	6.229 dBi

5 Metafilm-based Antenna

As previously mentioned, the two main drawbacks of microstrip patch antennas are low gain and narrow bandwidth. The gain being relatively insensitive to dielectric constant and thickness of substrate, several methods are in literatures to improve the gain. One of the methods involves the addition of a superstrate over the antenna. Section 5 discusses a method of using metafilm as a superstrate over the source antenna to enhance the performance. The proposed metafilm along with the source antenna is termed as metafilm-loaded antenna.

5.1 Design of Source Antenna

A microstrip patch antenna is designed as the source antenna by using the previous patch antenna design equations in Sect. 4. The source antenna is designed at 2.33 GHz on RT duriod substrate. The length and width of the patch have been calculated as 17 mm and 40 mm, respectively.

The designed microstrip patch antenna is simulated in CST Microwave Studio and the characteristics like return loss, 3-dB bandwidth, gain and directivity have been analyzed. Figure 10 shows the return loss characteristics and Fig. 11 shows the radiation pattern for the designed microstrip patch antenna.

Figure 10 shows that the designed microstrip patch antenna is resonating at 2.33 GHz with a return loss of −13.02 dB. The 3-dB bandwidth of the designed patch antenna is obtained as 95 MHz. The gain and directivity obtained at 2.33 GHz are 3.234 dB and 6.165 dBi, respectively. The summary of the performance parameters is given in Table 3.

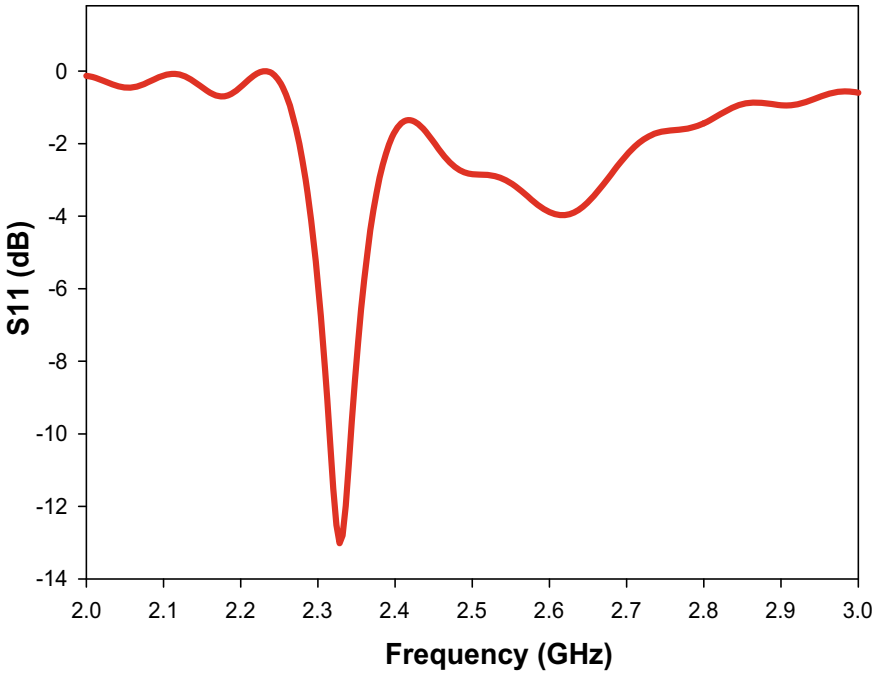

Fig. 10 Return loss characteristics of patch antenna

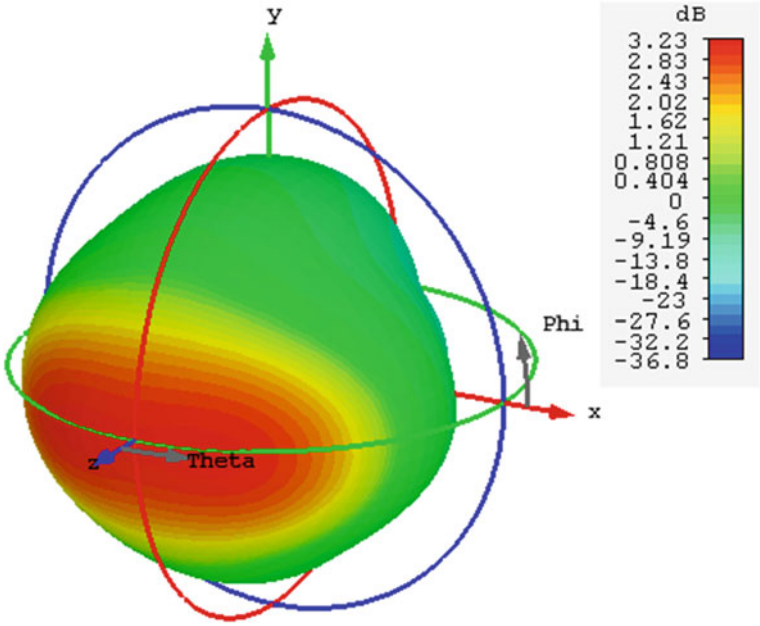

Fig. 11 3D-radiation pattern (gain) of patch antenna

Table 3 Performance parameters of microstrip patch antenna

Frequency	2.33 GHz
Return loss	−13.02 dB
Bandwidth	95 MHz
Realized gain	3.234 dB
Directivity	6.165 dBi

5.2 Design of Metafilm-Loaded Antenna

Metafilm-loaded antenna is designed by placing a metafilm above the source antenna as a superstrate. The characteristics of a metafilm are determined by the geometry and dimensions of the metafilm unit cell. The unit cell of the proposed metafilm superstrate consists of a rectangular loop with a diagonal strip as shown in Fig. 12. The length and width of the unit cell are 26 mm and 24 mm, respectively. The metallic ring width is 1 mm with a length of 23 mm and width of 22 mm. The base dielectric material of the metasurface is chosen same as antenna substrate.

The metafilm superstrate is designed by 16 such unit cells arranged in 4×4 layout. The superstrate is placed 10 mm above the source antenna as shown in Fig. 13.

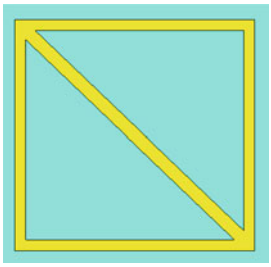

Fig. 12 Proposed metafilm unit cell

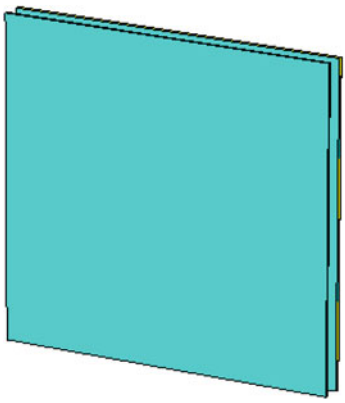

Fig. 13 Proposed metafilm-loaded patch antenna

The designed metafilm-loaded antenna is simulated and the characteristics like return loss, bandwidth, gain and directivity are analyzed for enhancement verification. Figure 14 shows the return loss characteristics and Fig. 15 shows the radiation pattern for the designed metafilm-loaded antenna.

Figure 14 shows that the metafilm-loaded antenna gives a return loss of −11.36 dB at the same frequency of 2.36 GHz. The 3 dB bandwidth of the microstrip patch antenna is obtained as 182 MHz. Figure 15 shows at 2.36 GHz the gain and directivity are obtained as 8.151 dB and 9.262 dBi, respectively. The summary of the performance parameters of metafilm-loaded antenna is given in Table 4.

It has been found that the metafilm-loaded antenna is performing better than the microstrip patch antenna alone. The gain improvement can be noted from Figs. 11 and 15. The realised gain is improved by 5 dB from 3.234 to 8.151 dB. The directivity is also improved from 6.165 to 9.262 dBi. The 3 dB bandwidth is increased from 95 to 182 MHz. There is an 87 MHz improvement in bandwidth. From all these simulated results it can be concluded that using metafilm as a superstrate over a source antenna can improve the characteristics such as bandwidth, gain and directivity with a small shift in the resonant frequency.

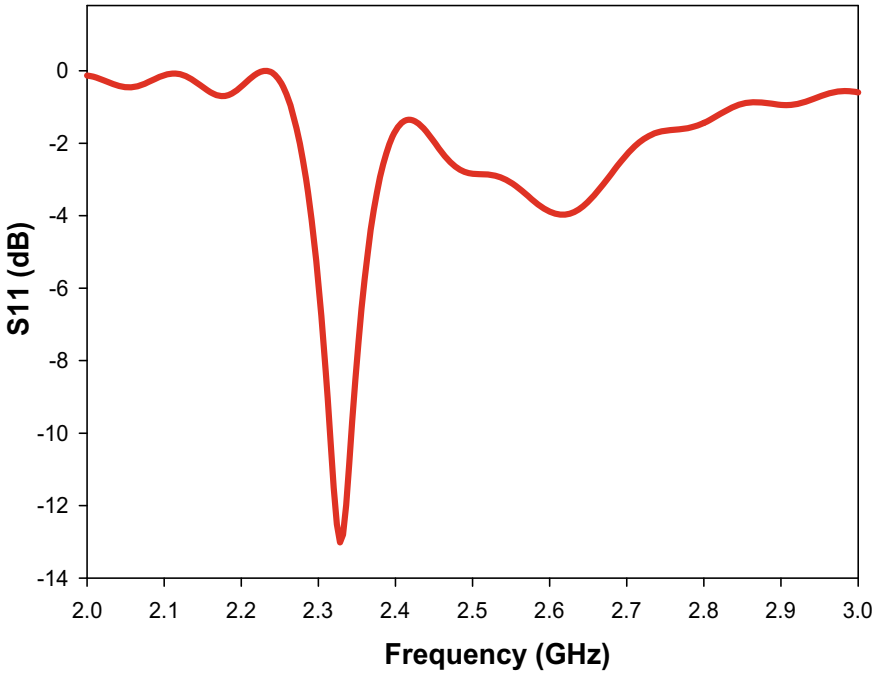

Fig. 14 Return loss characteristics of metafilm-loaded antenna

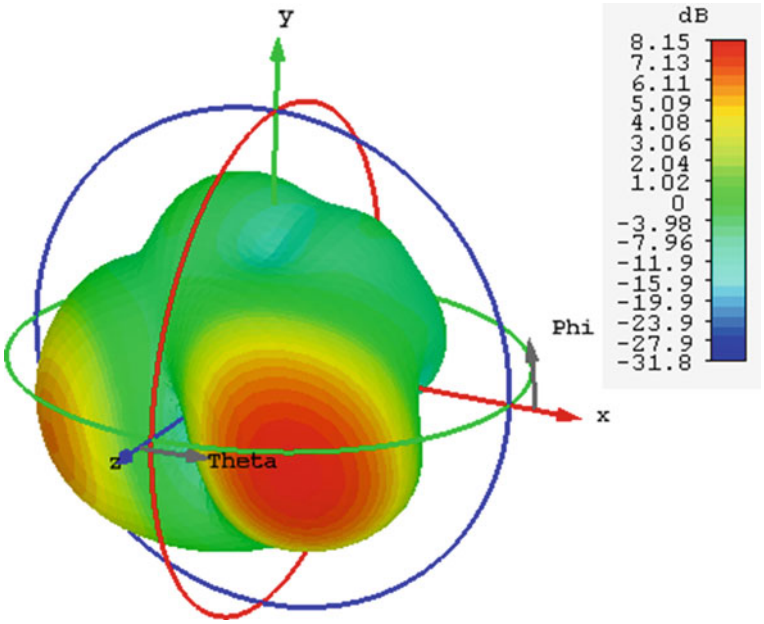

Fig. 15 3D-radiation pattern (gain) of metafilm-loaded antenna

Table 4 Performance parameters of metafilm antenna

Frequency	2.36 GHz
Return loss	−11.36 dB
Bandwidth	182 MHz
Realized gain	8.151 dB
Directivity	9.262 dBi

6 Conclusion

In this chapter, the possibility of metasurface has been explored for the application of antenna performance enhancement. Towards this, an extensive literature survey on the possible applications of the metasurface in the microwave regime has been carried out. It shows that currently there is a tremendous growth in the metasurface field in entire electromagnetic spectrum when compared to metamaterials. Several techniques for antenna performance enhancement have been studied from the available literatures.

A microstrip patch antenna has been designed as a source antenna for which the performance has to be improved. To retain the planar geometry of the entire antenna, superstrate technique has been chosen. Two different antennas are designed by placing two different superstrate such as metafilm and metascreen. The designed metasurfaces showed enhancement in antenna characteristics such as bandwidth and gain, at desired frequencies. The designed metascreen superstrate has improved the bandwidth of source antenna at 2.45 GHz by 75 MHz, without affecting the gain. The designed metafilm superstrate has improved both bandwidth and gain of the source antenna by 87 MHz and 5 dB at resonant frequency.

Acknowledgements The author (Ms Akshaya V V, MTech, CUSAT) acknowledges Prof. C K Aanandan, Professor, Department of Electronics, CUSAT, Kochi, for providing the facility for simulation and measurement.

References

1. Holloway CL, Kuester EF, Gordon JA, Hara JO, Booth J, Smith DR (2012) An overview of the theory and applications of metasurfaces: the two-dimensional equivalents of metamaterials. IEEE Antennas Propag Mag 10–35
2. Choudhury B (ed) (2017) Metamaterial inspired electromagnetic applications: role of intelligent systems. Springer, Singapore, p 226 (ISBN: 9789811038365)
3. Veselago VG (1968) The electromagnetic of substances with simultaneously negative values of eplison and mue. Sov Phys Usp 10:509–504
4. Kuester EF, Mohamed MA, Piket-May M, Holloway CL (2003) Averaged transition conditions for electromagnetic fields at a metafilm. IEEE Trans Antennas Propag 2641–2651
5. Holloway CL, Mohamed MA, Kuester EF, Dienstfrey A (2005) Reflection and transmission properties of a metafilm: with an application to a controllable surface composed of resonant particles. IEEE Trans Electromagn Compat 853–865

6. Chaimool S, Chung KL, Akkaraekthalin P (2010) Bandwidth and gain enhancement of microstrip patch antennas using reflective metasurfaces. IEICE Trans Commun E93:2496–2503
7. Chen K, Yang Z, Feng Y, Zhu B, Zhao J, Jiang T (2015) Improving microwave antenna gain and bandwidth with phase compensation metasurface. AIP Adv 067152 (1–8)
8. Islam MT, Ullah MH, Singh MJ, Faruque MRI (2013) A new metasurface superstrate structure for antenna performance enhancement. Materials 6:3226–3240
9. Zhu HL, Cheung SW, Cao YF, Yuk TI (2014) Frequency-reconfigurable antenna using metasurface. IEEE Trans Antenna Propag 62(1):80–88
10. Zhu HL, Cheung SW, Cao YF, Yuk TI (2014) Frequency reconfigurable slot antenna using metasurface. In: IEEE 8th European conference on antennas and propagation, pp 2575–2577
11. Zhu HL, Cheung SW, Yuk TI (2014) Design of polarization reconfigurable antenna using metasurface. IEEE Trans Antenna Propag 62(6):2891–2898
12. Zhu HL, Cheung SW, Yuk TI (2015) Mechanically pattern reconfigurable antenna using metasurfaces. IET Microwave Antennas Propag 9(12):1331–1336
13. Huang Y, Yang L, Li J, Wang Y, Wen G (2016) Polarization conversion of metasurface for the application of wide band low-profile circular polarization slot antenna. Appl Phys Lett 109:054101(1–5)
14. Cao YF, Cheung SW, Yuk TI, Zhu H (2015) High-gain circular polarization monopole antenna using MS for GNSS. IEEE Proc 1992–1993
15. Chen C, Li Z, Liu L, Xu J, Ning P, Xu B, Chen X, Gu C (2015) A circularly-polarized metasurfaced dipole antenna with wide axial-ratio beam width and RCS reduction functions. Prog Electromagnet Res 154:79–85

Chapter 10
Electromagnetic Bandgap Structures

R. Venkata Sravya and Runa Kumari

1 Introduction

In 1970s, Howell introduced Microstrip patch antenna. It is one of the most commonly used antennae in wireless communication, satellite communication, wearable applications and many more applications due to its properties like low weight, compact, low cost, conformal structure, easy integration with circuits, etc. Patch antenna has simple configuration designed with a substrate of dielectric constant, $\epsilon_r \geq 1$ with some height. While designing the patch antenna, the height of the substrate should have considered to be greater than $\lambda/4$ so that efficiency of antenna can be enhanced. To address the low gain issue of patch antenna, array antenna designs are proposed. In case of array antenna, the minimum required distance between any two array elements has to be $\lambda/2$. However, to design a compact antenna, the substrate height should be less than $\lambda/4$ and the distance between the array element is taken to be less than $\lambda/2$. As a result, surface waves are generated in substrate, which is added destructively with transmitting signal and degrade the performance of antenna [1].

To reduce the effects of the surface waves, different feeding techniques and different patch designs such as stacked patches, parasitic patches, proximity coupling, and patches with different slots like *U*-slot, *E*-shaped patch were proposed. In microwave circuits, the antenna is designed either with shorting pins, or different feeding techniques like *L*-probe, meandering microstrip line, or increasing the thickness of substrate to make it conformal and compact. These techniques have shortcomings such as it generates strong surface waves which result in back lobe radiation, reduced efficiency, low directivity and narrow bandwidth.

Another approach for designing a compact antenna with enhanced performance and efficiency is designing either substrate or ground with the electromagnetic

R. V. Sravya · R. Kumari (✉)
BITS-Pilani, Hyderabad, India
e-mail: runakumari@hyderabad.bits-pilani.ac.in

R. Kumari and B. Choudhury (eds.), *Multiscale Modelling of Advanced Materials*,
Materials Horizons: From Nature to Nanomaterials,
https://doi.org/10.1007/978-981-15-2267-3_10

bandgap structures (EBGs). The substrate with EBG structure addresses the problem of surface waves suppression, and it helps in providing an efficient low-profile antenna, gain enhancement, improved bandwidth and increased isolation for array antennas.

2 EBGs

Electromagnetic bandgap structures (EBGs) are arranged periodically or aperiodically to either assist or prevent the propagation of electromagnetic waves in a specific band of frequencies for all incident angles and all polarization states [2]. Usually, EBGs are arranged periodically and are used for preventing the surface waves in the substrate and coupling with ground plane. The behaviour of EBGs changes based on the incident electromagnetic waves like

i. When the incident wave is a surface wave ($k_x^2 + k_y^2 \leq k_0^2$, k_z is imaginary), EBGs show frequency bandgap which suppresses the propagation of surface waves as shown in Fig. 1b.
ii. When the incident wave is a plane wave ($k_x^2 + k_y^2 \leq k_0^2$, k_z is real value), EBGs show the property of perfect magnetic conductor (reflection phase is zero). This can be observed by plotting the reflection phase with respect to frequency of the structure as shown in Fig. 1c.

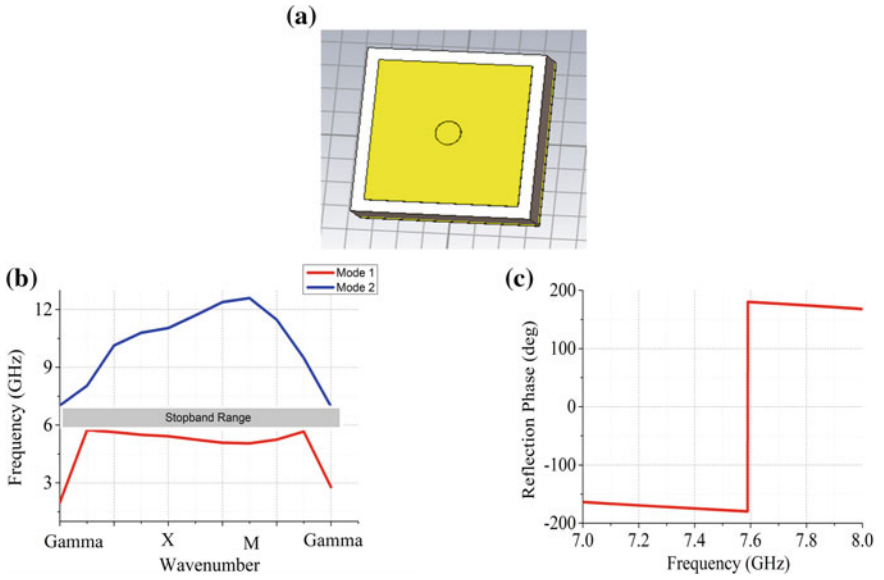

Fig. 1 **a** Unit cell of mushroom EBG ($W = 7$ mm, $g = 1$ mm, vias radius $= 1$ mm) **b** dispersion diagram **c** reflection phase

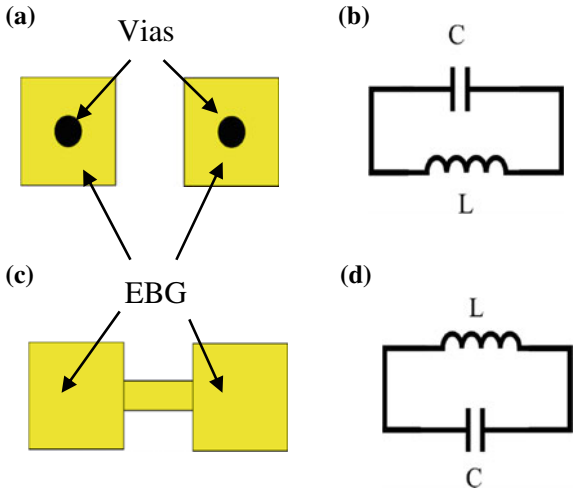

Fig. 2 **a** Mushroom EBG **b** equivalent circuit **c** uniplanar EBG **d** equivalent circuit

where k_x and k_y are wavenumbers in horizontal directions, k_z and k_0 are wave numbers in vertical direction and in free space, respectively.

The performance of EBGs can be analyzed using three different methods by using which the resonance frequency, stopband frequency range, reflection phase of EBG can be found out. They are

i. **Lumped Element Method**: Describes the EBG structure using the elements inductance '*L*', and capacitance '*C*'. Two examples of the EBG designs with their equivalent circuit are shown in Fig. 2.
ii. **Transmission Line Method**: The EBG is modelled as transmission line and the analysis is done by creating an array of the proposed EBG arranged on substrate with ground plane and a feed. The feed used can be either full length as shown in Fig. 3a or suspended as shown in Fig. 3b. The analysis can be done for the design by S_{11} and S_{21} plots. In Fig. 3c, S_{11} and S_{21} are plotted for an array of mushroom EBG where S_{11} specifies the resonant frequencies and S_{21} specifies the stopband range. For both types of feed line, i.e. either for full length or suspended, the plots of S_{11} and S_{21} are similar.
iii. **Full Wave Analysis Method**: A unit cell of the EBG is designed and analyzed using numerical methods such as method of moments (MoM), finite-element method (FEM) and finite difference time domain (FDTD). These numerical methods work on computational concepts and hence have the advantage like versatility and accuracy in analyzing EBG. It is also easier to get details like surface impedance, reflection phase and dispersion diagram. Unit cell analysis for a mushroom EBG is shown in Fig. 1.

Based on the geometric configuration, EBGs can be categorized as

i. Three-dimensional EBG
ii. Two-dimensional EBG
iii. One-dimensional EBG.

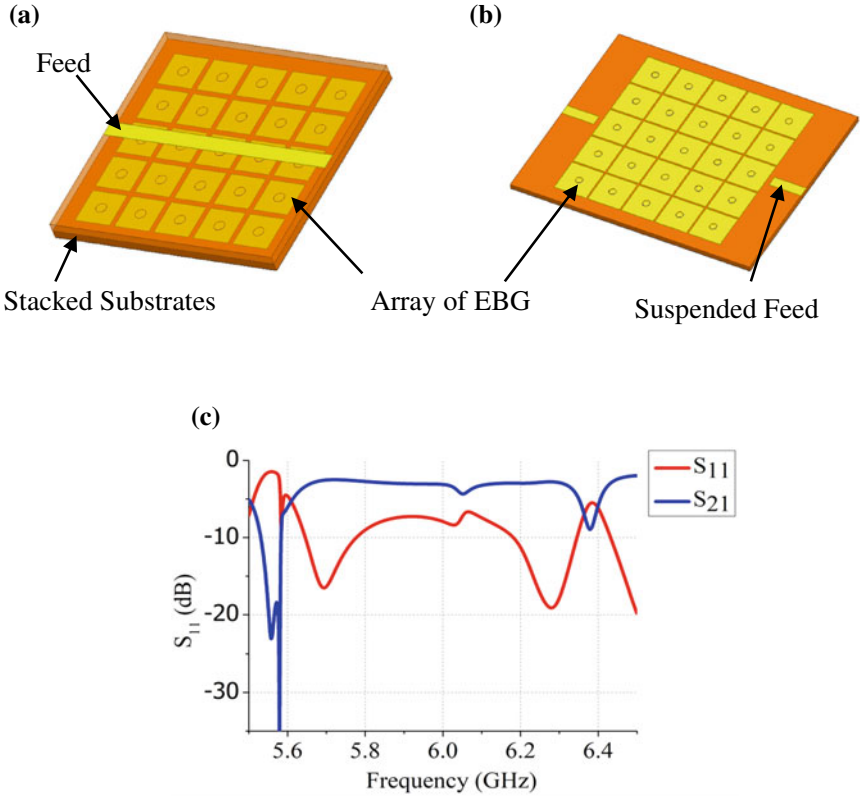

Fig. 3 Transmission line analysis with **a** full length feed **b** suspended feed **c** S_{11} and S_{21} plots

3 Three-Dimensional (3D) EBG

In the early years, only 3D EBGs have been designed. A successful attempt of 3D EBG design is obtained by Iowa State University called as woodpile structure. The 3D EBGs are periodically arranged in all three directions hence the name 3D EBG. The most important feature of these 3D EBGs is that they have complete bandgap, i.e. the propagation of electromagnetic fields is not allowed in any direction for any frequency. This property is used for base station antennas for enhancing gain [3]. A woodpile EBG is placed in front of a 1 × 4 array of slot antenna designed for 2.1 GHz with PEC reflector used at the rear side of antenna. The gain of antenna is enhanced to 14 dB from 5 dB by PEC reflector and it has been further enhanced to 17 dB by using EBGs. 3D EBGs have the advantage of preventing the propagation of EM fields in all directions, but they have a limitation that they are difficult to fabricate and integrate with antenna design.

4 Two-Dimensional (2D) EBG

4.1 Mushroom EBG

Mushroom EBG is one of the most commonly used 2D planar EBG structures. Figure 4 shows mushroom EBG along with its equivalent circuit. The structure consists of ground plane, dielectric substrate and periodic metal patch with vertical vias connecting periodic patch to ground plane.

The parameters that decide the performance of EBG are patch width W, gap width g, substrate height h, dielectric constant ϵ_r and via radius r. When $(W + g)$ is small compared to operating wavelength, EBG can be explained by using an equivalent lumped LC model. Mushroom EBG equivalent circuit can be represented by using L and C as shown in Fig. 4. The impedance value and resonant frequency are given by Eqs. (1) and (2), respectively.

$$Z = \frac{jwL}{1 - w^2LC} \tag{1}$$

$$f_0 = \frac{1}{2\pi\sqrt{LC}} \tag{2}$$

At resonant frequency, impedance tends to infinite and hence doesn't propagate any surface waves; whereas at low frequencies and high frequencies, TM and TE surface waves are supported, respectively. The value of capacitance is given by fringing capacitance between adjacent metal patches as given in Eq. (3):

$$C = \frac{W\varepsilon_0(1 + \varepsilon_r)}{\pi} \cosh^{-1}\left(\frac{W + g}{g}\right) \tag{3}$$

The inductance is generated because of the current loop consisting of vias and adjacent metal patches and it is given by Eq. (4):

$$L = \mu h \tag{4}$$

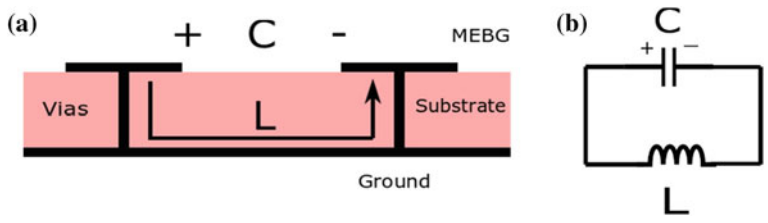

Fig. 4 **a** Side view of mushroom EBG with inductance and capacitance **b** equivalent circuit

In [4], the relationship between different shaped mushroom EBGs and their stop band range is discussed. In this paper, it has been shown that if the ratio of the occupied area (patch area) to the unit cell area (patch and periodicity combined structure) for different shaped EBGs is same, then the performance of the EBG design is also same irrespective of the shape of the EBG loaded patch. Hence the bandgap of EBG is dependent on the dimensions of patch, vias radius, substrate height, dielectric constant and periodicity and not on the shape of EBG.

4.1.1 The Influence of the Parameters on Stopband Range

Using full wave method analysis, a unit cell of mushroom EBG is designed to study the effect of different parameters on stopband range by studying the dispersion diagram. While the effect of one parameter is been studied, the other parameters are kept constant. An EBG with the dimensions given below is used as the reference EBG:

$$W = 0.137\lambda_{2.75\ \text{GHz}},\ g = 0.009\lambda_{2.75\ \text{GHz}},\ r = 0.009\lambda_{2.75\ \text{GHz}},$$
$$h = 0.014\lambda_{2.75\ \text{GHz}},\ \varepsilon_r = 4.4.$$

i. **Patch Width**

Different patch widths such as 0.091 $\lambda_{2.75\ \text{GHz}}$, 0.119 $\lambda_{2.75\ \text{GHz}}$, 0.155 $\lambda_{2.75\ \text{GHz}}$ and 0.183 $\lambda_{2.75\ \text{GHz}}$ have been analyzed.

When patch width increases, capacitance increases and hence the resonant frequency and bandwidth decreases. This is observed from Table 1, when the patch width increases, the lower frequency (f_l) and upper frequency (f_u) are decreased which consecutively decreases the bandwidth and resonant frequency.

ii. **Gap Width**

Different gap widths such as 0.00229 $\lambda_{2.75\ \text{GHz}}$, 0.0045 $\lambda_{2.75\ \text{GHz}}$, 0.009 $\lambda_{2.75\ \text{GHz}}$, 0.0183 $\lambda_{2.75\ \text{GHz}}$ and 0.027 $\lambda_{2.75\ \text{GHz}}$ are used for analysis.

Table 2 shows the effect of gap width on the bandgap. When gap width increases, capacitance decreases and hence resonant frequency and bandwidth increases. From Table 2, it has been perceived that when gap increases, the lower frequency decreases which increases the bandwidth.

Table 1 Effect of patch width on dispersion diagram

W ($\lambda_{2.75\ \text{GHz}}$)	f_l (GHz)	f_u (GHz)	BW (MHz)
0.091	3.98	4.82	840
0.119	3.01	3.47	460
0.137	2.6	2.9	300
0.155	2.24	2.49	250
0.183	1.87	2.05	180

Table 2 Effect of gap width on dispersion diagram

g ($\lambda_{2.75\ \text{GHz}}$)	f_l (GHz)	f_u (GHz)	BW (MHz)
0.00229	2.5	2.72	220
0.0045	2.54	2.78	240
0.009	2.57	2.91	340
0.0183	2.54	2.99	450
0.027	2.49	3.02	530

iii. **Vias Radius**

The vias radii considered are 0.00229 $\lambda_{2.75\ \text{GHz}}$, 0.0045 $\lambda_{2.75\ \text{GHz}}$, 0.009 $\lambda_{2.75\ \text{GHz}}$, 0.0137 $\lambda_{2.75\ \text{GHz}}$ and 0.0183 $\lambda_{2.75\ \text{GHz}}$ for analysis.

Table 3 shows the effect of vias radius on the bandgap. It is observed that when the vias radius increases, the lower frequency (f_l), upper frequency (f_u) and the inductance increases. The bandwidth also increases.

With a centred vias, a single resonant frequency for EBG is obtained. When the vias is offset along one direction either x-direction or y-direction, the reflection phase changes and the EBG design becomes polarization dependent. As a result, the patch gives two resonant frequency, one larger and other smaller than the original frequency.

iv. **Substrate Height**

The substrate height is altered from 0.0045 $\lambda_{2.75\ \text{GHz}}$, 0.009 $\lambda_{2.75\ \text{GHz}}$, 0.0183 $\lambda_{2.75\ \text{GHz}}$ and the effect of the substrate height is tabulated in Table 4. From the table, it has been realized that by changing the substrate height, the lower frequency, f_l decreases and the upper frequency f_u remains constant, which increases the bandwidth of the EBG design. When LC model is used for analyzing, it is observed that when height increases, inductance increases and hence resonant frequency decreases and bandwidth increases.

Table 3 Effect of vias radius on dispersion diagram

Vias radius ($\lambda_{2.75\ \text{GHz}}$)	f_l (GHz)	f_u (GHz)	BW (MHz)
0.00229	1.98	2.14	160
0.0045	2.23	2.44	210
0.009	2.57	2.91	340
0.0137	2.8	3.33	530
0.0183	2.96	3.76	800

Table 4 Effect of substrate height on dispersion diagram

h_{sub} ($\lambda_{2.75\ \text{GHz}}$)	f_l (GHz)	f_u (GHz)	BW (MHz)
0.0045	2.88	2.97	80
0.009	2.74	2.93	190
0.0137	2.47	2.90	430

Table 5 Effect of dielectric constant on dispersion diagram

ϵ_r	f_l (GHz)	f_u (GHz)	BW (MHz)
2.2	2.84	3.47	630
6.5	2.19	2.37	180
11.2	1.71	1.8	90

v. **Dielectric Constant**

Different substrates having almost the same loss tangent like Rogers R03003, Rogers R03006 and Rogers R03010 are considered. By changing the dielectric constant, the effect on stopband has been studied. From Table 5, it can be observed that for less dielectric constant, the bandwidth is maximum.

From the above parametric studies of the effect of parameters on stopband using dispersion diagram of a mushroom EBG, it has been concluded that for getting wide bandgap EBG, a thick substrate with low dielectric constant and less periodicity (less patch width and more gap width) should be used. The vias radius should be optimized such that resonant frequency is in the stopband range of the EBG.

4.2 Uniplanar EBG

Apart from mushroom EBG, the other 2D EBGs which has gained a lot of interest are uniplanar EBG. This EBG has no vias which makes the fabrication process easier than mushroom EBG. Similar to mushroom EBG, the uniplanar can be modelled with inductor and capacitance. The capacitance is generated due to spacing between two EBG patches. Instead of vertical vias, microstrip line is used for connecting the two patches which introduces an inductor. By inserting the microstrip line into patch or by using meandering line, the inductor can be increased. The capacitance can be increased by increasing the patch width and gap between the patches.

4.3 Spiral EBG

An important research topic in EBGs is minimizing the cell size of the EBG unit cell. Among the many techniques, Hilbert-curve focuses on the reduction of size and can be implemented for designing the EBGs. In Hilbert-curve designs, with increase in number of iterations, the inductance increases which results in lower resonant frequency. With the help of this concept, spiral EBGs are designed. In [5], a square EBG of 3.4 $\times$ 3.4 mm with periodicity 3.6 mm and with microstrip line width as 7.5 mm is used for designing a spiral EBG. Four closely spaced microstrip lines are used to get the spiral structure. The closeness of the microstrip lines helps in increasing the effective capacitance and effective use of the central area which increases the inductance and decreases the resonant frequency. When a layer of spiral

EBG is placed around a square radiating patch, a gain and bandwidth enhancement of 3 dB and 190 MHz are obtained.

A symmetrical spiral EBG is independent of the polarization and an unsymmetrical spiral EBG becomes dependent on the polarization of the surface waves. To maintain the symmetrical nature of EBG designs, double spiral and four arm designs are proposed.

4.4 Comparison of Mushroom, Uniplanar and Spiral EBGs

A mushroom EBG and a uniplanar EBG is designed with $W = 0.137\ \lambda_{2.75\ \text{GHz}}$, $g = 0.009\ \lambda_{2.75\ \text{GHz}}$, $h = 0.014\ \lambda_{2.75\ \text{GHz}}$ and $\varepsilon_r = 4.4$. The vias in mushroom EBG is designed with radius, $r = 0.009\ \lambda_{2.75\ \text{GHz}}$, and in uniplanar EBG, the microstrip line is designed with length, $l_s = 0.09\ \lambda_{2.75\ \text{GHz}}$. The full wave analysis has been done for both EBGs and compared. It is observed that for mushroom EBG, the stopband range is from 5 to 6 GHz with bandwidth 1 GHz. However for uniplanar EBG, it is obtained from 11 to 11.5 GHz. From the stopband range and resonant frequency, it has been established that a mushroom EBG has lower resonant frequency range with wide stopband range than uniplanar EBG. Though uniplanar EBG is easy to fabricate, it has high resonant frequency with narrow bandwidth making it less sensitive to incident angle and polarization.

Spiral EBGs help in decreasing the size of the EBG and hence the overall antenna size. The only drawback for spiral EBG is that it's very complicated to design and the optimization is difficult as the parameters used for designing such as microstrip line width, spacing between two lines which are dependent on each other changes the performance of EBG.

5 One-Dimensional EBG

One-dimensional EBGs are periodic in only one direction. They have periodicity of two different materials along one direction. These are simple and they have most of the features of 2D and 3D EBGs.

In [6], a MIMO antenna is designed with reflector designed with 1D EBG. To use the antenna for handset, the 1D patch and the strip lines are modified into spiral shape and placed as ground plane for the two-port MIMO antenna. The proposed design is extended for array of monopole antennas [7]. When the 1D EBGs are placed in between two monopoles, the mutual coupling is reduced by 42 dB and the radiation efficiency is increased to 82%.

6 Applications of EBGs

6.1 Gain and Bandwidth Enhancement

Boytayeb et al. [8] has created a cylindrical EBG substrate for enhancing the gain of antenna. A circular patch with coaxial feed placed 6 mm from the centre is designed for 2.6 GHz with gain 6 dB. The antenna design is surrounded cylindrically by metal strips as shown in Fig. 5. The concentric metal strips are etched with radial period of 21 mm with 2 mm gap between any two metal strips. On the metal strips, grounding vias of radius 1 mm and periodicity 10 mm is designed to achieve a gain improvement of 2 dB at 2.6 GHz. Mckinzie et al. designed 2 × 2 patch array with aperture feeding with '*I*' coupling slots on LTCC material at 60 GHz [9]. Along the strip line, mushroom EBG is placed to obtain a gain improvement of 3 dB. A polarization-dependent mushroom EBG is designed by creating two rectangular slots in the patch [10]. This new EBG design enhanced the gain of rectangular patch with coaxial feed by 2 dB at 3.3 GHz. By arranging the EBG in chessboard format, RCS of the antenna has been reduced by more than 4.3 dB at the resonance frequency.

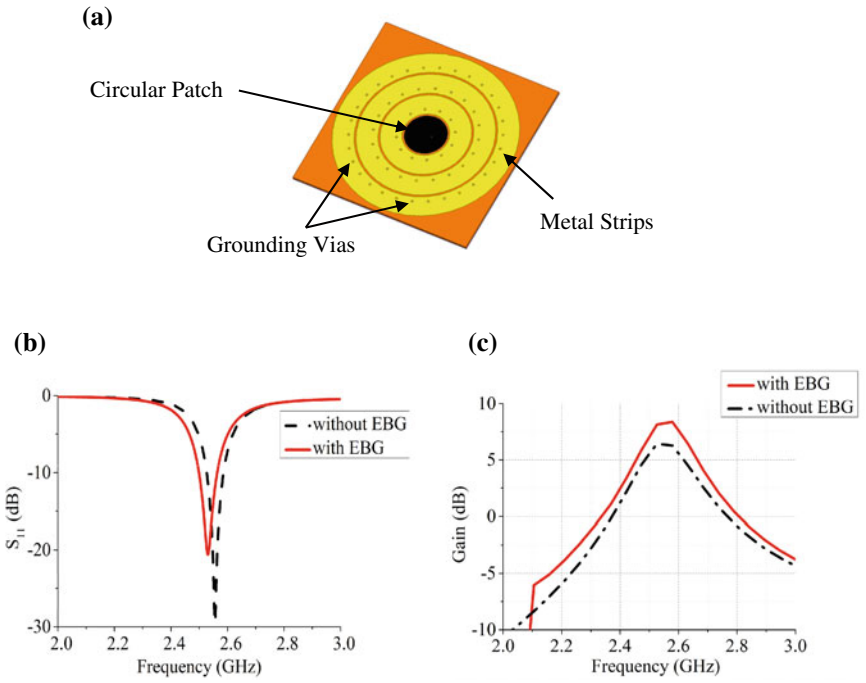

Fig. 5 **a** Design of circular patch with EBG **b** *S*-parameter **c** gain versus frequency with and without EBG

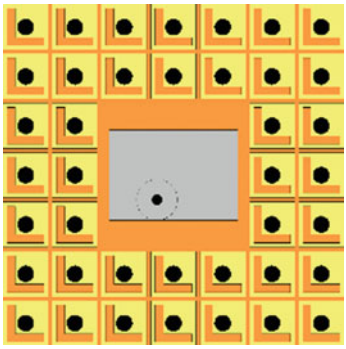

Fig. 6 Two layers of new EBG design placed around rectangular patch

Jiang et al. [11] presented that using EBG, a gain enhancement and RCS reduction can be achieved for 2 × 2 slot array. The design consists of the metallic ground with feeding network, substrate with leafshaped uniplanar EBG and an upper substrate with slot. The EBGs are placed in checker board format to enhance the gain by 2 dB and achieve 10 dB reduction of RCS in *X*-band for both polarizations. In [12], a new EBG is designed to enhance the gain of the rectangular patch by 1.2 dB. Two layers of the proposed EBG are placed around the patch to achieve gain enhancement as shown in Fig. 6.

In [13], two effects of EBGs, parasitic and cavity effects are discussed. Using the parasitic effect of mushroom EBG, the bandwidth of a coaxial fed patch antenna is enhanced. One row of mushroom EBG is placed at 15 mm ($\lambda/2$) distance from radiating edge in *E*-plane to get a bandwidth enhancement of 100 MHz. The transmission line analysis of mushroom EBG has been performed to get a bandwidth from 9.2 to 11.5 GHz [13]. For a dipole antenna with periodical arranged mushroom EBG, 40% of fractional bandwidth is achieved.

The uniplanar EBG placed on the package layer is modified by introducing a vertical inductive bridge [14]. Due to this variation, the EBG will have high impedance (high inductance) which increases the bandwidth. A new square loop slotted EBG with two vias has proposed in [15]. A transmission line analysis of 5 × 5 EBG array results in 320 MHz of bandwidth. With the introduction of multiple vias and square loop, the same results can also be achieved for reduced patch width. Further, the design is modified by using a hammer-shaped EBG with multiple vias and the transmission line analysis for this design is performed to obtain a bandwidth of 730 MHz [16].

6.2 Mutual Coupling Reduction

Designing array antennas for MIMO applications has gained importance in the recent years as they give high gain for a compact design and can be used for mobile communications. The important point that should be considered is that the isolation

between antennas should be large. To reduce these mutual coupling and to enhance the performance of the same, EBGs are used.

In [17], a leaf-shaped EBG is used to decrease the mutual coupling for 1 × 2 array of *E*-coupled patch antennas. An array of 4 × 3 of the proposed EBG is placed in between the array elements and a reduction of 20 dB is observed in the mutual coupling (S_{21}) of array design with EBG. In [18], a novel leaf-shaped EBG is designed to suppress the mutual coupling between two *E*-coupled rectangular patch antennas as shown in Fig. 7. The *E* fields on the substrate of the antenna with and without EBG are compared to show the mutual coupling reduction with the introduction of EBGs.

A new *H*-shaped EBG is proposed in [19]. Using this new EBG design, the mutual coupling between the circular patch antennas designed for 60 GHz for MIMO applications has been reduced. A 2 × 7 array of proposed EBGs is placed between two antenna elements. Using the same EBG, an isolation enhancement for two slotted aperture coupled DRA is achieved [19].

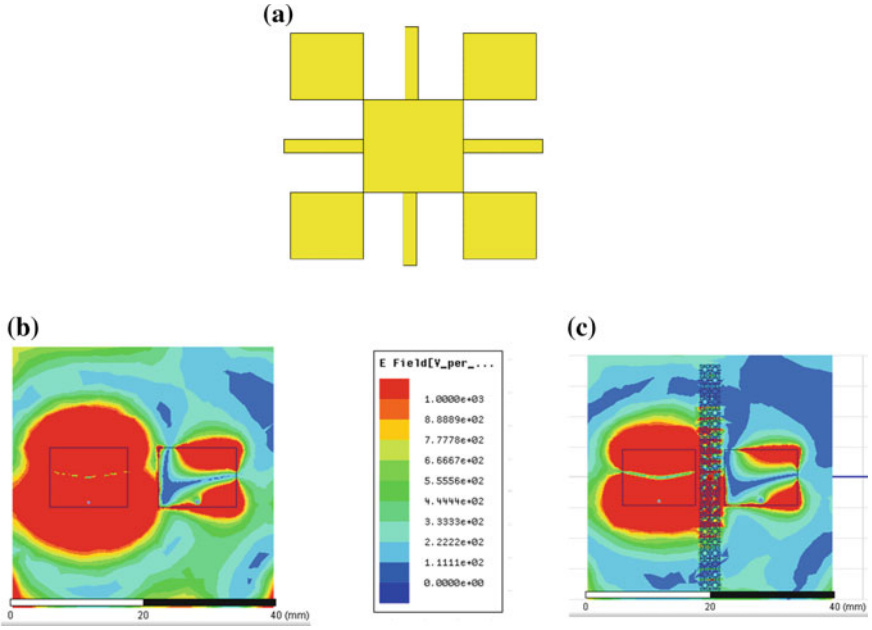

Fig. 7 **a** Proposed leaf shaped EBG **b** *E* fields without EBG **c** *E* fields with EBG

6.3 Biomedical Applications (SAR Reduction)

Nowadays, antennas are being used for wearable computing systems, communications for health monitoring, observing the vital signs in human, physical training, tracking and many more. In wearable systems, antennas play an important role and are placed in close proximity with human body. Hence the antenna used for these applications need to be robust, light weight, low profile and less coupling between human tissues and to meet the required SAR (Specific Absorption Rate) values. Using EBGs, the isolation between human body and the antenna is increased at the resonant frequency.

In [20], an *E*-shaped microstrip monopole is designed for 2.4 GHz on 0.7 mm denim material with conductive textile as the conductive layer. A uniplanar square loop EBG with four *T*-shaped slots is used to reduce the SAR. Due to introduction of slots, size of EBG is reduced and an array of EBGs is used as an AMC layer to reduce the backward radiations, hence reduces the SAR value from 6.19 to 0.0368 W/kg. Using jean fabric as the substrate, a microstrip patch antenna with inset feeding is designed [21]. One layer of mushroom EBG is placed around the patch to suppress the back lobes and hence reduces the SAR value from 0.04 to 0.0084 W/Kg. This concept is further modified by placing an *I*-slotted mushroom EBG rather than mushroom EBG [22]. The SAR values are reduced from 4.63 to 1.23 W/Kg.

6.4 Other Applications

EBGs are generally used with patch antenna for enhancing its gain or bandwidth and increasing the isolation in arrays. In recent years, they are used for wearable applications also. The efficiency of the antenna can also be increased by reducing the backlobe radiations. The other applications of EBGs include filter designing, reducing the scan blindness in beam steering antennas designs, increasing the electromagnetic compatibility. Using EBGs, frequency reconfigurability of the patches can also be achieved. EBGs are bandstop filters which can be cascaded to get multiple stopband ranges. By cascading of EBGs, the signal to noise ratio in PCBs can be enhanced for a large band of frequencies.

Another important application of EBG is an artificial ground plane design for wire antennas. Generally, dipole and monopole antennas have low efficiency when placed near a finite ground plane, as the image current and the actual current are in opposite directions. Hence, a compact antenna with less coupling effect of ground is difficult to design for wire antennas. To overcome this problem, an artificial ground plane using EBGs can be designed for wire antennas, which helps in reducing the coupling effect of the ground plane and a low-profile wire antenna can be obtained.

7 Conclusion

In this chapter, an overview of EBG theory is presented. The need for designing EBGs and how EBGs address the drawbacks of patch antenna is discussed. A large number of examples explaining the applications of EBGs in antenna, the procedure for decreasing the coupling in array antennas, wire antenna with ground are discussed. In PCB manufacturing, a wide signal to noise suppression is achieved with different EBG designs. Using EBGs, reduction in SAR values of antennas for wearable application can also be achieved.

References

1. Sievenpiper DF (1999) High impedance electromagnetic surfaces. PhD dissertation, University of California
2. Yang F, Rahmat-Samii Y (2009) Electromagnetic band gap structures in antenna engineering, 2nd edn. Cambridge University Press
3. Wongsan R, Kamphikul P (2016) Gain enhancement of slot array for base station using cavity of curved-woodpile metamaterial. In: 2016 International symposium on antennas and propagation (ISAP), pp 158–159
4. Hassan SMS, Mollah MN (2016) Identical performance from distinct conventional electromagnetic bandgap structures. IET Microwaves Antennas Propag 10(12):1251–1258
5. Ameelia Roseline A, Malathi K, Shrivastav AK (2011) Enhanced performance of a patch antenna using spiral-shaped electromagnetic bandgap structures for high-speed wireless networks. IET Microwaves, Antennas Propag 5(14):1750–1755
6. Kim SH, Lee JY, Nguyen TT, Jang JH (2013) High-performance MIMO antenna with 1-D EBG ground structures for handset application. IEEE Antennas Wirel Propag Lett 12:1468–1471
7. Lee JY, Kim SH, Jang J-H (2015) Reduction of mutual coupling in planar multiple antenna by using 1-D EBG and SRR structures. IEEE Trans Antennas Propag 63(9):4194–4198
8. Boutayeb H, Denidni TA (2007) Gain enhancement of a microstrip patch antenna using a cylindrical electromagnetic crystal substrate. IEEE Trans Antennas Propag 55(11):3140–3145
9. McKinzie WE, Nair DM, Thrasher BA, Smith MA, Hughes ED, Parisi JM (2016) 60 GHz LTCC patch antenna array with an integrated EBG structure for gain enhancement. IEEE Antennas Wirel Propag Lett 15:1522–1525
10. Han ZJ, Song W, Sheng XQ (2017) Gain enhancement and RCS reduction for patch antenna by using polarization-dependent EBG surface. IEEE Antennas Wirel Propag Lett 16:1631–1634
11. Jiang H, Xue Z, Li W, Ren W (2017) RCS reduction and gain enhancement for slot antenna array. In: 2017 IEEE international symposium on antennas and propagation & USNC/URSI national radio science meeting. San Diego, CA, USA, pp 2247–2248
12. Sravya RV, Kumari R (2018) Gain enhancement of patch antenna using L-slotted mushroom EBG. In: 2018 Conference on signal processing and communication engineering systems (SPACES). Vijayawada, pp 37–40
13. Goussetis G, Feresidis AP, Vardaxoglou JC (2004) Periodically loaded 1-D metallodielectric electromagnetic bandgap structures for miniaturisation and bandwidth enhancement. IEE Proceedings—Microwaves, Antennas Propag 151(6):481–485
14. Kim M, Koo K, Kim J, Kim J (2012) Vertical inductive bridge EBG (VIB-EBG) structure with size reduction and stopband enhancement for wideband SSN suppression. IEEE Microwave Wirel Compon Lett 22(8):403–405
15. Bhavarthe PP, Rathod SS, Reddy KTV (2017) A compact two via slot-type electromagnetic bandgap structure. IEEE Microwave Wirel Compon Lett 27(5):446–448

16. Bhavarthe PP, Rathod SS, Reddy KTV (2018) A compact two-via hammer spanner-type polarization-dependent electromagnetic bandgap structure. IEEE Microwave Wirel Compon Lett 28(4):284–286
17. Assimonis SD, Yioultsis TV, Antonopoulos CS (2012) Computational investigation and design of planar EBG structures for coupling reduction in antenna applications. IEEE Trans Magn 48(2):771–774
18. Arora A, Kumar N (2017) To reduce mutual coupling in microstrip patch antenna arrays elements using electromagnetic band gap structures for *X*-band. In: 2017 International conference on nextgen electronic technologies: silicon to software (ICNETS2). Chennai, India, pp 228–230
19. Al-Hasan MJ, Denidni TA, Sebak AR (2015) Millimeter-wave compact EBG structure for mutual coupling reduction applications. IEEE Trans Antennas Propag 63(2):823–828
20. Ashyap AYI et al (2017) Compact and low-profile textile EBG-based antenna for wearable medical applications. IEEE Antennas Wirel Propag Lett 16:2550–2553
21. Umar SM, Ahmad F, Khan WUR, Ullah S (2016) Specific absorption rate analysis of a WLAN antenna using mushroom-type electromagnetic bandgap (EBG) structure. In: 2016 13th International bhurban conference on applied sciences and technology (IBCAST). Islamabad, Pakistan, pp 631–635
22. Khan WUR, Umar SM, Ahmad F, Ullah S (2016) Specific absorption rate analysis of a WLAN antenna using slotted *I*-Type electromagentic bandgap (EBG) structure. In: 2016 International conference on intelligent systems engineering (ICISE), pp 110–115

Chapter 11
Survey on Dielectric Resonator and Substrate Integrated Waveguide-Based 5G MIMO Antenna with Different Mutual Coupling Reduction Techniques

Satyanarayan Rath and K. L. Sheeja

1 Introduction

The rapid growth and technological evolution of cellular communication technologies from 2G to 5G motivate the radio frequency researchers to consider the impedance bandwidth, data rates and latency of the transmitting antenna. So the low latency and high data rates are the most important key parameters of a transmitting antenna. Latency is related to processing speed and throughput is related to data rates [1].

In 3G though voice and broadband services are available, video calls are not possible. In 4G video calls were possible with data rates up to 100 Mbps [2, 3].

Though 4G standard supports high data rate, voice and video communication cannot be able to interface with the global IP network to achieve.

i. High scalability
ii. Energy efficiency of the network
iii. Connectivity of the network.

So diversification of 4G towards 5G is needed to improve the data rates and to lower the latency. At the end of 2020 implementation of 5G will be in compulsion to provide high quality service. Unlicensed 60 GHz spectrum is an attractive area of interest among all the 5G spectrums due to ultra-high data rates and low latency [4–6].

S. Rath (✉) · K. L. Sheeja
Department of Electronics & Telecommunication Engineering, VSSUT, Burla, Odisha, India
e-mail: satya_etc@yahoo.co.in

K. L. Sheeja
e-mail: sheejakl@gmail.com

R. Kumari and B. Choudhury (eds.), *Multiscale Modelling of Advanced Materials*,
Materials Horizons: From Nature to Nanomaterials,
https://doi.org/10.1007/978-981-15-2267-3_11

In order to implement 5G communication 5G antennas are needed. So attempts must be taken to design 5G antenna which must satisfy:

i. High bandwidth
ii. Minimum acceptable gain
iii. Low profile.

Earlier works say that dielectric resonator antenna provides lower mutual coupling levels. So DRA is a better choice to realize 5G antenna [7–10].

SIW fed antenna exhibits higher bandwidth and high gain if it will be interfaced to DRA [11].

So in order to meet the demands in the near future MIMO antenna can be a suggestive approach to facilitate the expected requirement such as data rate and latency. MIMO antenna possesses.

i. High interference reduction capability
ii. Gain diversity
iii. Multiplexing.

MIMO antenna is characterized by:

i. Envelope correlation coefficient(ECC)
ii. Degree of isolation.

ECC is directly related to mutual coupling between the ports of the antenna [7–10]. So in order to increase the spectral efficiency and ECC of MIMO antennas, care must be taken to reduce mutual coupling between the elements of the MIMO antenna.

The following isolation techniques may adopt to reduce the mutual coupling of the MIMO antenna according to applications [8–11].

i. DGS Structure in Ground Plane
ii. EBG Wall on The Substrate
iii. Meta Material Polarization-Rotator Wall
iv. Parasitic Element
v. Decoupling Network
vi. DGS Structure.

This chapter presents a logical approach to visualize 5G communication, DRA-based MIMO antenna, different isolation techniques of DRA-based MIMO antenna so that the comparison-based study leads to object-oriented approach.

2 5G Communication

As per the communication system standards data rates, impedance bandwidth and antenna gain are the three important antenna parameters which characterizes a communication system. Due to the rapid growth of communication enabling device the

number of devices connected to a communication network having Internet capability increases very fast with exponential distribution. As a result loading of network may occur. So a balanced loading is needed to overcome offloading. So if we diversify our current crowded operating frequency of the existing communication device or standard to a higher range of non-crowded carrier frequency then we can be able to achieve a balanced network [1–4]. So the communication requirements at the end of 2020 will enforce the communication users as well as communication providers to divert the existing communication standards from 4G to unlicensed 5G spectrum [6].

Taking the communication technology and communication standard into consideration the 5G spectrum may be classified as:

i. Spectrum below 6 GHz
ii. Spectrum above 6 GHz.

Spectrum below 6 GHz is specifically used where high coverage is required. Though maximum or optimum coverage is achieved, high data rate and high throughput are not achieved because data rate and throughput are directly dependent on carrier frequency. Though mobile communication is a better choice under 6 GHz for the current requirements, at the end of 2020 the updating of technologies in the field of mobile communication must be required to achieve data rates several hundred above the current data rate to meet the desired requirements. So it must be a compulsion to use 5G spectrum above 6 GHz in order to handle the high data rate mobile and wireless services [2–5].

We know coverage is inversely proportional to resonant frequency. But if we increase the resonant frequency then it will cause an increase in attenuation. So achievement of high data rate by increasing the resonant frequency causes significant increase in attenuation and decrease of coverage. So utilization of spectrum above 6 GHz is applicable to low coverage area. Hence to get maximum revenue spectrum above 6 GHz is applicable for high population density. So allocation of spectrum above 6 GHz is mainly assigned for urban areas. Use of unlicensed 60 GHz frequency is advisable for applications such as WLAN, WPAN and other specific indoor applications as the oxygen absorption phenomena is more at 60 GHz.

By taking the current use of spectrum, 5G spectrum may be classified as [1–4]:

i. Licensed 5G spectrum
ii. Unlicensed 5G spectrum.

As lower 5G spectrum will be crowded in the recent future, communication users and communication providers have to adopt unlicensed 60 GHz 5G spectrum. So the use of unlicensed 60 GHz carrier frequency is a courageous motivation to reduce the interference of spectrum and to achieving ultra-high data rates [1–3].

As high data rate, high impedance bandwidth with multiband features are the parameters achieved in case of unlicensed 60 GHz spectrum, these target requirements will be achieved to meet the expected demands at the end of 2020 [2–6].

3 5G MIMO Antenna

The requirement of data rate by the radio users is increasing very fast. So link capacity and spectral efficiency are the most motivated parameters in future communication. Link capacity can be assured by using multiple antennas at both transmitter and receiver sides irrespective of any modulation techniques. Similarly, spectral efficiency increases if we transmit many data signals over a single communication channel having multipath propagation. So MIMO antenna is a suggestive approach to assure high spectral efficiency and link reliability.

Multiple input multiple output (MIMO) is basically a communication technology which uses multiple radiating elements at both transmitter and receiver side to enhance the spectral efficiency.

As 5G antennas are active in nature and can be integrated, research can be done in 5G MIMO antenna to reduce the space of the antenna.

MIMO antenna is evaluated by means of

i. High degree of isolation between the antennas
ii. Envelope Correlation Coefficient(ECC).

High degree of isolation between the antennas can be obtained by increasing the physical separation between the elements of the antenna.

ECC is a function of mutual coupling and is proportional to coupling between the channels [7–10].

4 Isolation in 5G MIMO Antenna

Though MIMO antenna is capable to produce high link capacity, it suffers from high mutual coupling. Mutual coupling occurs due to the following parameters.

i. Surface wave
ii. Coupling between the feed lines
iii. Coupling due to spatial field
iv. Current produced in ground plane.

So care must be taken to reduce mutual coupling as high as possible; the mutual coupling can be reduced by increasing the physical separation between the antennas. The increase of physical separation between the antennas causes maximum space consumption by the MIMO antenna. So instead of increasing the physical separation between the elements of the MIMO antenna we may adopt the following mutual reduction techniques to improve isolations between the radiating elements.

i. Defective ground structure (DGS)
ii. Decoupling network
iii. Parasitic element

iv. Neutralization line
v. Electromagnetic Band Gap (EBG) structure
vi. Metamaterial Polarization-Rotator (MPR) wall
vii. Metasurface.

4.1 Defective Ground Structure

Implementation of DGS is capable to reduce mutual coupling if ground current or surface current exists in the ports between MIMO antennas. So DGS structure is capable to minimize surface current. In addition to minimizing ground current the DGS structure is also capable to provide high return loss and high gain. The DGS scheme is available in the following structure

i. Etching of slits and slots on the ground plane
ii. By placing slits on either sides of the patch.

4.2 Decoupling Network

Isolation between two consecutive elements of an antenna can be possible by introducing decoupling network between adjacent ports of a MIMO antenna. So the adjacent ports are decoupled from each other. This technique is mostly used for lower range of 5G spectrum.

4.3 Parasitic Element

Parasitic elements between the radiating elements of the MIMO antenna can be introduced to reduce mutual coupling. The parasitic element causes the creation of opposite coupling so as to minimize the existing coupling. This method is not suitable for 60 GHz operating frequency.

4.4 Neutralization of Line

Neutralization of lines in antenna theory is a technique where two adjacent antenna elements are separated by a distance such that mutual coupling is reduced. In other words neutralization line techniques cause a phase reversal between adjacent ports of a MIMO antenna. This method is applicable for lower range of mm waveband.

4.5 Electromagnetic Band Gap Structure

EBG structures are the periodic structures, which causes a frequency band gap so that surface wave propagation can be blocked to a large extent. The reduction of surface wave causes high isolation between the adjacent ports of a MIMO antenna.

4.6 Metamaterial Polarization-Rotator Wall

MPR wall is placed between the adjacent antenna elements of the MIM O antenna in which rotation of polarization occurs in such a way that the required isolation is achieved. Space reduction is the attractive features of MIMO antenna because the physical separation between the antenna elements of the MIMO antenna is less than half of the electrical wavelength at resonant frequency. Introduction of MPR wall between the adjacent port of the antenna is mainly used at 60 GHz frequency where untilted radiation pattern is achieved.

4.7 MetaSurface

Metasurface wall can be inserted between the adjacent ports to reduce mutual coupling. The metasurface is capable to reduce mutual coupling because for the operation band both the antennas are maintained orthogonal to each other. Metasurface wall is a better solution to reduce mutual coupling at 60 GHz resonant frequency. As metasurface acts as a band-stop filter, both sides of the wall are of different structures.

5 Related Research Work

Abdolmehdi Dadgarpour et al. had presented a suggestive technique to reduce the mutual coupling between two ports of a DRA-based MIMO antenna operating at 60 GHz resonant frequency. The effective reduction of mutual coupling was achieved by the incorporation of metasurface between two ports of the MIMO antenna arranged in H-field pattern [7].

The respective MIMO DRA structure is given in Fig. 1.

The MIMO antenna was consisting of multilayer substrate with two cylindrical dielectric resonators having relative permittivity of 10.2. The lower substrate was RT 6010 having dielectric constant of 10.2 and thickness of 0. 254 mm. The feed lines were constructed on the lower substrate which is required to excite the DRA's. The ground plane was located on the lower side of the substrate. The upper substrate was RT5880 having relative permittivity of 2.2 and thickness of 0.254 mm. The

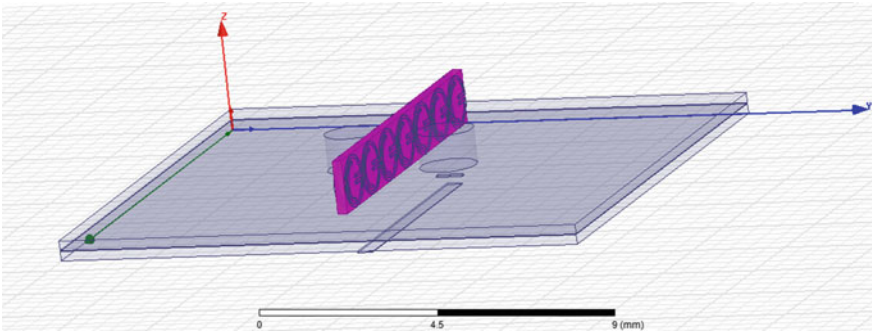

Fig. 1 MIMO DRA structure with metasurface shield

DRA's were placed on the top of the upper substrate whose dimensions were chosen in such a manner that maximum radiation occurred at 60 GHz frequency. Aperture coupling techniques were adopted using two rectangular slots to achieve the optimum bandwidth.

The metasurface wall used for reduction of mutual coupling is an array of split-ring resonator (SRR) which was integrated along E-Plane. The MPR wall consisting of seven-unit cell were arranged in a linear array. Each cell consists of two rings arranged in opposite manner. The gap between the rings is responsible for producing capacitances and the rings produce equivalent inductances. The unit cell split-ring resonators were arranged in an array to produce band-stop functionality between 57 GHz and 64 GHz.

The band-stop functionality was achieved by optimization of the size of individual SRR. The MPR wall was consisting of Roger RT 5880 as substrate having relative permittivity of 2.2, length of 14 mm, height of 2 mm and thickness of 0.254 mm. Each cylindrical dielectric resonator is having a radius of 0.75 mm and height of 0.95 mm. Aperture coupling techniques have been implemented to get improved bandwidth. The centre to centre distance between the two resonators is 2.5 mm.

The graph of S parameters of the MIMO antenna with metasurface and without metasurface signifies that the average isolation is around −18 dB over the frequency range of 57–64 GHz for MIMO antenna without MPR wall, but the implementation MPR wall between the ports of the DRA provides an average isolation of −30 dB over the frequency range of 57–64 GHz.

If we consider gain as the antenna parameter then we can state that MIMO antenna with metasurface is superior to MIMO antenna without metasurface by 1.5 dBi. The gain of the MIMO antenna without metasurface wall was 6.5 dBi and with metasurface was 7.9 dBi.

The graph of radiation pattern of the proposed MIMO antenna with and without metasurface gives the conclusion that the radiation pattern of the MIMO antenna with metasurface is tilted in nature, whereas the radiation pattern of the MIMO antenna without metasurface is untilted in nature.

Table 1 Result comparison

Sl. No	Parameter	Without metasurface	With metasurface
1	Average mutual coupling	−18 dB	−30 dB
2	Radiation efficiency	89%	91%
3	Bandwidth	7 GHz	7 GHz
4	Gain	6.5 dBi	7 dBi
5	Radiation pattern	Untilted	Tilted at 35°

The broadside radiation pattern of the proposed MIMO antenna with metasurface was found to be tilted of 35° around the main peak direction over the desired frequency range. Radiation pattern was not tilted in case of MIMO antenna without metasurface.

The radiation efficiency of the MIMO antenna without metasurface was found to be 89% and with metasurface was found to be 91%. The result comparison is given in Table 1.

Reza Karimian et al. had presented an efficient technique to reduce the mutual coupling between the ports of a MIMO antenna operating at 60 GHz resonant frequency using frequency selective surface wall. The reduction of mutual coupling was achieved due to the implementation of asymmetric frequency selective surface wall between the ports of the MIMO antenna [8].

The proposed MIMO antenna structure is given in Fig. 2.

The antenna was consisting of two cylindrical dielectric resonators made from RO3010 with relative permittivity of 10.2. The antenna consists of multilayer substrate. Both upper and lower substrate are made from RO3006 having dielectric constant of 6.15 and thickness of 0.8 mm each. The feed lines were constructed on the lower substrate which was used to excite the DRA's. The ground planes were located on the top of the lower substrate. The DRA's were placed on the top of

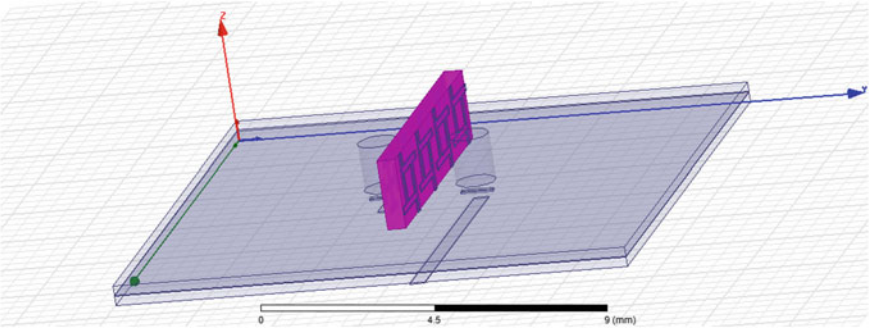

Fig. 2 Proposed MIMO antenna structure

Table 2 Dimension of single unit cell

Parameter	L1	L2	L3	L4	w
Length (mm)	0.625	0.75	0.75	1.325	0.2

the upper substrate whose dimensions were selected in such a manner that maximum radiation occurred at 60 GHz frequency. Aperture coupling technique was the feeding technique adopted in the antenna having two rectangular slots one for each cylindrical DRA to achieve the optimum bandwidth.

The frequency selective surface wall was used for the reduction of mutual coupling which was consisting of an array of frequency selective surface element (FSS) which are integrated on both sides of the wall made from RO 4003 having thickness of 0.5 mm and dielectric constant of 2.2. The wall is asymmetric because one side of the FSS wall is of Jerusalem cross specification and the other side is of fan structure so that the wall acts as band-pass filter.

The structure consists of four-unit cell arranged in a linear array to produce band-stop property in the desired band of the antenna to be operated.

The FSS wall is heterogeneous, i.e. one side of the wall is responsible for resonating at lower range of resonant frequency and the other side of the wall was resonating at higher range of resonant frequency so that the structure acts as a band-stop function.

The dimension of a single unit cell is listed in Table 2.

The band-stop functionality was achieved by optimization of the size of individual frequency selective surface.

The FSS wall is made from RO 4003 substrate having dielectric constant of 2.2, separate two cylindrical dielectric resonator having radius of 0.75 mm and height of 0.95 mm. Aperture coupling techniques have been implemented to get improved bandwidth. The centre to centre distance between the two resonators is 2.5 mm.

The graph of S parameters of the MIMO antenna without and with frequency selective surface proves that the average isolation is around −12 dB over the frequency range of 57–63 GHz for MIMO antenna without MPR wall but the implementation MPR wall between the ports of the DRA provides an average isolation of −30 dB over the frequency range of 57–63 GHz. If we consider the radiation pattern of the MIMO antenna with and without metasurface, then the conclusion led to slightly tilt of radiation pattern in H-Plane which was produced by the antenna with metasurface and untilted in the antenna with without metasurface.

If we consider gain as the antenna parameter then we can state that MIMO antenna with metasurface is superior to MIMO antenna without metasurface by 1.5 dBi.

The radiation efficiency of the MIMO antenna with metasurface was found to be 90% which is 1% more than that of radiation efficiency without metasurface. The envelope correlation coefficient was found to be 5e-6. The result comparison is given in Table 3.

Mohammadmahdi Farahani et al. had investigated and presented an efficient technique for reducing the mutual coupling between the adjacent ports of the

Table 3 Result comparison of MIMO antenna with and without metasurface

Sl. No	Parameter	Without metasurface	With metasurface
1	Average mutual coupling	−18 dB	−45 dB
2	Radiation efficiency	89%	90%
3	Bandwidth	7 GHz	6 GHz
4	Gain	Less than 3 dBi	3.9–4.8 dBi
5	Radiation pattern	Untilted	Tilted slightly

MIMO antenna operating at 60 GHz resonant frequency using meta material polarization-rotator wall [9].

The mutual coupling was reduced due to the implementation of meta material polarization-rotator wall between two DRA of the MIMO antenna placed in the H-field plane. Due to the meta material polarization-rotator wall, transverse electric modes of the antenna became orthogonal to each other. As a result, mutual coupling was reduced significantly.

Nearly 16 dB reduction of mutual coupling was achieved with ECC of 0.1e-6. The proposed MIMO antenna structure is given in Fig. 3

The antenna was consisting of two cylindrical dielectric resonators made from RT6010 with relative permittivity of 10.2. With the help of slots placed at the centre of the DRA antennas fundamental $HE_{11\delta}$ modes were excited. Both upper and lower substrates were made from RO30006 having dielectric constant of 2.2. The feed lines were constructed on the lower substrate which is required to excite the DRA's. The ground plane was located on the top of the lower substrate. The DRA's were placed on the top of the upper substrate whose dimensions were selected in such a manner that maximum radiation occurred at 60 GHz frequency. Aperture coupling techniques

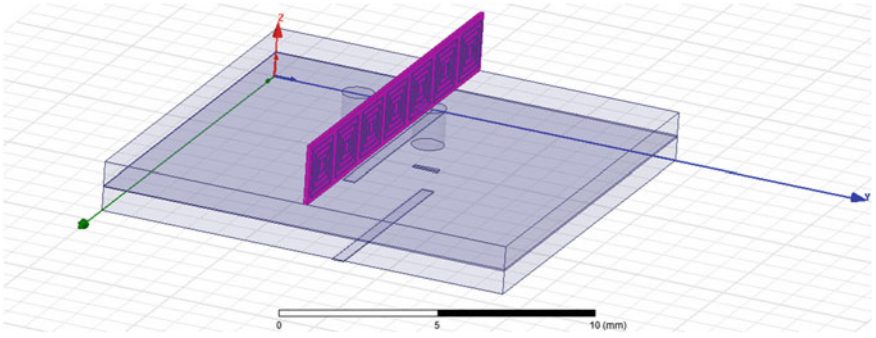

Fig. 3 The proposed MIMO antenna structure

Table 4 Antenna specification

	DRA
Radius	0.53 mm
Height	1.27 mm
Material used	Roger RT 6010
	Slot
Length	0.18 mm
Width	0.87 mm

were the feeding technique adopted in the antenna having two rectangular slots one for each cylindrical DRA to achieve the optimum bandwidth.

The antenna specification is attached in Table 4.

The MPR wall used for the reduction of mutual coupling was consisting of seven-unit cell arranged in a linear array.

The graph of S parameters of the MIMO antenna and radiation pattern without and with metasurface states that an average reduction of mutual coupling more than 16 dB (8 dB at 57 GHz, 22 dB at 60 GHz, 14 dB at 62 GHz) was achieved by the use of meta material polarization-rotator wall which is 6 dB above the MIMO antenna without meta material polarization-rotator wall.

The radiation pattern of the two-port MIMO antenna with meta material polarization-rotator wall was found to be non-tilted around the main peak direction over the desired frequency range. Broadside radiation pattern was tilted more than 30° in case of MIMO antenna with meta material polarization-rotator wall.

The radiation efficiency of the MIMO antenna without Meta material polarization-rotator wall was found to be 92% and with Meta material polarization-rotator wall was found to be 88%. The result comparison is given in Table 5.

Authors have investigated and presented electromagnetic band gap (EBG) structure to reduce the mutual coupling between the ports of MIMO antenna operating at 60 GHz resonant frequency [10].

The mutual coupling was reduced due to the implementation of EBG structure between two DRA of the MIMO antenna placed horizontally on the substrate. Due

Table 5 Result comparison

Sl. No	Parameter	Without metasurface	With metasurface
1	Average mutual coupling	−10 dB	−16 dB
2	Radiation efficiency	92%	88%
3	Bandwidth	7 GHz	7 GHz
4	Gain	–	–
5	Radiation pattern	Tilted at 35°	Untilted

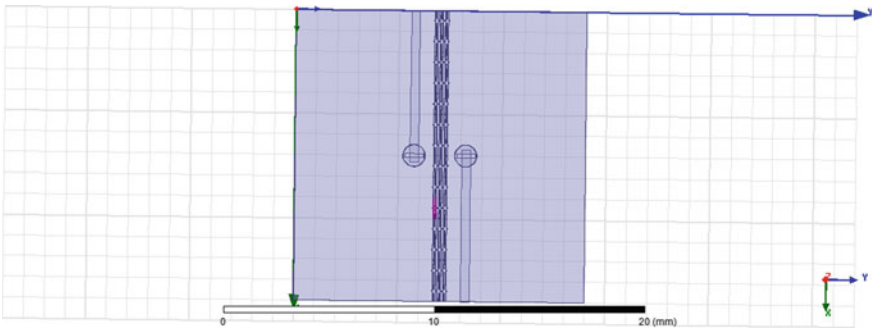

Fig. 4 The proposed MIMO antenna structure

to the EBG structure a band gap is created at the resonant frequency. TE modes of the antenna become orthogonal to each other. As a result, mutual coupling was reduced.

Nearly 16 dB average reduction of mutual coupling was achieved with the envelope correlation coefficient of 0.1e-6.

The presented MIMO antenna structure is given in Fig. 4.

The antenna consists of two cylindrical dielectric resonators made from RT6010 with relative permittivity of 10.2. With the help of slots placed at the centre of the DRA antennas fundamental $HE_{11\delta}$ modes were excited. The antenna was consisting of multilayer substrate. Both upper and lower substrate are made from RT5880 having dielectric constant of 2.2. The feed lines were constructed on the lower substrate which were required to excite the DRA's. The ground plane is located on the top of the lower substrate. The DRA's are placed on the top of the upper substrate whose dimensions are selected in such a manner that maximum radiation occurred at 60 GHz frequency. Aperture coupling techniques were the feeding techniques adopted in the antenna having two rectangular slots one for each cyllindrical DRA to achieve the optimum bandwidth.

The EBG structure used for reduction of mutual coupling was consisting of an array of splits which are integrated on the top surface of the substrate. The wall was made from Roger RT 5880 which is having the dielectric constant of 2.2. The structure consists of the unit cell arranged in a linear array.

The graph of S parameter and radiation pattern of the EBG structure-based MIMO antenna shows that on an average 16 dB (8 dB at 57 GHz, 22 dB at 60 GHz, 14 dB at 62 GHz) of mutual coupling was achieved by the implementation of electromagnetic band gap structure which is 6 dB above the MIMO antenna without electromagnetic band gap structure.

The graph of radiation pattern of the MIMO antenna with electromagnetic band gap structure states that the radiation pattern of the EBG structure-based MIMO antenna was found to be slightly tilted around the main peak direction over the desired frequency range. Radiation pattern was tilted more than 30° in case of MIMO antenna with meta material polarization-rotator wall. The result comparison is given in Table 6.

Table 6 The result comparison

Sl. No	Parameter	Without EBG structure	With EBG structure
1	Average mutual coupling	−12 dB	−35 dB
2	Radiation efficiency	–	–
3	Bandwidth	7 GHz	7 GHz
4	Gain	–	–
5	Radiation pattern	Tilted at 35°	Slightly tilted

Zhu et al. have proposed a wide-band linear polarized SIW fed antenna with complementary source. The SIW structure was capable to produce a bandwidth of 14 GHz with gain of 8.7 dBi [11].

A broad wall coupler having four ways was applied to 2 × 2 sub array which was able to reduce the cross polarization level of the antenna. Similarly taking base as 2 × 2 array 4 × 4 and 8 × 8 arrays were used to get high bandwidth.

The antenna geometry is given in Fig. 5

The planar dipoles excited with two vias had been adopted in place of inverted L-wires because the planar dipoles were able to work at millimeter wave frequency.

The presented antenna was consisting of two dipoles fabricated on the top surface of the substrate-1. The dipoles were aligned with reference to x-axis. For the ease of fabrication the edges of the dipole were maintained as curved surface. A cavity with length C_j was surrounded by two dipoles which was formed on substrate integrated waveguide (SIW). A square opening was done on the metal cladding of the upper surface of the substrate-1.

The energy was coupled to radiating elements from the SIW feed with the help of dipole which were fed separately by individual pair of vias placed on the opposite side of the slot. At the end of the slots two standing vias were placed which were

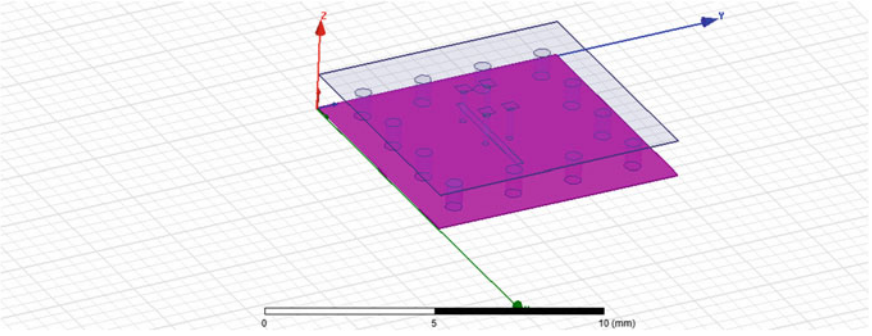

Fig. 5 The antenna geometry

Table 7 The dimensions of the antenna

Parameters	L1	L2	L3	L4	L5	L6	C1
Values	0.7	1.1	0.6	1.8	0.75	0.6	3.6
Parameters	R1	R2	R3	R4	S1	S2	W1
Values	0.25	0.15	0.15	0.35	0.8	1.2	2.4
Parameters	H1	H2	D1	D2	A1	B1	E1
Values	0.787	0.787	0.7	1.5	2.2	0.2	5

separated by a distance of 1.5 mm. So the antenna elements on substrate-1 became symmetric with respect to azimuthal axis (Both x and y).

The length and width of the slot were 2.2 mm and 0.2 mm, respectively, which are responsible to feed the radiating elements which were cut on the bottom surface of the substrate-1. Insertion of a metallic post was done in the substrate beside the slots as a result better impedance matching coupling of energy from SIW feed to radiating element occurs. Roger 5880 with relative permittivity of 2.2 and thickness of 0.787 mm was used for the PCB substrate. The dimensions of the antenna are given in Table 7.

The graph of different parameters of the antenna stated by the authors concludes that a peak antenna gain of 9.4 dBi was obtained which is much suitable at 5G communication compared to the existing techniques. A wide bandwidth of 14 GHz was achieved which is nearly twice that of existing methods. The graph of E-Plane and H-Plane radiation shows that a stable unidirectional radiation pattern in broadside direction having low cross polarization (−20bdB) was achieved.

6 Conclusion

In this chapter, the comparison base study of various 5G antennas resonating at 60 GHz frequency along with applicable isolation techniques were studied. Through the comparative study, this chapter clarifies that at 60 GHz frequency SIW-based antenna is a suggestive approach because it ensures higher bandwidth in comparison to other non-SIW structure. SIW-based DRA is the best solution at unlicensed 60 GHz frequency. To justify high spectral efficiency various isolation techniques were studied. The use of FSS structure is able to reduce mutual coupling to an extent of dB. But radiation pattern is tilting in nature. The other drawback is that the FSS structure network is not symmetric around the wall. So design and fabrication process is complex. The implementation of electromagnetic band gap structure in MIMO antenna is able to reduce vertical dimension of the antenna as a result size reduction occurs but high bandwidth in comparison to FSS structure is not achieved. Also the radiation pattern is tilting in nature. The use of meta material polarization-rotator wall between the ports of a MIMO antenna is able to produce a non-tilted radiation pattern in the broad side direction. But gain achievement is less compared to

FSS structure. The SIW-based antenna ensures high gain compared to other existing antennas at 60 GHz frequency. So through this chapter it can be clarified that the substrate integrated waveguide-based dielectric resonator antenna with meta material polarization-rotator wall is a better solution to get non-tilted high bandwidth and high gain antenna applicable for unlicensed 60 GHz 5G communications. This comparison-based study chapter found that all the isolation techniques have been designed for same resonant frequency. So this chapter suggests that substrate integrated waveguide-based multiple antennas with different resonant frequencies can be embedded on a common substrate with meta material polarization-rotator wall. Multiband applications are another challengeable area which has not been analyzed through these comparative researches. So substrate integrated waveguide-based multiple antennas with different resonant frequencies and multibands can be embedded on a common substrate with meta material polarization-rotator wall.

References

1. Ancan G, Bobrovs V, Ancans A, Kalibatiene D (2017) Spectrum considerations for 5G mobile communication systems.‖ Procedia Comput Sci 104:509–516
2. Shimodaira H, Tran GK, Sakaguchi K, Araki K (2015) Investigation on millimeter-wave spectrum for 5G. In: 2015 IEEE conference on standards for communications and networking (CSCN), pp 143–148
3. Mitra RN, Agrawal DP (2015) 5G mobile technology: a survey. ICT Express 1:132–137
4. Shimodaira H, Tran GK, Sakaguchi K, Araki K(2015) Investigation on millimeter-wave spectrum for 5G. In: 2015 IEEE conference on standards for communications and networking (CSCN), pp 143–148
5. Wang T, Li G, Ding J, Miao Q, Li J, Wang Y (2015) 5G spectrum: is China ready? IEEE Commun Mag 53(7):58–65
6. Wireless Gigabit Alliance, Beaverton. www.wirelessgigabitalliance.org
7. Dadgarpour Abdolmehdi, Zarghooni Behnam, Virdee BS, Denidni Tayeb, Kishk Ahmed (2016) Mutual coupling reduction in dielectric resonator antennas using metasurface shield for 60 GHz MIMO systems. IEEE Antennas Wirel Propag Lett 16:1–1. https://doi.org/10.1109/LAWP.2016.2585127
8. Karimian R, Kesavan A, Nedil M, Denidni TA (2016) Low power mutual coupling 60 Ghz MIMO antenna system with frequency selective surface wall. IEEE Antennas Wirel Propag Lett. https://doi.org/10.1109/lawp.2016.2578179
9. Farahani M et al (2017) Mutual coupling reduction in millimeter-wave MIMO antenna array using a metamaterial polarization-rotator wall. IEEE Antennas Wirel Propag Lett. https://doi.org/10.1109/lawp.2017.2717404
10. Al-Hasan MJ, Denidni TA, Sebak AR (2014) Millimeter-wave compact EBG structure for mutual coupling reduction applications. IEEE Trans Antennas Propag. https://doi.org/10.1109/tap.2014.2381229
11. Zhu Q, Ng KB, Chan CH, Luk K-M (2017) Surface—integrated-waveguide—fed array antenna covering 57–71 Ghz band for 5G application. IEEE Trans Antennas Propag. https://doi.org/10.1109/tap.2017.2723080